UNIVERSITÀ DEGLI STUDI DI SALERNO

Dipartimento di Fisica E.R. Caianiello

CORSO DI DOTTORATO DI RICERCA IN FISICA E TECNOLOGIE EMERGENTI

XXXVIII Ciclo

TESI DI DOTTORATO

Surface and Interface Effects in Transition-Metal-Dichalcogenide-based Functional Optoelectronic Devices

Supervisor:

Prof. Antonio Di Bartolomeo

Candidata:

Kimberly Intonti

Matr.: 8860200004

Coordinatore di dottorato:

Prof.ssa Roberta Citro

ANNO ACCADEMICO 2024/2025

Table of Contents

Introduction

Two-dimensional (2D) transition metal dichalcogenides (TMDs) have attracted significant interest in recent years as versatile building blocks for next-generation electronic and optoelectronic technologies. Their atomic-scale thickness, large surface-to-volume ratio, tunable band structures, and strong light-matter interactions enable a rich variety of transport and photoresponse mechanisms, while simultaneously making their physical behaviour highly sensitive to the surrounding environment, the presence of structural defects, and interface quality. As a result, understanding and controlling the interplay between material properties, device architecture, and external stimuli represents a crucial step toward reliably integrating 2D materials into functional optoelectronic devices.

Chapter 1 provides an overview of the structural, electronic, optical, and mechanical properties of TMDs, together with a description of synthesis techniques, device fabrication procedures, and the main application fields. It also discusses the main technological challenges that must be addressed to enable the effective integration of 2D materials into advanced electronic platforms, including digital, analog, and AI chips.

Chapter 2 introduces the experimental methodologies employed throughout this thesis, spanning morphological and spectroscopic characterization, adsorption-related processes, and the key electrical and optoelectronic figures of merit used to assess charge transport and photogeneration mechanisms in transistors and photodetectors. In its final part, it reports the specifics of the instruments used in this work.

The following chapters summarize the main experimental outcomes of the PhD research activity, progressively moving from material stability and interface control to device-level optimization and multifunctional optoelectronic functionalities.

A key prerequisite for the development of reliable 2D technologies lies in ensuring stable surfaces and high-quality interfaces. In this context, Chapter 3 investigates the evolution over time of the oxidation process of $ZrSe_2$, an air-sensitive group-IV TMD. Because its oxidation naturally produces a technologically relevant high-k oxide, $ZrSe_2$ offers the opportunity to achieve a clean and smooth 2D semiconductor/oxide interface. Through a synergistic combination of AFM, SEM, STM, STEM-EDX, XPS, Raman spectroscopy, and DFT

simulations, this chapter elucidates the oxidation-driven transformation of $ZrSe_2$. Oxidation is found to initiate at surface defects and edges, leading over time to the formation of Se-rich protrusions and nanowires. Encapsulation is therefore required to limit these degradation pathways, underscoring the decisive role of surface passivation and interface quality for robust device operation. Further details are reported in the work "*Oxidation-driven structural, chemical and electrical transformation in $ZrSe_2$*" by K. Intonti et al. (Materials Today Advances, DOI: https://doi.org/10.1016/j.mtadv.2025.100654).

Whereas Chapter 3 focuses on material oxidation as a stability constraint, other TMD semiconductors are characterized by reversible surface interactions with ambient species. In this case, surface-mediated processes represent both a source of tunability and a key performance bottleneck, motivating a systematic investigation of their impact on device properties.

Chapter 4 explores this interplay through pressure- and temperature-dependent studies of few-layer ReS_2 field-effect transistors. At ambient pressure, adsorption of air molecules at surface defect sites introduces electron trapping, reducing conductivity and mobility, broadening hysteresis, and giving rise to slow photocurrent dynamics with persistent photoconductivity. Progressive desorption under vacuum enhances carrier density and leads to a faster and more reproducible photoresponse, as reported in the study "*Pressure-dependent photoconductivity in two-dimensional ReS_2*", by K. Intonti et al. (IEEE Xplore, DOI: 10.1109/NMDC57951.2023.10343870).

Temperature-dependent measurements in the 80–350 K range further elucidate trap-mediated and contact-limited transport at the Cr/Au–ReS_2 and SiO_2-ReS_2 interfaces, enabling the estimation of the Schottky barrier height and interface trap density. The photoresponse evolves from fast and linear dynamics at low temperature to slower rise and decay times at elevated temperatures, driven by enhanced bolometric contributions and thermally activated surface processes, as discussed in "*Temperature-dependent conduction and photoresponse in few-layer ReS_2*" by K. Intonti et al. (ACS Applied Materials & Interfaces, DOI: 10.1021/acsami.3c12973).

These results confirm the critical role of surface defects and interface traps in determining the response of 2D-based devices, particularly in terms of speed and stability. Motivated by the need for more robust and efficient architectures, Chapter 5 explores mixed-dimensional ReS_2/Si van der Waals heterojunctions, where a vertical built-in electric field enables rapid separation of photogenerated carriers and more reproducible switching behaviour.

The 2D ReS_2/3D Si van der Waals heterojunctions combine the strong light–matter interaction and direct bandgap of ReS_2 with mature silicon processing technology. The ReS_2/n-Si device exhibits diode-like behaviour in the dark, consistent with first-principles calculations confirming a type-II band alignment at the ReS_2/Si interface. A linear, stable, multimode

photodetection response is recorded under illumination, enabling self-powered operation with fast microsecond-scale switching and a responsivity of approximately 0.10 mA/W at 10 mW incident power. All these results are published in "*ReS_2/Si 2D/3D Vertical Heterojunction as a Self-Powered Photodiode*" by K. Intonti et al. (Applied Physics Letters DOI: 10.1063/5.0231243). Further optimization of the device geometry and fabrication process yields improved responsivity (up to 10^3 A/W) and enhanced weak-signal detectivity across the visible-NIR range, with reliable operation also at low temperature.

Beyond ensuring stability and interface control, this thesis also demonstrates in Chapter 6 how the intrinsic responsiveness of 2D materials can be exploited to realize adaptive and multifunctional electronic architectures. Ambipolar semiconductors were selected because their band structure enables both p- and n-type conduction, providing a wider and more versatile set of electro-optical responses than unipolar 2D materials.

In this framework, a $MoTe_2$-based FET is shown to exhibit gate-tunable bidirectional photoconductivity, where both positive and negative photocurrent emerge depending on the electrostatic configuration and the dynamics of interface trap states, providing a proof-of-concept analogy with retinal ON/OFF-like responses. Results are published in *"Gate-driven bi-directional photoresponse in $MoTe_2$-based field effect transistors"* by K. Intonti et al. (IEEE Xplore, DOI 10.1109/NANO63165.2025.11113515).

A light-induced transition from ambipolar to anti-ambipolar behaviour is observed in WSe_2-based transistors. The resulting characteristic Λ-shaped transfer curve gives rise to three distinct current levels across different gate-voltage regions. This multilevel behavior can enable ternary or multi-bit logic architectures, extending beyond conventional binary operation. The results of the study are reported in *"Ambipolar to anti-ambipolar light-induced transition in WSe_2-based FETs"* by K. Intonti et al. (Materials Horizons, DOI: https://doi.org/10.1039/D5MH01871D)

As summarized in the Conclusions, this thesis provides a cohesive framework that connects fundamental mechanisms, device optimization, and advanced optoelectronic functionalities. By systematically examining how structural properties, external stimuli, and device architecture influence charge transport and photoresponse in 2D semiconductors, it highlights the versatility and technological potential of TMD-based systems. Overall, this work offers design guidelines for developing more reliable, efficient, and reconfigurable photodetectors and adaptive nanoelectronic architectures based on 2D materials.

Chapter 1

The roadmap of 2D Materials and Devices

2D materials properties, applications, and future perspectives

1.1 Introduction

Since the introduction of integrated circuits in 1958, technological progress has been driven by Moore's law, which has served as a benchmark for scaling, performance enhancement, and cost reduction in semiconductor devices.

In 1965, Gordon Moore predicted that the number of components integrated on a chip at minimum cost would double every year, a 'prediction' later adjusted to every two years[1]. This trend, later known as 'Moore's law', has guided the evolution of microelectronics for five more decades, through continuous transistor miniaturization[2]. However, starting from the early 2000s, as device dimensions approached the nanoscale, conventional silicon-based transistors have faced serious limitations. Effects such as enhanced carrier scattering due to thickness fluctuation, mobility degradation, increased leakage currents caused by quantum tunneling, heat dissipation issues, and other short-channel effects progressively constrained device performance and scalability[3,4]. To overcome these challenges, innovation has increasingly shifted from pure dimensional scaling toward functional scaling approaches. These include the introduction of strained silicon, high-k gate dielectrics, and advanced transistor architectures such as FinFETs, gate-all-around FETs (GAAFETs), and complementary FETs (CFETs)[5,6]. While these strategies have successfully extended the 'More Moore' paradigm, further progress requires disruptive technological breakthroughs. At the same time, the demand for higher computational power and increased integration density continues to rise, driven by emerging fields such as the Internet of Things and artificial intelligence. These technological pressures have shifted attention toward finding new materials and device concepts in the More Moore challenge. At the same time, two complementary routes have been delineated: 'More than Moore', which enhances system functionality through heterogeneous integration, improved circuit designs, and new applications; and 'Beyond Moore', which pursues unconventional device concepts for memory, neuromorphic and quantum technologies[7,8].
In this context, exploring new semiconductor materials capable of maintaining strong

electrical performance at extremely small dimensions is crucial. Two-dimensional (2D) materials have emerged as promising candidates due to their atomically thin, dangling-bond-free structure that enables high mobilities even below 1 nm, suppresses leakage currents, and ensures exceptional gate control allowing channel lengths to be scaled beyond the limits of silicon[9]
. Their ultrathin bodies also reduce parasitic capacitance, enabling high operating frequencies. Moreover, 2D materials demonstrate compatibility with silicon and they offer unique advantages for monolithic 3D integration since they can be synthesized or transferred as freestanding layers[10,11].

These features position 2D materials as strong contenders across all three development pathways:

- More Moore - as next-generation channel materials capable of extending CMOS scaling;
- More than Moore - owing to their high surface-to-volume ratio, mechanical flexibility, and compatibility with heterogeneous integration for sensing, flexible electronics, and photonics[12–14];
- Beyond Moore - through their quantum properties and potential use in neuromorphic and quantum devices[15–17].

Despite this promise, several bottlenecks hinder their full incorporation into semiconductor manufacturing. Large-scale synthesis of single-crystal 2D films remains challenging, and device processes often lack compatibility with current foundry standards. Variability in material quality, contact engineering, and dielectric integration further limit reproducibility compared to mature silicon technology[18]. However, even if 2D materials may not yet support complex circuit integration, they are expected to enter back-end-of-line processing by around 2032 according to IMEC projections[19,20]. Therefore, this chapter provides a short review of the main properties, applications, and challenges of these materials.

1.2 Transition metal dichalcogenides

Graphene was the first 2D material to be discovered, in 2004, through mechanical exfoliation. It rapidly attracted global attention for its exceptional properties, including high transparency, superior thermal and electrical conductivity, and a large specific surface area[21]. These characteristics enable a wide range of applications, such as energy storage, solar cells, aerospace composites, catalysis, and the hydrogen evolution reaction. However, graphene's integration into digital electronics is limited by its zero-energy bandgap. Consequently, research has shifted toward other 2D materials, with Transition Metal Dichalcogenides (TMDs) emerging as leaders in the field due to their versatile and unique semiconductor properties.

1.2.1 Structural properties

TMDs are a large family of 2D materials with molecular formula MX_2, where M is a transition metal (TM) of groups 4-10 and X is a chalcogen (S, Se or Te). The M-X covalent bond length

depends on the size of both the transition metal and the chalcogen ion, and it varies approximately between 3.15 and 4.03 Å[22].

The TMDs can be layered or non-layered depending on the TM belonging to groups IV-VII or VIII-X in the periodic table. Group IV-VII TMDs are predominantly layered, while some group VIII-X TMDs are commonly found in non-layered structures. Each layer typically has a thickness of 0.6-0.7 nm, consisting of a plane of metal atoms sandwiched between two planes of chalcogen atoms[23,24].

According to the coordination of the transition metal atom, single layer TMDs can crystallize in various structural phases such as trigonal prismatic (2H), octahedral (1T) or distorted octahedral (1T'). In the 2H phase the three atomic planes follow an ABA stacking sequence along the c-axis, where the top and bottom chalcogen atoms are aligned vertically. Each metal atom is covalently bonded to six chalcogen atoms in a trigonal prismatic coordination, resulting in a honeycomb lattice when viewed from the top, as shown in Figure 1.1[24,25]. This phase is typically semiconducting and is thermodynamically stable at room temperature for most group VI TMDs.

The 1T phase adopts an ABC stacking sequence, in which the two chalcogen atoms are positioned along a vertical line passing through the central metal atom, leading to octahedral coordination. This configuration produces a hexagonal lattice, shown in Figure 1.1, and is generally metallic[26]. The dimerization-induced distortion of transition metal atoms along the z direction modifies the displacements of X atoms in the same direction resulting in the 1T′ phase, which can exhibit semimetallic or topologically non-trivial electronic properties[27]. In both 2H and 1T structures, the primitive unit cell contains one transition metal atom and two chalcogen atoms. The relative stability of these phases depends on the specific transition metal, the chalcogen species, and external factors such as strain or doping. In a macroscopic bulk crystal structure with an even number of layers, the crystal structure has an inversion center. In the monolayer case or for any odd number of layers, the crystal may or may not have an inversion center. As a consequence, the lack of inversion symmetry allows unusually strong optical second harmonic generation (SHG) in monolayer structure[28].

According to the ligand field theory, the metallic nature of the 1T phase is caused by the partially filled t_{2g} band (d_{xy}, d_{xz}, d_{yz}). In contrast, the semiconducting behavior of the 2H phase is due to the filled d_{z2} and empty d_{xy} and $d_{x^2-y^2}$ orbitals[23]. The type of symmetry adopted by a TMD depends primarily on d orbital filling. Group IV TMDs preferentially adopt the 1T phase, whereas both octahedral and trigonal prismatic phases are observed in group V TMDs[29]. Group VI TMDs exhibit the 2H phase, and group VII are typically in a distorted octahedral structure. Group X TMDs are all in an octahedral arrangement[30].

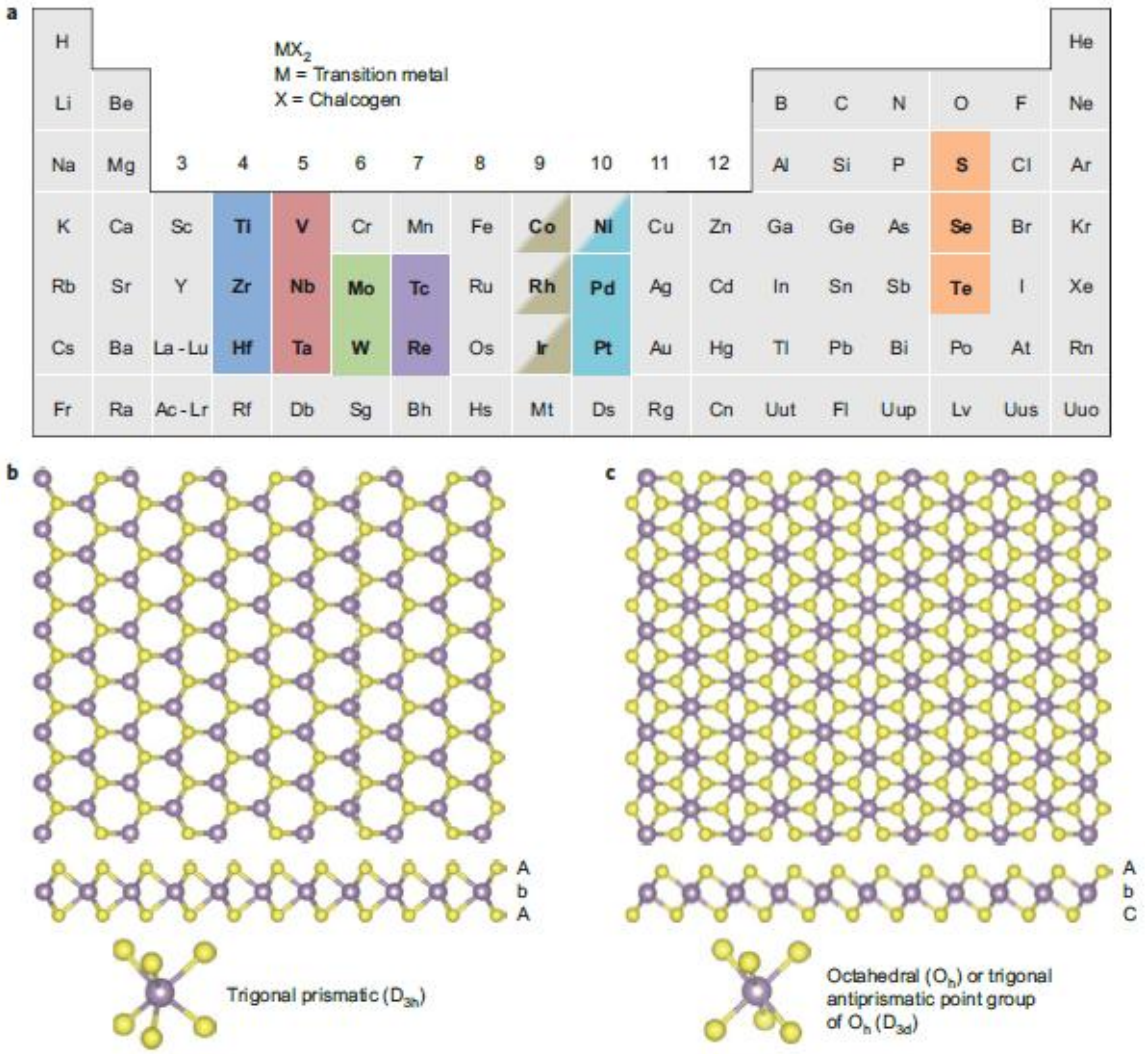

Figure 1.1: About 40 different layered TMD compounds exist. The transition metals and the three chalcogen elements that predominantly crystallize in layered structure are highlighted in the periodic table. Partial highlights for Co, Rh, Ir and Ni indicate that only some of the dichalcogenides form layered structures. (b),(c), *c*-Axis and section view of single-layer TMD with trigonal prismatic (b) and octahedral (c) coordinations[31].

1.2.2 Electronic properties

One of the key advantages of 2D TMDs is the variety of electronic properties they exhibit, spanning from semiconductors to superconductors depending on their chemical composition. Depending on the material, TMD-monolayers exhibit a broad spectrum of bandgaps, as evident from Figure 1.2, covering the visible to near-infrared spectral range (0.5-2 eV)[26,32,33]. As a result of quantum confinement effects and changes in the hybridization between transition-metal and chalcogen atomic orbitals, many TMDs, such as those in Figure 1.3, experience a transition from an indirect to a direct bandgap when reduced from the bulk to the monolayer limit[34].

This transition leads to a pronounced increase in light absorption and photoluminescence efficiency.

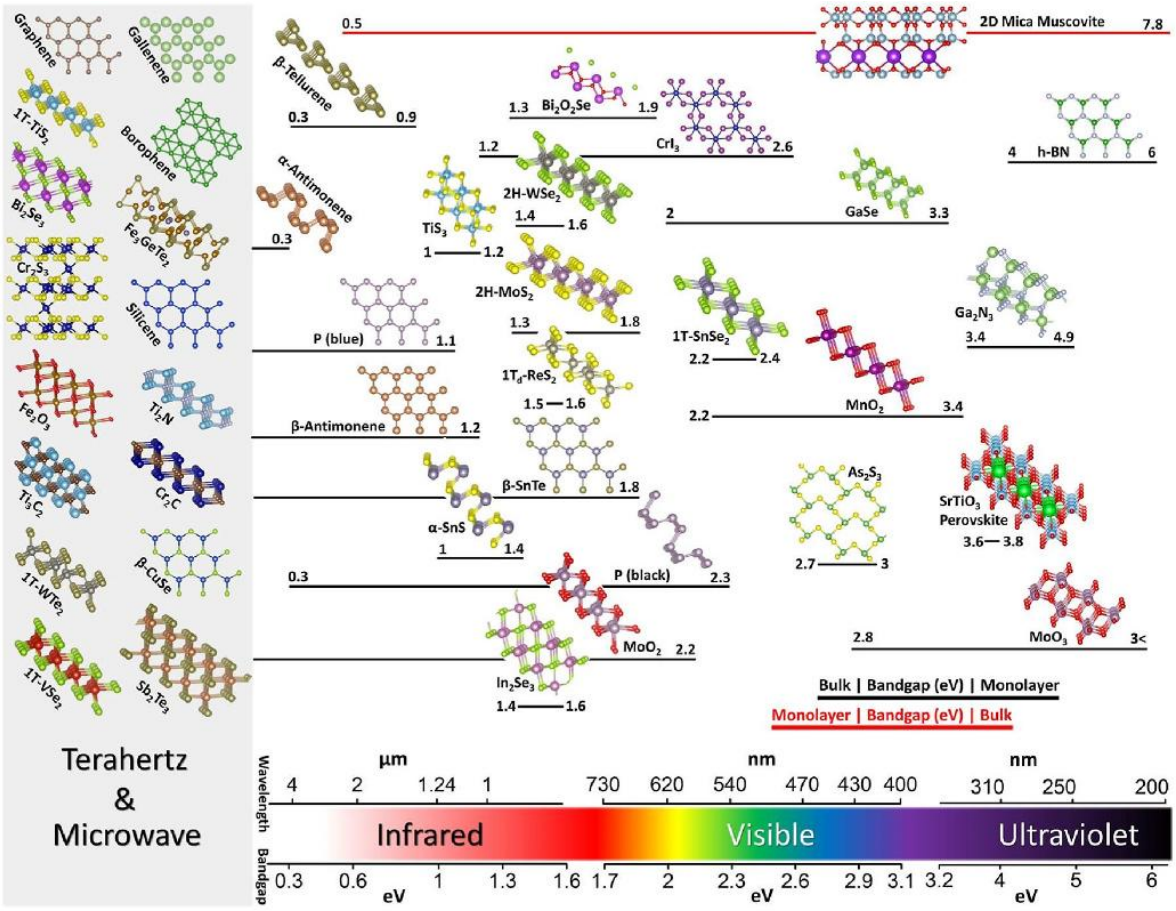

Figure 1.2: Bandgaps of a selected family of 2D materials[33].

The electrical properties of TMDs can be widely tuned through thickness control, substitutional doping, mechanical deformation, plasma treatments, and electrostatic gating[35–38]. This tunability enables access to different transport regimes and allows control over carrier type, concentration, and mobility. Owing to their atomically thin nature, TMDs exhibit strong electrostatic control but also enhanced sensitivity to their surrounding environment, which makes their electrical response strongly dependent on surface chemistry and interfaces.

Further degrees of freedom arise from van der Waals heterostructures (vdW Hs) formed by stacking different 2D materials[39,40]. In these systems, interlayer coupling and band alignment govern charge transfer, band offsets, and carrier separation, enabling tailored electronic and optoelectronic functionalities. The absence of dangling bonds at the surface of 2D materials facilitates the formation of clean and mechanically flexible interfaces, while interface quality remains a key factor in determining device performance.

1.2.3 Optical properties

The optical properties of TMDs are closely related to their band structure. In particular, the transition to a direct bandgap that most TMDs undergo when reduced to the monolayer form is a desirable feature for optoelectronic applications and visible-light photodetectors[41]. With regard to optical absorption, the material can absorb photons with energy greater than the bandgap energy. Experimental techniques such as UV–Vis spectroscopy, photoluminescence, and Raman spectroscopy are widely used to study these properties. In most TMDs, the photoluminescence intensity strongly depends on the number of layers and increases significantly when the material is thinned from multilayer to monolayer form.[42,43]

Strong quantum confinement and reduced dielectric screening in two dimensions lead to enhanced Coulomb interactions and the formation of tightly bound excitons with large binding energies, which dominate the optical response even at room temperature[44–46]. Consequently, the optical conductivity and absorption spectra of TMDs are strongly influenced by excitonic resonances and are sensitive to external parameters such as layer number, interlayer spacing, strain, and dielectric environment.

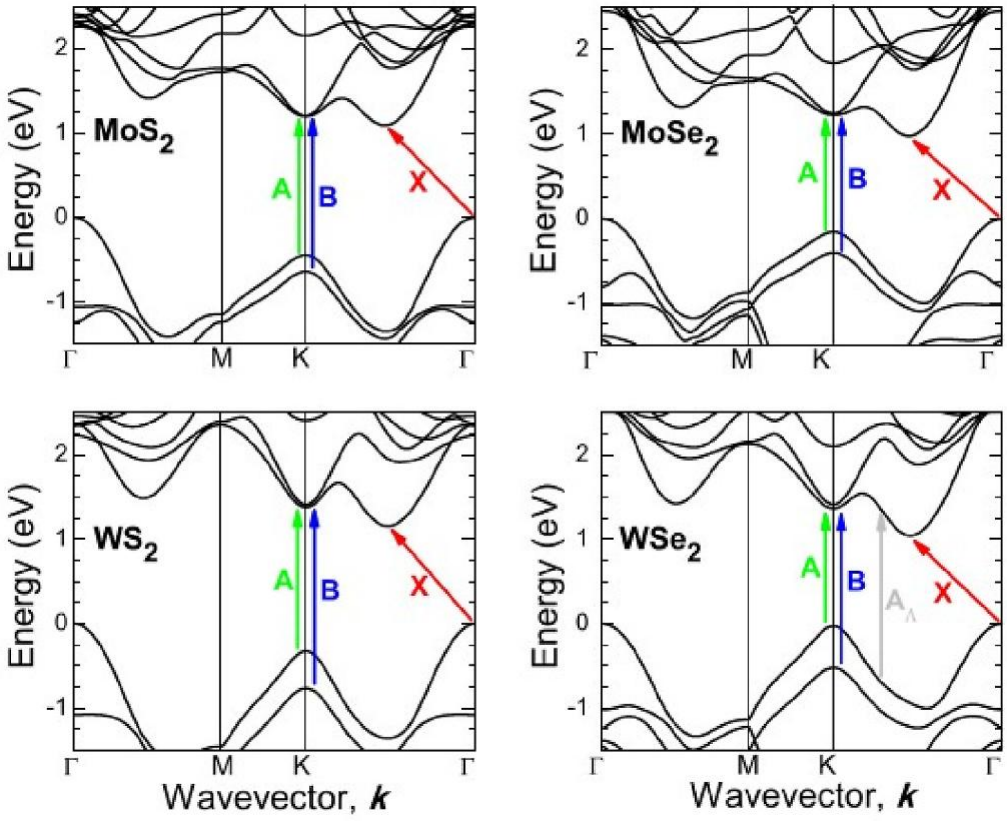

Figure 1.3: Electronic band structure for (a) MoS_2, (b) $MoSe_2$, (c) WS_2, and (d) WSe_2[47].

Importantly, lattice defects and surface states provide a common framework linking the electrical and optical behavior of TMDs. Defects are defined as local disruptions of the

periodicity and symmetry within an ideal crystal lattice that introduce localized energy levels within the bandgap, acting as charge trapping centers that affect carrier transport while simultaneously enabling additional optical transitions[48]. These defect-related states contribute to sub-bandgap absorption, photoconductivity, and non-ideal transport characteristics, directly coupling material quality and surface chemistry to both the electrical and optical response[49]. Overall, the interplay between tunable band structure, excitonic effects, and defect-mediated processes underpins the performance of TMD-based photodetectors, phototransistors, and related optoelectronic devices.

1.2.4 Mechanical properties

TMDs are mechanically strong and flexible, thanks to the strong covalent bonds between the atoms within the same plane. Unlike 3D materials, it is difficult to measure the mechanical properties of 2D materials since they are not equally deformable. Atomic force microscopy can address this problem and is employed to study mechanical properties such as Young's modulus, pretension, and strain[50]. The pretension of 2D materials relies on intrinsic mechanical properties as well as on the fabrication methodology. Semiconducting TMDs with metal atoms from group VI are promising for flexible optoelectronic devices[51]. From DFT calculations, the mechanical properties of many TMDs show a linear relationship with the charge transfer between the metal and the X element. These studies also confirm the dependence of mechanical properties on the chemical composition. The strong hybridization between the vacant p orbital of the chalcogen and the d orbital of the metal is the root cause of these mechanical characteristics[51].

1.2.5 Material synthesis

The synthesis techniques of 2D materials can be classified into top-down and bottom-up approaches, as depicted in Figure 1.4[52]. Top-down methods start from a bulk crystal and progressively isolate thinner layers by overcoming the weak van der Waals forces that hold the layers together. In contrast, bottom-up techniques rely on the assembly of the material directly from atomic or molecular precursors.

Among top-down approaches, mechanical exfoliation is the most widely used technique for fundamental research. In this method, monolayer or few-layer flakes are obtained by physically cleaving bulk crystals. Since only van der Waals interactions need to be overcome, this technique yields high-quality crystalline samples suitable for studying intrinsic electrical, optical, and vibrational properties. Several parameters, such as exfoliation speed and ambient atmosphere, have been shown to influence flake quality, as demonstrated for graphene and WSe_2[53]. However, mechanical exfoliation offers limited control over flake thickness, requires skilled handling, and involves post-processing steps, such as transfer onto substrates and defect removal, that hinder scalability and large-area production[54]. To further increase the size of exfoliated flakes, enhancing the adhesion between the crystal source and the substrate, for instance by heating the substrate, is crucial. New approaches to achieve large area monolayers include Au-assisted exfoliation that can produce millimeter-scale, high-quality monolayers, but

remain unsuitable for wafer-scale, uniform integration[55]. Scalability is further limited by the availability and crystallinity of source materials.

Other top-down methods include liquid-phase and chemical exfoliation, which allow the production of two-dimensional layers in solution[56,57]. These techniques provide higher yield and faster processing compared to mechanical exfoliation but typically result in lower crystalline quality and a higher density of defects. Liquid exfoliation can be categorized into four different forms such as oxidation, intercalation, ion exchange, and ultrasonic cleavage. In the chemical exfoliation method, the effective exfoliation of the bulk material is achieved by inserting intercalators into the intermediate layers of the bulk crystal, with the aid of ultrasonication in water. Organometallic compounds are the typically used intercalators[58]. In solvent-based exfoliation method, the layered compounds are dispersed in common solvents and deposited either as individual flakes or as thin films. Later, this method was modified by regulating the sonication time to obtain relatively large flake size and concentration.

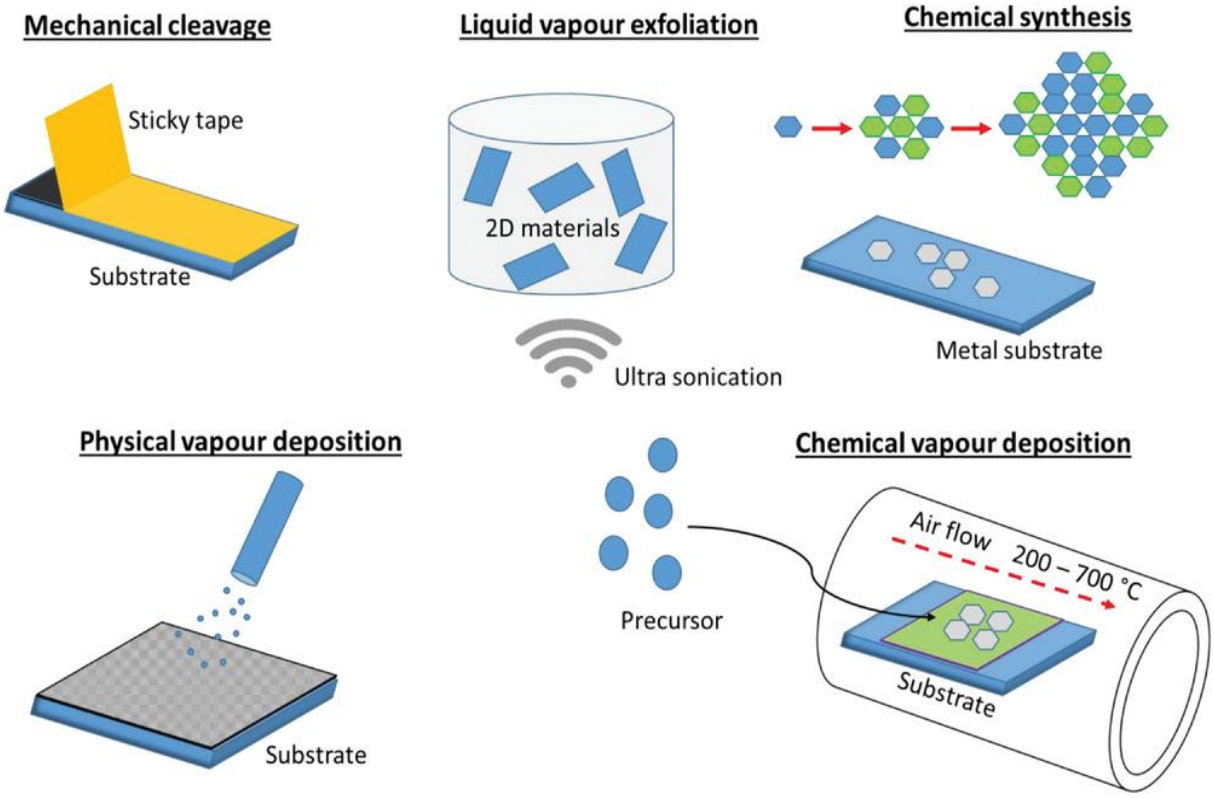

Figure 1.4: Synthesis processes of 2D materials[59].

Bottom-up synthesis methods encompass a wide range of techniques, including wet-chemical routes, epitaxial growth, pulsed laser deposition, and, most notably, chemical vapor deposition (CVD). CVD has emerged as the most impactful bottom-up approach for the controlled growth of large-area 2D materials. In this process, gaseous precursors are introduced into a reaction chamber, where high temperatures promote chemical reactions and subsequent deposition onto a suitable substrate. By tuning parameters such as temperature, precursor

concentration, and partial pressure, CVD allows precise control over layer thickness, morphology, and crystalline quality[60]. However, growth quality is highly sensitive to substrate imperfections, leading to grain boundaries, wrinkles, and thickness fluctuations that compromise device yield. Orientation-controlled growth on lattice-matched substrates such as sapphire or Au(111) can produce highly crystalline TMD films[61].

Metal–organic CVD (MOCVD) provides superior uniformity, better control over precursor delivery, and greater flexibility in substrate choice. This method differs from CVD because it employs metal-organic compounds as precursors and achieves uniform supply throughout the entire substrate. It can yield high-mobility, wafer-scale TMDs and has recently enabled CMOS-compatible, low-temperature ($< 300°C$) growth with promising electronic performance. However, precursor chemistry and growth kinetics still require optimization for widespread adoption[62].

Recently, there has been interest in the development of large-area and high quality epilayers using molecular beam epitaxy, which can be used to carefully control the composition, thickness, and structural phase of TMDs[63,64]. However, many issues are related to this method, such as defect density, grain size control, electronic transport.

Other promising methods include solution-based techniques that are used to prepare large lateral size 2D TMDs flakes with excellent layer-to-layer controllability. The benefits of these methods are the use of inexpensive precursors, scalability, easy sorting and separation, easy attainment of desired size and thickness, and excellent solubility.

Atomic layer deposition (ALD) is a gas-phase thin film deposition technique that is promising for industrial production of 2D materials. ALD exploits spatially or temporally separated, self-limiting surface reactions of gas-phase precursors. The first metal precursor is pulsed onto the surface where they adsorb and react with the surface groups until all the available reaction sites are consumed or blocked. Next, the second precursor is pulsed to replace the remaining ligands of the first precursor with reactive groups that contain the nonmetal element of the film. ALD cycles are repeated many times to obtain the desired film thickness[65].

1.2.6 Fabrication techniques

Lithography is a fundamental set of techniques used in the fabrication of electronic devices, enabling the definition of device geometries and the patterning of conductive paths on a substrate. In the context of micro- and nano-electronics, lithography refers to the process of transferring a predefined pattern onto a material layer in order to shape the active regions of a device or to define metallic leads. Depending on the nature of the radiation used to generate the pattern, lithographic techniques are commonly classified into photolithography and electron-beam lithography.

Photolithography relies on light to transfer a pattern onto a photosensitive layer, known as photoresist, deposited on the substrate. The process exploits the selective exposure of the photoresist through a photomask, so that only specific regions undergo a chemical transformation, and can subsequently be removed. Photoresists can be either positive or

negative, depending on whether the exposed regions become soluble or insoluble in the developer solution. The resist is typically deposited by spin coating, which ensures uniform thickness across the wafer.

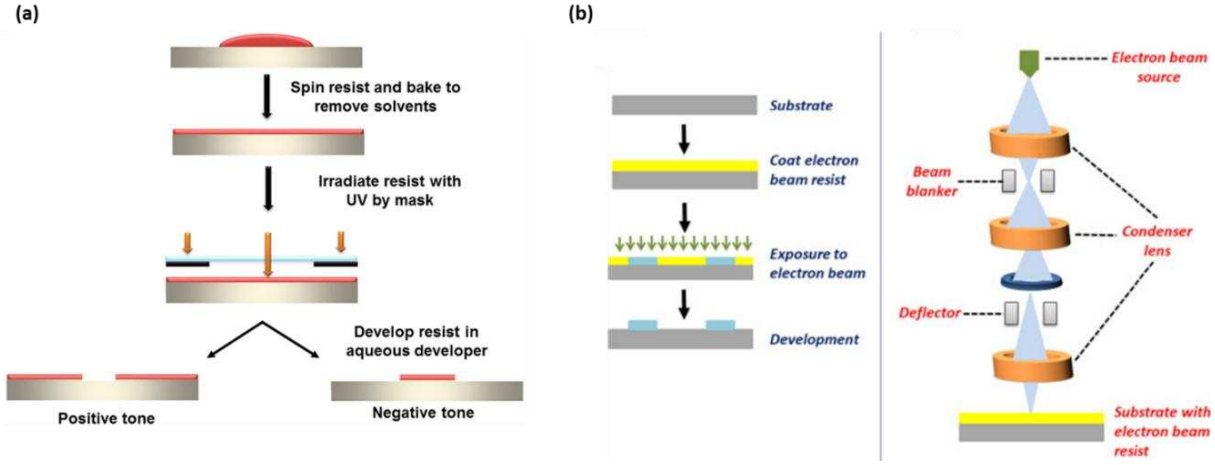

Figure 1.5: (a) Schematic illustration of a photolithography process[66]. (b) Fabrication steps involved in electron beam lithography (left) and schematic representation of the operation of an electron beam lithography unit (right).

A standard photolithography process involves several sequential steps, displayed in Figure 1.5a. First, the substrate, often consisting of a silicon wafer covered by an oxide layer, is thoroughly cleaned to remove organic and inorganic contaminants using chemical solutions or oxygen plasma. The wafer is then dehydrated by heating to eliminate residual moisture, and an adhesion promoter is applied to improve photoresist bonding. After resist deposition, a photomask containing the desired pattern, typically realized on a transparent quartz plate with opaque chromium features, is aligned with the wafer. The resist is then exposed to light, followed by development, during which the unwanted portions of the resist are removed. The resulting resist pattern serves as a protective mask during the etching step, which transfers the pattern into the underlying layer through either wet (isotropic) or dry (plasma-based) etching processes. Finally, the remaining resist is removed through lift-off, leaving the patterned substrate.

Owing to its simplicity, high throughput, and compatibility with wafer-scale processing, photolithography is the dominant technique used in industrial integrated circuit fabrication. However, its resolution is fundamentally limited by optical diffraction effects, which become increasingly severe as feature sizes approach the wavelength of the exposing radiation. To overcome these limitations, lithography has evolved from the use of visible and near-ultraviolet light sources to deep ultraviolet (DUV) lasers, such as KrF (248 nm) and ArF (193 nm). State-of-the-art industrial processes combine 193 nm lithography with immersion techniques, while next-generation lithography approaches, including extreme ultraviolet (EUV) lithography at 13.5 nm, X-ray lithography, and ion- or electron-based methods, are actively developed to further extend patterning resolution.

Electron-beam lithography (EBL) represents one of the most precise techniques for nanofabrication. In this case, the pattern is written directly onto an electron-sensitive resist using a focused electron beam, eliminating the need for a physical mask. The electron beam is typically generated by thermionic emission from a heated filament, such as tungsten or tungsten–zirconia alloys, selected for their narrow energy spread. Beam focusing and deflection are achieved using electrostatic or magnetic lens systems, allowing the pattern to be drawn with nanometer-scale precision based on a digitally defined design- see Figure 1.5b.

The main advantages of EBL are its unparalleled resolution, often below 10 nm, and its design flexibility, making it an indispensable tool for prototyping, research-scale devices, and mask fabrication. However, these benefits come at the expense of extremely low throughput. Since the exposure is performed serially and the writing time scales with both the exposed area and the required dose, EBL becomes impractical for large-area fabrication. As a result, despite its exceptional resolution, electron-beam lithography is unsuitable for mass production and is primarily employed for small-area devices, research applications, and the fabrication of photomasks used in optical lithography.

1.2.7 Applications

Thanks to their remarkable versatility in electrical, optical, chemical, and mechanical properties, TMDs are key materials for a broad spectrum of technological applications, as summarized in Figure 1.6, ranging from electronics and optoelectronics to sensing, energy conversion, and catalysis.[52]

One of the most mature and extensively explored application domains of TMDs is nanoelectronics, particularly field-effect transistors (FETs). Monolayer and few-layer TMDs such as MoS_2[67,68], WS_2[69], WSe_2[70], and $MoTe_2$[71] exhibit sizable bandgaps (typically between 1 and 2 eV), enabling high on/off current ratios exceeding 10^6–10^8, which are essential for logic operations. Their atomically thin nature ensures excellent electrostatic control over the channel, suppressing short-channel effects and enabling aggressive device scaling beyond the limits of conventional silicon technology. Experimental demonstrations of TMD-based FETs have reported room-temperature mobilities ranging from a few to several hundred $cm^2\ V^{-1}\ s^{-1}$, with further improvements achieved through high-k dielectrics, contact engineering, and encapsulation strategies[72]. These characteristics make TMDs promising candidates for low-power electronics, flexible transistors, and future complementary metal–oxide–semiconductor (CMOS)-compatible architectures.

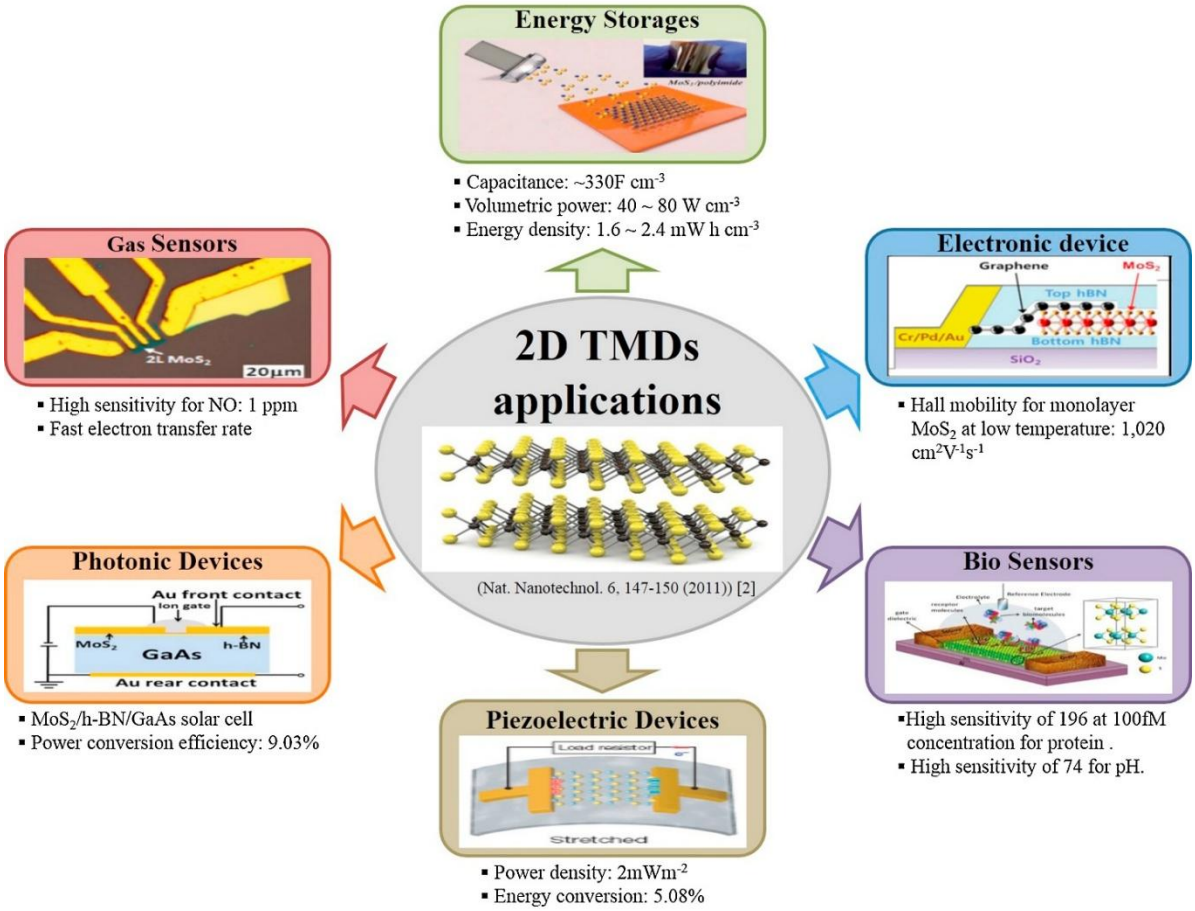

Figure 1.6: Electronic, opto-electronic and energy devices based on 2D TMDs[26].

Closely related to electronic applications are optoelectronic devices, where TMDs offer unique advantages stemming from their direct bandgap in the monolayer limit. As a result, TMDs have been widely investigated for photodetectors, phototransistors, light-emitting devices, and photovoltaic systems[73,74]. TMD-based photodetectors exhibit broadband sensitivity, fast response times, and high responsivities, which can be further enhanced through defect engineering, heterostructure formation, or photogating effects[75]. Moreover, as already mentioned, strong excitonic effects arising from reduced dielectric screening and quantum confinement dominate the optical response even at room temperature, enabling efficient light emission and absorption in ultrathin active layers[44]. These features are particularly attractive for miniaturized and low-dimensional optoelectronic platforms.

Another important application area is sensing, where the extremely high surface-to-volume ratio of TMDs plays a central role[76,77]. In gas and chemical sensors, adsorbed molecules can strongly modulate the carrier concentration and conductivity of TMD channels through charge transfer and trapping mechanisms. This sensitivity enables the detection of gases such as NO_2, NH_3, and O_2 at very low concentrations, often down to the parts-per-billion level[78–80]. Similarly, TMD-based biosensors exploit surface functionalization and electrostatic coupling to detect biomolecules, proteins, or DNA with high selectivity and sensitivity[81]. While surface sensitivity

is advantageous for sensing, it also highlights the need for careful control of defects and environmental exposure to ensure stability and reproducibility in practical devices[82].

TMDs have also attracted significant attention in the field of energy conversion and storage[83,84]. Their layered structure, chemical stability, and tunable electronic properties make them suitable for applications such as electrocatalysis, batteries, and supercapacitors. In particular, TMDs like MoS_2 and WS_2 have been extensively studied as catalysts for the hydrogen evolution reaction (HER), where edge sites and defect states act as active catalytic centers[85,86]. Compared to noble metal catalysts, TMD-based catalysts offer a cost-effective and earth-abundant alternative, with performance that can be optimized through phase engineering, defect introduction, and heterostructure formation. In energy storage, TMD nanosheets have been explored as electrode materials in lithium-ion batteries and supercapacitors, benefiting from their large surface area, mechanical flexibility, and ability to accommodate ion intercalation.

Beyond conventional electronics and energy applications, TMDs are increasingly relevant for flexible, wearable, and transparent technologies[87]. Their mechanical robustness, combined with atomic thinness and compatibility with flexible substrates, enables the fabrication of bendable electronic and optoelectronic devices without significant degradation of performance[88]. TMD-based transistors and photodetectors have been demonstrated on plastic and polymer substrates, highlighting their potential for next-generation wearable systems, flexible displays, and conformal sensors.

The integration of TMDs into van der Waals heterostructures further expands their application space[89–91]. By stacking different 2D materials with complementary properties, it is possible to engineer band alignment, interlayer charge transfer, and excitonic dynamics with high control. TMD heterostructures have enabled novel device concepts such as atomically thin p–n junctions, tunneling transistors, and multi-functional photodetectors. These architectures are particularly appealing for multifunctional devices that combine logic, sensing, and photodetection within a single platform.

1.2.8 Process Engineering for 2D Chips

Despite the significant progress achieved in recent years[92], the translation of TMD-based devices into industrial technologies is still hindered by several fundamental challenges. Among these, large-area synthesis with low defect density, control of contact resistance, and long-term environmental stability remain critical factors limiting scalability, yield, and device-to-device uniformity[93].

Reliable 2D electronic systems require wafer-scale single-crystal materials with controlled thickness and reproducible electronic properties. While the demonstration of CVD-grown MoS_2 wafers up to 12 inches represents an important milestone toward large-scale integration, growth quality remains highly sensitive to substrate properties, precursor chemistry, and thermal budget[94]. As a result, defects such as grain boundaries, wrinkles, point defects, and thickness non-uniformities are still commonly observed and significantly degrade carrier transport and

device performance. Orientation-controlled growth on lattice-matched substrates can improve crystallinity and reduce grain boundaries, but the high temperatures typically required often exceed back-end-of-line (BEOL) limits, thus restricting compatibility with standard CMOS processing[95]. Conversely, lowering the growth temperature improves integration prospects but generally leads to increased defect densities and reduced lateral transport performance[96].

At the device level, the development of high-performance 2D FETs requires the adoption of architectures specifically tailored to atomically thin channels, different from conventional silicon-based design rules. Currently, the typical structures of 2D FETs are based on top-gated and bottom-gated transistors that are suitable for fundamental research studies, but are not suitable for dimensional scaling and robust electrostatic control[68,96]. This has motivated extensive efforts to reduce both gate and channel lengths, which led to sub-nanometer gate electrodes[97], sub-100-nm channel lengths[98], and vertically stacked transistor geometries[99]. While these achievements highlight the exceptional geometric scalability of 2D materials, they also reveal new limitations, including enhanced short-channel effects, increased band-to-band tunneling, and degradation of the on/off ratio at extremely small dimensions.

To address these issues, advanced multigate architectures inspired by state-of-the-art CMOS technologies, such as double-gate[100], FinFET, and gate-all-around configurations[101], have been increasingly explored using 2D channels[102]. These architectures take advantage of the atomic thickness and clean interfaces of 2D semiconductors to achieve excellent electrostatic control and suppressed leakage currents, demonstrating performance metrics competitive with silicon devices. Nevertheless, most of these demonstrations still rely on research-scale fabrication tools, non-scalable lithography, and manual transfer steps.

Alongside device geometry, the integration of high-quality gate dielectrics represents a second major bottleneck. As the channel thickness shrinks to the atomic scale, the dielectric interface becomes a dominant factor affecting carrier scattering, mobility, threshold voltage stability, and overall transistor performance[103]. Achieving low equivalent oxide thickness (EOT) while maintaining low leakage currents requires dielectrics with high permittivity, excellent uniformity, and atomically sharp interfaces. Conventional dielectrics such as SiO_2 and HfO_2 are still widely used, but their direct deposition onto 2D surfaces is hindered by the absence of dangling bonds, which impedes nucleation and often results in non-uniform coverage or increased interface trap densities. This has led to strong interest in vdW dielectrics, including h-BN, CaF_2, Bi_2SeO_5 and $SrTiO_3$, which naturally form clean, dangling-bond-free interfaces compatible with 2D channels[104,105].

The use of vdW dielectrics has produced impressive results. For example, Bi_2SeO_5 has been employed to achieve sub-0.5-nm EOT gate stacks, with leakage levels compliant with IRDS low-power specifications[106]. h-BN, the most widely explored 2D dielectric, has been synthesized over wafer-scale areas and used in FET arrays[107], although its relatively low dielectric constant limits aggressive EOT scaling. Even with these promising candidates, the integration challenge remains significant. ALD, the most scalable approach for high-k dielectrics, requires the presence of surface functional groups, which are absent in pristine 2D

channels. Several strategies have been developed to promote ALD nucleation: the use of molecular seeding layers such as PTCDA, controlled chemical pretreatments to introduce temporary reactive sites, and the transfer of dielectrics pre-grown on sacrificial substrates. Each method must balance interface quality, mobility preservation, mechanical stability, manufacturability, and thermal budget constraints[108].

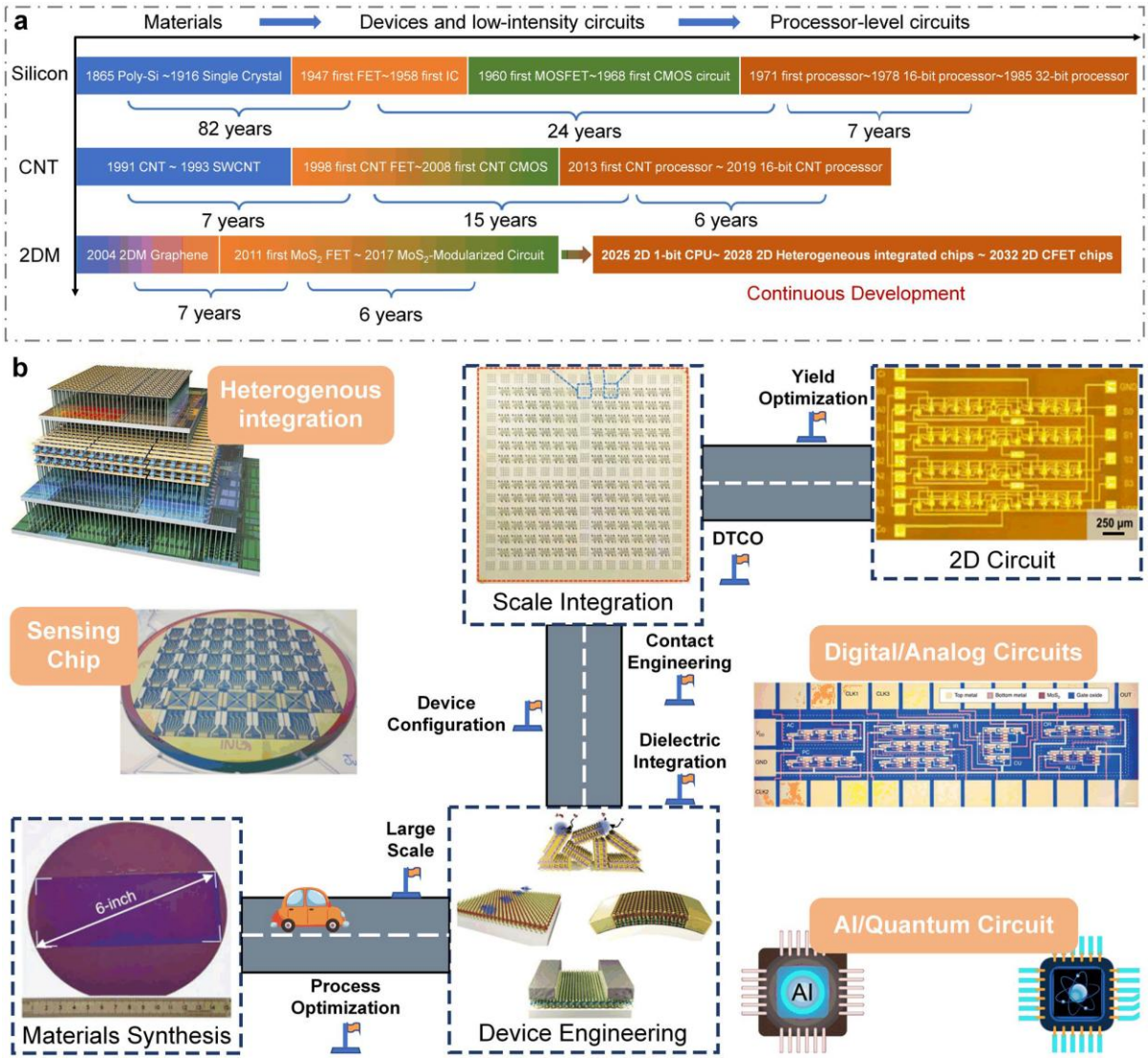

Figure 1.7: Schematic diagram of the general roadmap for 2D circuits. a Development timeline of silicon-based, carbon nanotube-based, and 2D ICs. b Route for the realization of 2D circuits and possible applications in the future.

A third pillar of 2D FET engineering is contact optimization, a factor that often determines the ultimate performance of 2D devices. The interface between a metal electrode and a 2D semiconductor is prone to the formation of metal-induced gap states (MIGS), which produce strong Fermi-level pinning and limit the ability to engineer Schottky barrier heights. This

results in large contact resistance, mobility degradation, and difficulty achieving symmetric electron and hole injection[109].

Three categories of strategies have emerged to address these challenges. The first involves selecting novel contact materials with low density of states at the Fermi level, such as bismuth, antimony, and scandium. These materials minimize MIGS formation and significantly reduce contact resistance. For instance, Sb/MoS_2 interfaces have achieved contact resistances near 40 Ω μm and on/off ratios above 10^8, meeting IRDS projections for future nodes[110].

The second approach focuses on interface modification, particularly through phase engineering. Several TMDs can undergo reversible transitions between semiconducting 2H and metallic 1T phases, creating atomically sharp homojunctions with low barriers and improved carrier injection[111]. Phase transitions can be induced by laser irradiation, electrostatic doping, or plasma treatments[112]. While powerful, these methods may introduce defects or rely on metastable phases, and thus require careful control to preserve long-term device stability.

The third strategy leverages alternative contact geometries, such as vdW contacts and edge contacts. VdW contacts rely on transferring pre-patterned metal electrodes onto the 2D semiconductor, thus avoiding direct chemical bonding and reducing interface disorder. Edge contacts, first developed for graphene, exploit atomically exposed edges to inject carriers efficiently and reduce contact resistance[113]. Although both techniques offer substantial advantages, they also introduce alignment challenges, mechanical fragility, and processing complexity that must be addressed for scalable implementation.

1.2.9 2D Materials towards 2D Chips

2D materials offer unique advantages for both digital and analog integrated circuits due to their atomically thin channels, excellent electrostatic control, and ability to form vdW heterostructures[114]. These features enable high-performance FETs with favorable transport properties and reduced short-channel effects compared to bulk silicon, making 2D semiconductors attractive for next-generation chips that integrate logic, memory, and mixed-signal functionality[115].

In digital electronics, early work demonstrated basic logic gates using semiconducting 2D materials, overcoming limitations of zero-bandgap graphene by adopting TMDs such as MoS_2. A key milestone was the demonstration of a MoS_2 logic inverter operating at room temperature[116], followed by larger-area integrated circuits based on CVD-grown 2D films[117,118]. Complex digital functions, including SRAM cells and ring oscillators, have been achieved, and a 2D-material microprocessor comprising over 100 transistors showcases the feasibility of functional 2D digital ICs[119–123]. Complementary logic architectures using ambipolar materials such as WSe_2 have also improved voltage gain and noise margins[123].

For analog and RF circuits, 2D materials bring benefits such as high carrier mobility and low intrinsic noise. Graphene FETs have been used to realize high-frequency transistors with cutoff frequencies surpassing 300 GHz[124], and analog components including frequency multipliers have been demonstrated[125]. Semiconducting 2D materials like MoS_2 support better current

saturation and higher intrinsic gain, enabling analog building blocks such as operational amplifiers and phase-locked loops in MoS_2 circuits[126].Despite these advances, analog system maturity lags behind digital due to sensitivity to variability and environmental factors.

Beyond conventional ICs, 2D materials are promising for in-memory and in-sensor computing, addressing bottlenecks of von Neumann architectures by co-locating memory and computation[127]. Thanks to their atomically thin nature, 2D materials are expected to be superior to bulk materials in building low power synaptic devices. In the two-terminal synaptic devices, the switching mechanism includes vacancy migration[128], phase transition[129], ferroelectric polarization[130], and metal filament formation. The latter, combined with the atomic-scale thickness make the device exhibit the spike-timing dependent plasticity with low switching voltages[131].

In addition to advances in devices, arrays development will provide great opportunities in the field of in-memory computing. Flexibility of 2D materials can be exploited to have flexible neuromorphic systems by using printing technologies[132]. Moreover, self-selective memory cells built from 2D heterostructures demonstrate high selectivity and reduced leakage in crossbar arrays[133], and emerging dual-gate 2D memtransistor arrays exhibit a lower energy consumption and decoupling of reading and writing operations[134]. For in-sensor computing, retinomorphic 2D heterostructure arrays combine photodetection with local preprocessing to mimic biological retina functions[135] and programmable black phosphorus phototransistors have been used for multispectral in-sensor processing[136].

Overall, the breadth of 2D material device demonstrations highlights their potential across digital, analog, and unconventional compute paradigms. Continued progress in wafer-scale synthesis, device uniformity, and circuit design infrastructure will be critical to translate these laboratory achievements into scalable chip technologies. The roadmap is outlined in Figure 1.7.

References

(1) Moore, G. Progress In Digital Integrated Electronics [Technical Literaiture, Copyright 1975 IEEE. Reprinted, with Permission. Technical Digest. International Electron Devices Meeting, IEEE, 1975, Pp. 11-13.]. *Solid-State Circuits Newsletter, IEEE* **2006**, *20*, 36–37. https://doi.org/10.1109/N-SSC.2006.4804410.

(2) Hu, C. Future CMOS Scaling and Reliability. *Proceedings of the IEEE* **1993**, *81* (5), 682–689. https://doi.org/10.1109/5.220900.

(3) Pop, E.; Sinha, S.; Goodson, K. E. Heat Generation and Transport in Nanometer-Scale Transistors. *Proceedings of the IEEE* **2006**, *94* (8), 1587–1601. https://doi.org/10.1109/JPROC.2006.879794.

(4) Yan, R.-H.; Ourmazd, A.; Lee, K. F. Scaling the Si MOSFET: From Bulk to SOI to Bulk. *IEEE Transactions on Electron Devices* **1992**, *39* (7), 1704–1710. https://doi.org/10.1109/16.141237.

(5) Ryckaert, J.; Baert, R.; Verkest, D.; Na, M.; Weckx, P.; Jang, D.; Schuddinck, P.; Chehab, B.; Patli, S.; Sarkar, S.; Zografos, O. Enabling Sub-5nm CMOS Technology Scaling Thinner and Taller!; 2019; p 29.4.1-29.4.4. https://doi.org/10.1109/IEDM19573.2019.8993631.

(6) Hisamoto, D.; Lee, W.-C.; Kedzierski, J.; Takeuchi, H.; Asano, K.; Kuo, C.; Anderson, E.; King Liu, T.-J.; Bokor, J.; hu, C. FinFET-a Self-Aligned Double-Gate MOSFET Scalable to 20 Nm. *Electron Devices, IEEE Transactions on* **2001**, *47*, 2320–2325. https://doi.org/10.1109/16.887014.

(7) Nikonov, D. E.; Young, I. A. Overview of Beyond-CMOS Devices and a Uniform Methodology for Their Benchmarking. *Proceedings of the IEEE* **2013**, *101* (12), 2498–2533. https://doi.org/10.1109/JPROC.2013.2252317.

(8) Zeng, S.; Tang, Z.; Liu, C.; Zhou, P. Electronics Based on Two-Dimensional Materials: Status and Outlook. *Nano Res.* **2021**, *14* (6), 1752–1767. https://doi.org/10.1007/s12274-020-2945-z.

(9) Radisavljevic, B.; Radenovic, A.; Brivio, J.; Giacometti, V.; Kis, A. Single-Layer MoS2 Transistors. *Nature Nanotech* **2011**, *6* (3), 147–150. https://doi.org/10.1038/nnano.2010.279.

(10) Yoo, S. J. B.; Guan, B.; Scott, R. P. Heterogeneous 2D/3D Photonic Integrated Microsystems. *Microsyst Nanoeng* **2016**, *2* (1), 16030. https://doi.org/10.1038/micronano.2016.30.

(11) Shim, J.; Bae, S.-H.; Kong, W.; Lee, D.; Qiao, K.; Nezich, D.; Park, Y.; Zhao, R.; Sundaram, S.; li, X.; Yeon, H.; Choi, C.; Kum, H.; Yue, R.; Zhou, G.; Ou, Y.; Lee, K.; Moodera, J.; Zhao, X.; Kim, J. Controlled Crack Propagation for Atomic Precision Handling of Wafer-Scale Two-Dimensional Materials. *Science* **2018**. https://doi.org/10.1126/science.aat8126.

(12) Xie, Z.; Avila, R.; Huang, Y.; Rogers, J. A. Flexible and Stretchable Antennas for Biointegrated Electronics. *Advanced Materials* **2020**, *32* (15), 1902767. https://doi.org/10.1002/adma.201902767.

(13) Yang, S.; Jiang, C.; Wei, S. Gas Sensing in 2D Materials. *Appl. Phys. Rev.* **2017**, *4* (2), 021304. https://doi.org/10.1063/1.4983310.

(14) Choi, C.; Lee, Y.; Cho, K. W.; Koo, J. H.; Kim, D.-H. Wearable and Implantable Soft Bioelectronics Using Two-Dimensional Materials. *Acc. Chem. Res.* **2019**, *52* (1), 73–81. https://doi.org/10.1021/acs.accounts.8b00491.

(15) Cui, C.; Xue, F.; Hu, W.-J.; Li, L.-J. Two-Dimensional Materials with Piezoelectric and Ferroelectric Functionalities. *npj 2D Mater Appl* **2018**, *2* (1), 18. https://doi.org/10.1038/s41699-018-0063-5.

(16) Pal, A.; Zhang, S.; Chavan, T.; Agashiwala, K.; Yeh, C.-H.; Cao, W.; Banerjee, K. Quantum-Engineered Devices Based on 2D Materials for Next-Generation Information Processing and Storage. *Advanced Materials* **2023**, *35* (27), 2109894. https://doi.org/10.1002/adma.202109894.

(17) Liu, C.; Chen, H.; Wang, S.; Liu, Q.; Jiang, Y.-G.; Zhang, D. W.; Liu, M.; Zhou, P. Two-Dimensional Materials for next-Generation Computing Technologies. *Nat. Nanotechnol.* **2020**, *15* (7), 545–557. https://doi.org/10.1038/s41565-020-0724-3.

(18) Kim, K. S.; Kwon, J.; Ryu, H.; Kim, C.; Kim, H.; Lee, E.-K.; Lee, D.; Seo, S.; Han, N. M.; Suh, J. M.; Kim, J.; Song, M.-K.; Lee, S.; Seol, M.; Kim, J. The Future of Two-Dimensional Semiconductors beyond Moore's Law. *Nat. Nanotechnol.* **2024**, *19* (7), 895–906. https://doi.org/10.1038/s41565-024-01695-1.

(19) *Editions – IRDS*. https://irds.ieee.org/editions/ (accessed 2026-01-15).

(20) *Introducing 2D materials in the logic technology roadmap*. imec. https://www.imec-int.com/en/articles/introducing-2d-materials-logic-technology-roadmap-five-good-reasons-three-major-challenges (accessed 2026-01-15).

(21) Geim, A. K.; Novoselov, K. S. The Rise of Graphene. *Nature Mater* **2007**, *6* (3), 183–191. https://doi.org/10.1038/nmat1849.

(22) Han, S. A.; Bhatia, R.; Kim, S.-W. Synthesis, Properties and Potential Applications of Two-Dimensional Transition Metal Dichalcogenides. *Nano Convergence* **2015**, *2* (1), 17. https://doi.org/10.1186/s40580-015-0048-4.

(23) Chhowalla, M.; Shin, H.; Eda, G.; Li, L.; Loh, K.; Zhang, H. The Chemistry of Two-Dimensional Layered Transition Metal Dichalcogenide Nanosheets. *Nature chemistry* **2013**, *5*, 263–275. https://doi.org/10.1038/nchem.1589.

(24) Ahmadi, M.; Zabihi, O.; Jeon, S.; Yoonessi, M.; Dasari, A.; Ramakrishna, S.; Naebe, M. 2D Transition Metal Dichalcogenide Nanomaterials: Advances, Opportunities, and Challenges in Multi-Functional Polymer Nanocomposites. *J. Mater. Chem. A* **2020**, *8* (3), 845–883. https://doi.org/10.1039/C9TA10130F.

(25) Manzeli, S.; Ovchinnikov, D.; Pasquier, D.; Yazyev, O.; Kis, A. 2D Transition Metal Dichalcogenides. *Nature Reviews Materials* **2017**, *2*. https://doi.org/10.1038/natrevmats.2017.33.

(26) Choi, W.; Choudhary, N.; Han, G. H.; Park, J.; Akinwande, D.; Lee, Y. H. Recent Development of Two-Dimensional Transition Metal Dichalcogenides and Their Applications. *Materials Today* **2017**, *20* (3), 116–130. https://doi.org/10.1016/j.mattod.2016.10.002.

(27) Keum, D. H.; Cho, S.; Kim, J. H.; Choe, D.-H.; Sung, H.-J.; Kan, M.; Kang, H.; Hwang, J.-Y.; Kim, S. W.; Yang, H.; Chang, K. J.; Lee, Y. H. Bandgap Opening in Few-Layered Monoclinic MoTe2. *Nature Phys* **2015**, *11* (6), 482–486. https://doi.org/10.1038/nphys3314.

(28) Kumar, N.; Najmaei, S.; Cui, Q.; Ceballos, F.; Ajayan, P. M.; Lou, J.; Zhao, H. Second Harmonic Microscopy of Monolayer MoS${}_{2}$. *Phys. Rev. B* **2013**, *87* (16), 161403. https://doi.org/10.1103/PhysRevB.87.161403.

(29) Kolobov, A. V.; Tominaga, J. *Two-Dimensional Transition-Metal Dichalcogenides*; Springer, 2016.

(30) Knoch, J. *Nanoelectronics: Device Physics, Fabrication, Simulation*; De Gruyter Oldenbourg, 2020. https://doi.org/10.1515/9783110575507.

(31) Kim, T.; Kim, Y.; Park, S.; Kim, Y.; Jang, H. Two-Dimensional Transition Metal Disulfides for Chemoresistive Gas Sensing: Perspective and Challenges. *Chemosensors* **2017**, *5*. https://doi.org/10.3390/chemosensors5020015.

(32) Xia, F.; Wang, H.; Xiao, D.; Dubey, M.; Ramasubramaniam, A. Two-Dimensional Material Nanophotonics. *Nature Photon* **2014**, *8* (12), 899–907. https://doi.org/10.1038/nphoton.2014.271.

(33) Chaves, A.; Azadani, J. G.; Alsalman, H.; da Costa, D. R.; Frisenda, R.; Chaves, A. J.; Song, S. H.; Kim, Y. D.; He, D.; Zhou, J.; Castellanos-Gomez, A.; Peeters, F. M.; Liu, Z.; Hinkle, C. L.; Oh, S.-H.; Ye, P. D.; Koester, S. J.; Lee, Y. H.; Avouris, P.; Wang, X.; Low, T. Bandgap Engineering of Two-Dimensional Semiconductor Materials. *npj 2D Mater Appl* **2020**, *4* (1), 29. https://doi.org/10.1038/s41699-020-00162-4.

(34) Kuc, A.; Zibouche, N.; Heine, T. Influence of Quantum Confinement on the Electronic Structure of the Transition Metal Sulfide TS${}_{2}$. *Phys. Rev. B* **2011**, *83* (24), 245213. https://doi.org/10.1103/PhysRevB.83.245213.

(35) Ghorbani-Asl, M.; Borini, S.; Kuc, A.; Heine, T. Strain-Dependent Modulation of Conductivity in Single-Layer Transition-Metal Dichalcogenides. *Phys. Rev. B* **2013**, *87* (23), 235434. https://doi.org/10.1103/PhysRevB.87.235434.

(36) Wang, Q. H.; Kalantar-Zadeh, K.; Kis, A.; Coleman, J. N.; Strano, M. S. Electronics and Optoelectronics of Two-Dimensional Transition Metal Dichalcogenides. *Nature Nanotech* **2012**, *7* (11), 699–712. https://doi.org/10.1038/nnano.2012.193.

(37) Feng, S.; Lin, Z.; Gan, X.; Lv, R.; Terrones, M. Doping Two-Dimensional Materials: Ultra-Sensitive Sensors, Band Gap Tuning and Ferromagnetic Monolayers. *Nanoscale Horizons* **2017**, *2* (2), 72–80. https://doi.org/10.1039/C6NH00192K.

(38) KC, S.; Longo, R. C.; Addou, R.; Wallace, R. M.; Cho, K. Impact of Intrinsic Atomic Defects on the Electronic Structure of MoS2 Monolayers. *Nanotechnology* **2014**, *25* (37), 375703. https://doi.org/10.1088/0957-4484/25/37/375703.

(39) Viscardi, L.; Durante, O.; De Stefano, S.; Intonti, K.; Kumar, A.; Pelella, A.; Giubileo, F.; Kharsah, O.; Daniel, L.; Sleziona, S.; Schleberger, M.; Di Bartolomeo, A. Dominant N-Type Conduction and Fast Photoresponse in BP/MoS2 Heterostructures. *Surfaces and Interfaces* **2024**, *49*, 104445. https://doi.org/10.1016/j.surfin.2024.104445.

(40) Geim, A. K.; Grigorieva, I. V. Van Der Waals Heterostructures. *Nature* **2013**, *499* (7459), 419–425. https://doi.org/10.1038/nature12385.

(41) Tang, W.; Rassay, S.; Ravindra, N. Electronic & Optical Properties of Transition-Metal Dichalcogenides. *Madridge Journal of Nanotechnology & Nanoscience* **2017**, *2*, 58–64. https://doi.org/10.18689/mjnn-1000111.

(42) Huo, N.; Wei, Z.; Meng, X.; Kang, J.; Wu, F.; Li, S.-S.; Wei, S.-H.; Li, J. Interlayer Coupling and Optoelectronic Properties of Ultrathin Two-Dimensional Heterostructures Based on Graphene, MoS2 and WS2. *J. Mater. Chem. C* **2015**, *3* (21), 5467–5473. https://doi.org/10.1039/C5TC00698H.

(43) Lv, R.; Robinson, J. A.; Schaak, R. E.; Sun, D.; Sun, Y.; Mallouk, T. E.; Terrones, M. Transition Metal Dichalcogenides and Beyond: Synthesis, Properties, and Applications of Single- and Few-Layer Nanosheets. *Acc. Chem. Res.* **2015**, *48* (1), 56–64. https://doi.org/10.1021/ar5002846.

(44) Ramasubramaniam, A. Large Excitonic Effects in Monolayers of Molybdenum and Tungsten Dichalcogenides. *Phys. Rev. B* **2012**, *86* (11), 115409. https://doi.org/10.1103/PhysRevB.86.115409.

(45) Komsa, H.-P.; Krasheninnikov, A. V. Effects of Confinement and Environment on the Electronic Structure and Exciton Binding Energy of MoS${}_{2}$ from First Principles. *Phys. Rev. B* **2012**, *86* (24), 241201. https://doi.org/10.1103/PhysRevB.86.241201.

(46) Mak, K. F.; He, K.; Lee, C.; Lee, G. H.; Hone, J.; Heinz, T. F.; Shan, J. Tightly Bound Trions in Monolayer MoS2. *Nature Mater* **2013**, *12* (3), 207–211. https://doi.org/10.1038/nmat3505.

(47) Joseph, S.; Mohan, J.; Lakshmy, S.; Thomas, S.; Chakraborty, B.; Thomas, S.; Kalarikkal, N. A Review of the Synthesis, Properties, and Applications of 2D Transition Metal Dichalcogenides and Their Heterostructures. *Materials Chemistry and Physics* **2023**, *297*, 127332. https://doi.org/10.1016/j.matchemphys.2023.127332.

(48) Pandey, M.; Rasmussen, F. A.; Kuhar, K.; Olsen, T.; Jacobsen, K. W.; Thygesen, K. S. Defect-Tolerant Monolayer Transition Metal Dichalcogenides. *Nano Lett.* **2016**, *16* (4), 2234–2239. https://doi.org/10.1021/acs.nanolett.5b04513.

(49) Akkanen, S.-T. M.; Fernandez, H. A.; Sun, Z. Optical Modification of 2D Materials: Methods and Applications. *Advanced Materials* **2022**, *34* (19), 2110152. https://doi.org/10.1002/adma.202110152.

(50) Kim, J. H.; Jeong, J. H.; Kim, N.; Joshi, R.; Lee, G.-H. Mechanical Properties of Two-Dimensional Materials and Their Applications. *J. Phys. D: Appl. Phys.* **2018**, *52* (8), 083001. https://doi.org/10.1088/1361-6463/aaf465.

(51) Li, J.; Medhekar, N. V.; Shenoy, V. B. Bonding Charge Density and Ultimate Strength of Monolayer Transition Metal Dichalcogenides. *J. Phys. Chem. C* **2013**, *117* (30), 15842–15848. https://doi.org/10.1021/jp403986v.

(52) Shanmugam, V.; Mensah, R. A.; Babu, K.; Gawusu, S.; Chanda, A.; Tu, Y.; Neisiany, R. E.; Försth, M.; Sas, G.; Das, O. A Review of the Synthesis, Properties, and Applications of 2D Materials. *Particle & Particle Systems Characterization* **2022**, *39* (6), 2200031. https://doi.org/10.1002/ppsc.202200031.

(53) Yuan, L.; Ge, J.; Peng, X.; Zhang, Q.; Wu, Z.; Jian, Y.; Xiong, X.; Yin, H.; Han, J. A Reliable Way of Mechanical Exfoliation of Large Scale Two Dimensional Materials with High Quality. *AIP Advances* **2016**, *6* (12), 125201. https://doi.org/10.1063/1.4967967.

(54) Gasbarro, A.; Masuda, Y.-S.; Lubecke, V. High-Throughput Evaluation of Mechanical Exfoliation Using Optical Classification of Two-Dimensional Materials. *Micromachines* **2025**, *16*, 1084. https://doi.org/10.3390/mi16101084.

(55) Huang, Y.; Pan, Y.-H.; Yang, R.; Bao, L.-H.; Meng, L.; Luo, H.-L.; Cai, Y.-Q.; Liu, G.-D.; Zhao, W.-J.; Zhou, Z.; Wu, L.-M.; Zhu, Z.-L.; Huang, M.; Liu, L.-W.; Liu, L.; Cheng, P.; Wu, K.-H.; Tian, S.-B.; Gu, C.-Z.; Shi, Y.-G.; Guo, Y.-F.; Cheng, Z. G.; Hu, J.-P.; Zhao, L.; Yang, G.-H.; Sutter, E.; Sutter, P.; Wang, Y.-L.; Ji, W.; Zhou, X.-J.; Gao, H.-J. Universal Mechanical Exfoliation of Large-Area 2D Crystals. *Nat Commun* **2020**, *11* (1), 2453. https://doi.org/10.1038/s41467-020-16266-w.

(56) Huo, C.; Yan, Z.; Song, X. F.; Zeng, H. 2D Materials via Liquid Exfoliation: A Review on Fabrication and Applications. *Science Bulletin* **2015**, *60*. https://doi.org/10.1007/s11434-015-0936-3.

(57) Joensen, P.; Frindt, R. F.; Morrison, S. R. Single-Layer MoS2. *Materials Research Bulletin* **1986**, *21* (4), 457–461. https://doi.org/10.1016/0025-5408(86)90011-5.

(58) Zeng, Z.; Yin, Z.; Huang, X.; Li, H.; He, Q.; Lu, G.; Boey, F.; Zhang, H. Single-Layer Semiconducting Nanosheets: High-Yield Preparation and Device Fabrication. *Angewandte Chemie International Edition* **2011**, *50* (47), 11093–11097. https://doi.org/10.1002/anie.201106004.

(59) Shanmugam, V.; Mensah, R. A.; Babu, K.; Gawusu, S.; Chanda, A.; Tu, Y.; Neisiany, R. E.; Försth, M.; Sas, G.; Das, O. A Review of the Synthesis, Properties, and Applications of 2D Materials. *Particle & Particle Systems Characterization* **2022**, *39* (6), 2200031. https://doi.org/10.1002/ppsc.202200031.

(60) Lee, Y.-H.; Zhang, X.-Q.; Zhang, W.; Chang, M.-T.; Lin, C.-T.; Chang, K.-D.; Yu, Y.-C.; Wang, J. T.-W.; Chang, C.-S.; Li, L.-J.; Lin, T.-W. Synthesis of Large-Area MoS2 Atomic Layers with Chemical Vapor Deposition. *Advanced Materials* **2012**, *24* (17), 2320–2325. https://doi.org/10.1002/adma.201104798.

(61) Li, T.; Guo, W.; Ma, L.; Li, W.; Yu, Z.; Han, Z.; Gao, S.; Liu, L.; Fan, D.; Wang, Z.; Yang, Y.; Lin, W.; Luo, Z.; Chen, X.; Dai, N.; Tu, X.; Pan, D.; Yao, Y.; Wang, P.; Nie, Y.; Wang, J.; Shi, Y.; Wang, X. Epitaxial Growth of Wafer-Scale Molybdenum Disulfide Semiconductor Single Crystals on Sapphire. *Nat. Nanotechnol.* **2021**, *16* (11), 1201–1207. https://doi.org/10.1038/s41565-021-00963-8.

(62) Ye, Z.; Tan, C.; Huang, X.; Ouyang, Y.; Yang, L.; Wang, Z.; Dong, M. Emerging MoS2 Wafer-Scale Technique for Integrated Circuits. *Nano-Micro Lett.* **2023**, *15* (1), 38. https://doi.org/10.1007/s40820-022-01010-4.

(63) Nakano, M.; Wang, Y.; Kashiwabara, Y.; Matsuoka, H.; Iwasa, Y. Layer-by-Layer Epitaxial Growth of Scalable WSe2 on Sapphire by Molecular Beam Epitaxy. *Nano Lett.* **2017**, *17* (9), 5595–5599. https://doi.org/10.1021/acs.nanolett.7b02420.

(64) Park, J. H.; Vishwanath, S.; Liu, X.; Zhou, H.; Eichfeld, S. M.; Fullerton-Shirey, S. K.; Robinson, J. A.; Feenstra, R. M.; Furdyna, J.; Jena, D.; Xing, H. G.; Kummel, A. C. Scanning Tunneling Microscopy and Spectroscopy of Air Exposure Effects on Molecular Beam Epitaxy Grown WSe2 Monolayers and Bilayers. *ACS Nano* **2016**, *10* (4), 4258–4267. https://doi.org/10.1021/acsnano.5b07698.

(65) Mattinen, M.; Leskelä, M.; Ritala, M. Atomic Layer Deposition of 2D Metal Dichalcogenides for Electronics, Catalysis, Energy Storage, and Beyond. *Advanced Materials Interfaces* **2021**, *8* (6), 2001677. https://doi.org/10.1002/admi.202001677.

(66) Sharma, B.; Sharma, A. Microfluidics: Recent Advances Toward Lab-on-Chip Applications in Bioanalysis. *Advanced Engineering Materials* **2021**, *24*. https://doi.org/10.1002/adem.202100738.

(67) Liu, L.; Lu, Y.; Guo, J. On Monolayer \rm MoS_2 Field-Effect Transistors at the Scaling Limit. *IEEE Transactions on Electron Devices* **2013**, *60* (12), 4133–4139. https://doi.org/10.1109/TED.2013.2284591.

(68) Radisavljevic, B.; Radenovic, A.; Brivio, J.; Giacometti, V.; Kis, A. Single-Layer MoS2 Transistors. *Nature Nanotech* **2011**, *6* (3), 147–150. https://doi.org/10.1038/nnano.2010.279.

(69) Jin, L.; Wen, J.; Odlyzko, M.; Seaton, N.; Li, R.; Haratipour, N.; Koester, S. J. High-Performance WS2 MOSFETs with Bilayer WS2 Contacts. *ACS Omega* **2024**, *9* (29), 32159–32166. https://doi.org/10.1021/acsomega.4c04431.

(70) Andreev, M.; Kang, J.; Lee, T.; Park, J.-H. WSe2 Field-Effect Transistor with Electron-Beam-Induced W-Shaped IV Characteristic and Its Application to a Ternary NAND Gate. In *2023 7th IEEE Electron Devices Technology & Manufacturing Conference (EDTM)*; 2023; pp 1–3. https://doi.org/10.1109/EDTM55494.2023.10103021.

(71) Pradhan, N. R.; Rhodes, D.; Feng, S.; Xin, Y.; Memaran, S.; Moon, B.-H.; Terrones, H.; Terrones, M.; Balicas, L. Field-Effect Transistors Based on Few-Layered α-MoTe2. *ACS Nano* **2014**, *8* (6), 5911–5920. https://doi.org/10.1021/nn501013c.

(72) Ahmed, S.; Yi, J. Two-Dimensional Transition Metal Dichalcogenides and Their Charge Carrier Mobilities in Field-Effect Transistors. *Nano-Micro Lett.* **2017**, *9* (4), 50. https://doi.org/10.1007/s40820-017-0152-6.

(73) Yang, C.; Wang, G.; Liu, M.; Yao, F.; Li, H. Mechanism, Material, Design, and Implementation Principle of Two-Dimensional Material Photodetectors. *Nanomaterials* **2021**, *11* (10), 2688. https://doi.org/10.3390/nano11102688.

(74) Pospischil, A.; Mueller, T. Optoelectronic Devices Based on Atomically Thin Transition Metal Dichalcogenides. *Applied Sciences* **2016**, *6*, 78. https://doi.org/10.3390/app6030078.

(75) Long, M.; Wang, P.; Fang, H.; Hu, W. Progress, Challenges, and Opportunities for 2D Material Based Photodetectors. *Advanced Functional Materials* **2019**, *29* (19), 1803807. https://doi.org/10.1002/adfm.201803807.

(76) Varghese, S. S.; Varghese, S. H.; Swaminathan, S.; Singh, K. K.; Mittal, V. Two-Dimensional Materials for Sensing: Graphene and Beyond. *Electronics* **2015**, *4* (3), 651–687. https://doi.org/10.3390/electronics4030651.

(77) Mirzaei, A.; Kim, J.-Y.; Kim, H. W.; Kim, S. S. Resistive Gas Sensors Based on 2D TMDs and MXenes. *Acc. Chem. Res.* **2024**, *57* (16), 2395–2413. https://doi.org/10.1021/acs.accounts.4c00323.

(78) Perkins, F. K.; Friedman, A. L.; Cobas, E.; Campbell, P. M.; Jernigan, G. G.; Jonker, B. T. Chemical Vapor Sensing with Monolayer MoS2. *Nano Lett.* **2013**, *13* (2), 668–673. https://doi.org/10.1021/nl3043079.

(79) He, Q.; Zeng, Z.; Yin, Z.; Li, H.; Wu, S.; Huang, X.; Zhang, H. Fabrication of Flexible MoS2 Thin-Film Transistor Arrays for Practical Gas-Sensing Applications. *Small* **2012**, *8* (19), 2994–2999. https://doi.org/10.1002/smll.201201224.

(80) Schleicher, M.; Fyta, M. Lateral MoS2 Heterostructure for Sensing Small Gas Molecules. *ACS Appl. Electron. Mater.* **2020**, *2* (1), 74–83. https://doi.org/10.1021/acsaelm.9b00495.

(81) Yuan, Y.; Li, R.; Liu, Z. Establishing Water-Soluble Layered WS2 Nanosheet as a Platform for Biosensing. *Anal. Chem.* **2014**, *86* (7), 3610–3615. https://doi.org/10.1021/ac5002096.

(82) Lin, Y.-F.; Xu, Y.; Lin, C.-Y.; Suen, Y.-W.; Yamamoto, M.; Nakaharai, S.; Ueno, K.; Tsukagoshi, K. Origin of Noise in Layered MoTe2 Transistors and Its Possible Use for Environmental Sensors. *Advanced Materials* **2015**, *27* (42), 6612–6619. https://doi.org/10.1002/adma.201502677.

(83) Roy, S.; Joseph, A.; Zhang, X.; Bhattacharyya, S.; Puthirath, A. B.; Biswas, A.; Tiwary, C. S.; Vajtai, R.; Ajayan, P. M. Engineered Two-Dimensional Transition Metal Dichalcogenides for Energy Conversion and Storage. *Chem. Rev.* **2024**, *124* (16), 9376–9456. https://doi.org/10.1021/acs.chemrev.3c00937.

(84) Xu, J.; Zhang, J.; Zhang, W.; Lee, C.-S. Interlayer Nanoarchitectonics of Two-Dimensional Transition-Metal Dichalcogenides Nanosheets for Energy Storage and Conversion Applications. *Advanced Energy Materials* **2017**, *7* (23), 1700571. https://doi.org/10.1002/aenm.201700571.

(85) Bolar, S.; Shit, S.; Murmu, N. C.; Samanta, P.; Kuila, T. Activation Strategy of MoS2 as HER Electrocatalyst through Doping-Induced Lattice Strain, Band Gap Engineering, and Active Crystal Plane Design. *ACS Appl. Mater. Interfaces* **2021**, *13* (1), 765–780. https://doi.org/10.1021/acsami.0c20500.

(86) Lukowski, M. A.; Daniel, A. S.; English, C. R.; Meng, F.; Forticaux, A.; Hamers, R. J.; Jin, S. Highly Active Hydrogen Evolution Catalysis from Metallic WS2 Nanosheets. *Energy Environ. Sci.* **2014**, *7* (8), 2608–2613. https://doi.org/10.1039/C4EE01329H.

(87) *Elastic properties of chemical-vapor-deposited monolayer MoS2, WS2, and their bilayer heterostructures - PubMed*. https://pubmed.ncbi.nlm.nih.gov/25120033/ (accessed 2026-01-15).

(88) Chang, H.-Y.; Yogeesh, M. N.; Ghosh, R.; Rai, A.; Sanne, A.; Yang, S.; Lu, N.; Banerjee, S. K.; Akinwande, D. Large-Area Monolayer MoS2 for Flexible Low-Power RF Nanoelectronics in the GHz Regime. *Advanced Materials* **2016**, *28* (9), 1818–1823. https://doi.org/10.1002/adma.201504309.

(89) Sakthivel, R.; Keerthi, M.; Chung, R.-J.; He, J.-H. Heterostructures of 2D Materials and Their Applications in Biosensing. *Progress in Materials Science* **2023**, *132*, 101024. https://doi.org/10.1016/j.pmatsci.2022.101024.

(90) Xue, S.; Wu, G.; Li, M.; Liu, Z.; Deng, Y.; Han, W.; Lv, X.; Wan, S.; Xi, X.; Yang, D.; Dong, A. Generalized Assembly of Sandwich-like 0D/2D/0D Heterostructures with Highly Exposed Surfaces toward Superior Electrochemical Performances. *Nano Res.* **2022**, *15* (1), 255–263. https://doi.org/10.1007/s12274-021-3468-y.

(91) 2D Material Based Heterostructures for Solar Light Driven Photocatalytic H2 Production. *Materials Advances* **2022**, *3* (8), 3389–3417. https://doi.org/10.1039/d2ma00191h.

(92) Desai, S. B.; Madhvapathy, S. R.; Sachid, A. B.; Llinas, J. P.; Wang, Q.; Ahn, G. H.; Pitner, G.; Kim, M. J.; Bokor, J.; Hu, C.; Wong, H.-S. P.; Javey, A. MoS2 Transistors with 1-Nanometer Gate Lengths. *Science* **2016**, *354* (6308), 99–102. https://doi.org/10.1126/science.aah4698.

(93) Liu, A.; Zhang, X.; Liu, Z.; Li, Y.; Peng, X.; Li, X.; Qin, Y.; Hu, C.; Qiu, Y.; Jiang, H.; Wang, Y.; Li, Y.; Tang, J.; Liu, J.; Guo, H.; Deng, T.; Peng, S.; Tian, H.; Ren, T.-L. The Roadmap of 2D Materials and Devices Toward Chips. *Nano-Micro Lett.* **2024**, *16* (1), 119. https://doi.org/10.1007/s40820-023-01273-5.

(94) Xue, G.; Sui, X.; Yin, P.; Zhou, Z.; Li, X.; Cheng, Y.; Guo, Q.; Zhang, S.; Wen, Y.; Zuo, Y.; Zhao, C.; Wu, M.; Gao, P.; Li, Q.; He, J.; Wang, E.; Zhang, G.; Liu, C.; Liu, K. Modularized Batch Production of 12-Inch Transition Metal Dichalcogenides by Local Element Supply. *Science Bulletin* **2023**, *68* (14), 1514–1521. https://doi.org/10.1016/j.scib.2023.06.037.

(95) Briggs, N.; Subramanian, S.; Lin, Z.; Li, X.; Zhang, X.; Zhang, K.; Xiao, K.; Geohegan, D.; Wallace, R.; Chen, L.-Q.; Terrones, M.; Ebrahimi, A.; Das, S.; Redwing, J.; Hinkle, C.; Momeni, K.; van Duin, A.; Crespi, V.; Kar, S.; Robinson, J. A. A Roadmap for Electronic Grade 2D Materials. *2D Mater.* **2019**, *6* (2), 022001. https://doi.org/10.1088/2053-1583/aaf836.

(96) Li, L.; Yu, Y.; Ye, G. J.; Ge, Q.; Ou, X.; Wu, H.; Feng, D.; Chen, X. H.; Zhang, Y. Black Phosphorus Field-Effect Transistors. *Nature Nanotech* **2014**, *9* (5), 372–377. https://doi.org/10.1038/nnano.2014.35.

(97) Desai, S. B.; Madhvapathy, S. R.; Sachid, A. B.; Llinas, J. P.; Wang, Q.; Ahn, G. H.; Pitner, G.; Kim, M. J.; Bokor, J.; Hu, C.; Wong, H.-S. P.; Javey, A. MoS2 Transistors with 1-Nanometer Gate Lengths. *Science* **2016**, *354* (6308), 99–102. https://doi.org/10.1126/science.aah4698.

(98) Wu, R.; Tao, Q.; Li, J.; Li, W.; Chen, Y.; Lu, Z.; Shu, Z.; Zhao, B.; Ma, H.; Zhang, Z.; Yang, X.; Li, B.; Duan, H.; Liao, L.; Liu, Y.; Duan, X.; Duan, X. Bilayer Tungsten Diselenide Transistors with On-State Currents Exceeding 1.5 Milliamperes per Micrometre. *Nat Electron* **2022**, *5* (8), 497–504. https://doi.org/10.1038/s41928-022-00800-3.

(99) Liu, L.; Kong, L.; Li, Q.; He, C.; Ren, L.; Tao, Q.; Yang, X.; Lin, J.; Zhao, B.; Li, Z.; Chen, Y.; Li, W.; Song, W.; Lu, Z.; Li, G.; Li, S.; Duan, X.; Pan, A.; Liao, L.; Liu, Y. Transferred van Der Waals Metal Electrodes for Sub-1-Nm MoS2 Vertical Transistors. *Nat Electron* **2021**, *4* (5), 342–347. https://doi.org/10.1038/s41928-021-00566-0.

(100) Jiang, J.; Xu, L.; Qiu, C.; Peng, L.-M. Ballistic Two-Dimensional InSe Transistors. *Nature* **2023**, *616* (7957), 470–475. https://doi.org/10.1038/s41586-023-05819-w.

(101) Chung, Y.-Y.; Chou, B.-J.; Hsu, C.-F.; Yun, W.-S.; Li, M.-Y.; Su, S.-K.; Liao, Y.-T.; Lee, M.-C.; Huang, G.-W.; Liew, S.-L.; Shen, Y.-Y.; Chang, W.-H.; Chen, C.-W.; Kei, C.-C.; Wang, H.; Philip Wong, H.-S.; Lee, T. Y.; Chien, C.-H.; Cheng, C.-C.; Radu, I. P. First Demonstration of GAA Monolayer-MoS2 Nanosheet nFET with 410μA μ m ID 1V VD at 40nm Gate Length. In *2022 International Electron Devices Meeting (IEDM)*; 2022; p 34.5.1-34.5.4. https://doi.org/10.1109/IEDM45625.2022.10019563.

(102) Tan, C.; Yu, M.; Tang, J.; Gao, X.; Yin, Y.; Zhang, Y.; Wang, J.; Gao, X.; Zhang, C.; Zhou, X.; Zheng, L.; Liu, H.; Jiang, K.; Ding, F.; Peng, H. 2D Fin Field-Effect Transistors Integrated with Epitaxial High-k Gate Oxide. *Nature* **2023**, *616* (7955), 66–72. https://doi.org/10.1038/s41586-023-05797-z.

(103) Liu, A.; Peng, X.; Peng, S.; Tian, H. Dielectrics for 2-D Electronics: From Device to Circuit Applications. *IEEE Transactions on Electron Devices* **2023**, *70* (4), 1474–1498. https://doi.org/10.1109/TED.2022.3220483.

(104) Fukamachi, S.; Solís-Fernández, P.; Kawahara, K.; Tanaka, D.; Otake, T.; Lin, Y.-C.; Suenaga, K.; Ago, H. Large-Area Synthesis and Transfer of Multilayer Hexagonal Boron Nitride for Enhanced Graphene Device Arrays. *Nat Electron* **2023**, *6* (2), 126–136. https://doi.org/10.1038/s41928-022-00911-x.

(105) Huang, J.-K.; Wan, Y.; Shi, J.; Zhang, J.; Wang, Z.; Wang, W.; Yang, N.; Liu, Y.; Lin, C.-H.; Guan, X.; Hu, L.; Yang, Z.-L.; Huang, B.-C.; Chiu, Y.-P.; Yang, J.; Tung, V.; Wang, D.; Kalantar-Zadeh, K.; Wu, T.; Zu, X.; Qiao, L.; Li, L.-J.; Li, S. High-k Perovskite Membranes as Insulators for Two-Dimensional Transistors. *Nature* **2022**, *605* (7909), 262–267. https://doi.org/10.1038/s41586-022-04588-2.

(106) Fortin-Deschênes, M.; Pu, R.; Zhou, Y.-F.; Ma, C.; Cheung, P.; Watanabe, K.; Taniguchi, T.; Zhang, F.; Du, X.; Xia, F. Uncovering Topological Edge States in Twisted Bilayer Graphene. *Nano Lett.* **2022**, *22* (15), 6186–6193. https://doi.org/10.1021/acs.nanolett.2c01481.

(107) Fukamachi, S.; Solís-Fernández, P.; Kawahara, K.; Tanaka, D.; Otake, T.; Lin, Y.-C.; Suenaga, K.; Ago, H. Large-Area Synthesis and Transfer of Multilayer Hexagonal Boron Nitride for Enhanced Graphene Device Arrays. *Nat Electron* **2023**, *6* (2), 126–136. https://doi.org/10.1038/s41928-022-00911-x.

(108) Kim, H. G.; Lee, H.-B.-R. Atomic Layer Deposition on 2D Materials. *Chem. Mater.* **2017**, *29* (9), 3809–3826. https://doi.org/10.1021/acs.chemmater.6b05103.

(109) Schulman, D. S.; Arnold, A. J.; Das, S. Contact Engineering for 2D Materials and Devices. *Chem. Soc. Rev.* **2018**, *47* (9), 3037–3058. https://doi.org/10.1039/C7CS00828G.

(110) Das, S.; Chen, H.-Y.; Penumatcha, A. V.; Appenzeller, J. High Performance Multilayer MoS2 Transistors with Scandium Contacts. *Nano Lett.* **2013**, *13* (1), 100–105. https://doi.org/10.1021/nl303583v.

(111) Cho, S.; Kim, S.; Kim, J. H.; Zhao, J.; Seok, J.; Keum, D. H.; Baik, J.; Choe, D.-H.; Chang, K. J.; Suenaga, K.; Kim, S. W.; Lee, Y. H.; Yang, H. Phase Patterning for Ohmic Homojunction Contact in MoTe2. *Science* **2015**, *349* (6248), 625–628. https://doi.org/10.1126/science.aab3175.

(112) Wang, Y.; Xiao, J.; Zhu, H.; Li, Y.; Alsaid, Y.; Fong, K. Y.; Zhou, Y.; Wang, S.; Shi, W.; Wang, Y.; Zettl, A.; Reed, E. J.; Zhang, X. Structural Phase Transition in Monolayer MoTe2 Driven by Electrostatic Doping. *Nature* **2017**, *550* (7677), 487–491. https://doi.org/10.1038/nature24043.

(113) Cheng, Z.; Yu, Y.; Singh, S.; Price, K.; Noyce, S. G.; Lin, Y.-C.; Cao, L.; Franklin, A. D. Immunity to Contact Scaling in MoS2 Transistors Using in Situ Edge Contacts. *Nano Lett.* **2019**, *19* (8), 5077–5085. https://doi.org/10.1021/acs.nanolett.9b01355.

(114) Kilby, J. S. Invention of the Integrated Circuit. *IEEE Transactions on Electron Devices* **1976**, *23* (7), 648–654. https://doi.org/10.1109/T-ED.1976.18467.

(115) Su, S.-K.; Chuu, C.-P.; Li, M.-Y.; Cheng, C.-C.; Wong, H.-S. P.; Li, L.-J. Layered Semiconducting 2D Materials for Future Transistor Applications. *Small Structures* **2021**, *2* (5), 2000103. https://doi.org/10.1002/sstr.202000103.

(116) Radisavljevic, B.; Radenovic, A.; Brivio, J.; Giacometti, V.; Kis, A. Single-Layer MoS2 Transistors. *Nature Nanotech* **2011**, *6* (3), 147–150. https://doi.org/10.1038/nnano.2010.279.

(117) Yu, L.; Lee, Y.-H.; Ling, X.; Santos, E. J. G.; Shin, Y. C.; Lin, Y.; Dubey, M.; Kaxiras, E.; Kong, J.; Wang, H.; Palacios, T. Graphene/MoS2 Hybrid Technology for Large-Scale Two-Dimensional Electronics. *Nano Lett.* **2014**, *14* (6), 3055–3063. https://doi.org/10.1021/nl404795z.

(118) Dathbun, A.; Kim, Y.; Kim, S.; Yoo, Y.; Kang, M. S.; Lee, C.; Cho, J. H. Large-Area CVD-Grown Sub-2 V ReS2 Transistors and Logic Gates. *Nano Lett.* **2017**, *17* (5), 2999–3005. https://doi.org/10.1021/acs.nanolett.7b00315.

(119) Wang, H.; Yu, L.; Lee, Y.-H.; Shi, Y.; Hsu, A.; Chin, M. L.; Li, L.-J.; Dubey, M.; Kong, J.; Palacios, T. Integrated Circuits Based on Bilayer MoS2 Transistors. *Nano Lett.* **2012**, *12* (9), 4674–4680. https://doi.org/10.1021/nl302015v.

(120) Li, J.; Li, J.; Ding, Y.; Liu, C.; Hou, X.; Chen, H.; Xiong, Y.; Zhang, D. W.; Chai, Y.; Zhou, P. Highly Area-Efficient Low-Power SRAM Cell with 2 Transistors and 2 Resistors. In *2019 IEEE International Electron Devices Meeting (IEDM)*; 2019; p 23.3.1-23.3.4. https://doi.org/10.1109/IEDM19573.2019.8993520.

(121) Wang, X.; Chen, X.; Ma, J.; Gou, S.; Guo, X.; Tong, L.; Zhu, J.; Xia, Y.; Wang, D.; Sheng, C.; Chen, H.; Sun, Z.; Ma, S.; Riaud, A.; Xu, Z.; Cong, C.; Qiu, Z.; Zhou, P.; Xie, Y.; Bian, L.; Bao, W. Pass-Transistor Logic Circuits Based on Wafer-Scale 2D Semiconductors. *Advanced Materials* **2022**, *34* (48), 2202472. https://doi.org/10.1002/adma.202202472.

(122) Wang, X.; Chen, X.; Ma, J.; Gou, S.; Guo, X.; Tong, L.; Zhu, J.; Xia, Y.; Wang, D.; Sheng, C.; Chen, H.; Sun, Z.; Ma, S.; Riaud, A.; Xu, Z.; Cong, C.; Qiu, Z.; Zhou, P.; Xie, Y.; Bian, L.; Bao, W. Pass-Transistor Logic Circuits Based on Wafer-Scale 2D Semiconductors. *Advanced Materials* **2022**, *34* (48), 2202472. https://doi.org/10.1002/adma.202202472.

(123) Wachter, S.; Polyushkin, D. K.; Bethge, O.; Mueller, T. A Microprocessor Based on a Two-Dimensional Semiconductor. *Nat Commun* **2017**, *8* (1), 14948. https://doi.org/10.1038/ncomms14948.

(124) Wu, Y.; Jenkins, K. A.; Valdes-Garcia, A.; Farmer, D. B.; Zhu, Y.; Bol, A. A.; Dimitrakopoulos, C.; Zhu, W.; Xia, F.; Avouris, P.; Lin, Y.-M. State-of-the-Art Graphene High-Frequency Electronics. *Nano Lett.* **2012**, *12* (6), 3062–3067. https://doi.org/10.1021/nl300904k.

(125) Wang, H.; Nezich, D.; Kong, J.; Palacios, T. Graphene Frequency Multipliers. *IEEE Electron Device Letters* **2009**, *30* (5), 547–549. https://doi.org/10.1109/LED.2009.2016443.

(126) Adesina, N. O.; Srivastava, A.; Ullah Khan, A.; Xu, J. An Ultra-Low Power MOS2 Tunnel Field Effect Transistor PLL Design for IoT Applications. In *2021 IEEE International IOT, Electronics and Mechatronics Conference (IEMTRONICS)*; 2021; pp 1–6. https://doi.org/10.1109/IEMTRONICS52119.2021.9422641.

(127) Horowitz, M. 1.1 Computing's Energy Problem (and What We Can Do about It). In *2014 IEEE International Solid-State Circuits Conference Digest of Technical Papers (ISSCC)*; 2014; pp 10–14. https://doi.org/10.1109/ISSCC.2014.6757323.

(128) Yan, X.; Zhao, Q.; Chen, A. P.; Zhao, J.; Zhou, Z.; Wang, J.; Wang, H.; Zhang, L.; Li, X.; Xiao, Z.; Wang, K.; Qin, C.; Wang, G.; Pei, Y.; Li, H.; Ren, D.; Chen, J.; Liu, Q. Vacancy-Induced Synaptic Behavior in 2D WS2 Nanosheet–Based Memristor for Low-Power Neuromorphic Computing. *Small* **2019**, *15* (24), 1901423. https://doi.org/10.1002/smll.201901423.

(129) Zhang, F.; Zhang, H.; Krylyuk, S.; Milligan, C. A.; Zhu, Y.; Zemlyanov, D. Y.; Bendersky, L. A.; Burton, B. P.; Davydov, A. V.; Appenzeller, J. Electric-Field Induced Structural Transition in Vertical MoTe2- and Mo1–xWxTe2-Based Resistive Memories. *Nature Mater* **2019**, *18* (1), 55–61. https://doi.org/10.1038/s41563-018-0234-y.

(130) Zhang, Y.; Wang, L.; Chen, H.; Ma, T.; Lu, X.; Loh, K. P. Analog and Digital Mode α-In2Se3 Memristive Devices for Neuromorphic and Memory Applications. *Advanced Electronic Materials* **2021**, *7* (12), 2100609. https://doi.org/10.1002/aelm.202100609.

(131) Xu, R.; Jang, H.; Lee, M.-H.; Amanov, D.; Cho, Y.; Kim, H.; Park, S.; Shin, H.; Ham, D. Vertical MoS2 Double-Layer Memristor with Electrochemical Metallization as an Atomic-Scale Synapse with Switching Thresholds Approaching 100 mV. *Nano Lett.* **2019**, *19* (4), 2411–2417. https://doi.org/10.1021/acs.nanolett.8b05140.

(132) Feng, X.; Li, Y.; Wang, L.; Chen, S.; Yu, Z. G.; Tan, W. C.; Macadam, N.; Hu, G.; Huang, L.; Chen, L.; Gong, X.; Chi, D.; Hasan, T.; Thean, A. V.-Y.; Zhang, Y.-W.; Ang, K.-W. A Fully Printed Flexible MoS2 Memristive Artificial Synapse with Femtojoule Switching Energy. *Advanced Electronic Materials* **2019**, *5* (12), 1900740. https://doi.org/10.1002/aelm.201900740.

(133) Sun, L.; Zhang, Y.; Han, G.; Hwang, G.; Jiang, J.; Joo, B.; Watanabe, K.; Taniguchi, T.; Kim, Y.-M.; Yu, W. J.; Kong, B.-S.; Zhao, R.; Yang, H. Self-Selective van Der Waals Heterostructures for Large Scale Memory Array. *Nat Commun* **2019**, *10* (1), 3161. https://doi.org/10.1038/s41467-019-11187-9.

(134) Lee, H.-S.; Sangwan, V. K.; Rojas, W. A. G.; Bergeron, H.; Jeong, H. Y.; Yuan, J.; Su, K.; Hersam, M. C. Dual-Gated MoS2 Memtransistor Crossbar Array. *Advanced Functional Materials* **2020**, *30* (45), 2003683. https://doi.org/10.1002/adfm.202003683.

(135) Wang, S.; Wang, C.-Y.; Wang, P.; Wang, C.; Li, Z.-A.; Pan, C.; Dai, Y.; Gao, A.; Liu, C.; Liu, J.; Yang, H.; Liu, X.; Cheng, B.; Chen, K.; Wang, Z.; Watanabe, K.; Taniguchi, T.; Liang, S.-J.; Miao, F. Networking Retinomorphic Sensor with Memristive Crossbar for Brain-Inspired Visual Perception. *Natl Sci Rev* **2021**, *8* (2), nwaa172. https://doi.org/10.1093/nsr/nwaa172.

(136) Lee, S.; Peng, R.; Wu, C.; Li, M. Programmable Black Phosphorus Image Sensor for Broadband Optoelectronic Edge Computing. *Nat Commun* **2022**, *13* (1), 1485. https://doi.org/10.1038/s41467-022-29171-1.

Chapter 2

Fundamental Mechanisms and Characterization Methodologies

From Structural Characterization to Optoelectronic Figures of Merit in TMD-Based Devices

2.1 Structural and morphological characterization of 2d materials

A comprehensive understanding of 2D materials requires detailed structural and morphological characterization, as their physical, electrical, and optical properties are intrinsically linked to atomic arrangement, surface morphology, and defect distribution. Owing to their reduced dimensionality and high surface-to-volume ratio, even subtle structural variations can induce pronounced changes in device behavior[1]. For this reason, structural and morphological analysis represents a foundational step in the study of pristine 2D materials and a prerequisite for interpreting their electronic and optoelectronic response.

In TMDs, the layered crystal structure is defined by strong in-plane covalent bonding and weak out-of-plane van der Waals interactions (vdW). While this bonding anisotropy enables mechanical exfoliation and vdW Hs assembly, it also renders the material highly sensitive to surface processes such as adsorption, oxidation, and reconstruction. Structural characterization techniques are therefore essential not only to assess crystallinity and thickness, but also to identify the onset of degradation pathways and defect-driven transformations.

2.1.1 Defects in 2D materials

Defects are defined as local disruptions of the periodicity and symmetry within an ideal crystal lattice. In 2D materials, and particularly in TMDs, the reduced dimensionality, coupled with the several synthesis and post-growth methods can generate a variety of intrinsic and extrinsic defects[2]. They play a central role in determining structural, electronic, optical, and chemical properties of TMDs. At the nanoscale, even a low density of defects can strongly interact with interfaces and the environment, ultimately governing the physicochemical response of the

material. Crucially, defects are not necessarily adverse features: through "defect engineering," they can be precisely controlled to give the material specific, desired properties[3].

From a geometrical perspective, defects in 2D materials can be classified according to their dimensionality: (i) zero-dimensional (0D) point defects, such as vacancies, antisites, adatoms, Stone–Wales defects, and substitutional impurities; (ii) one-dimensional (1D) line defects, including dislocations and grain boundaries; and (iii) two-dimensional (2D) planar defects, such as wrinkles, folds, cracks, and multilayer overlaps[4]. Some of them are displayed in Figure 2.1. In this work, the discussion is limited to point and line defects, which are most relevant for pristine monolayer TMDs and their surface reactivity.

2.1.1.1 Thermodynamic Description of Defect Formation

A key quantity describing the stability and concentration of a defect is its formation energy E_f, which determines the equilibrium defect density at thermodynamic equilibrium. For a defect X at a charge state q, the formation energy is expressed as:

$$E_f[X^q] = E_{tot}[X^q] - E_{tot}[host] - \sum_i n_i \mu_i + q(E_F + E_v) \qquad (2.1)$$

where $E_{tot}[X^q]$ is the total energy of the supercell containing the defect X, $E_{tot}[host]$ is the total energy of the pristine supercell, n_i is the number of atoms of species i added or removed from the supercell to form the defect, μ_i represents the corresponding chemical potential, E_v is the valence band maximum (VBM), and E_F is the Fermi level with respect to the VBM[5,6].

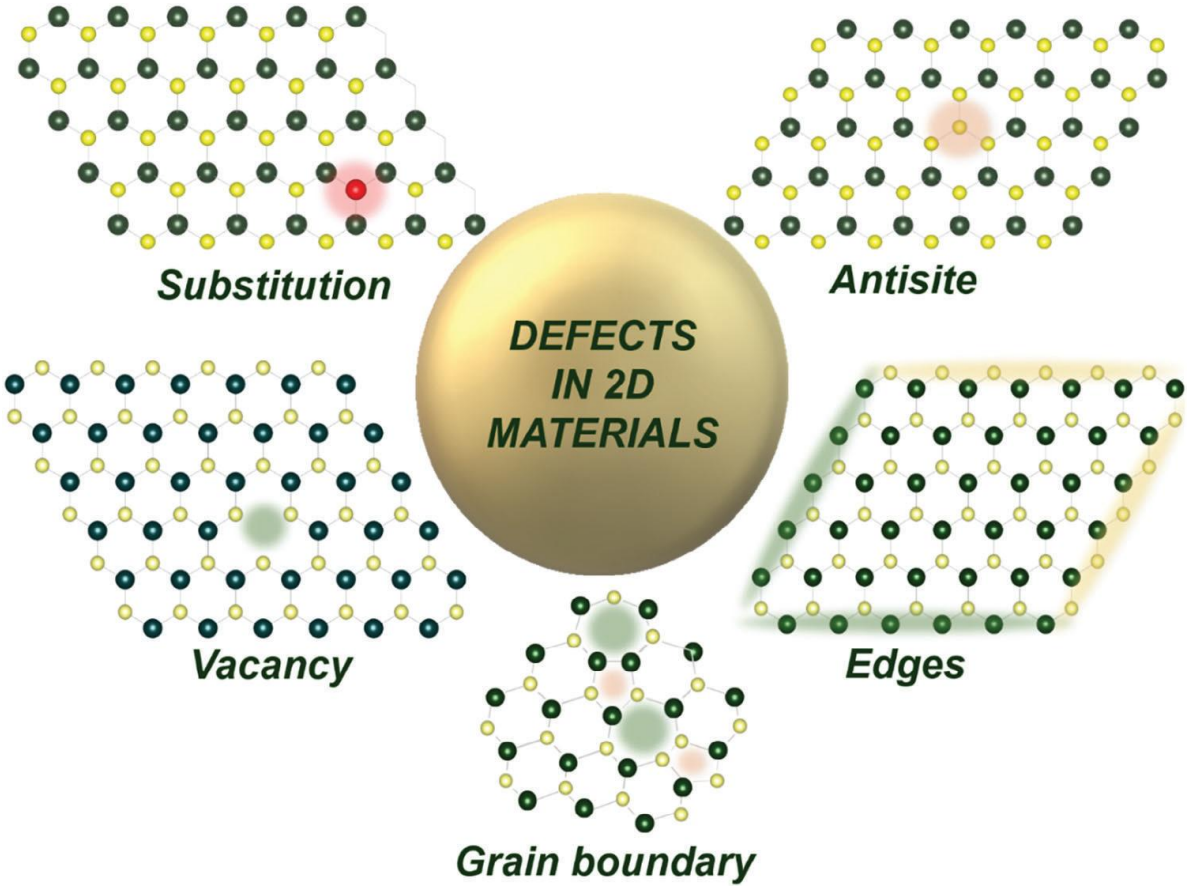

Figure 2.1: Classification of defects in 2D materials[1]

In the dilute limit, finite-size electrostatic corrections must be included to obtain the isolated defect formation energy:

$$E_{f,\infty} = E_f + E_{corr} \qquad (2.2)$$

Formation energies can result from additional entropy contributions such as vibrational contributions, electronic contributions and magnetic excitation.
A more general thermodynamic description is provided by the Gibbs free energy of defect formation:

$$G_f = F_{def} - F_{host} + pV_f - \sum_i n_i \mu_i + q(E_v + E_F) + E_{corr} \qquad (2.3)$$

where F_{def} and F_{host} are the Helmholtz free energies of the defective and pristine systems, respectively, and E_{corr} accounts for spurious electrostatic interactions. The free energy includes electronic, quasi-harmonic, and anharmonic vibrational contributions, reflecting the fact that defect formation locally modifies bonding and lattice dynamics.

The chemical potentials μ_i depend on experimental growth conditions and are constrained by thermodynamic equilibrium with competing phases. For instance, in the Mo–S system:

$$\mu_{MoS_2} = \mu_{Mo} + 2\mu_S \qquad (2.4)$$

with additional bounds imposed by the stability of elemental Mo and S phases[7].

2.1.1.2 Point Defects in TMDs

Point defects in TMD monolayers can be intrinsic or extrinsic. Intrinsic defects arise from thermally driven lattice fluctuations and include vacancies and interstitial atoms, while extrinsic defects originate from foreign atoms introduced during synthesis or post-processing, and are often referred as impurity defects.

In group-VI TMDs such as MoS_2, the most commonly observed intrinsic point defects are chalcogen vacancies (V_S), disulfur vacancies (V_{S_2}), vacancy complexes involving the metal atom, and antisite defects where a metal atom substitutes a chalcogen site or viceversa[8].

First-principles calculations indicate that sulfur vacancies exhibit the lowest formation energy (typically ~ 1.3–1.5 eV under Mo-rich conditions), making them the most abundant intrinsic defects under thermodynamic equilibrium[9,10]. In contrast, metal vacancies have significantly higher formation energies and are therefore much less likely to form. Sulfur vacancies introduce localized states deep within the bandgap and behave as deep acceptors, with stable charge states of 0 and -1 when the Fermi level lies inside the gap[11]. These defects strongly influence charge transport, carrier trapping, catalytic activity, and chemical reactivity, particularly toward oxygen adsorption.

As better described below, adatom defects can adhere to the surface of materials through weak vdW interactions (physisorption) or strong covalent bonding (chemisorption). Chemisorption in TMDs is particularly intricate since adatoms can locate above the metal atoms or above the chalcogen atoms, on a metal-chalcogen bonds, and above or within the center of hexagonal voids[12].

Substitutions, instead, usually arise from impurities introduced during the synthesis processes, determining variations in chemical composition and dramatic alterations in the structure of 2D materials[13]. However, dopants, like Fe, Co, Ni and Re as well as non-metal

atoms such as N,O and P can be also intentionally introduced with controlled composition and concentrations in TMD layers to modify and optimize their properties[14].

In 2D materials, dislocations are point-like topological defects that represent the termination of a semi-infinite row of atoms, effectively acting as the 2D equivalent of an edge dislocation. While in graphene these defects typically manifest as 5|7 (pentagon-heptagon) pairs that maintain stable carbon-carbon bonding, the situation is more complex in TMDs. Because TMDs consist of two different atomic species, odd-membered rings like the 5|7 pair force the formation of energetically unfavorable homo-elemental bonds (e.g., Mo-Mo or S-S). To avoid this chemical penalty, TMDs often exhibit alternative configurations such as 4|8 or 6|8 rings, which preserve the alternating atomic order at the expense of higher local elastic strain[15,16].

2.1.1.3 Line Defects and Grain Boundaries

In TMD monolayers, specific vacancies can cluster into line defects because of the low migration barriers. These features appear as single- and double-line vacancies aligned along the zig-zag direction[17]. In particular, single and double chalcogen vacancies have a lower formation energy in the zig-zag direction compared to those along the armchair direction[18].

Grain boundaries in TMDs correspond to interfaces between the domains of the material having distinct crystallographic orientations, which result in periodic arrays of dislocations. They typically form during growth processes like CVD, which often yield polycrystalline films, where grain boundaries originate from the atomic stitching between grains with different lattice orientations. In TMD monolayers, these grain boundaries consist of periodic arrays of dislocations characterized by non-hexagonal ring structures (e.g., 5|7, 4|6, 6|8 configurations) that locally perturb stoichiometry and atomic coordination[19,20]. These extended defects can significantly modify the local band structure, giving rise to metallic states, enhanced or quenched photoluminescence, and even magnetism[21,22] .

In certain TMDs such as $MoTe_2$, vacancy agglomeration can lead to the formation of inversion domains and mirror twin boundaries, whose structure and electronic properties depend sensitively on growth conditions and lattice polarity[23,24] .

2.1.1.4 Defect Mobility and Evolution

Defects in 2D materials are not static entities. Their mobility is determined by activation (diffusion, migration) energy barriers that they have to overcome in the diffusion process. The diffusion constant D is given as:

$$D = \nu\alpha^2 \exp\left(-\frac{E}{k_B T}\right) \qquad (2.5)$$

where E is the activation energy, α is the lattice constant, and ν is a characteristic frequency[25]. In monolayer MoS_2, the migration barrier for sulfur vacancies is approximately 2.3 eV, implying negligible diffusion below $\sim 400°C$ but possible redistribution at growth temperatures[26,27]. This dynamic behavior is particularly relevant for defect-mediated surface reactions, oxidation processes, and long-term device stability.

2.1.2 Adsorption/desorption processes on 2D materials surfaces

As reported in the previous section, lattice defects represent the most chemically active sites, as they interact more strongly with the environment than the pristine crystal lattice. The adsorption of gas molecules on two-dimensional semiconductors has been systematically classified by Liu et al.[28] into two main categories: physisorption and chemisorption. Physisorption is governed by weak physical interactions, such as van der Waals forces, and typically keeps the adsorbed species at a distance of about 2 Å from the surface. In contrast, chemisorption involves the formation of strong chemical bonds between the adsorbate and the atoms of the crystal lattice, effectively incorporating the adsorbed species into the material. The adsorption energy of a chalcogen vacancy V_X, the most common among point defects, can be estimated as

$$E_{ad} = E(V_X + \text{mol}) - E(V_X) - E(\text{mol}) \qquad (2.6)$$

where $E(V_X + \text{mol})$ is the total energy of the system with a molecule adsorbed at a vacancy site, while $E(V_X)$ and $E(\text{mol})$ correspond to the energies of the isolated vacancy and the free molecule, respectively.

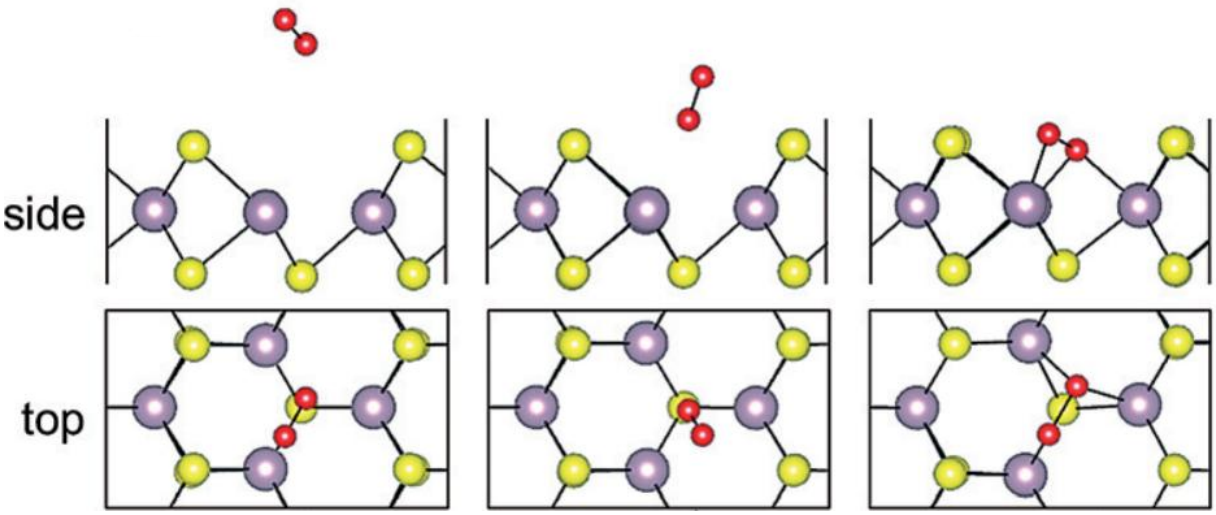

Figure 2.2: Reaction pathway of O_2 with Vx in MoS_2, from the physiosorbed to chemisorbed state. S yellow, Mo purple.[28]

Most atmospheric molecules, including H_2O, interact with TMD surfaces primarily through physisorption, leading to relatively small adsorption energies and reversible effects at room temperature. In contrast, molecular oxygen can undergo both physisorption and chemisorption, as shown in Figure 2.2. O_2 is unique among common air constituents in its ability to chemically bind to chalcogen vacancy sites under ambient conditions, a process associated with significantly higher adsorption energies and substantial modifications of the electronic structure.

From an energetic perspective, chemisorption proceeds through a metastable intermediate state and requires overcoming an activation energy barrier (0.74 eV for MoS_2). The barriers

for the same cation decrease from S to Se to Te. For oxygen molecules, this barrier is sufficiently low that the thermal energy available at room temperature enables the transition to the chemisorbed state. For most other molecular species, the activation barrier is too high to be overcome under ambient conditions, restricting their interaction with the surface to physisorption only.

The consequences of these two adsorption mechanisms are markedly different[29]. Property changes induced by physiosorbed species are generally unstable at room temperature. The low desorption barrier allows molecules to detach easily and the system to return to its initial state. Conversely, once oxygen becomes chemisorbed and reaches thermodynamic equilibrium, the reverse process requires energies that are not accessible under ambient conditions. As a result, oxygen chemisorption leads to effectively irreversible modifications of the material properties, as long as the environmental conditions remain unchanged[30].

2.1.3 Microscopy, Spectroscopy, and Atomistic Modeling of 2D Materials

No single technique can fully capture the complexity of structural phenomena in two-dimensional materials. Consequently, correlative approaches that combine atomic force microscopy (AFM), scanning electron microscopy (SEM), Raman spectroscopy, X-ray photoelectron spectroscopy (XPS), scanning tunneling microscopy (STM), and density functional theory (DFT) are increasingly adopted to obtain a coherent and reliable picture. Morphological techniques establish spatial evolution of surface features, spectroscopic tools identify chemical and structural modifications, and theoretical modeling provides microscopic interpretation. This integrated methodology is particularly effective for distinguishing intrinsic material properties from extrinsic effects induced by processing, environment, or measurement conditions.

AFM is one of the most widely employed techniques for the morphological analysis of 2D materials. AFM provides nanometer-scale lateral resolution and sub-angstrom vertical sensitivity, enabling accurate determination of layer thickness, surface roughness, step edges, and flake uniformity. In pristine TMDs, AFM height profiles are used to distinguish monolayers, few-layer regions, and bulk-like domains, as well as to monitor morphological changes induced by environmental exposure, thermal treatments, or fabrication processes[31]. In addition, phase-contrast and force-modulation AFM modes can reveal variations in mechanical properties and surface adhesion, often associated with oxidation, contamination, or defect formation. Recently, AFM has been used to investigate the relationships between the topographical, mechanical, electrical, chemical and electrochemical properties of 2D materials, through its advanced application modes, such as PeakForce mode, lift mode, conductive AFM, and AFM-based scanning electrochemical microscopy (AFM-SECM).[32,33]

SEM complements AFM by enabling rapid, large-area imaging of surface morphology, flake distribution, and degradation patterns. Although SEM lacks atomic resolution, it is particularly effective for identifying macroscopic features such as cracks, wrinkles, grain boundaries, and thickness-related contrast variations. In studies of environmental aging and oxidation, SEM

allows visualization of spatially heterogeneous processes that often initiate at edges or defect-rich regions[34].

Scanning transmission electron microscopy (STEM) is a popular tool for direct observation of crystalline structure, grain boundaries and defects of 2D materials. It provides atomically resolved images and spectroscopic data, by employing multiple electron detectors and various signals in parallel. Materials prepared for STEM need to be electron-transparent, so that electrons can transmit through the sample with minimal scattering. Electrons are collected by the different detectors, thereby improving signal-to-noise. Typical STEM samples, including tissue sections, lamellae, and nanoparticles on the order of 100 nm thickness or less, meet the criteria for electron transparency. Another advantage is the direct control of resolution and depth of focus and the interpretation of STEM images is straightforward since atoms may appear white or black[35,36].

Raman spectroscopy is a fast and nondestructive technique with high spatial and spectral resolution, used for probing the fundamental properties of 2D materials[37,38]. Raman peaks of lattice vibrations in 2D materials display features like peak position, full width at half maximum (FWHM), intensity and line shape that provide useful information like quantum interference, phonon frequency, electron-phonon coupling, electronic states, etc[39]. Deviations from reference spectra, such as peak shifts or broadening, are commonly associated with lattice distortions, charge transfer, or chemical modification. In detail, in 2D materials, intralayer and interlayer modes can be identified, derived from intralayer covalent bonds and interlayer vdW interactions. Intralayer modes provide information on composition and structural phases[40]. Their response to external perturbation enables the investigation of properties such as temperature dependence of phonon anharmonicity, electron-phonon coupling, strain dependence of elastic constants, and defect concentration dependence of the phonon confinement effect, etc[41,42]. The interlayer modes involve layer-to-layer vibrations and can be used to study the interlayer coupling in 2D materials, which is sensitive to the thickness and stacking order of the material[43].

XPS provides quantitative information on elemental composition, chemical bonding, and oxidation states. For pristine TMDs, XPS is essential for verifying stoichiometry and identifying intrinsic defects such as chalcogen vacancies. Upon exposure to ambient conditions, XPS enables detection of oxidation products, sub-oxide species, and chemical shifts associated with charge transfer. Because of its surface sensitivity, XPS is particularly well suited for studying surface-driven processes that dominate the behavior of 2D materials[44].

At the atomic scale, STM offers direct access to surface structure and electronic states. STM enables real-space imaging of atomic lattices, point defects, vacancy complexes, and adsorbates on pristine 2D crystals[45]. When combined with scanning tunneling spectroscopy (STS), it provides local density-of-states information, allowing direct correlation between structural defects and electronic states within the bandgap[46]. Although STM requires conductive or semiconductive samples and ultrahigh-vacuum conditions, it remains a benchmark technique for atomic-scale characterization.

DFT calculations play a crucial complementary role in structural characterization by providing an atomistic framework for interpreting experimental observations. For pristine TMDs, DFT enables prediction of stable crystal phases, defect formation energies, adsorption

configurations, and oxidation pathways[47]. By comparing calculated vibrational spectra, binding energies, and electronic structures with experimental Raman, XPS, and STM data, DFT helps disentangle competing mechanisms and assign microscopic origins to the observed phenomena.

2.2 Electrical characterization of 2d materials-based field effect transistors

A metallic gate, an insulating gate oxide and a semiconductor channel connecting the source and drain electrodes make up the fundamental components of a 2D FET. The source-drain voltage V_{ds} establishes the current flow in the semiconductor channel, and the applied gate voltage V_{gs} modulates it by altering the conductivity of the channel region. Due to the lack of effective doping methods, metallic electrodes at the source-drain junction produce Schottky connections, in contrast to conventional bulk semiconductor FETs. Back-gated 2D FETs, which are still in the research stage, usually have thick gate oxides, which require high gate voltages (>10 V) to switch the device from the OFF to the ON state. Additionally, the gating properties of 2D FETs are complicated by the complex back gating of both the channel and contact regions. Figure 2.3 summarizes the main techniques and figures of merit to electrically characterize 2D FETs.

2.2.1 Output characteristics

The drain current I_d is measured as a function of V_{ds} at various V_{gs} to determine FETs' output characteristics. When small V_{ds} are applied, important parameters can be extracted as the device acts as a linear resistor in this region. The drain current for an n-type 2D FET in the linear regime, assuming channel-dominated behaviour, can be expressed by the following formula,

$$I_d = \frac{\mu_n W C_{ox}}{L}\left[(V_{gs} - V_{th})V_{ds}\right] \qquad (2.7)$$

Where L, W, μ_n, C_{ox} and V_{th} are the channel length, channel width, channel electron mobility, oxide capacitance and the threshold voltage, respectively. However, only a portion of V_{ds} drops across the channel when contact resistance R_c is involved, so the equation must be changed to account for this aspect:

$$I_d = \frac{\mu_n W C_{ox}}{L}\left[(V_{gs} - V_{th})(V_{ds} - I_d 2R_c)\right] \qquad (2.8)$$

The contact resistance for the source and drain junctions at low V_{ds} is referred to as $2R_c$ in this context. As the contact region is simultaneously gated in 2D FETs with a global back gate, R_c is a function of both V_{gs} and V_{ds}. Thus, the linearity of the output characteristic can be used as a simple check to ascertain how contact resistance affects FET performance. Because of the simultaneous gating of the contact and channel regions, contacts can exhibit different behaviours (Ohmic or Schottky) at different gate voltages. However, because doped Schottky connections can resemble Ohmic features due to an increase of the tunneling component at the source junction, the linear behaviour does not offer any information regarding the process

underlying the Ohmic nature of contacts. Therefore, accurate μ, V_{th}, and R_c extraction is crucial to comprehending the current flow in 2D FETs.

It is essential to observe current saturation over a wide V_{ds} window in order to use 2D FET in analog, digital, and high-power applications. I_d grows linearly with V_{ds} before reaching saturation region, which is defined by a constant I_d independent of V_{ds}. Obtaining saturation in 2D devices at desirable levels of V_{ds} is still difficult because of high contact resistance, low channel mobility, and high-field dispersion, despite numerous publications showing current saturation in various TMD-FETs[49,50].

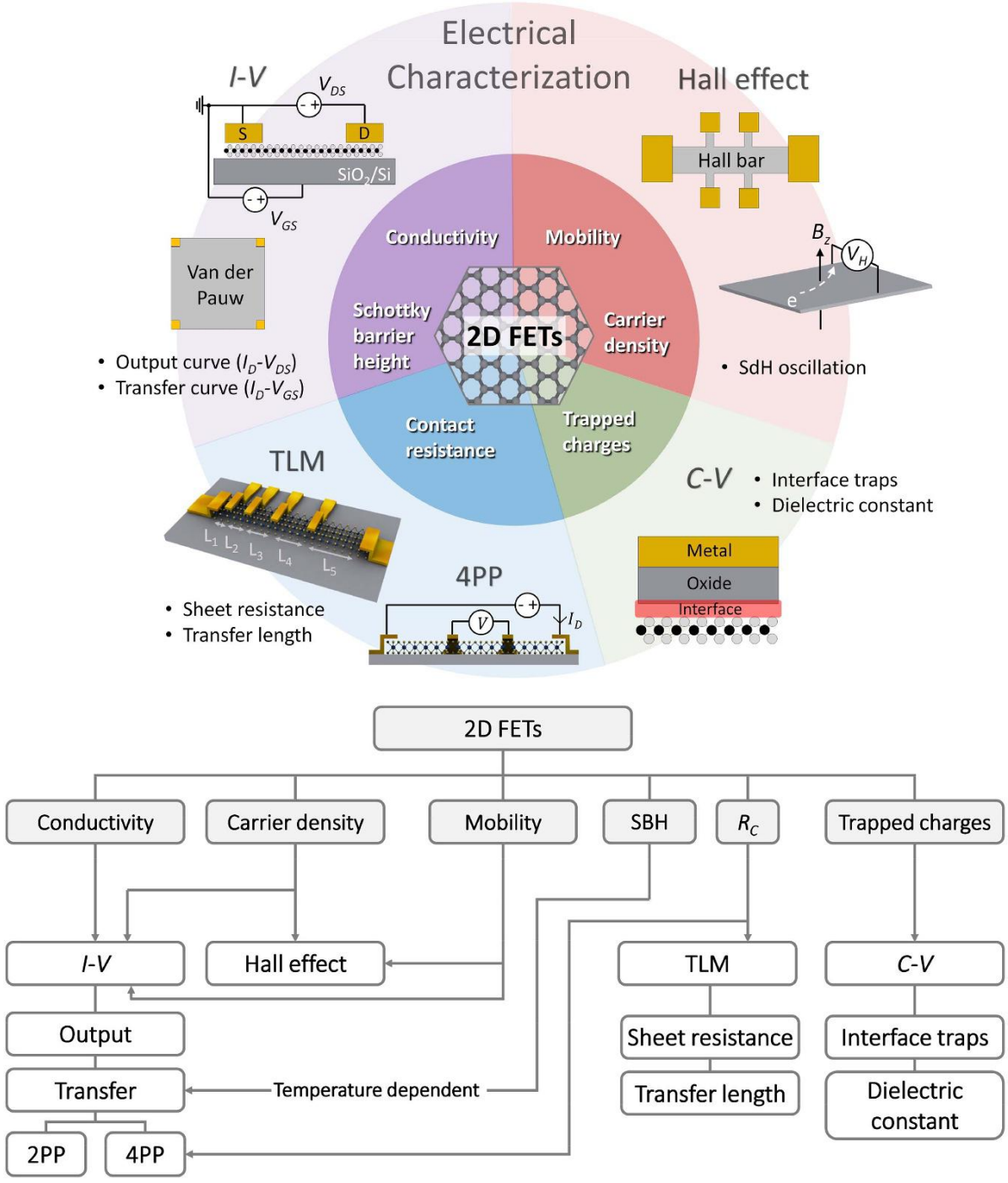

Figure 2.3 : Key parameters of 2D FETs and relevant characterization methods.[48]

2.2.2 Transfer characteristics

The transfer characteristics, derived by measuring I_d as a function of V_{gs} at constant V_{ds} can also be used to access FETs' electrical performance. Important parameters, including transconductance g_m, V_{th} and subthreshold swing (SS) are extracted from these curves. The transfer characteristics of an n-channel FET show ON-state current for V_{gs} higher than V_{th} that can be extracted from the transfer characteristic using a variety of techniques, including linear extrapolation, the second derivative of transconductance, and Ghibaudo's method[51]. For electronics to be energy-efficient, the power supply voltage must be reduced, and lowering the supply voltage is one of the best strategies to manage the power density. In order to lower power consumption, it is important to get beyond the abruptness (thermionic limit of 60 mV/decade) that results from the thermal carrier injection process. SS, which is defined as the inverse of the slope of $\log(I_d)$ versus V_{gs}, is a measure of a FET's abruptness, and controls how well the energy barrier at the source terminal may be tuned. Since a small SS indicates a high I_{on}/I_{off} ratio for low supply voltages, a small SS over a wide current range must be attained. The SS can be calculated as follows:

$$SS = \frac{dV_{gs}}{d(logI_d)} = \frac{\log(10)k_BT}{q}\left(1 + \frac{C_{CH}}{C_{oX}}\right) \qquad (2.9)$$

where C_{CH} is the channel capacitance, q is the elementary charge and k_B is the Boltzmann constant. For an ideal 2D FET $C_{CH} \ll C_{ox}$ in the subthreshold region. However, most 2D FETs are fabricated on thick SiO_2 substrate with large interface trap density, yielding large SS values. Large C_{ox} might be achieved by using ionic gated transistors, which results in SS values very close to 60 mV/decade and mobility values close to the phonon scattering limit. This makes ionic transistors effective for quantitatively characterizing the electronic properties of 2D materials[52].

The interfacial traps between 2D channel and SiO_2 also might induce unwanted hysteresis in the transfer characteristics[53]. This can be improved by encapsulation of 2D materials with an insulating 2D material like h-BN[54].

2.2.3 Carrier doping density

Electrical conductivity σ is linked to the charge carrier density n through the relation $\sigma = \frac{1}{qn\mu}$. Carrier density in a semiconductor can be generally tuned with substitutional doping; however, it is not so easy in 2D materials because of their nanometer-scale thickness. Despite this restriction, few reports on substitutional doping in 2D materials have been published. For example, group-V elements such as niobium and group-VII such as rhenium can be incorporated into the crystal lattice of group VI TMDs during their growth[55]. However, solid solubility, thickness and binding energy of 2D materials may limit the doping density.

It's emblematic that even though a high substitutional Nb dopant concentration up to 10^{14} cm^{-2} has been achieved in monolayer CVD grown WS_2, the estimated active dopant density was only $6 \cdot 10^{12}$ cm^{-2} [56].

It is typically assumed that the doping concentration in conventional semiconductors at room temperature is the same as the free carrier concentration, since free carriers are produced

from fully ionized dopant atoms implanted in the semiconductor. A variety of methods can be used to measure the doping concentration in bulk semiconductors. By contrast, doping density in 2D material is primarily determined by electrical characterization, as it is induced by electrostatic gating or charge transfer, which directly modulate the free carrier density in the material and not by external doping.

2.2.4 Field-effect mobility

From the measured transfer properties, two types of metal-oxide-semiconductor (MOS) FET motilities can be deduced: effective mobility and field-effect mobility. The drain conductance of a MOSFET biased in the linear regime is used to determine the effective mobility. Given a small V_{ds} and a negligible diffusive current, a general expression for the drain current of a MOSFET can be stated as follows:

$$I_d \sim \frac{W}{L} \mu_{eff} Q_n V_{ds} \quad (2.10)$$

$$V_g > V_{th} \text{ and } V_{ds} \ll (V_g - V_{th})$$

Where $Q_n = C_{OX}(V_g - V_{th})$ is the sheet charge density of the channel. The ideal method for determining Q_n is to independently measure the capacitance or Hall effect of the MOSFET structure. However, due to the small size of many exfoliated samples, it is uncommon to measure the capacitance of 2D MOSFETS because the signal is too weak and complex to be detected with any degree of accuracy. For an ideal device, effective mobility is then given by

$$\mu_{eff} = \frac{g_d}{Q_n} \frac{L}{W} \quad (2.11)$$

Where g_d is the drain conductance, given by $g_d = \frac{\partial I_d}{\partial V_{ds}}$. This expression is not reliable if the output characteristics don't show a linear dependence on V_{ds} around the bias point for which the mobility was retrieved since it means that the device doesn't follow the equation from which it was derived. Similarly, if the transfer characteristics do not show a linear dependence on V_{gs} near the bias point for which the mobility is extracted, the use of the equation to calculate Q_n is questionable because the behaviour of the device does not match the charge model.

Field-effect mobility, instead, is derived from the transconductance $g_m = \frac{\partial I_d}{\partial V_{gs}}$ of a MOSFET biased in the linear regime, given by

$$\mu_{FE} = \frac{g_m}{C_{ox} V_{ds}} \frac{L}{W} \quad (2.12)$$

It is indicated as μ in the following chapters.

2.2.5 Contact resistance and Schottky barriers

The absence of simple and controllable doping strategies in two-dimensional semiconductors leads to large contact resistance (R_c) at metal–semiconductor interfaces. In contrast to conventional semiconductors such as Si and GaAs, where R_c can approach the quantum limit, 2D materials, especially TMDs with bandgaps of 0.5–2 eV, typically exhibit contact resistances

more than an order of magnitude higher. This behavior originates from Schottky barrier formation caused by Fermi-level pinning due to intrinsic defects and processing-induced states, as well as from weak van der Waals bonding between metals and 2D layers, which introduces additional tunneling resistance[57,58].

High contact resistance not only limits the ON current and determines device polarity, but also dominates the electrical characteristics of back-gated 2D FETs, often masking intrinsic channel transport. Therefore, reliable determination of contact resistance is essential for understanding, optimizing, and benchmarking 2D devices. To this end, techniques such as the transfer length method (TLM) and temperature-dependent Arrhenius analysis are commonly employed to quantify R_c and Schottky barrier heights.

Schottky barrier height is commonly estimated using standard back-gated FET structures through temperature-dependent electrical measurements[59].The most widely used approach is the Arrhenius method, based on the analysis of temperature-dependent transfer or output characteristics. Carrier injection at the reverse-biased source contact occurs through three main mechanisms: thermionic emission over the barrier, thermionic field emission, and field emission through the barrier[60]. Their relative contributions depend on the applied gate voltage. In the OFF state, transport is dominated by thermionic emission, and the drain current can be expressed as

$$I_{ds}(V_{gs}) = WA^*_{2D}T^{\frac{3}{2}}\exp\left(-\frac{q\phi_{B,eff}(V_{gs})}{k_BT}\right)\left[1-\exp\left(-\frac{qV_{ds}}{k_BT}\right)\right], \quad (2.13)$$

where $\phi_{B,eff}(V_{GS})$ is the gate-dependent effective barrier height and A^*_{2D} is the modified Richardson constant.

By rewriting the current in Arrhenius form, the effective barrier height can be extracted as

$$\phi_{B,eff}(V_{GS}) = \frac{k_B}{q}\left[\frac{d\ln\left(\frac{I_d}{T^{\frac{3}{2}}}\right)}{d\left(\frac{1}{T}\right)}\right] \quad (2.14)$$

As the gate voltage increases, the barrier width is reduced and tunneling contributions become dominant, leading to weaker temperature dependence. The actual Schottky barrier height, ϕ_{Bn} is identified at the flat-band voltage, where the conduction band aligns with the barrier and $\phi_{B,eff}$ deviates from its linear dependence on V_{gs}[61].

Despite its widespread use, the Arrhenius method has important limitations in 2D materials. The transition from thermionic to tunneling transport is often poorly defined due to interface traps, surface adsorbates, van der Waals gaps, and non-uniform doping. Moreover, at low temperatures the thermionic current rapidly decreases and becomes negligible compared to tunneling currents, leading to unreliable extraction. These limitations must be carefully considered when interpreting temperature-dependent measurements in 2D FETs.

2.3 Photodetection devices: operating mechanisms and performance characterization

2D materials have been largely used in photodetectors thanks to their advantages in device fabrication and manipulation, such as integration flexibility, availability of a wide range of bandgaps, weak light-detection capability, optical operation through an ultra-broad wavelength band, fulfilment of photonic demands at low cost and applicability in photodetection with high-performance. In this section, the fundamental photonic effects and working mechanisms (Figure 2.4) are summarized.

2.3.1 Photogeneration mechanisms

The photovoltaic effect is attributed to the photogenerated charge carrier's separation by the built-in electric fields formed in p-n junctions or Schottky junctions and they then contribute to the photocurrent. An external bias is not needed in this case[62]. However, a related concept is impact ionization, which occurs when the photoexcited carriers are accelerated by a strong electric field and lead to carrier multiplication. It is the fundamental mechanism of avalanche photodetectors[63].

The photothermoelectric effect is the indirect conversion of light into electrical signals caused by variations in light absorption in different regions. The change in electron thermal motion due to this effect creates a temperature gradient within the device. These thermal processes increase the temperature of the active material according to the Seebeck effect[64] , which leads to a change in its electronic properties and so modifies the material's potential difference. The Seebeck effect can be explained by the emergence of photo-thermoelectric voltage between different regions whose temperature is not the same. Photothermoelectric voltage V_{PTE} is governed by the equation $V_{PTE}=(S_2–S_1)\Delta T$, where ΔT is the temperature difference between two regions, whereas S_1 and S_2 are the thermoelectric coefficients of the active material. The magnitude of the thermoelectric coefficient is closely related to the conductance in a region[65].

The photoconductive effect takes place when the incident photons, of a specific wavelength, cause a change in the channel electrical conductivity σ[66]. Electron-hole pairs generated by incident light enhance the carrier density n. When a voltage bias is applied, they flow according to the external electric field. Correspondingly the total current I_{tot} under illumination is higher than the dark current and the photocurrent $I_{ph} = I_{tot} - I_{dark}$ has the same direction as the applied bias voltage. Recombination of the separated charges may also be possible. Photoconductor-based devices require an external electric field to function, in contrast to photovoltaic effect-based devices, which can operate with zero bias.

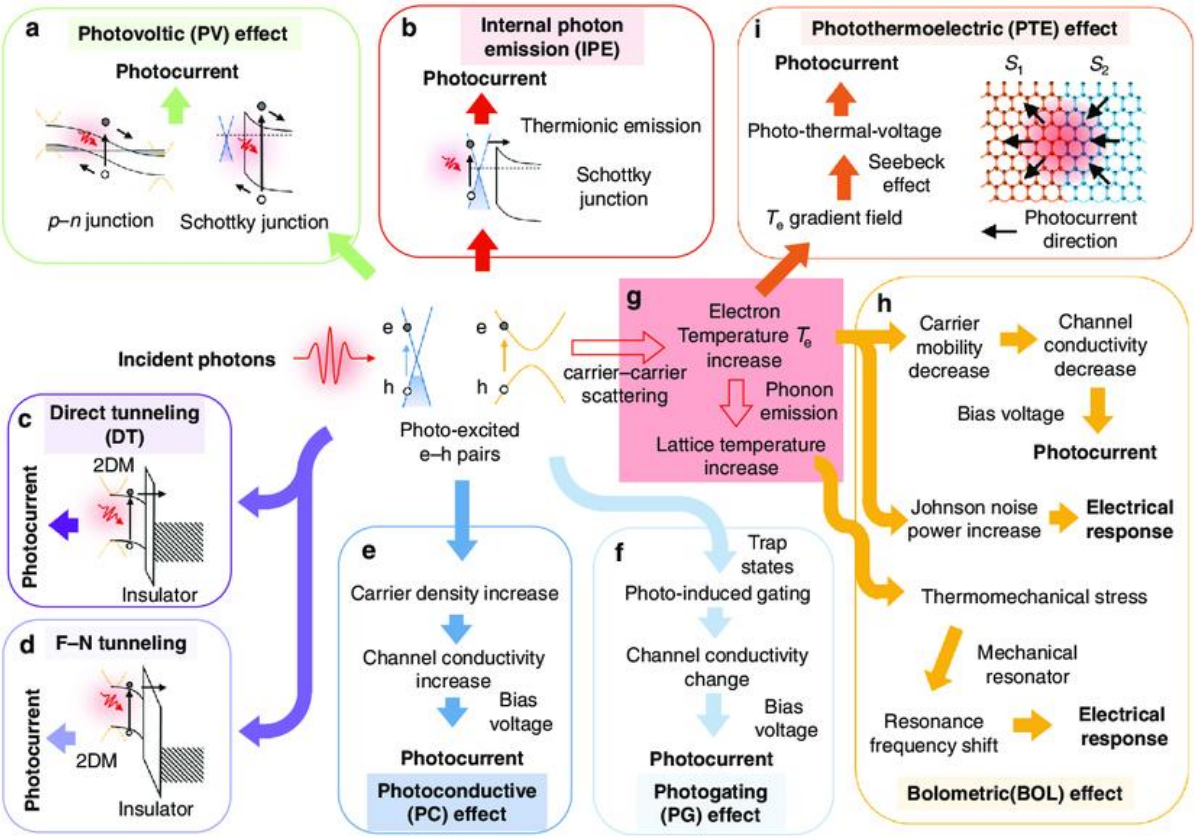

Figure 2.4: Photon type mechanisms: (a) photovoltaic effect, (b) internal photon emission (IPE) effect, (c) direct tunneling effect, (d) Fowler-Nordheim tunneling, (e) photoconductive (PC) effect, (f) photo-gating (PG) effect, (g) thermal relaxation process in 2DMs. Thermal-type mechanisms: (h) bolometric effect (BOL), (i) photo-thermoelectric (PTE)[67].

A photogating effect is a modification of the photoconductive effect which is usually observed in 2D material-based devices having surface defects. Basically, electrons or holes of the photoexcited e-h pairs are trapped by the trap states of the channel[68].The de-trapping of photo charges is a slow process; therefore it enhances the photogenerated carrier lifetime τ_L, during which the other polarity carriers transit through the channel with a transit time $\tau_{tr} < \tau_L$. The transit time depends on carrier mobility, device channel length and the applied voltage. The photoconductive gain of a device is exactly the ratio between these two times ($G = \tau_L/\tau_{tr}$) and it generally ranges from 5 to 10^{11} [66]. In phototransistors with source, drain and gate electrodes, the trapped carriers act as a localized extra gate that has an impact on the carrier density as well as on the conductivity of the active material. The direction of the photocurrent is decided by not only the applied bias but also by the original doping level of the channel[69].

The bolometric effects develop when an active material's resistivity changes as a result of absorption of light. The material resistivity can be changed through two processes: 1) variation of carrier mobility attributed to temperature change and 2) change in the carrier concentration. The material's thermal resistance and heat capacity are crucial factors that influence the sensitivity and response time for a device operating on the bolometric effect. The bolometric effect, in contrast to the photo-thermoelectric effect, necessitates external biasing for the

creation of photocurrent, whereas photo-thermoelectric effect-based devices can function without it.[70]

Internal photon emission (IPE) is the main working mechanism of the traditional Schottky photodetectors. In IPE-based 2D materials photodetectors, hot carriers with sufficient energy may be emitted over the Schottky barrier and contribute to the photocurrent[71].

Direct tunnelling (D-T) and Fowler-Nordheim (F-N) tunnelling are the main operation mechanisms in traditional metal-insulator-metal tunnelling diodes. These mechanisms have also been applied in photodetectors where an insulator is introduced between a metal and a semiconductor. Direct tunnelling can occur when the insulator layer is very thin[72]. For what concerns F-N tunnelling, instead, the photo-excited carriers transit through a triangular-shaped barrier, which requires a higher bias voltage. For these tunnelling photodetectors, the insulator layer can help reduce the dark current significantly[72,73].

2.3.2 Operating mechanisms and device configurations

The two main device classes of light detectors are photoconductors and photodiodes.[74] Photoconductive detectors operate by exploiting the increase in electrical conductivity induced by the photogeneration of free charge carriers. They can be classified as intrinsic or extrinsic. Intrinsic photoconductors rely on photon absorption with energy exceeding the semiconductor bandgap, leading to the generation of electron–hole pairs; consequently, their spectral response is primarily determined by the bandgap of the material. Extrinsic photoconductors, instead, involve the photoionization of impurity or defect states within the bandgap, typically activating only one type of carrier.

Photoconductors are inherently unipolar devices, and the detected signal is given by the difference between the light and dark conductivity. As already described, when the carrier persistence time exceeds the transit time across the device, photoconductive gain can occur, allowing multiple charges to be collected per absorbed photon. This persistence is governed by carrier recombination dynamics and is often enhanced by trap states, which delay recombination and hinder the release of one carrier species. Traps therefore play a central role in photoconduction, a mechanism studied since the early development of semiconductor physics.

Photodiodes rely on the use of at least two media, at least one of them being a semiconductor, in which a significant difference in materials' work functions produces a built-in potential. The electrons and holes generated by the photon move to opposite contacts, so the quantum efficiency (defined in the following section) is typically not higher than 1. However, they have faster response times than photoconductors.

In a p–n junction photodiode, photons with energy exceeding the semiconductor bandgap generate carriers in the neutral regions on both sides of the junction. Carriers created within a diffusion length reach the space-charge region, where they are separated by the built-in electric field, producing a photocurrent under short-circuit conditions or a photovoltage under open-circuit operation.

A Schottky barrier photodiode is formed at a metal–semiconductor interface and operates as a majority-carrier device. The potential barrier at the interface separates photogenerated

carriers created either in the depletion region or in the neutral semiconductor. Compared to p–n junction photodiodes, Schottky devices offer simpler fabrication and faster response times, although they typically suffer from higher dark currents.
In a metal–insulator–semiconductor (MIS) photodiode, a thin insulating layer separates the metal electrode from the semiconductor. By applying an appropriate gate bias, a depletion region is formed at the semiconductor surface, enabling charge collection on the photogate. The performance of MIS photodiodes strongly depends on the insulator thickness, gate capacitance, and background doping, while excessively thin insulators may lead to quantum tunneling effects.

Avalanche photodiodes (APDs) exploit carrier multiplication under high reverse bias. When photogenerated carriers enter a strong electric field region, they gain sufficient energy to initiate impact ionization, resulting in avalanche multiplication. APDs combine high sensitivity, fast response, and high quantum efficiency, making them suitable for detecting weak optical signals.

2.3.3 Figures of merit for photodetectors

A photodetector is a device that converts light signals into electrical signals. In order to evaluate the performance of a photodetector, several parameters can be estimated[75].

2.3.3.1 Responsivity

Photoresponsivity or responsivity is the most employed parameter used to assess the performance of a photodetector[76]. It quantifies the ability to convert light into electrical signals, and it is calculated as:

$$R = I_{ph}/P_{inc} \quad (2.15)$$

I_{ph} is the photocurrent, which is the difference between the current level under illumination and the dark current $I_{ph} = I_{light} - I_{dark}$. P_{inc} is the optical power incident on the device, which relates the power density of the light source, which is the ratio between the power density P and the area of the light spot A_{spot}, with the active area of the device according to the formula:

$$P_{inc} = \left(\frac{P}{A_{spot}}\right) \cdot A_{active} \quad (2.16)$$

Responsivity depends on both the wavelength and intensity of the incident light. It is preferable that responsivity does not depend on the intensity. In photovoltaic devices, photoresponsivity can be calculated as the ratio of the voltage induced by light V_p and the incident optical power:

$$R = V_p/P_{inc} \quad (2.17)$$

The spectral response range is defined as the wavelength interval between the cutoff wavelengths at which the responsivity decreases to half of its maximum value.

2.3.3.2 Quantum efficiency and gain

Quantum efficiency quantifies the sensitivity of a photodetector and describes how effectively incident photons are converted into electrical charge carriers[77]. It is classified into external quantum efficiency (EQE) and internal quantum efficiency (IQE). EQE is defined as the ratio between the number of charge carriers generated in the circuit and the number of photons incident on the device:

$$\mathrm{EQE} = \frac{\mathrm{I_{ph}hv}}{\mathrm{qP}} = \frac{\mathrm{Rhc}}{\mathrm{q\lambda}} \qquad (2.18)$$

where q is the elementary charge, h is the Planck constat, ν and λ are the frequency and wavelength of the incident light, and c is the speed of light. Since not all incident photons are absorbed by the active material due to reflection and transmission losses, the absorbed optical power at any depth z inside the material is expressed as:

$$\mathrm{P_z} = \mathrm{P_{inc}}(1 - \mathrm{R_f})(1 - \mathrm{e}^{-az}) \qquad (2.19)$$

where $\mathrm{R_f}$ is the reflectivity of the material and a is the material absorption coefficient. The fraction of absorbed photons is of the form $\eta = (1 - R_f)(1 - e^{-ad})$, where d is the active material thickness having the highest reflectivity.

The IQE is instead defines as the ratio of the number of electron-hole pairs generated in the device to the number of photons absorbed by it. Consequently, EQE and IQE are related through:

$$\mathrm{EQE} = \eta \cdot \mathrm{IQE} \qquad (2.20)$$

Gain (G) is defined as the ratio of the number of photogenerated charge carriers collected in the circuit to the number of photons absorbed by the device:[78]

$$\mathrm{G} = \left(\frac{\mathrm{I_{ph}}}{P_{ads}}\right)\left(\frac{h\nu}{q}\right) \qquad (2.21)$$

It can also be expressed as the ratio between the carrier life time and the drift transit time:

$$\mathrm{G} = \frac{\tau_e}{t_{tre}} + \frac{\tau_p}{t_{trp}} \qquad (2.22)$$

Where τ_e and τ_p are the lifetimes of photogenerated electrons and holes, respectively, while t_{tre} and t_{trp} are the transit times. In standard photodiodes the lifetime of photogenerated carriers is equal to the transit time and the gain is 1.

2.3.3.3 Noise equivalent power and detectivity

The noise equivalent power (NEP) is the minimum power of light having a signal-to-noise ratio of 1 at the frequency of 1 Hz. It quantifies the ability to detect weak optical signal, and it is expressed as:

$$\mathrm{NEP} = \mathrm{I_N}/\mathrm{R} \qquad (2.23)$$

where I_N denotes the noise current at a frequency bandwidth of 1 Hz. A low NEP is preferred to achieve a good optical performance. However, since, typically, a better performance is indicated by a larger value, another parameter, called detectivity is used to evaluate this property. A photodetector detectivity is the reciprocal of NEP:

$$D = 1/NEP. \quad (2.24)$$

Detectivity depends on the A_{active} of the device. In order to facilitate the comparison between photodetectors with different areas, specific detectivity is used. It is the localized detectivity at a specific unit area, with a frequency bandwidth of 1 Hz, which is represented as

$$D^* = \frac{AB^{\frac{1}{2}}}{NEP} \quad (2.25)$$

where A is the device area and B is the bandwidth. If only shot noise dominates, the specific detectivity can be calculated as:

$$D^* = \frac{R\sqrt{A}}{\sqrt{2qI_d}} \quad (2.26)$$

2.3.3.4 Response times

The response time of a photodetector quantifies the speed at which the device converts an incoming light signal into an electrical output. It is determined by measuring two key parameters: the rise time and the decay time. The rise time is defined as the interval required for the electrical signal to increase from 10 % to 90 % of its peak steady-state value, while the decay time is the period required for the signal to drop from 90 % back to 10 %. The response time depends on the lifetime of the photogenerated carriers and their mobility. In photodiodes, it is determined by the diffusion time of the carriers to exit the depletion region, the drift time within the depletion region and the junction capacitance.

2.3.3.5 Linear Dynamic range

In practical applications, it is preferred for a photodetector to have a linear dependence of the electrical signal on the optical power to avoid distortion and easily correlate the two quantities. However, at high-light powers, the photocurrent saturates. Linear Dynamic Range is the parameter used to evaluate the linear response capability. It is defined as the power range within which the device has a linear response to incident light.

$$r_{LDP} = 20\,Log(\frac{P_{max}}{P_{min}}) \quad (2.27)$$

P_{min} e P_{max} are the minimum and maximum light powers at which the devices exhibit linear response[79].

2.4 Experimental methods

The instruments used for structural and morphological characterization and the details of theoretical modeling are provided in the correspondent chapters. Herein, some specifics on the

instruments used for the electro-optical characterization, common to the following chapters, are reported.

2.4.1 Electrical measurements

Electrical measurements were performed using cryogenic probe stations, specifically a Janis probe station and a TTPX LakeShore probe station (Figure 2.5a). Both setups consist of a radiation shield stage inside a vacuum chamber and are equipped with four probe arms terminated with tungsten tips/nails. These probes can be accurately positioned onto the sample placed on the sample holder through micromanipulators (Figure 2.5).

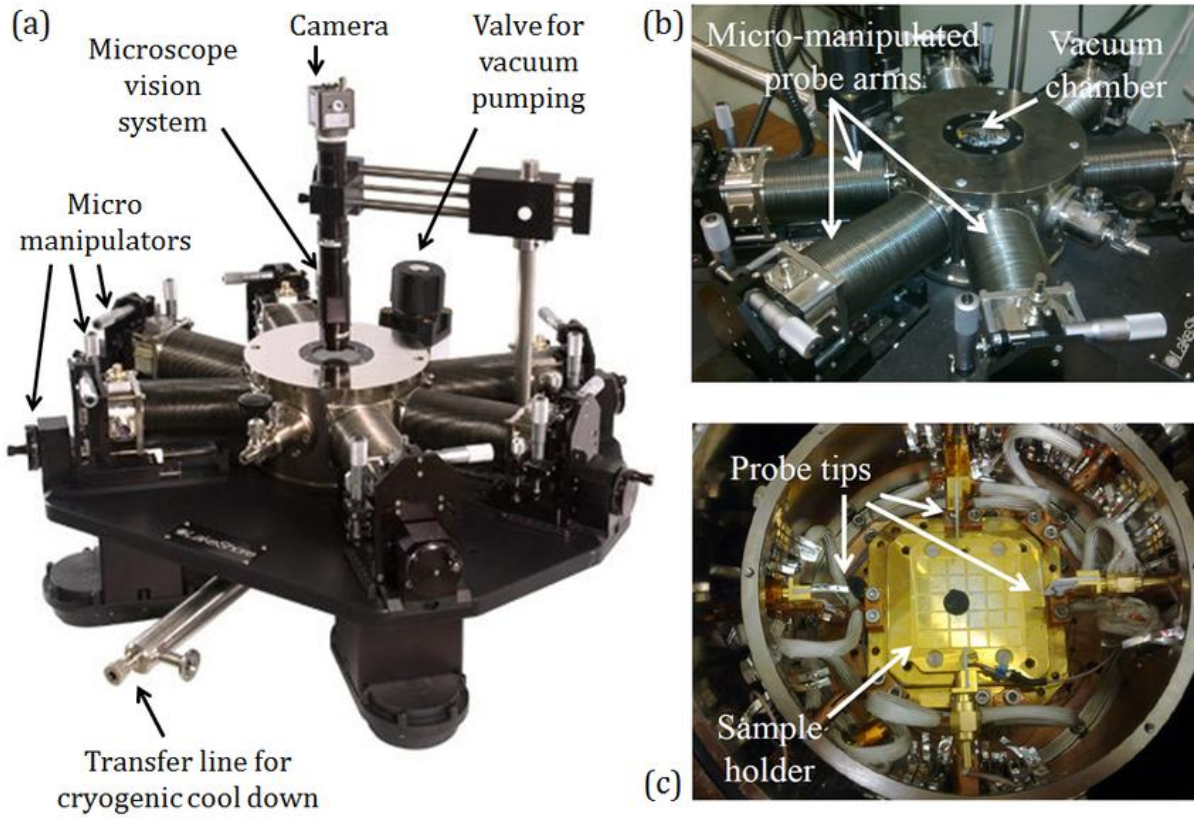

Figure 2.5: (a),(b) General external view of the TTPX Lakeshore probe station. (c) Interior of the probe station test chamber.

The probes are interfaced with a Keithley 4200 Semiconductor Characterization System (SCS), a modular and configurable parameter analyzer designed for comprehensive DC I-V, C-V and pulsed electrical characterization of semiconductor devices. The instrument includes an embedded Windows-based computer and the Keithley Interactive Test Environment (KITE) enabling automated measurements sequences. It features Source-Measure Units (SMUs) supporting current measurements from 1pA to 100 mA and voltage measurements from 200 mV to 200V with high resolution down to 0.1 pA and 1 µV in measurement mode (Figure 2.6a).

Pressure-dependent experiments were conducted using a two-stage pumping system, consisting of an Agilent rotary pump for the initial evacuation down to millibar range, followed by a turbomolecular pump to achieve high-vacuum conditions, reaching pressure as low as 10^{-5} mbar.

For temperature- dependent measurements, the probe stations were equipped with a specialized thermal stage providing precise control over the sample environment. High temperature characterization up to 400 K was enabled in the Janis Probe Station by a resistive heating element regulated through a Scientific Instruments Model 9700 temperature controller. The system operates via a current-controlled heater output (up to 50 W) delivered to a resistive load between 25 and 50 Ω integrated into the sample stage. Temperature feedback is obtained through compatible sensing elements such as thermal resistors or diodes, excited with constant currents between 10 mA and 1 mA. Stable temperature regulation is achieved using a PID (Proportional-Integral-Derivative) closed-loop algorithm, which continuously adjusts the heater power to minimize deviations from the set point. Additionally, a hardware-controlled bar graph on the front panel provides a real-time visual indication of the power being applied to the sample stage. The Lakeshore probe station is coupled with the LakeShore Model 372 temperature controller.

Low temperature operation was achieved through a pressure-driven cryogen transfer system. Liquid nitrogen stored in a high-capacity dewar is delivered to the cold finger inside the measurement chamber by pressurizing the dewar headspace with gaseous nitrogen. This controlled pressure differential drives the liquid through a vacuum-insulated transfer line, enabling continuous cooling of the sample stage down to 77 K. By adjusting the gas pressure and exhaust flow, stable thermal equilibrium can be maintained. The vacuum environment prevents moisture condensation on the device surface, enabling reliable low-temperature measurements. Coupling this system with the temperature controller further allows stabilization at intermediate temperature between 77 and 400 K.

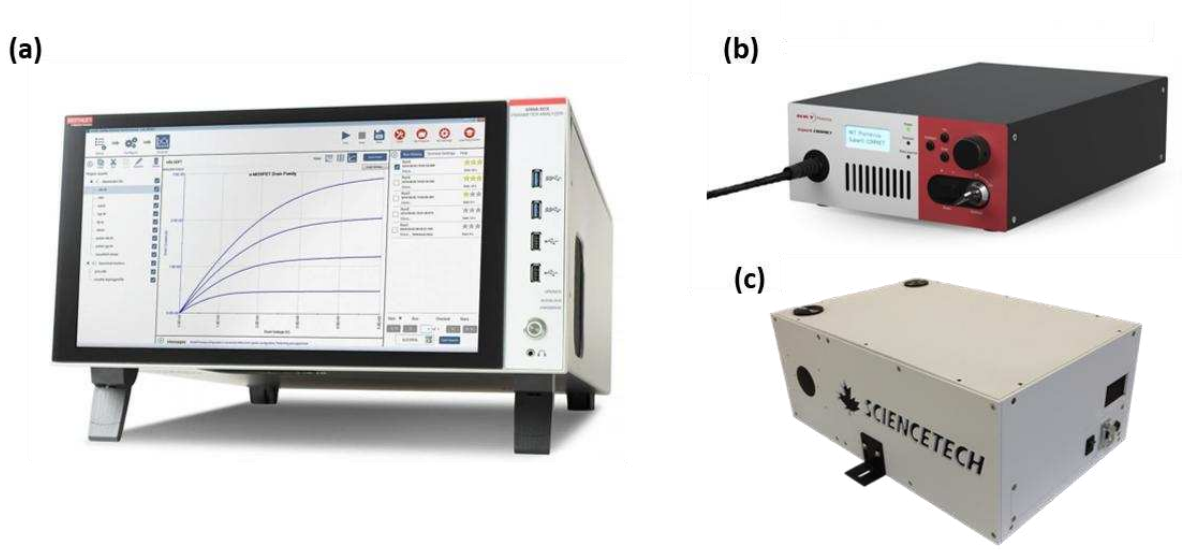

Figure 2.6: (a) Semiconductor characterization system, Keithley 4200. (b) Supercontinuum white light laser, SuperK Compact, NKT Photonics. (c) Monochromator, Sciencetech.

The electrical characterization setup of the Lakeshore probe station was integrated with an optical excitation platform for optoelectronic characterization. Light was delivered into the chamber through a high-stability optical fiber, whose output can be aligned and focused onto the device using manipulators. One of the employed light source was a SuperK Compact (NKT Photonics), a broadband supercontinuum laser providing emission from 450 to 2400 nm (Figure 2.6b). Wavelength selection was achieved by coupling the output into a Sciencetech 0.25 m fast monochromator (Figure 2.6c), equipped with a motorized triple-grating turret for high-resolution tuning from the ultraviolet to the near-infrared.

Optical power and temporal excitation parameters were controlled via dedicated software. Time-resolved switching behavior was investigated using a function generator to modulate the laser on/off cycles, while an oscilloscope was employed to capture fast transient responses. Such measurements are essential for probing recombination dynamics of photogenerated carriers and other complex photo-induced transport mechanisms.

References

(1) Telkhozhayeva, M.; Girshevitz, O. Roadmap toward Controlled Ion Beam-Induced Defects in 2D Materials. *Adv. Funct. Mater.* **2024**, *34* (45), 2404615. https://doi.org/10.1002/adfm.202404615.

(2) Hong, J.; Hu, Z.; Probert, M.; Li, K.; Lv, D.; Yang, X.; Gu, L.; Mao, N.; Feng, Q.; Xie, L.; Zhang, J.; Wu, D.; Zhang, Z.; Jin, C.; Ji, W.; Zhang, X.; Yuan, J.; Zhang, Z. Exploring Atomic Defects in Molybdenum Disulphide Monolayers. *Nat. Commun.* **2015**, *6* (1), 6293. https://doi.org/10.1038/ncomms7293.

(3) Hossen, M. F.; Shendokar, S.; Aravamudhan, S. Defects and Defect Engineering of Two-Dimensional Transition Metal Dichalcogenide (2D TMDC) Materials. *Nanomaterials* **2024**, *14* (5), 410. https://doi.org/10.3390/nano14050410.

(4) Lin, Z.; Carvalho, B. R.; Kahn, E.; Lv, R.; Rao, R.; Terrones, H.; Pimenta, M. A.; Terrones, M. Defect Engineering of Two-Dimensional Transition Metal Dichalcogenides. *2D Mater.* **2016**, *3* (2), 022002. https://doi.org/10.1088/2053-1583/3/2/022002.

(5) Freysoldt, C.; Grabowski, B.; Hickel, T.; Neugebauer, J.; Kresse, G.; Janotti, A.; Van De Walle, C. G. First-Principles Calculations for Point Defects in Solids. *Rev. Mod. Phys.* **2014**, *86* (1), 253–305. https://doi.org/10.1103/RevModPhys.86.253.

(6) Van de Walle, C. G.; Neugebauer, J. First-Principles Calculations for Defects and Impurities: Applications to III-Nitrides. *J. Appl. Phys.* **2004**, *95* (8), 3851–3879. https://doi.org/10.1063/1.1682673.

(7) Komsa, H.-P.; Krasheninnikov, A. V. Native Defects in Bulk and Monolayer ${\mathrm{MoS}}_{2}$ from First Principles. *Phys. Rev. B* **2015**, *91* (12), 125304. https://doi.org/10.1103/PhysRevB.91.125304.

(8) Zhou, W.; Zou, X.; Najmaei, S.; Liu, Z.; Shi, Y.; Kong, J.; Lou, J.; Ajayan, P. M.; Yakobson, B. I.; Idrobo, J.-C. Intrinsic Structural Defects in Monolayer Molybdenum Disulfide. *Nano Lett.* **2013**, *13* (6), 2615–2622. https://doi.org/10.1021/nl4007479.

(9) Noh, J.-Y.; Kim, H.; Kim, Y.-S. Stability and Electronic Structures of Native Defects in Single-Layer ${\mathrm{MoS}}_{2}$. *Phys. Rev. B* **2014**, *89* (20), 205417. https://doi.org/10.1103/PhysRevB.89.205417.

(10) Liu, D.; Guo, Y.; Fang, L.; Robertson, J. Sulfur Vacancies in Monolayer MoS2 and Its Electrical Contacts. *Appl. Phys. Lett.* **2013**, *103* (18), 183113. https://doi.org/10.1063/1.4824893.

(11) Singh, A.; Singh, A. K. Origin of n-Type Conductivity of Monolayer ${\mathrm{MoS}}_{2}$. *Phys. Rev. B* **2019**, *99* (12), 121201. https://doi.org/10.1103/PhysRevB.99.121201.

(12) Nan, H.; Wang, Z.; Wang, W.; Liang, Z.; Lu, Y.; Chen, Q.; He, D.; Tan, P.; Miao, F.; Wang, X.; Wang, J.; Ni, Z. Strong Photoluminescence Enhancement of MoS2 through Defect Engineering and Oxygen Bonding. *ACS Nano* **2014**, *8* (6), 5738–5745. https://doi.org/10.1021/nn500532f.

(13) Latiff, N. M.; Wang, L.; Mayorga-Martinez, C. C.; Sofer, Z.; Fisher, A. C.; Pumera, M. Valence and Oxide Impurities in MoS2 and WS2 Dramatically Change Their Electrocatalytic Activity towards Proton Reduction. *Nanoscale* **2016**, *8* (37), 16752–16760. https://doi.org/10.1039/C6NR03086F.

(14) Zhou, J.; Lin, J.; Sims, H.; Jiang, C.; Cong, C.; Brehm, J. A.; Zhang, Z.; Niu, L.; Chen, Y.; Zhou, Y.; Wang, Y.; Liu, F.; Zhu, C.; Yu, T.; Suenaga, K.; Mishra, R.; Pantelides, S. T.; Zhu, Z.-G.; Gao, W.; Liu, Z.; Zhou, W. Synthesis of Co-Doped MoS2 Monolayers with Enhanced Valley Splitting. *Adv. Mater.* **2020**, *32* (11), 1906536. https://doi.org/10.1002/adma.201906536.

(15) Zhou, W.; Zou, X.; Najmaei, S.; Liu, Z.; Shi, Y.; Kong, J.; Lou, J.; Ajayan, P. M.; Yakobson, B. I.; Idrobo, J.-C. Intrinsic Structural Defects in Monolayer Molybdenum Disulfide. *Nano Lett.* **2013**, *13* (6), 2615–2622. https://doi.org/10.1021/nl4007479.

(16) Zou, X.; Liu, Y.; Yakobson, B. I. Predicting Dislocations and Grain Boundaries in Two-Dimensional Metal-Disulfides from the First Principles. *Nano Lett.* **2013**, *13* (1), 253–258. https://doi.org/10.1021/nl3040042.

(17) Komsa, H.-P.; Kurasch, S.; Lehtinen, O.; Kaiser, U.; Krasheninnikov, A. V. From Point to Extended Defects in Two-Dimensional MoS${}_{2}$: Evolution of Atomic Structure under Electron Irradiation. *Phys. Rev. B* **2013**, *88* (3), 035301. https://doi.org/10.1103/PhysRevB.88.035301.

(18) Han, Y.; Hu, T.; Li, R.; Zhou, J.; Dong, J. Stabilities and Electronic Properties of Monolayer MoS2 with One or Two Sulfur Line Vacancy Defects. *Phys. Chem. Chem. Phys.* **2015**, *17* (5), 3813–3819. https://doi.org/10.1039/C4CP04319G.

(19) Najmaei, S.; Liu, Z.; Zhou, W.; Zou, X.; Shi, G.; Lei, S.; Yakobson, B. I.; Idrobo, J.-C.; Ajayan, P. M.; Lou, J. Vapour Phase Growth and Grain Boundary Structure of Molybdenum Disulphide Atomic Layers. *Nat. Mater.* **2013**, *12* (8), 754–759. https://doi.org/10.1038/nmat3673.

(20) Zou, X.; Liu, Y.; Yakobson, B. I. Predicting Dislocations and Grain Boundaries in Two-Dimensional Metal-Disulfides from the First Principles. *Nano Lett.* **2013**, *13* (1), 253–258. https://doi.org/10.1021/nl3040042.

(21) Gao, N.; Guo, Y.; Zhou, S.; Bai, Y.; Zhao, J. Structures and Magnetic Properties of MoS2 Grain Boundaries with Antisite Defects. *J. Phys. Chem. C* **2017**, *121* (22), 12261–12269. https://doi.org/10.1021/acs.jpcc.7b03106.

(22) van der Zande, A. M.; Huang, P. Y.; Chenet, D. A.; Berkelbach, T. C.; You, Y.; Lee, G.-H.; Heinz, T. F.; Reichman, D. R.; Muller, D. A.; Hone, J. C. Grains and Grain Boundaries in Highly Crystalline Monolayer Molybdenum Disulphide. *Nat. Mater.* **2013**, *12* (6), 554–561. https://doi.org/10.1038/nmat3633.

(23) Alanwoko, O.; Kruklinskii, D.; Ghorbani-Asl, M.; Krasheninnikov, A. V.; Batzill, M. When Defects Become the Crystal: Periodic Mirror-Twin Boundary Phases in Substoichiometric 2D-MoTe2. *Nano Lett.* **2025**. https://doi.org/10.1021/acs.nanolett.5c05258.

(24) Lehnert, T.; Ghorbani-Asl, M.; Köster, J.; Lee, Z.; Krasheninnikov, A. V.; Kaiser, U. Electron-Beam-Driven Structure Evolution of Single-Layer $MoTe_2$ for Quantum Devices. *ACS Appl. Nano Mater.* **2019**, *2* (5), 3262–3270. https://doi.org/10.1021/acsanm.9b00616.

(25) Kittel, C. *Introduction to Solid State Physics*, 8. ed., [repr.].; Wiley: Hoboken, NJ, 20.

(26) Banhart, F.; Kotakoski, J.; Krasheninnikov, A. V. Structural Defects in Graphene. *ACS Nano* **2011**, *5* (1), 26–41. https://doi.org/10.1021/nn102598m.

(27) Noh, J.-Y.; Kim, H.; Kim, Y.-S. Stability and Electronic Structures of Native Defects in Single-Layer ${\mathrm{MoS}}_{2}$. *Phys. Rev. B* **2014**, *89* (20), 205417. https://doi.org/10.1103/PhysRevB.89.205417.

(28) Liu, Y.; Stradins, P.; Wei, S.-H. Air Passivation of Chalcogen Vacancies in Two-Dimensional Semiconductors. *Angew. Chem. Int. Ed.* **2016**, *55* (3), 965–968. https://doi.org/10.1002/anie.201508828.

(29) Li, Y.; Yan, J.; Chen, J.; Yu, T.; Ren, H.; Liu, X.; Liu, W.; Yang, G.; Xu, C.; Bao, Q.; Liu, Y.; Xu, H. Unraveling the Synergetic Mechanism of Physisorption and Chemisorption in Laser-Irradiated Monolayer WS2. *Nano Res.* **2021**, *14* (11), 4274–4280. https://doi.org/10.1007/s12274-021-3667-6.

(30) Wang, Y.; He, Z.; Zhang, J.; Liu, H.; Lai, X.; Liu, B.; Chen, Y.; Wang, F.; Zhang, L. UV Illumination Enhanced Desorption of Oxygen Molecules from Monolayer MoS2 Surface. *Nano Res.* **2020**, *13* (2), 358–365. https://doi.org/10.1007/s12274-020-2614-2.

(31) Shearer, C. J.; Slattery, A. D.; Stapleton, A. J.; Shapter, J. G.; Gibson, C. T. Accurate Thickness Measurement of Graphene. *Nanotechnology* **2016**, *27* (12), 125704. https://doi.org/10.1088/0957-4484/27/12/125704.

(32) Zhang, H.; Huang, J.; Wang, Y.; Liu, R.; Huai, X.; Jiang, J.; Anfuso, C. Atomic Force Microscopy for Two-Dimensional Materials: A Tutorial Review. *Opt. Commun.* **2018**, *406*, 3–17. https://doi.org/10.1016/j.optcom.2017.05.015.

(33) Brotons-Alcázar, I.; Terreblanche, Jason. S.; Giménez-Santamarina, S.; Gutiérrez-Finol, G. M.; Ryder, K. S.; Forment-Aliaga, A.; Coronado, E. Atomic Force Microscopy beyond Topography: Chemical Sensing of 2D Material Surfaces through Adhesion Measurements. *ACS Appl. Mater. Interfaces* **2024**, *16* (15), 19711–19719. https://doi.org/10.1021/acsami.3c19254.

(34) Longo, A.; Palomba, M.; Giubileo, F.; Carotenuto, G. Contrast Enhancement in 2D Nanomaterial SEM Images. *Eng. Proc.* **2025**, *87* (1), 81. https://doi.org/10.3390/engproc2025087081.

(35) Graaf, S. de; Ahmadi, M.; Lazić, I.; Bosch, E. G. T.; Kooi, B. J. Imaging Atomic Motion of Light Elements in 2D Materials with 30 kV Electron Microscopy. *Nanoscale* **2021**, *13* (48), 20683–20691. https://doi.org/10.1039/D1NR06614E.

(36) Nellist, P. D. The Principles of STEM Imaging. In *Scanning Transmission Electron Microscopy: Imaging and Analysis*; Pennycook, S. J., Nellist, P. D., Eds.; Springer: New York, NY, 2011; pp 91–115. https://doi.org/10.1007/978-1-4419-7200-2_2.

(37) Wu, J.-B.; Lin, M.-L.; Cong, X.; Liu, H.-N.; Tan, P.-H. Raman Spectroscopy of Graphene-Based Materials and Its Applications in Related Devices. *Chem. Soc. Rev.* **2018**, *47* (5), 1822–1873. https://doi.org/10.1039/C6CS00915H.

(38) Cong, X.; Liu, X.-L.; Lin, M.-L.; Tan, P.-H. Application of Raman Spectroscopy to Probe Fundamental Properties of Two-Dimensional Materials. *Npj 2D Mater. Appl.* **2020**, *4* (1), 13. https://doi.org/10.1038/s41699-020-0140-4.

(39) Raman Spectroscopy of Two-Dimensional Materials. **2019**, *276*. https://doi.org/10.1007/978-981-13-1828-3.

(40) Tan, P. H.; Han, W. P.; Zhao, W. J.; Wu, Z. H.; Chang, K.; Wang, H.; Wang, Y. F.; Bonini, N.; Marzari, N.; Pugno, N.; Savini, G.; Lombardo, A.; Ferrari, A. C. The Shear Mode of Multilayer Graphene. *Nat. Mater.* **2012**, *11* (4), 294–300. https://doi.org/10.1038/nmat3245.

(41) Lee, J.-U.; Woo, S.; Park, J.; Park, H. C.; Son, Y.-W.; Cheong, H. Strain-Shear Coupling in Bilayer MoS2. *Nat. Commun.* **2017**, *8* (1), 1370. https://doi.org/10.1038/s41467-017-01487-3.

(42) Lin, T.; Cong, X.; Lin, M.-L.; Liu, X.-L.; Tan, P.-H. The Phonon Confinement Effect in Two-Dimensional Nanocrystals of Black Phosphorus with Anisotropic Phonon Dispersions. *Nanoscale* **2018**, *10* (18), 8704–8711. https://doi.org/10.1039/C8NR01531G.

(43) Liang, L.; Zhang, J.; Sumpter, B. G.; Tan, Q.-H.; Tan, P.-H.; Meunier, V. Low-Frequency Shear and Layer-Breathing Modes in Raman Scattering of Two-Dimensional Materials. *ACS Nano* **2017**, *11* (12), 11777–11802. https://doi.org/10.1021/acsnano.7b06551.

(44) *Valence-level Photoelectron Spectroscopy of MoS2 | Kratos Analytical*. https://www.kratos.com/application-note/valence-level-photoelectron-spectroscopy-of-mos2/ (accessed 2026-01-25).

(45) Su, S.; Zhao, J.; Ly, T. H. Scanning Probe Microscopies for Characterizations of 2D Materials. *Small Methods* **2024**, *8* (11), 2400211. https://doi.org/10.1002/smtd.202400211.

(46) Morgenstern, M. Scanning Tunneling Microscopy and Spectroscopy of Graphene on Insulating Substrates. *Phys. Status Solidi B* **2011**, *248* (11), 2423–2434. https://doi.org/10.1002/pssb.201147312.

(47) Atomistic Modeling by Density Functional Theory of Two-Dimensional Materials. In *Synthesis, Modeling, and Characterization of 2D Materials, and Their Heterostructures*; Elsevier, 2020; pp 113–123. https://doi.org/10.1016/B978-0-12-818475-2.00006-4.

(48) Mitta, S. B.; Choi, M. S.; Nipane, A.; Ali, F.; Kim, C.; Teherani, J. T.; Hone, J.; Yoo, W. J. Electrical Characterization of 2D Materials-Based Field-Effect Transistors. *2D Mater.* **2020**, *8* (1), 012002. https://doi.org/10.1088/2053-1583/abc187.

(49) Kim, S.; Konar, A.; Hwang, W.-S.; Lee, J. H.; Lee, J.; Yang, J.; Jung, C.; Kim, H.; Yoo, J.-B.; Choi, J.-Y.; Jin, Y. W.; Lee, S. Y.; Jena, D.; Choi, W.; Kim, K. High-Mobility and Low-Power Thin-Film Transistors Based on Multilayer MoS2 Crystals. *Nat. Commun.* **2012**, *3* (1), 1011. https://doi.org/10.1038/ncomms2018.

(50) Fang, H.; Chuang, S.; Chang, T. C.; Takei, K.; Takahashi, T.; Javey, A. High-Performance Single Layered WSe_2 p-FETs with Chemically Doped Contacts. *Nano Lett.* **2012**, *12* (7), 3788–3792. https://doi.org/10.1021/nl301702r.

(51) Ortiz-Conde, A.; García Sánchez, F. J.; Liou, J. J.; Cerdeira, A.; Estrada, M.; Yue, Y. A Review of Recent MOSFET Threshold Voltage Extraction Methods. *Microelectron. Reliab.* **2002**, *42* (4), 583–596. https://doi.org/10.1016/S0026-2714(02)00027-6.

(52) Prakash, A.; Appenzeller, J. Bandgap Extraction and Device Analysis of Ionic Liquid Gated WSe2 Schottky Barrier Transistors. *ACS Nano* **2017**, *11* (2), 1626–1632. https://doi.org/10.1021/acsnano.6b07360.

(53) Di Bartolomeo, A.; Genovese, L.; Giubileo, F.; Iemmo, L.; Luongo, G.; Foller, T.; Schleberger, M. Hysteresis in the Transfer Characteristics of MoS2 Transistors. *2D Mater.* **2017**, *5* (1), 015014. https://doi.org/10.1088/2053-1583/aa91a7.

(54) Vu, Q. A.; Fan, S.; Lee, S. H.; Joo, M.-K.; Yu, W. J.; Lee, Y. H. Near-Zero Hysteresis and near-Ideal Subthreshold Swing in h-BN Encapsulated Single-Layer MoS2 Field-Effect Transistors. *2D Mater.* **2018**, *5* (3), 031001. https://doi.org/10.1088/2053-1583/aab672.

(55) Mukherjee, R.; Chuang, H. J.; Koehler, M. R.; Combs, N.; Patchen, A.; Zhou, Z. X.; Mandrus, D. Substitutional Electron and Hole Doping of ${\mathrm{WSe}}_{2}$: Synthesis, Electrical Characterization, and Observation of Band-to-Band Tunneling. *Phys. Rev. Appl.* **2017**, *7* (3), 034011. https://doi.org/10.1103/PhysRevApplied.7.034011.

(56) Qin, Z.; Loh, L.; Wang, J.; Xu, X.; Zhang, Q.; Haas, B.; Alvarez, C.; Okuno, H.; Yong, J. Z.; Schultz, T.; Koch, N.; Dan, J.; Pennycook, S. J.; Zeng, D.; Bosman, M.; Eda, G. Growth of Nb-Doped Monolayer WS2 by Liquid-Phase Precursor Mixing. *ACS Nano* **2019**, *13* (9), 10768–10775. https://doi.org/10.1021/acsnano.9b05574.

(57) Jung, Y.; Choi, M. S.; Nipane, A.; Borah, A.; Kim, B.; Zangiabadi, A.; Taniguchi, T.; Watanabe, K.; Yoo, W. J.; Hone, J.; Teherani, J. T. Transferred via Contacts as a Platform for Ideal Two-Dimensional Transistors. *Nat. Electron.* **2019**, *2* (5), 187–194. https://doi.org/10.1038/s41928-019-0245-y.

(58) Liu, Y.; Guo, J.; Zhu, E.; Liao, L.; Lee, S.-J.; Ding, M.; Shakir, I.; Gambin, V.; Huang, Y.; Duan, X. Approaching the Schottky–Mott Limit in van Der Waals Metal–Semiconductor Junctions. *Nature* **2018**, *557* (7707), 696–700. https://doi.org/10.1038/s41586-018-0129-8.

(59) Yuan, H.; Cheng, G.; You, L.; Li, H.; Zhu, H.; Li, W.; Kopanski, J. J.; Obeng, Y. S.; Hight Walker, A. R.; Gundlach, D. J.; Richter, C. A.; Ioannou, D. E.; Li, Q. Influence of Metal–MoS2 Interface on MoS2 Transistor Performance: Comparison of Ag and Ti Contacts. *ACS Appl. Mater. Interfaces* **2015**, *7* (2), 1180–1187. https://doi.org/10.1021/am506921y.

(60) Anwar, A.; Nabet, B.; Culp, J.; Castro, F. Effects of Electron Confinement on Thermionic Emission Current in a Modulation Doped Heterostructure. *J. Appl. Phys.* **1999**, *85* (5), 2663–2666. https://doi.org/10.1063/1.369627.

(61) Allain, A.; Kang, J.; Banerjee, K.; Kis, A. Electrical Contacts to Two-Dimensional Semiconductors. *Nat. Mater.* **2015**, *14* (12), 1195–1205. https://doi.org/10.1038/nmat4452.

(62) Di Bartolomeo, A. Graphene Schottky Diodes: An Experimental Review of the Rectifying Graphene/Semiconductor Heterojunction. *Phys. Rep.* **2016**, *606*, 1–58. https://doi.org/10.1016/j.physrep.2015.10.003.

(63) Zhou, Z.; Kang, M.; Fang, Y.; Martyniuk, P.; Wang, H. Avalanche Multiplication in Two-Dimensional Layered Materials: Principles and Applications. *Nanomaterials* **2025**, *15* (9), 636. https://doi.org/10.3390/nano15090636.

(64) Buscema, M.; Island, J. O.; Groenendijk, D. J.; Blanter, S. I.; Steele, G. A.; Zant, H. S. J. van der; Castellanos-Gomez, A. Photocurrent Generation with Two-Dimensional van Der Waals Semiconductors. *Chem. Soc. Rev.* **2015**, *44* (11), 3691–3718. https://doi.org/10.1039/C5CS00106D.

(65) Fronzi, M.; Mele, P.; V. Ellis, A.; Stampfl, C. Advances in van Der Waals Thermoelectric Materials: Prospects and Challenges. *RSC Appl. Interfaces* **2025**, *2* (4), 852–872. https://doi.org/10.1039/D4LF00383G.

(66) Long, M.; Wang, P.; Fang, H.; Hu, W. Progress, Challenges, and Opportunities for 2D Material Based Photodetectors. *Adv. Funct. Mater.* **2019**, *29* (19), 1803807. https://doi.org/10.1002/adfm.201803807.

(67) Liu, C.; Guo, J.; Yu, L.; Li, J.; Zhang, M.; Li, H.; Shi, Y.; Dai, D. Silicon/2D-Material Photodetectors: From near-Infrared to Mid-Infrared. *Light Sci. Appl.* **2021**, *10*. https://doi.org/10.1038/s41377-021-00551-4.

(68) Koppens, F. H. L.; Mueller, T.; Avouris, P.; Ferrari, A. C.; Vitiello, M. S.; Polini, M. Photodetectors Based on Graphene, Other Two-Dimensional Materials and Hybrid Systems. *Nat. Nanotechnol.* **2014**, *9* (10), 780–793. https://doi.org/10.1038/nnano.2014.215.

(69) Buscema, M.; Island, J. O.; Groenendijk, D. J.; Blanter, S. I.; Steele, G. A.; Zant, H. S. J. van der; Castellanos-Gomez, A. Photocurrent Generation with Two-Dimensional van Der Waals Semiconductors. *Chem. Soc. Rev.* **2015**, *44* (11), 3691–3718. https://doi.org/10.1039/C5CS00106D.

(70) Kasirga, T. S. Thermal Conductivity Measurements via the Bolometric Effect. In *Thermal Conductivity Measurements in Atomically Thin Materials and Devices*; Kasirga, T. S., Ed.; Springer: Singapore, 2020; pp 29–50. https://doi.org/10.1007/978-981-15-5348-6_3.

(71) Scales, C.; Berini, P. Thin-Film Schottky Barrier Photodetector Models. *IEEE J. Quantum Electron.* **2010**, *46* (5), 633–643. https://doi.org/10.1109/JQE.2010.2046720.

(72) Tunnel Devices. In *Physics of Semiconductor Devices*; John Wiley & Sons, Ltd, 2006; pp 415–465. https://doi.org/10.1002/9780470068328.ch8.

(73) Ma, Q.; Andersen, T. I.; Nair, N. L.; Gabor, N. M.; Massicotte, M.; Lui, C. H.; Young, A. F.; Fang, W.; Watanabe, K.; Taniguchi, T.; Kong, J.; Gedik, N.; Koppens, F. H. L.; Jarillo-Herrero, P. Tuning Ultrafast Electron Thermalization Pathways in a van Der Waals Heterostructure. *Nat. Phys.* **2016**, *12* (5), 455–459. https://doi.org/10.1038/nphys3620.

(74) Bielecki, Z.; Achtenberg, K.; Kopytko, M.; Mikolajczyk, J.; Wojtas, J.; Rogalski, A. Review of Photodetectors Characterization Methods. *Bull. Pol. Acad. Sci. Tech. Sci.* **2022**, *70*. https://doi.org/10.24425/bpasts.2022.140534.

(75) Wei, Y.; Lan, C.; Zhou, S.; Li, C. Recent Advances in Photodetectors Based on Two-Dimensional Material/Si Heterojunctions. *Appl. Sci.* **2023**, *13* (19), 11037. https://doi.org/10.3390/app131911037.

(76) Cai, X.; Wang, S.; Peng, L.-M. Recent Progress of Photodetector Based on Carbon Nanotube Film and Application in Optoelectronic Integration. *Nano Res. Energy* **2023**, *2* (2), e9120058. https://doi.org/10.26599/NRE.2023.9120058.

(77) Saleh, B. E. A. *Fundamentals of Photonics I: Optics/ Bahaa E.A. Saleh, Malvin Carl Teich*, Third edition.; Wiley series in pure and applied optics; Wiley: Hoboken, NJ, 2019.

(78) Yang, M.; Chang, H.; Chen, J.; Zhu, X. Multiplier Effects of Photodetectors—Source of Gain. *Coatings* **2023**, *13* (6), 1088. https://doi.org/10.3390/coatings13061088.

(79) Bao, C.; Chen, Z.; Fang, Y.; Wei, H.; Deng, Y.; Xiao, X.; Li, L.; Huang, J. Low-Noise and Large-Linear-Dynamic-Range Photodetectors Based on Hybrid-Perovskite Thin-Single-Crystals. *Adv. Mater.* **2017**, *29* (39), 1703209. https://doi.org/10.1002/adma.201703209.

Chapter 3

Surface effects in TMD-based devices: $ZrSe_2$ as a case study

Oxidation study and encapsulation strategies of $ZrSe_2$ -based devices

3.1 Introduction

A fundamental challenge for 2D semiconductor technologies lies in achieving stable, well-controlled and high-quality interfaces with the surrounding environment and other device components like dielectric layers and metal contacts. Owing to their atomically thin nature and high surface-to-volume ratio, 2D materials are intrinsically sensitive to surface chemistry, making environmental interactions a decisive factor in determining their structural integrity, electronic properties, and long-term device reliability.

This issue is particularly critical for air-sensitive transition metal dichalcogenides belonging to the IV-B group, such as $ZrSe_2$, which combine attractive transport properties with the potential advantage of forming a technologically relevant high-k native oxide, suitable as a gate dielectric. However, exploiting this feature requires a detailed understanding of the oxidation mechanisms and their impact on morphology and electronic structure.

In this chapter, the surface reactivity and oxidation-driven evolution of exfoliated $ZrSe_2$ is investigated through a correlative approach combining microscopy, spectroscopy, and density functional theory. Oxidation initiates at defects and flake edges, promoting selenium segregation and the progressive formation of Se-rich protrusions and nanowire-like structures. Finally, an encapsulation strategy with an ultrathin ZrO_2 overlayer is proved to effectively mitigate these degradation pathways, highlighting the importance of surface passivation for the integration of air-sensitive 2D semiconductors.

3.2 IV Group TMDs

Among IV-B group TMDs, 2D materials like Zr- and Hf- selenides and sulphides have gained increasing interest as potential silicon alternatives, since they combine large work function and high mobility with the additional advantage of having a high-k dielectric as native oxide[1]. This

aspect makes them particularly appealing compared to group VI TMDs as it may minimize interfacial incompatibility with the deposited dielectrics, given that both the semiconductor and its oxide share the same transition metal. Defective interfaces between the 2D semiconductor and the oxide can, indeed, limit device switching properties, reduce ON-state current and induce trap-mediated photogeneration mechanisms. In this context, ZrX_2/ZrO_2 and HfX_2/HfO_2 (where X is a chalcogen) represent promising semiconductor/insulator combinations, analogous to Si/SiO_2, with the further advantage that ZrX_2-HfX_2 are layered materials that can be reduced to ultrathin 2D layers[2]. The preparation of clean interfaces with the dielectric is still considered one of the key bottlenecks to overcome before 2D semiconductors can be fully applied in electronic devices[3].

However, to obtain a reliable and smooth 2D semiconductor/oxide interface, it is necessary to first comprehend in detail how the oxidation process manifests itself, on what time scale, how it impacts the material's morphology and whether it causes structural changes. Many 2D semiconductors, such as silicene[4], BP[5], and also some group VI-TMDs[6], exhibit a severe reaction to ambient air[7]. This reduces the device's performance because oxygen and water adsorption can significantly alter its physical, chemical and electronic properties[8,9], or even result in complete degradation. Understanding the fundamental aspects of the oxidation process would help in intentionally preventing 2D semiconductors from oxidation and in identifying appropriate methodologies to preserve them in specific conditions[10].

For IV-B group TMDs, as the radius grows from Ti to Hf, the mobility of MX_2 composites increases, but the air stability dramatically drops[7]. Their kinetic energy barrier for oxidation is, indeed, very low. Even a short exposure to ambient air causes these materials to oxidize quickly, leading to the formation of the respective transition metal oxides (TMOs) on their surface[8]. Theoretical calculations reveal that the oxidation preferably takes place at the flake edges with 50% terminated in sulphur or is initiated by a sulphur vacancy[8]. This is confirmed by experimental works showing that the oxidation region grows around 80 nm into the flake of TiS_2 from the edges after 21 days in H_2O[11]. Other studies confirm that moisture, more than oxygen, is the main obstacle to long-term stability in these materials[12].

Hf-based composites also exhibit significant degradation when exposed to air. The surface of HfS_2 flakes displays small protrusions after oxidation while their thickness increases because of oxygen intercalation, according to optical images and AFM measurements[13]. Both humidity and oxygen molecules contribute to the occurrence of these features. In the case of $HfSe_2$, Hf is oxidising into HfO_2, breaking the bonds with Se atoms that coalesce into blisters on the surface. The process is more dramatic and faster in $HfSe_2$ compared to HfS_2. Signs of degradation are visible on $HfSe_2$ flakes after 1 day, while 9 days are needed for HfS_2[8].

The air stability of ZrX_2 is also notably poor. Raman measurements have been shown to be unreliable to identify monolayer/bilayer ZrS_2 and the Raman peak of thin flakes disappears after a couple of days[14,15]. As in the case of HfX_2, the oxidation effects on the selenide counterpart were observed to be even more significant. $ZrSe_2$ is particularly promising as it is a semiconductor with a bandgap of approximately 1 eV in its bulk form - similar to silicon - which increases to around 1.5 eV when reduced to a monolayer. A 1 eV bandgap is well-suited for low-voltage operation and helps to reduce direct tunnelling and leakage current[16]. Another notable feature of $ZrSe_2$ is its demonstrated negative differential resistance in nanoribbon form,

which makes it a promising candidate for spintronic devices[17]. Its native oxide, ZrO_2, has a wide bandgap of 5.3 eV and belongs to the class of high-k dielectrics, which have increasingly replaced SiO_2 in modern electronics due to their higher dielectric constant. However, despite extensive efforts using various deposition and growth methods , including thermal and plasma oxidation, a reliable approach for obtaining a smooth, homogeneous TMO layer has yet to be established[18].

In the following, a comprehensive, time-resolved study of the ambient degradation of $ZrSe_2$, with particular emphasis on the morphological and structural evolution induced by oxidation, is presented. A ZrO_2-based encapsulation strategy is proposed to mitigate these effects and enable the fabrication of field effect transistors.

3.3 Materials and methods

3.3.1 Morphological and structural characterization

All the $ZrSe_2$ flakes were mechanically exfoliated from their bulk crystal using the Scotch tape technique. The flakes on the scotch tape were then gently pressed on intrinsic silicon substrates or Si/SiO_2 (85 nm) substrates. AFM measurements were performed with Bruker AFM (Dimension Icon Model) in tapping mode using an FMV-A 7 nm tip to avoid any contact between the AFM tip and the surface. For each sample, a 20x20 μm^2 scan was performed with 512 scan lines and a frequency of 0.4 Hz, trying to repeatedly scan the same location. The acquired data was analysed using Gwyddion Software. A Tescan Amber X FIB-SEM with Oxford Ultim Max Energy Dispersive X-ray Spectroscopy (EDX) was used for surface and elemental characterization. The energy of the beam was set to 5 keV and the BC was 1 nA to properly detect all the features of the surface. Raman spectra were acquired with a Horiba XploRA™ Plus confocal Raman microscope equipped with a 70 mW, 532 nm laser. All the Raman spectra, if not otherwise specified, were acquired with a power of 0.5%, with an acquisition time of 10 s and an accumulation time of 10 s, using a 50x objective.

The cross-sectional lamellas were prepared using a Tescan Solaris Ga+ DualBeam focused ion beam (FIB) system for high-resolution structural analysis. Prior to ion milling, protective layers were sequentially deposited over the region of interest to minimize beam-induced damage. The lamellas were then extracted and mounted onto a copper grid. Thinning to electron transparency was performed at an accelerating voltage of 30 kV, while final polishing was carried out at 5 kV using an in-situ ion beam to minimize surface damage and amorphization. Subsequent cross-sectional imaging was conducted directly on the Tescan Solaris system using dark-field scanning transmission electron microscopy (DF-STEM) at 30 kV, employing a 100 pA beam current in immersion mode, enabling measurement of structural features. All imaging and data acquisition were performed using the Essence™ software.

STEM imaging and correlated EDX was performed on a Tescan Tensor rapid precession 4DSTEM microscope at an accelerating voltage of 100 kV, a probe current of 50 pA and a convergence angle of 9.78 mrad. The probe size during EDX measurement was 1.5 nm. Cross-sections were aligned to the Si substrate axis using a double tilt holder. EDX frame acquisition

time was 56 microseconds. Between the different measurements, all flakes under investigation have been stored in the cleanroom environment.

XPS was performed using a monochromatic Al Kα source (E_k=1486.7 eV) and an Omicron EA125 hemispherical analyzer that was calibrated using three different metals Au (83.9 eV), Cu (932.6 eV), and Ag (368.2 eV). XPS spectra were acquired using a pass energy of 15 eV and an energy resolution of 0.05 eV. $ZrSe_2$ crystals were then loaded into an ultra-high vacuum XPS chamber, with a base pressure of ~2.0×10^{-10} mbar. XPS analysis was conducted on a freshly exfoliated sample, an aged (oxidized) sample, and on a sample after 24 hours of air exposure. The sample was exfoliated twice using Scotch tape in a fume hood. It was then transferred to the load-lock chamber of the XPS instrument, where a final exfoliation was performed under N_2 atmosphere. The analysis of XPS data was conducted using the analytical software Analyzer[19].

STM measurements were conducted on a bulk $ZrSe_2$ crystal exfoliated in the load-lock chamber of an ultrahigh-vacuum (UHV) system at a pressure of 5×10^{-7} mbar. The exfoliated sample was immediately transferred to the measurement chamber, maintained at a base pressure of 5×10^{-10} mbar. STM imaging was performed at room temperature in constant-current mode using an Omicron system equipped with an electrochemically etched tungsten tip. To assess the effects of air exposure, additional measurements were carried out on aged samples following exposure to ambient conditions for varying durations

3.3.2 Density Functional Theory calculations

DFT calculations were performed using the Generalized Gradient Approximation (GGA) for the exchange-correlation potential, as implemented in the QuantumATK simulation package[20]. A medium-basis set Linear Combination of Atomic Orbitals (LCAO) approach was employed, utilizing GGA norm-conserving pseudopotentials from the PseudoDojo library[21]. For Brillouin zone integration, a k-point grid was generated using the Monkhorst-Pack scheme[22], achieving a density of approximately 10 k-points per $Å^{-1}$. An energy cutoff of 105 Hartree was applied to the discretized real-space grid. Van der Waals interactions were included using the Grimme DFT-D3 dispersion correction method[23]. All atomic positions were fully relaxed during structural optimization until the residual forces on each atom were reduced below 1×10^{-2} eV/Å, ensuring well-converged geometries. A vacuum layer exceeding 2 nm was introduced in the in-plane direction to prevent interactions between periodic images of the nanoribbons, effectively simulating bulk-like behaviour.

3.3.3 Device fabrication and characterization

$ZrSe_2$ flakes were mechanically exfoliated onto Si/SiO_2 substrates (85 nm oxide thickness) within an inert atmosphere glovebox. The samples were subsequently transferred to an electron beam evaporator for encapsulation with a nominal 2 nm thick ZrO_2 film. Air exposure during this transfer process was strictly limited to approximately 40 seconds, solely for mounting the substrates into the evaporator. Following encapsulation, back-gated field-effect transistors (FETs) were fabricated by patterning and depositing Cr/Au (15/150 nm) contact electrodes

via electron beam evaporation. All completed devices were stored in the glovebox between measurements to minimize ambient exposure.

3.4 Results and discussion

3.4.1 Time dependent study of early stages of oxidation

This section summarizes the results of the continuous SEM/AFM investigation conducted for a month on mechanically exfoliated $ZrSe_2$ flakes, transferred on a Si substrate. In order to capture the initial stages of the oxidation process, the samples were loaded into the SEM immediately after exfoliation and were exposed to air only briefly - just long enough for the chamber to be pumped down (a few minutes). Large flakes were selected with multiple terraces to maximize the exposed surface area and enable the examination of different types of edges, as shown in Figure 3.1.

Figure 3.1a shows a zoomed-out optical image of a representative $ZrSe_2$ flake highlighting its characteristic contrast on the Si substrate. The slight colour variations between the terraces correspond to differences in thickness. Immediately after exfoliation, $ZrSe_2$ exhibits early-stage degradation, as shown in the SEM image in Figure 3.1b, even though the oxygen atomic percentage is below the EDX detection limit, according to the EDX spectrum in Figure 3.1c. The Zr:Se stoichiometric ratio is approximately 0.61, indicating a non-stoichiometric composition and the presence of selenium vacancies, which likely act as adsorption sites for oxygen.

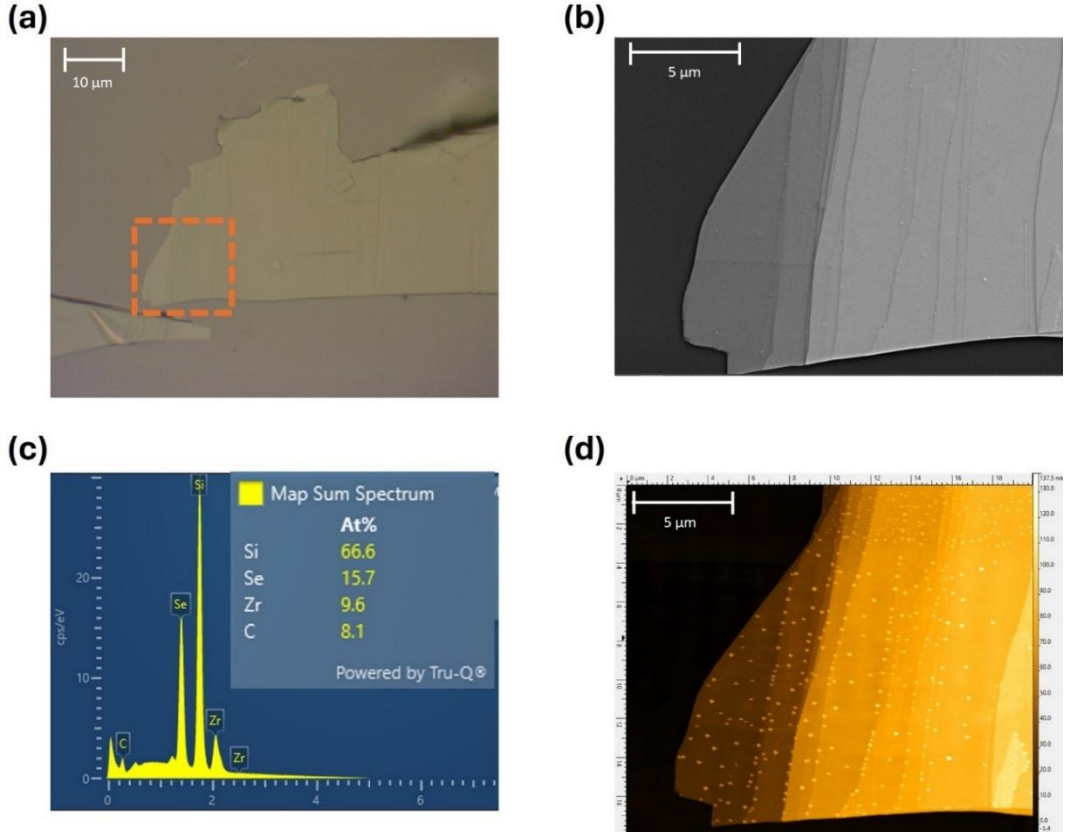

Figure 3.1: Early signs of ambient oxidation. (a) Optical image of a freshly exfoliated $ZrSe_2$ flake. The

dashed orange box indicates the region examined in subsequent analyses. (b) SEM image of the selected area taken within minutes of exfoliation, showing early-stage degradation. (c) EDX spectrum acquired from the same region. (d) AFM image acquired three hours later, showing increased density of hemispherical protrusions (bright spots), mostly along step edges. These features correspond to raised structures, not pits, with heights up to ~35 nm.

Numerous small hemispherical protrusions are located mainly along the step edges of the terraces, with some also scattered on the surface. Oxidation at the edges of 2D materials is a common phenomenon that has been previously reported[24,25]. The step-edges are optimal nucleation sites for the growth of these features because they contain broken bonds. The AFM measurement shown in Figure 3.1d, carried out three hours later, reveals a significantly higher density of these features, which appear prominently as white dots across both edge and surface regions. The AFM profiles confirms that these protrusions are not holes but raised features extending to a height of around 35 nm, which is thicker than the thinnest region of the flake.

The same AFM and SEM analyses were performed on different $ZrSe_2$ flakes 1, 5, 12 and 30 days after their exfoliation, as shown in Figure 3.2a, 3.2b, 3.2c, and 3.2d, respectively. For this study multi-terraced flakes with similar thicknesses were selected. Figure 3.2a reveals that the degradation process is very fast, since a high density of protrusions already formed after 24 hours both at the edges and on the surface of the flake. Figures 3.2b and 3.2c show a higher density of larger protrusions, compared with the freshly exfoliated flakes. However, the protrusions are not homogeneously distributed over the surface. Indeed, some areas are clean, suggesting that this process is triggered by both point defects on the surface in addition to the edges[26,27]. Even bigger protrusions are then clearly visible on the flake scanned after a 30-days period, revealing a persistent growth process of these features.

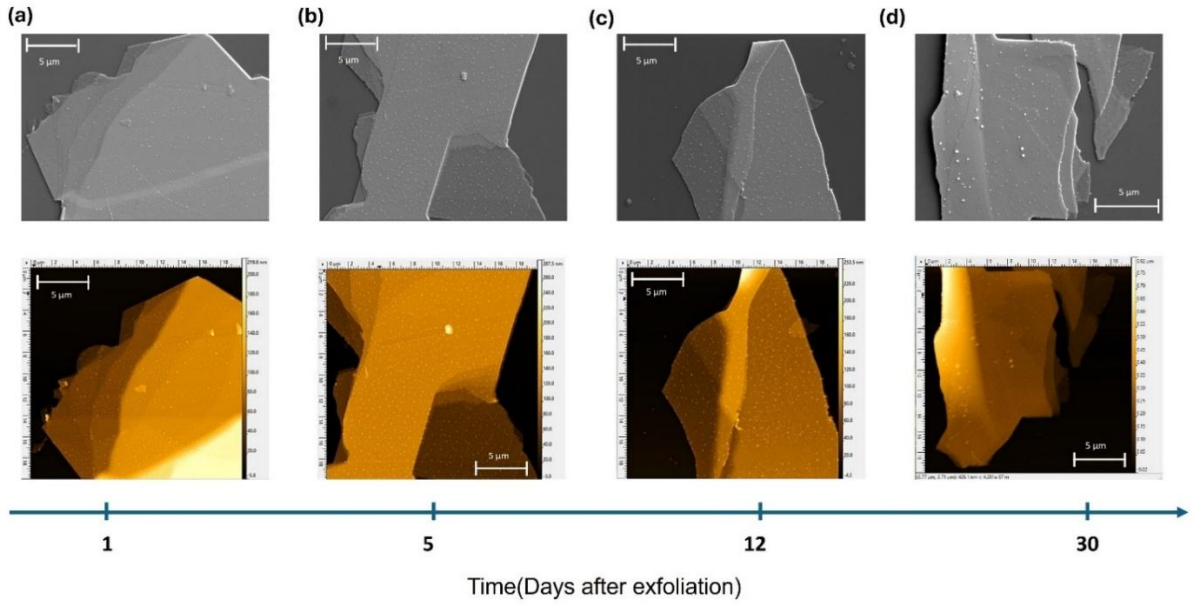

Figure 3.2: Time evolution of $ZrSe_2$ surface modification under ambient condition. (top) SEM and (bottom) AFM images of flakes (a) one, (b) five, (c) twelve and (d) thirty days after their exfoliation.

It was also seen using optical microscopy that the flakes in Figure 3.2 underwent a constant and dramatic colour change along the oxidation process, as shown in Figure 3.3.

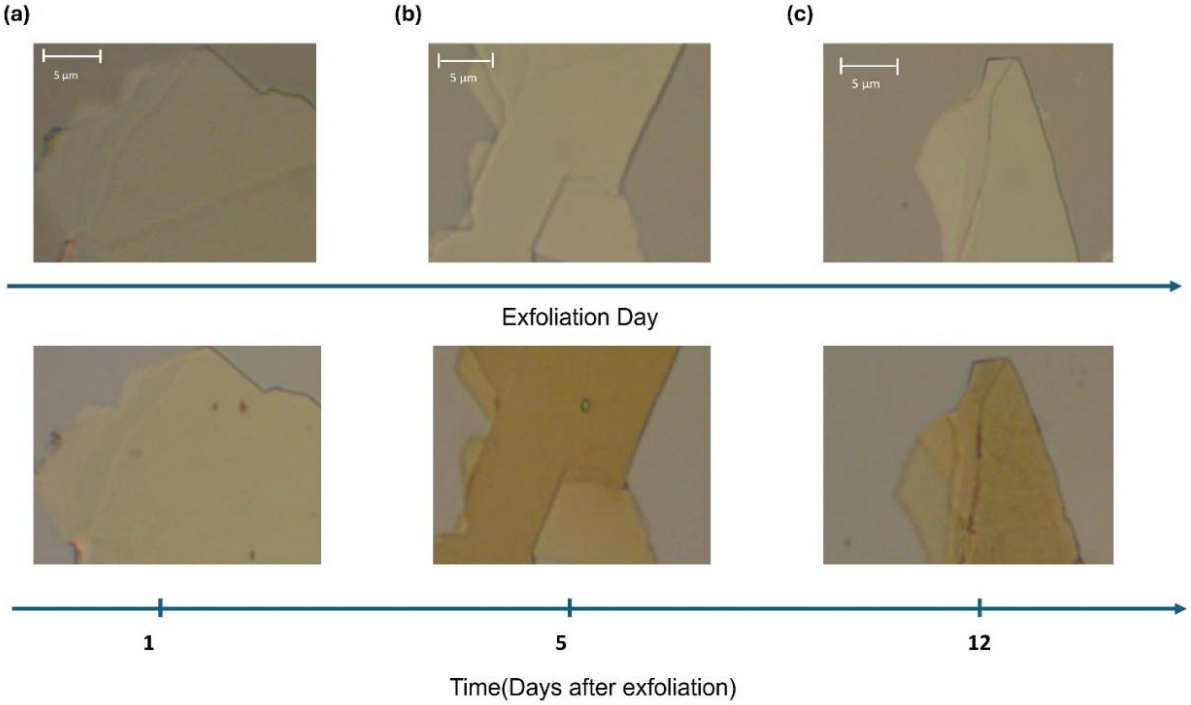

Figure 3.3: Optical images of three $ZrSe_2$ flakes on Si acquired (a) on the exfoliation day (top) and the day after (bottom); (b) on the exfoliation day and five days after; (c) on the exfoliation day and twelve days after.

To complement these results with atomic-scale information, STM on freshly cleaved $ZrSe_2$ crystals was performed. This technique allowed to track surface changes during controlled air exposure with high spatial resolution. After an initial exfoliation under ultrahigh vacuum (UHV) conditions, a bulk $ZrSe_2$ crystal was subjected to successive air exposures of increasing time duration in the load-lock of the UHV system. Following each exposure, the sample was reintroduced into the analysis chamber under UHV conditions for STM measurements. The results are summarized in Figure 3.4. The pristine sample exhibits an atomically flat surface with a root-mean-square (RMS) roughness of approximately 0.21 nm, measured over an 880 nm lateral area, as shown in Figure 3.4a. A higher-magnification image over an $18 \times 18\,\mathrm{nm}^2$ area clearly resolves the atomic lattice of $ZrSe_2$. The in-plane lattice parameter is 0.37 ± 0.02 nm, in good agreement with literature values[28,29].

After 4 minutes of air exposure, the surface roughness increases by a factor of ~3, while remaining sub-nanometric (Figure 3.4b). The magnified view reveals the formation of numerous surface defects, primarily consisting of vacancy aggregates, often decorated with adsorbates and sub-nanometric clusters, see Figure 3.5. For longer air exposures, the atomic lattice is no longer visible, and the surface appears fully amorphous, with RMS roughness values reaching 4.88 nm and 7.39 nm after 17 and 47 minutes of total exposure, respectively (Figures 3.4c and 3.4d). Interestingly, after 17 minutes, the surface corrugation becomes anisotropic, which is also evident in the corresponding Fast Fourier Transform (FFT) image as shown in the inset

of Figure 3.5c. This anisotropy is lost after 47 minutes, with the surface appearing rougher and the FFT showing isotropy (Figure 3.5d).

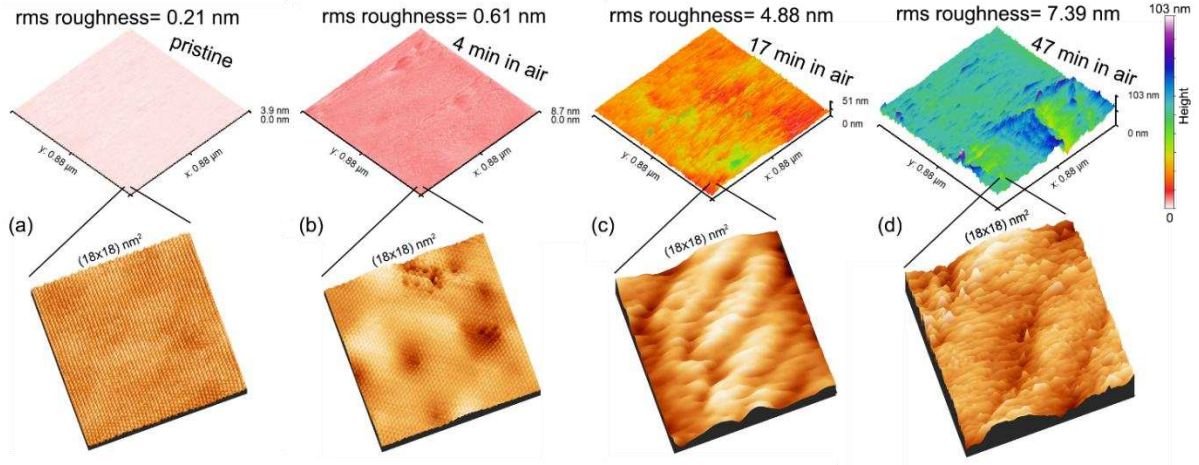

Figure 3.4: Atomic-scale evolution of $ZrSe_2$ surface under ambient conditions. (Top panels) 3D STM topographic images illustrating the evolution of surface roughness following incremental air exposure durations. (a)-(d): freshly cleaved $ZrSe_2$ crystal in UHV, and the same sample after 4, 17, and 47 minutes of air exposure, respectively. All images are presented with the same height scale; the corresponding height ranges and root-mean-square (RMS) roughness values are noted. (Bottom panels) STM images showing 18 × 18 nm^2 zoom-ups of the surface in each condition. STM scanning parameters: (a) V = −1.0 V, I = 40 nA; (b) V = −0.5 V, I = 21 nA; (c) V = −3.9 V, I = 4.7 nA; (d) V = −3.8 V, I = 4.0 nA

The reason why measurements at specific time intervals after exfoliation in Figure 3.2 were performed on different flakes rather than repeated on the same flake is that SEM dramatically modifies the surface of the flake when it is repeatedly scanned, interfering with the natural degradation process, as described in Section 3.2. Therefore, for each flake in Figure 3.2, SEM analysis was performed after acquiring AFM images.

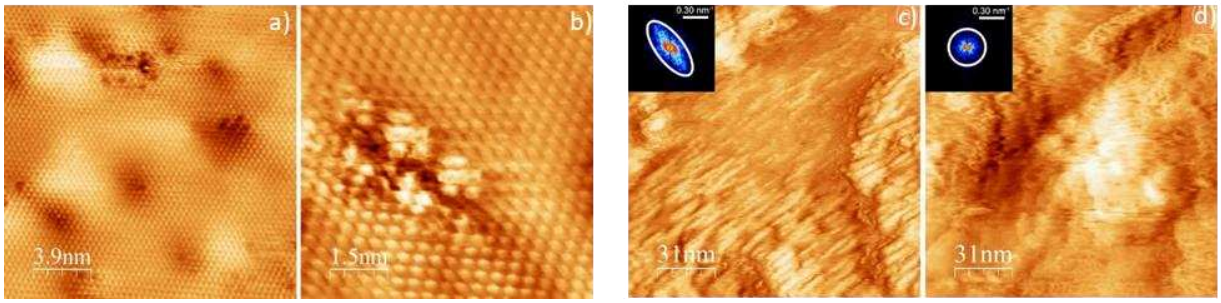

Figure 3.5: (a) and (b) STM image showing defects on the surface after 4 min exposure to air. STM scanning parameters: V= -0.5 V, I=21 nA. STM images after (c) 17 min and (d) 47 min exposure to air. In the insets, the corresponding FFT is reported. STM scanning parameters: (c) V= -3.9 V, I=4.7 nA; (d) V=-3.8 V, I= 4.0 nA.

3.4.2 Electron beam effects on oxidation progression and surface morphology

The impact of SEM on the $ZrSe_2$ surface was evaluated over one month through repeated SEM, EDX, and AFM analyses on the same flake.

Figure 3.6a shows that a higher density of protrusions is detected, one day after the exfoliation, compared to the density of protrusion immediately after exfoliation shown in Figure 3.1. EDX oxygen maps confirm oxygen adsorption on the $ZrSe_2$ flake. The atomic percentage of the chemical species involved, extracted from the EDX spectra of the flake in Figure 3.6, are shown in Figure 3.7a. These results are the outcome of an average over the entire scanned area.

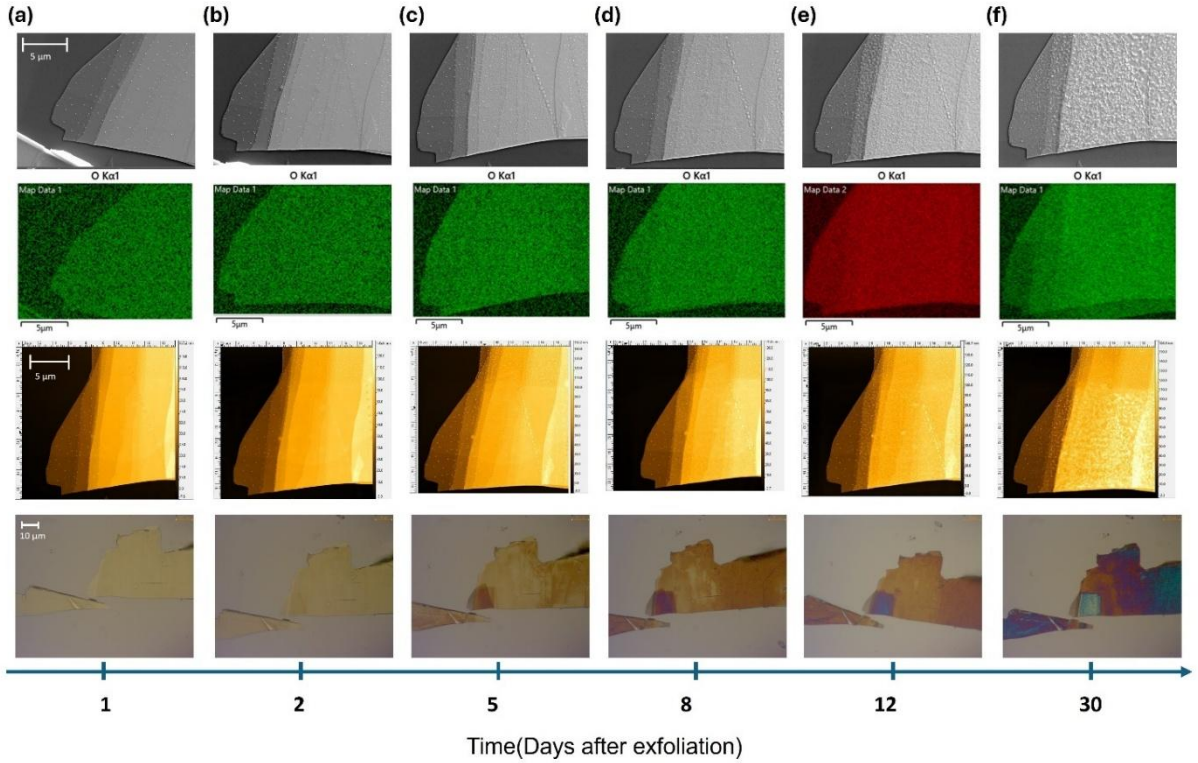

Figure 3.6: Study of the time-dependent surface topology of a $ZrSe_2$ flake. The vertical column corresponds to SEM, Oxygen EDX Map, AFM, Optical microscopy images after (a) one, (b) two, (c) five, (d) eight, (e) twelve and (f) thirty days from exfoliation.

Some fluctuations in the behaviour could be attributed to the difficulty in scanning the exact same area of the flake. Despite this, the overall trends are considered qualitatively reliable. The Zr:Se stoichiometric ratio is constant over time, while the oxygen atomic percentage increases with time, following an exponential law, as shown in the inset. At the same time, the AFM results show that the average thickness of each flake terrace overall increases over time; the phenomenon being most significant for the thinnest parts. The thickness of the thinnest region is almost doubled in a month (from 20 to 40 nm), while the thicker part raises by 30% - see Figure 3.7b. This trend is attributable to oxygen atoms that

intercalate and expand the separation between the $ZrSe_2$ layers, in addition to absorbing on the surface[13].

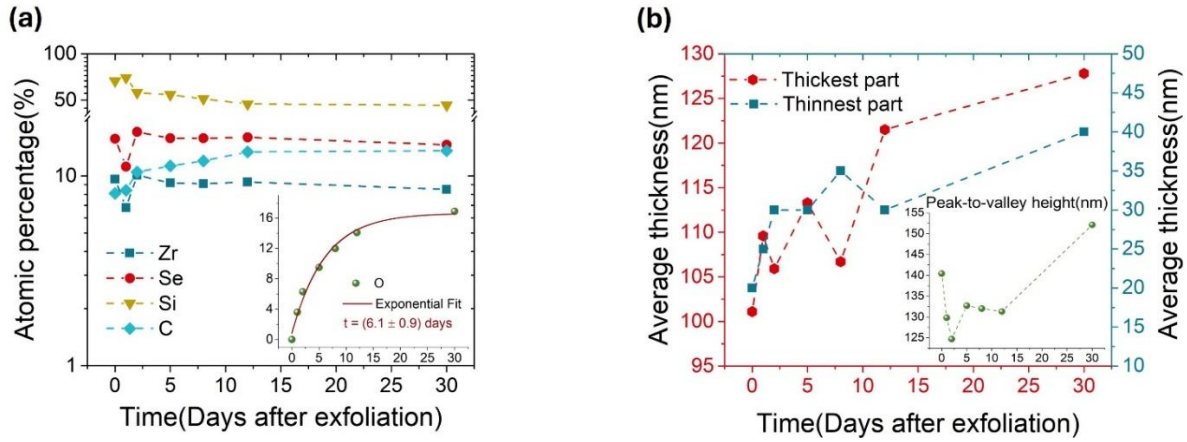

Figure 3.7: (a) Atomic percentage of Zr, Se, Si and C over time, collected from EDX summary spectra. The inset shows the exponential increasing trend of the O concentration. (b) Average thickness over time of the thickest (left) and the thinnest (right) part of the flake. The peak-to-valley height extracted from AFM measurements is reported in the inset.

The thickness values were estimated by averaging five horizontal AFM profiles taken from consistent positions across all images (see Figure 3.8). The protrusions appear in the AFM profiles as sharp peaks rising above the terraces and are especially prominent in the initial scans.

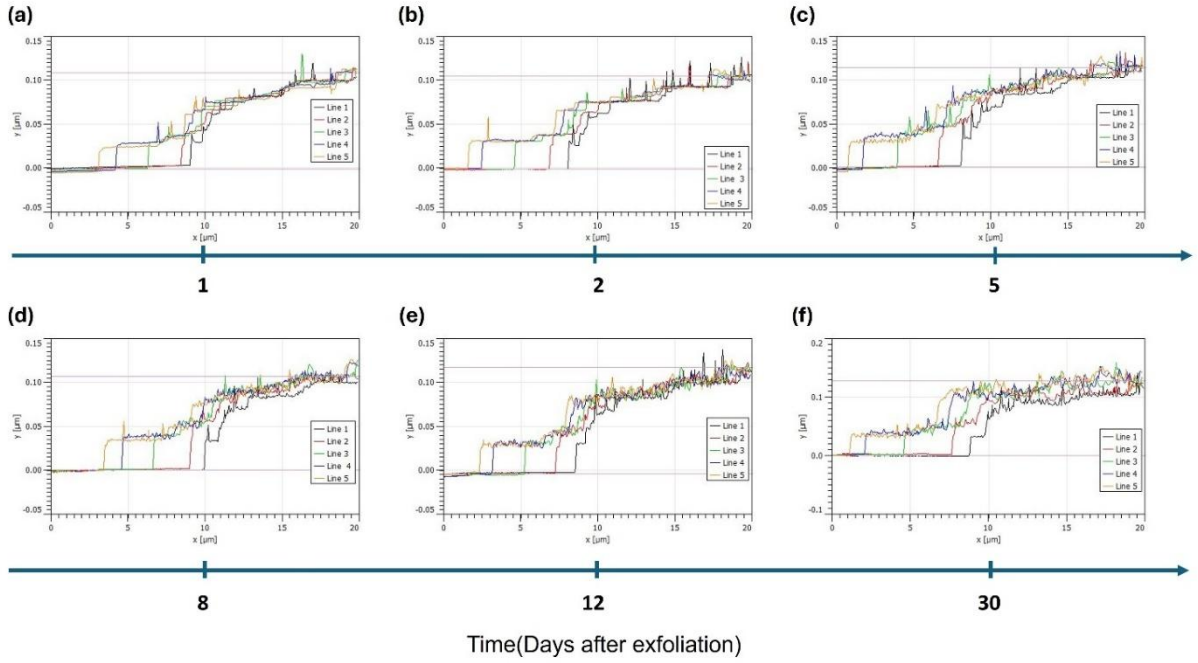

Figure 3.8: AFM profiles acquired on the $ZrSe_2$ flake in Figure 3.6 (a) one (b) two, (c) five, (d) eight, (e) twelve, and (f) 30 days after the exfoliation.

Figure 3.6 compared to Figure 3.2 highlights significant variations in the surface morphology of $ZrSe_2$ flakes aged under identical conditions. These differences become particularly evident at the most advanced aging stage, where the flake in Figure 3.6f gives the appearance of partial surface melting, started after five days from exfoliation.

Additionally, the protrusions gradually fade rather than increasing in density or size, making them difficult to distinguish after one month. This is revealed both by SEM images and AFM images/profiles. The combination of these two phenomena, as visualized in the AFM profiles in Figure 3.8, explains the decreasing peak-to-valley height trend shown in the inset of Figure 3.7b.

These SEM-induced differences are further illustrated in Figure 3.9, which compares a region that was repeatedly scanned over the course of a month - visible as the light blue square indicated by the arrow in the optical image - with adjacent unscanned areas of the same flake. Since the regions under investigation, marked by the solid orange and blue rectangles in Figure 3.9a, belong to the same flake, potential variations due to growth, exfoliation, or storage conditions can be ruled out. The 50 × 50 μm^2 scans shown in Figures 3.9b and 3.9c already reveal a clear difference between the repeatedly scanned region (dashed orange rectangle) and the rest of the flake. This contrast becomes even more evident when comparing Figure 3.9d, which zooms into the area repeatedly scanned over a month, with Figure 3.9e, showing a fresh scan of a previously unexposed area.

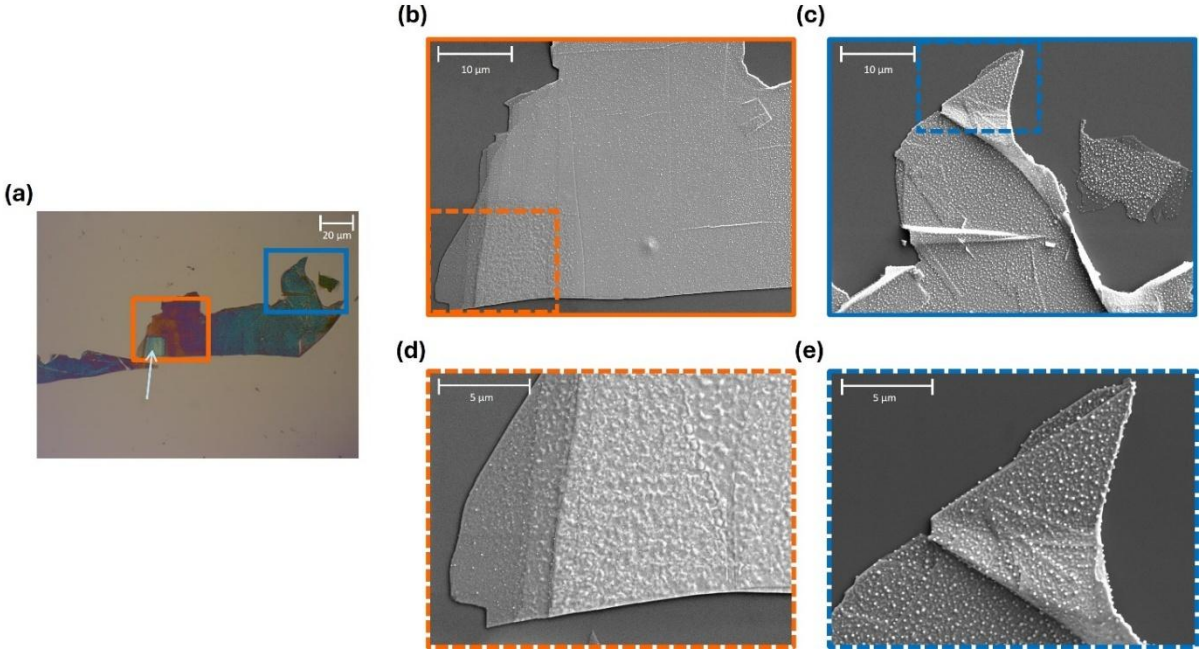

Figure 3.9 (a) Optical image of the whole flake investigated in Figure 3.6, a month after the exfoliation. The solid orange and blue rectangles identify the areas where the 50x50 μm^2 scans (b) and (c) are performed. The dashed orange and blue rectangles in (b) and (c) indicate where the 20x20 μm^2 scans (d) and (e) are performed. The area in (d) was repeatedly SEM-scanned over a month, while (e) reports the first scan of this area.

It appears the electron beam modifies the surface by hindering the growth of protrusions and limiting the formation of new ones. This effect is likely due to beam-induced redistribution

of surface elements, partially 'melting' the surface. Even a couple of months after the last scan, the surface of the flake investigated in Figure 3.6 does not show new or enlarged protrusions suggesting that SEM exposure may irreversibly alter the flake's surface. Moreover, SEM not only prevents the formation of new protrusions, but also appears to remove or restructure existing oxidized features, even after they are already formed.

3.4.3 Oxidation-induced Se segregation and blister formation

While sections 3.4.1 and 3.4.2 concentrate on the initial phases of oxidation, the following sections investigate the oxidation process over extended exposure times. Initial insights are provided by optical microscopy. Figures 3.10 and 3.11 report on the apparent colour variation of $ZrSe_2$ flakes on Si/SiO_2 (85 nm) substrates, after several months. The specific colour variation and the time scale on which the variation occurs depend on the thickness of the investigated regions. Comparing figures a and b of each plot qualitatively shows that, after 24 days, green/dark-green flakes (~ 20 nm and below) convert in blue flakes, yellow parts (~ 50 nm) become darker, light blue (~ 70/80 nm) becomes orange and light grey (~ 100 nm) converts in green. Moreover, the thicker flakes keep changing their colour over three months: The 50 nm regions become darker, the 70-80 nm parts become red, and the 100 nm parts become purple. It looks like that the thinner ones (below 20 nm), instead, reach the self-limiting point earlier, since no colour change is perceptible between one and two months – look at the Figures 3.10b and 3.10c. This colour change might be attributed to the degree of oxidation of Zr over time: It might be due to the combination of the different coloured zirconium oxides in the oxidation layer[30] with the original apparent contrast due to the thickness of the flake. Additionally, looking at the large surface in Figure 3.11, it is possible to identify the development of red dots, at the edges and on the surface of the multiple terraces, which correspond to the protrusions observed with SEM and AFM.

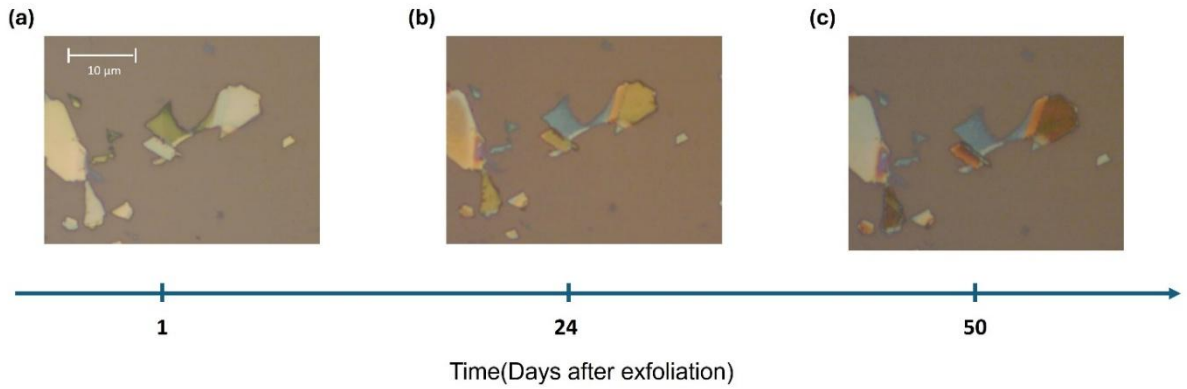

Figure 3.10: Optical images of $ZrSe_2$ on Si/SiO_2 acquired (a) on the exfoliation day and around (b) 1, (c) 2 months later.

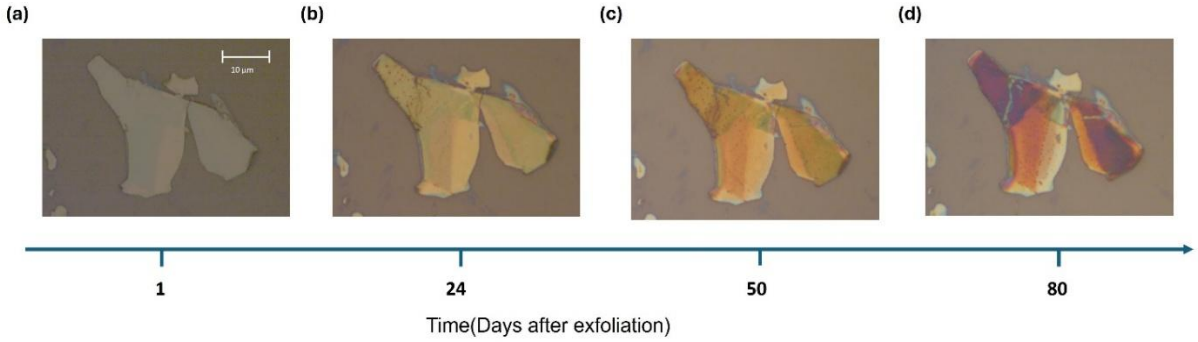

Figure 3.11: Optical images of $ZrSe_2$ on Si/SiO_2 acquired (a) on the exfoliation day and around (b) 1, (c) 2, and (d) 3 months later.

To understand the chemical composition of the features on the $ZrSe_2$ surface, multiple aged flakes were analysed using EDX. Figure 3.12a shows a thin 1-month-old flake, in which two distinct features can be observed: localized hemispherical blisters of different dimensions and planar surface modification that might be the initial stage of the formation of the protrusions. They grow both on the surface and laterally from the edges and have diameters up to ~300 nm. Oxidation-induced surface deformations have been observed in other materials[8,13]. EDX maps of the flake showing the spatial distribution of Zr, Se and O, reveal Se segregation. It is likely that oxygen causes displacement of Se atoms to form ZrO_2.

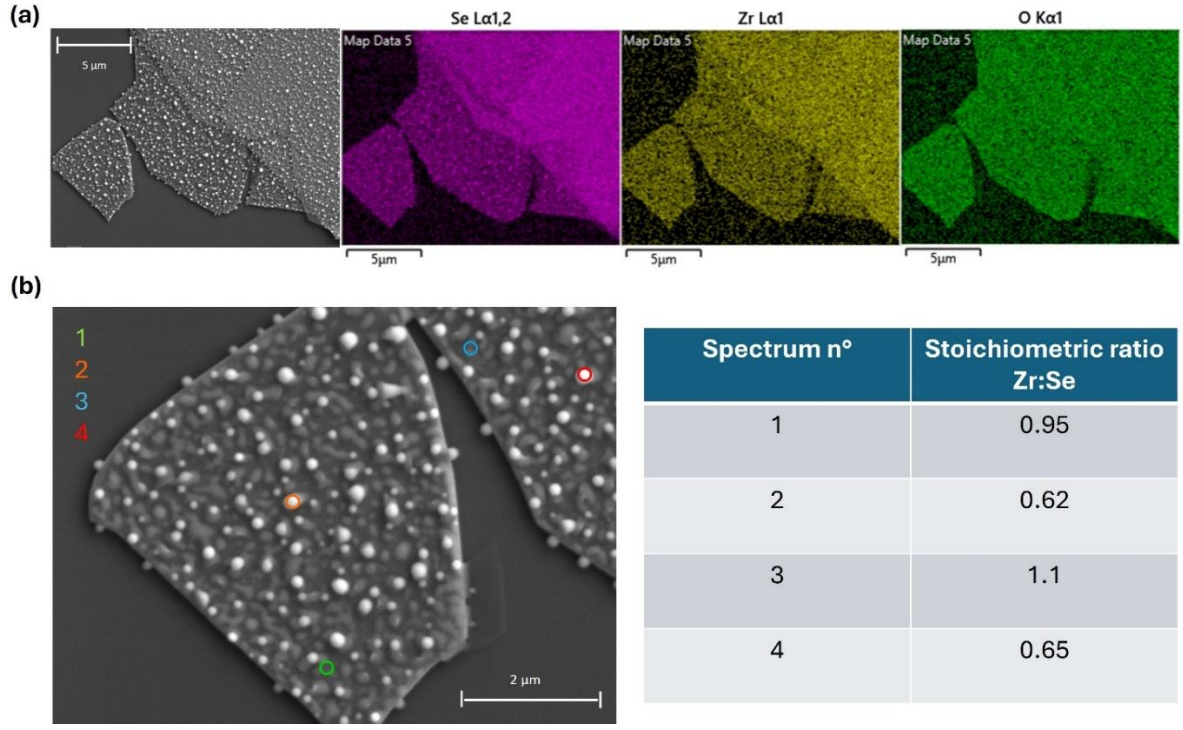

Spectrum n°	Stoichiometric ratio Zr:Se
1	0.95
2	0.62
3	1.1
4	0.65

Figure 3.12: Se segregation and blister formation in aged $ZrSe_2$. (a) SEM image and EDX elemental maps (Se, Zr, O) of a $ZrSe_2$ flake one-month post-exfoliation, showing Se-rich blisters and surface modifications. (b) Zoomed SEM image with marked points (1-4) corresponding to EDX point analyses. Stoichiometric ratios extracted from EDX spectra acquired from blistered and unmodified areas confirm

Se enrichment (Se:Zr ≈ 0.65) in protrusions, indicating chemical inhomogeneity arising from oxidation-driven Se displacement and ZrO_2 formation, as reported in the table.

Similar mechanisms have been reported in previous works for other materials[31]. Se migration is supported by EDX point spectra acquired from several protrusions and protrusion-free areas - see Figure 3.12b. The concentration of Zr and Se is almost the same far from the protrusions, as shown by the spectra 1 and 3. This confirms that the sample becomes chemically inhomogeneous after prolonged oxidation.

The oldest flakes, such as the 4-month-old samples shown in Figure 3.13, exhibit this mechanism even more clearly. The largest hemispherical protrusions reach diameters of approximately 500 nm. As the oxidation process proceeds, densely-packed groups of protrusions appear to coalesce into a single, larger one, leaving a smoother, flatter area surrounding them. These results highlight that the process is not self-limiting, and that Se aggregation occurs readily at room temperature without any external stimulus. EDX maps confirm the absence of both Zr and O at the protrusions, as highlighted by the triangular shape in Figure 3.13a. EDX spectra collected on the oldest flakes confirm a non-uniform distribution of the chemical species. The Zr:Se stoichiometric ratio ranges from 0.7 to 0.91 on bubble-free regions and from 0.57 to 0.29 on them – see the Table in Figure 3.13b.

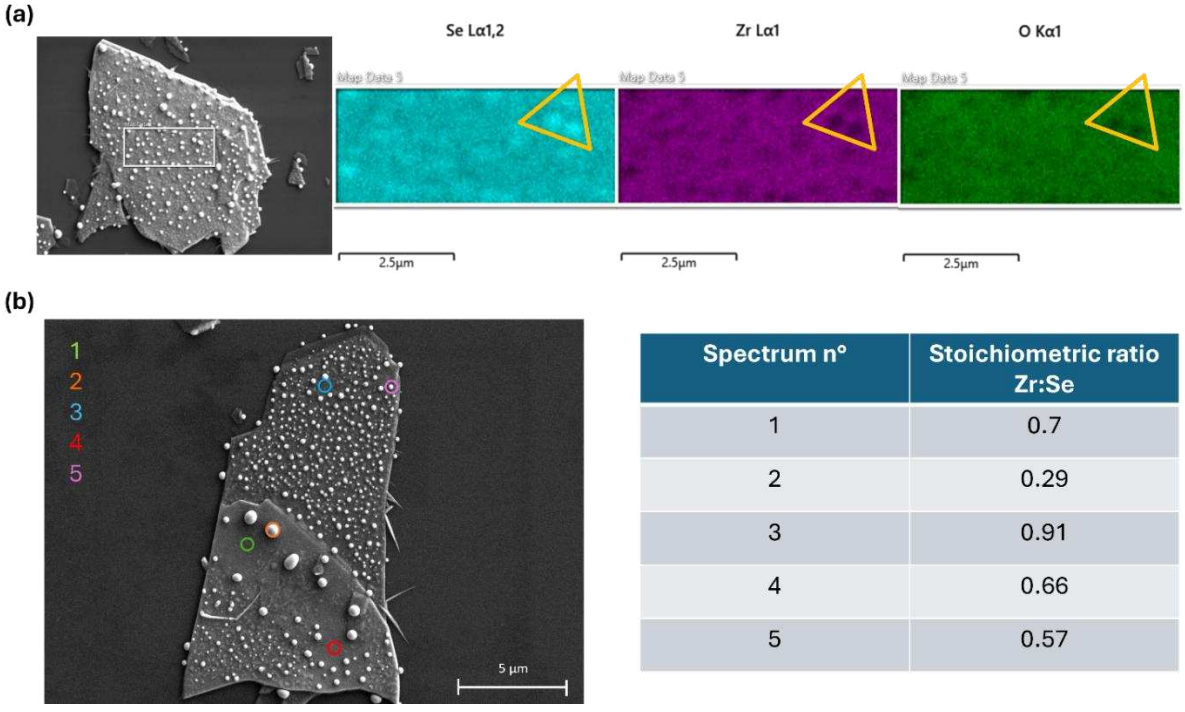

Spectrum n°	Stoichiometric ratio Zr:Se
1	0.7
2	0.29
3	0.91
4	0.66
5	0.57

Figure 3.13: Enhanced Se aggregation and nanowire formation in aged $ZrSe_2$. (a) SEM image showing surface degradation of a flake aged for 4 months, characterized by numerous Se-rich protrusions. The white rectangle indicates the region selected for EDX elemental mapping of Se, Zr, and O highlighting Se redistribution and local chemical inhomogeneity. The yellow triangular markers indicate representative areas where three Se-rich blisters are clearly identified. (b) SEM image of a flake showing a protrusion-rich surface, with marked points (1-5) corresponding to EDX point analyses. The table reporting the stoichiometric ratio extracted from EDX spectra on blistered and flat areas reveals

significant compositional variation across the flake, with strong Se enrichment in specific regions (Zr:Se as low as 0.29 on blisters). Nanowire formation is also observed in aged samples.

Cross sectional EDX was performed normal to the flake surface in Figure 3.14 from the top of a protrusion deep into the Si/SiO_2 substrate. Figures 3.14a and 3.14b show a SEM image of a $ZrSe_2$ flake with the approximate location of FIB lamella extraction highlighted, and the FIB-SEM cross-section image of the $ZrSe_2$ flake on Si/SiO_2, respectively. Looking at Figure 3.14c, from left to right, there is the Si substrate, then the 85 nm thick SiO_2 that appears as a dark region, the $ZrSe_2$ flake and the protrusion on top of it. The oxygen concentration reaches its maximum at the interface between the SiO_2 and the flake and then it decreases. The Zr concentration reaches its maximum in correspondence of the flake, but only a low amount is detected in the protrusion, which is predominantly made of Se, as expected. Two peaks can be identified in the Se spectrum, one in correspondence with the flake and the other at the centre of the protrusion.

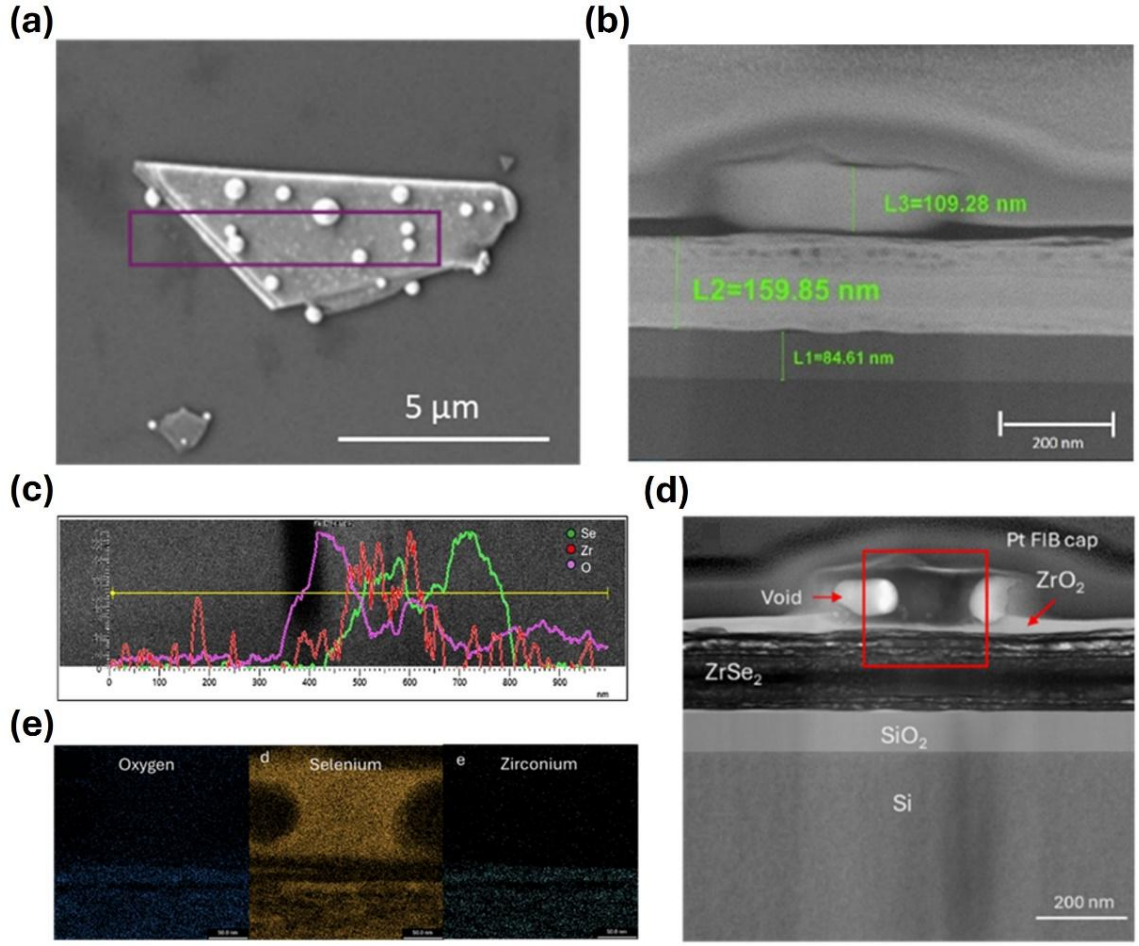

Figure 3.14: Cross-sectional STEM and EDX analysis of blisters. (a) SEM image of $ZrSe_2$ flake with the approximate location of the FIB lamella extraction highlighted. (b) FIB-SEM cross-section image of the $ZrSe_2$ flake on a Si/SiO_2 substrate. (c) Cross-sectional EDX line spectra, showing elemental distribution across the substrate, flake, and protrusion. (d) STEM survey image of the large protrusion and underlying layers. The red box highlights the region where correlated EDX was recorded. (e) Correlated EDX maps of the protrusion, showing strong Se segregation.

A FIB cross-section of a protrusion was measured in a Tescan Tensor 4DSTEM system with correlated EDX operated at an accelerating voltage of 100 kV and a probe current of 1 nA, see Figure 3.14d and 3.14e. The convergence angle was 9.78 mrad. During the measurement of the protrusion, voids began to form in the lamella, necessitating a reduction of the beam current to 500 pA, which stabilized the sample. Figure 3.14d shows the structure of the protrusion and underlying flake. The protrusion is embedded in a ZrO_2 layer measuring 20-50 nm which extends beneath the protrusion, separating it from the underlying $ZrSe_2$. The $ZrSe_2$ layer exhibits phase separation into alternating layers of Se rich and Se depleted regions. The dark band at the surface is composed of almost pure Se, while the bright voids are composed of almost pure ZrO_2. The darker central region is well mixed, with a Zr:Se ratio of ~20:50, making the flake slightly Se rich. A thin layer of carbon, less than 5 nm thick, resides between the substrate and $ZrSe_2$ flake, which is likely residue from the transfer process. Since the ZrO_2 layer extends beneath the protrusion, this indicates the blister formed on top of the oxide, not through it - further suggesting the Se blister may have formed as a consequence of Se segregation from $ZrSe_2$ due to oxidation. Se poorly wets oxide substrates at room temperature, which can lead to the formation of blisters in selenium melts. The segregated Se near the ZrO_2 layer may therefore have spontaneously aggregated into blisters on the surface oxide[32].

3.4.4 Nanowires formation

As shown in Figure 3.15a, aged flakes reveal that selenium not only accumulates as hemispherical protrusions but can also spontaneously self-assemble into nanowires, with widths reaching up to ~100 nm. The same was observed in Figure 3.13b.

The FIB cross-section of the flake in Figure 3.15a, presented in Figure 3.15b, shows two such nanowires embedded in the structure. These nanowires are coated with a thin carbon layer, although distinguishing it from the surrounding e-beam deposited platinum - used to protect the sample during FIB processing - is challenging (see Figures 3.15b). Interestingly, the nanowires have etched into the underlying SiO_2 substrate. However, this is not due to reduction processes, as they contain negligible oxygen (Figure 3.15c). Instead, EDX point scans confirm that the wires are composed of pure Se, as further demonstrated in Figures 3.15d and 3.15e. Their high crystallinity, supported by structural data in Figure 3.15f suggests that these nanowires result from a spontaneous growth mechanism during aging.

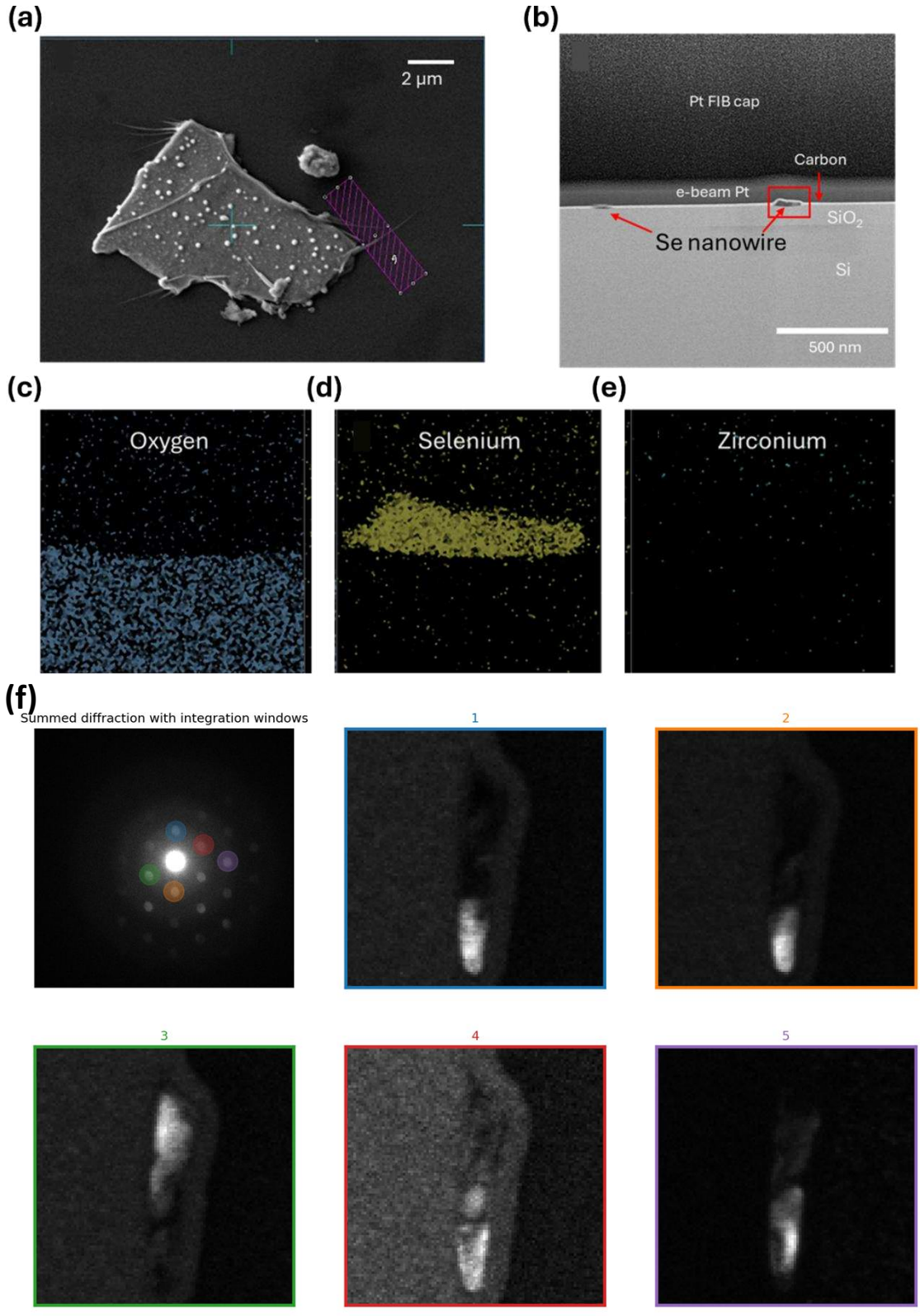

Figure 3.15: Spontaneous formation of Se nanowires on aged $ZrSe_2$ Flakes. (a) SEM image of an aged $ZrSe_2$ flake showing surface nanowires, with the FIB lamella extraction region marked in purple. (b) STEM cross-sectional image highlighting two Se nanowires embedded in the flake structure. (c-e) EDX elemental maps confirming the nanowires are composed of pure Se with negligible oxygen or zirconium

content. (f) Diffraction pattern from the Se nanowire showing high crystallinity. 1 – 5 4DSTEM maps using the inverse masks colour coded in the diffraction image.

Characteristic dimensions of the nanowires in Figure 3.16a were measured through AFM - see Figure 3.16b. The AFM profile in Figure 3.16c indicates that the maximum diameter of the nanowires protruding over the substrate is around 44 nm, while it reaches up to 124 nm for those lying flat on the surface, as reported in Figure 3.16d.

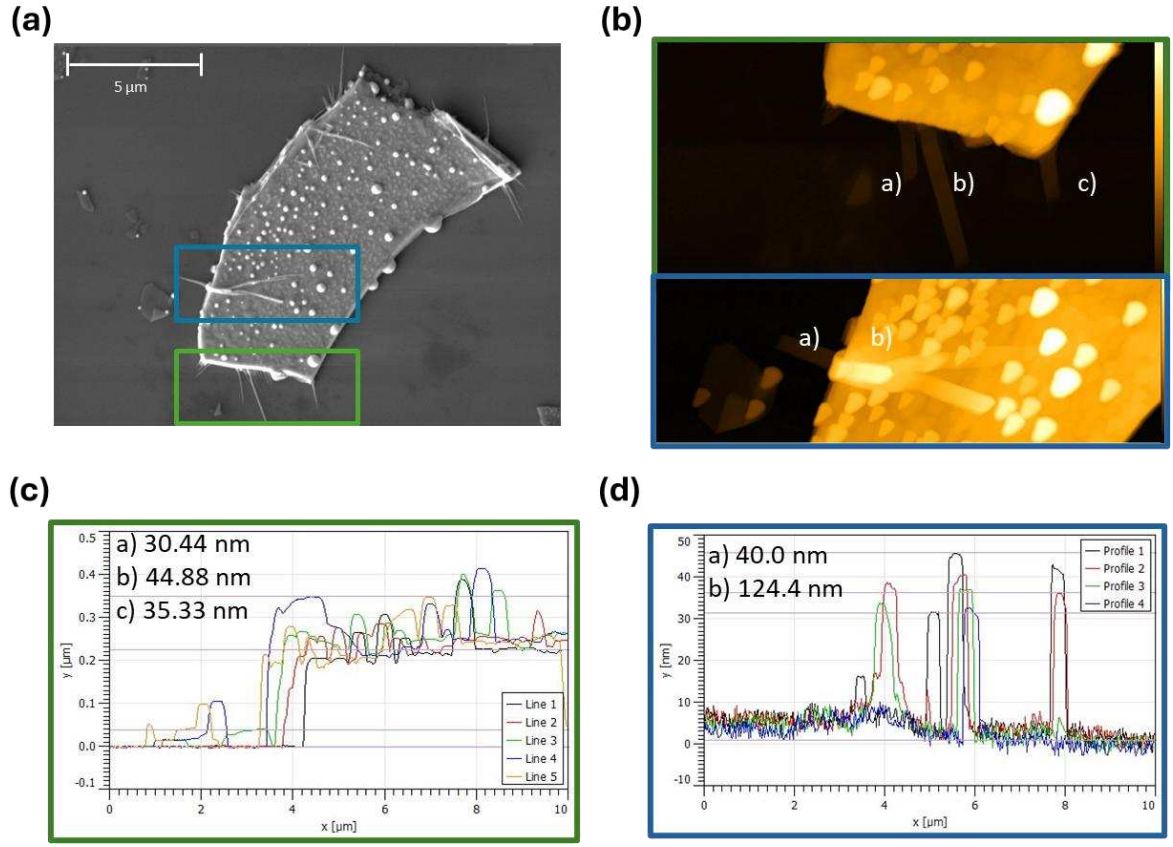

Figure 3.16: (a) SEM image of an aged flake displaying nanowires, with AFM scan regions outlined in green and blue. (b) AFM topography images of selected regions. (c),(d) AFM profiles showing the corresponding height and width of the nanowires.

Considerable research has focused on synthesizing Se-based nanostructures such as nanowires, nanotubes, and nanorods, given selenium's intriguing physical properties, like high photoconductivity, piezoelectricity, thermoelectricity, and nonlinear optical responses[33]. Se exists in several allotropic forms, including trigonal, monoclinic, and amorphous phases. Of these, the trigonal structure is thermodynamically the most stable, and its chain-like configuration naturally supports 1D anisotropic growth[34].

Se nanowires are typically grown from precursor solutions or solid compounds[35,36]. They can be synthesized using various methods - for instance, by dispersing amorphous selenium (a-Se) nanoparticles in ethanol and storing them in the dark at room temperature, which gradually dissolves the a-Se and leads to the formation of trigonal Se (t-Se) seeds and eventually t-Se nanowires. According to the literature, an alternative approach involves dispersing the

nanoparticles in water and heating them to 85 °C. A modest temperature increase is sufficient to trigger the amorphous-to-trigonal phase transition, given its relatively low transformation energy of only 6.63 kJ/mol[37].

Additional SEM images of several $ZrSe_2$ aged flakes confirm that Se nanowire growth initiates at Se-rich protrusions - both at the flake edges and across the surface. As further discussed in the following section, identifying the phase of Se in the hemispherical protrusions is challenging. It can be assumed to be amorphous, as these features result from air exposure-induced oxidation. However, the tubular morphology of the nanowires and the diffraction pattern in Figure 3.15 suggest that they adopt a trigonal phase. This transition is likely favoured by the lower surface energy of t-Se compared to a-Se[38]. Thus, the formation of Se nanowires from oxidized $ZrSe_2$ warrants deeper investigation, with the aim of enabling controlled growth and the exploitation of their intrinsic properties[39,40].

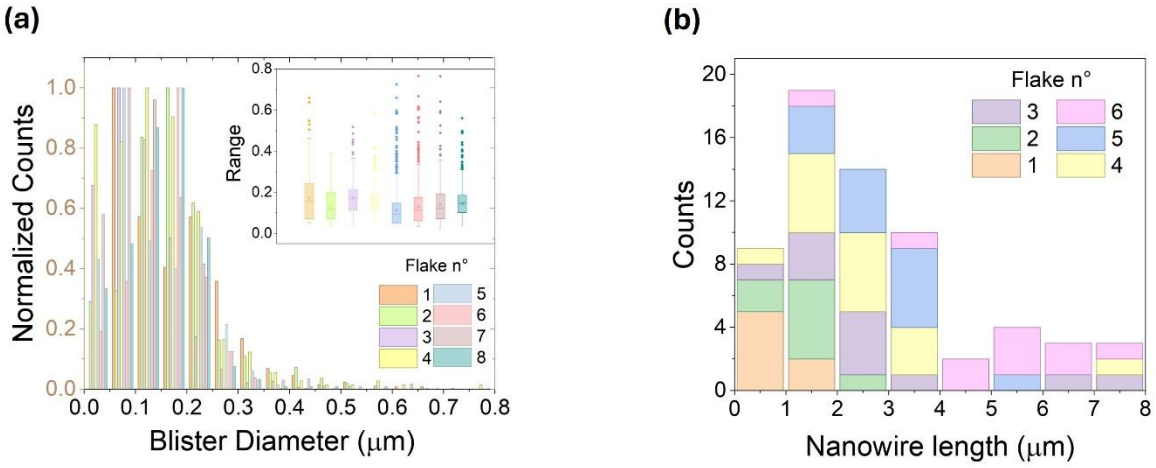

Figure 3.17: (a) Column bar plot showing the distribution of blister diameters on aged flakes, with each colour corresponding to a different flake. The inset box chart summarizes the distribution parameters: the median is indicated by a line within the coloured box, the "x" marks the arithmetic mean, the box edges represent the quartiles, and the isolated dots correspond to outliers. (b) Stacked histogram showing the length of nanowires on flakes aged for 4 and 5 months.

Figure 3.17a shows the statistical analysis concerning blisters formed on several flakes exposed to air for extended periods, exfoliated on different substrates and from different batches. Blister dimensions were quantified by image analysis. The column bar plot displays, for each analyzed flake (color-coded), the normalized distribution of blister diameters, while the inset box chart summarizes the corresponding statistical parameters. The blister diameters range from 0.025 to 0.775 μm, with a median value of approximately 0.13 μm. The length of nanowires grown on flakes aged for 4 and 5 months is reported in Figure 3.17b, finding values ranging from 0.42 to 7.8 μm. Nanowires can also extend from multiple protrusions and merge into longer continuous structures. In this case, lengths up to 10-15 microns have been measured.

3.4.5 Phase evolution and chemical modification

Raman spectroscopy provides further insights into how the oxidation process evolves over time. $ZrSe_2$ flakes were mechanically exfoliated onto a p^+-Si/SiO_2 substrate, and the Raman spectrum was acquired multiple times over a month on the same flake, only changing the location of the laser spot. During this period, the sample was stored in the cleanroom environment.

$ZrSe_2$ presents a 1T structure with a P-3m1 space group and the unit cell is given by $\alpha=\beta=90°$, $\gamma=120°$ and a=b=3.772(2) Å, c=6.1258(5) Å. The Raman spectrum acquired immediately after exfoliation is shown in Figure 3.18a. A small peak corresponding to the in-plane mode E_g appears at (145.3 ± 1.7) cm^{-1} and a sharp one, associated with the out-of-plane A_{1g} mode, is visible at (193.51 ± 0.03) cm^{-1}. These values are consistent with the ones reported in literature[41]. In addition, the IR-active modes E_u was detected at 211 cm^{-1} and the A_{2u} at (261 ± 2) cm^{-1} [42,43].

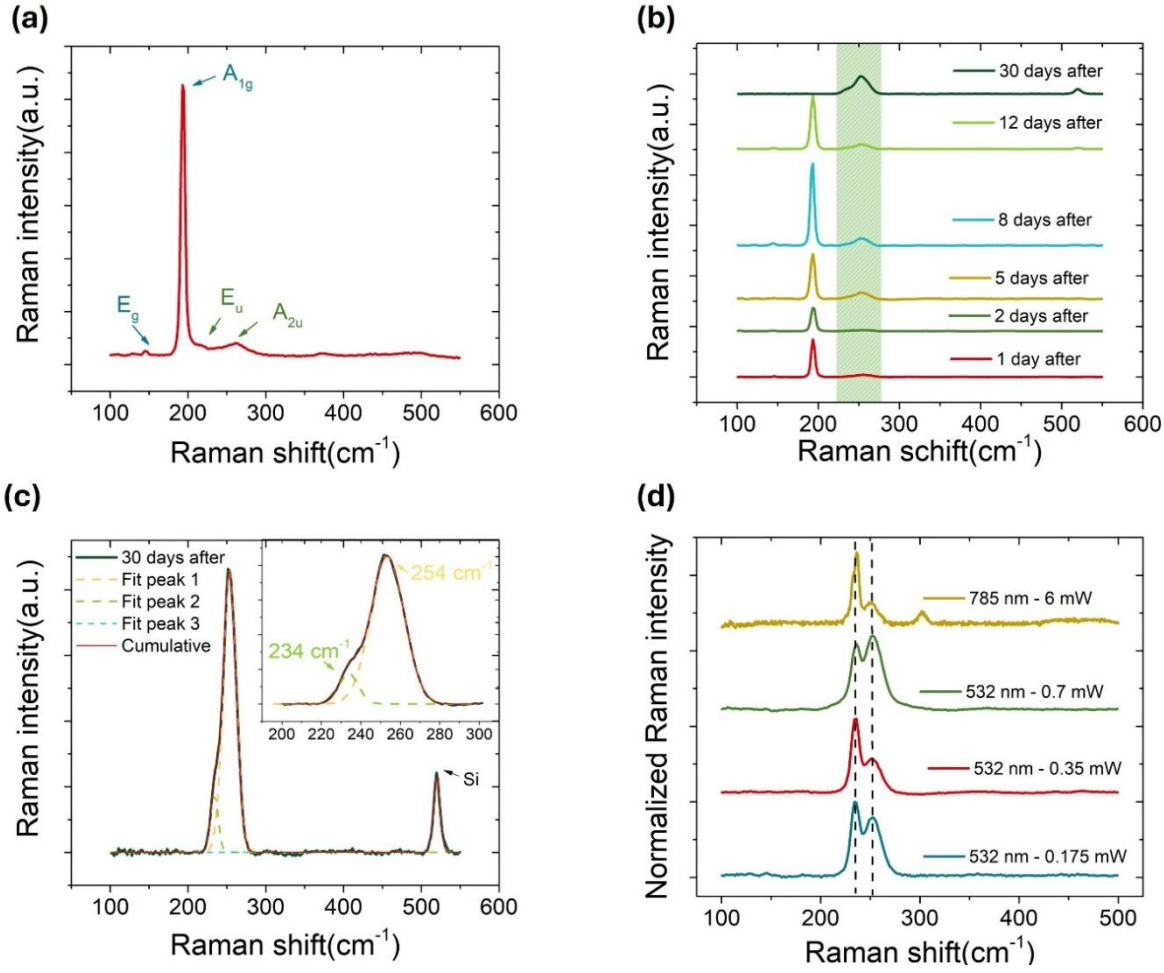

Figure 3.18: Time evolution of $ZrSe_2$ Raman spectra during ambient air exposure. (a) Raman spectrum of freshly exfoliated $ZrSe_2$ showing E_g, A_{1g}, E_u, and A_{2u} modes. (b) Raman spectra acquired at multiple time points over 30 days; the shaded region highlights the emerging broad peak. (c) Spectrum after 30 days, showing the disappearance of $ZrSe_2$ modes and the appearance of an a-Se peak (~254 cm^{-1}); inset: peak fitting reveals contributions at 234 and 254 cm^{-1}. The inset in (c) shows a zoom on the Se peak.

The dashed lines display the fit of the peaks, while the solid ones are the result of the cumulative fit. (d) Raman spectra after 3 months acquired at different excitation wavelengths and powers.

Figure 3.18b shows the spectra acquired 1, 2, 5, 8, 12, and 30 days after exfoliation. Over the first 12 days, both E_g and A_{1g} $ZrSe_2$ peaks are clearly visible, and no significant shift is observed. The A_{2u} peak, normally located around 261-264 cm^{-1} in fresh exfoliated flakes, is replaced by a broad peak around 253 cm^{-1} that gradually increases over time (see Table 3.1). After one month, the E_g and A_{1g} are no longer detectable. The top spectrum, also shown in Figure 3.18c, displays only a peak besides the Si peak, which is attributed to likely amorphous Se (a-Se)[43,44]. This assignment is consistent with the formation of blisters through a spontaneous aggregation process, where an initially amorphous structure is expected. This result further confirms the nature of the hemispherical protrusions described in the previous section. The disappearance of the $ZrSe_2$ peaks after a certain period that likely depends on the thickness of the flake, reveals that the exposure to air modifies dramatically and irreversibly the chemical structure of the material.

It is not straightforward to identify the precise structure of Se through Raman spectroscopy. As mentioned above, the two principal crystalline Se allotropes are the trigonal form (t-Se), consisting of ordered polymeric Se_n chains, and the monoclinic Se (m-Se) with ordered Se_8 rings. However, the structural parameters of these two phases are so similar that Raman spectroscopy itself can induce a photo- and heat-driven ring-to-chain transition. To minimize this effect, above bandgap excitation lasers with low photon flux and below bandgap excitation laser at low temperature are needed[44,45], but the Raman setup used in this work, as described in the methods section, does not fully meet these requirements.

Table 3.1. Position of $ZrSe_2$ and Se peaks

Time (Days after exfoliation)	E_g	A_{1g}	Se
1	146 .0 ± 0.9	193.47 ± 0.1	254.9 ± 0.5
2	143.8 ± 1.3	193.75 ± 0.02	253.8 ± 0.9
5	144.9 ± 1.3	193.02 ± 0.02	236.2 ± 2.5 253.9 ± 0.7
8	144.2 ±0.6	192.56 ±0.01	253.08 ± 0.2
12	145.1 ± 0.8	193.27 ± 0.02	236.1 ± 2.7 254.3 ± 0.7
30			233.91 ± 0.15 253.45 0.5

Based on the collected spectrum, the Se peak shown in Figure 3.18c can be fitted as an envelope of one weaker peak at (233.9 ± 0.2) cm^{-1} and a more distinct one at (253.45 ± 0.05) cm^{-1}. The first peak might be attributed to the bond-stretching vibrational mode of ordered Se chains in t-Se, which typically occurs at 236 cm^{-1}, while the second corresponds to the bond stretching vibrational mode of Se rings[46]. Raman spectroscopy thus confirms the Se-rich nature

of the blisters and suggests that they may be a mixture of ordered chains and disordered rings, but additional structural analyses would be required for confirmation.

The spectra were acquired again two months later, varying the absolute power from 0.175 to 0.7 mW (corresponding to 0.25 to 1% of the nominal laser intensity), as reported in Figure 3.18d, over the 100-500 cm^{-1} range. The two Se peaks are clearly visible and well separated; the first one located around 234-235 cm^{-1} and the other one around 252-253 cm^{-1}. The relative intensities of the two peaks change with laser power, in agreement with previous reports in literature. The response was analysed also under a below-bandgap excitation laser (785 nm), which required a higher power intensity of 6 mW. The spectrum shows a peak at (235.6 ± 0.2) cm^{-1} and the other one at (251.9 ± 0.9) cm^{-1} where the 251 nm peak is associated with a disordered chain structure. A spectral profile similar to that reported in Figure 3.18c was also observed at several intensities on other flakes on the same chip. However, for the reasons discussed above, these results cannot be considered conclusive about the nature of selenium within the blisters.

3.4.6 Chemical status of the exposed $ZrSe_2$ surface

Figure 3.19a presents high-resolution XPS spectra of the Zr 3*d* and Se 3*d* core levels for a freshly exfoliated $ZrSe_2$ surface, compared with the same flake after 1 hour of air exposure. The surface of the freshly exfoliated crystal is dominated by the Zr-Se chemical state, as detected in both the Zr $3d_{5/2}$ and Se *3d5/2* spectra at BE positions of 181.2 eV and 53.8 eV, respectively[47]. A secondary chemical state in the Zr 3*d* spectrum appears at 182.5 eV, attributed to Zr-O[48], indicating minor oxidation even though exfoliation was performed under an N_2 atmosphere. A small Zr 4*s* peak is also observed at 52.4 eV[49].

After 1 hour of exposure to ambient air, further oxidation is clearly evident from the increased intensity of the Zr-O peak. Additionally, the Se 3*d* spectrum displays a new peak at BE of 54.9 eV, associated with the formation of Se-Se compound[50]. These XPS results are consistent with the EDX analysis, which reveals Se-rich blisters on the oxidized ZrO_2 surface. The bulk crystal oxidized over prolonged air exposure shows surface oxidation, as indicated by the XPS data in Figure 3.19b. This spectrum reveals the presence of zirconium oxide (Zr-O), along with signals corresponding to elemental selenium (Se-Se). Notably, the core-level peaks in the sample are shifted by ~1.0 eV to higher binding energy (BE) due to the formation of native ZrO_2.

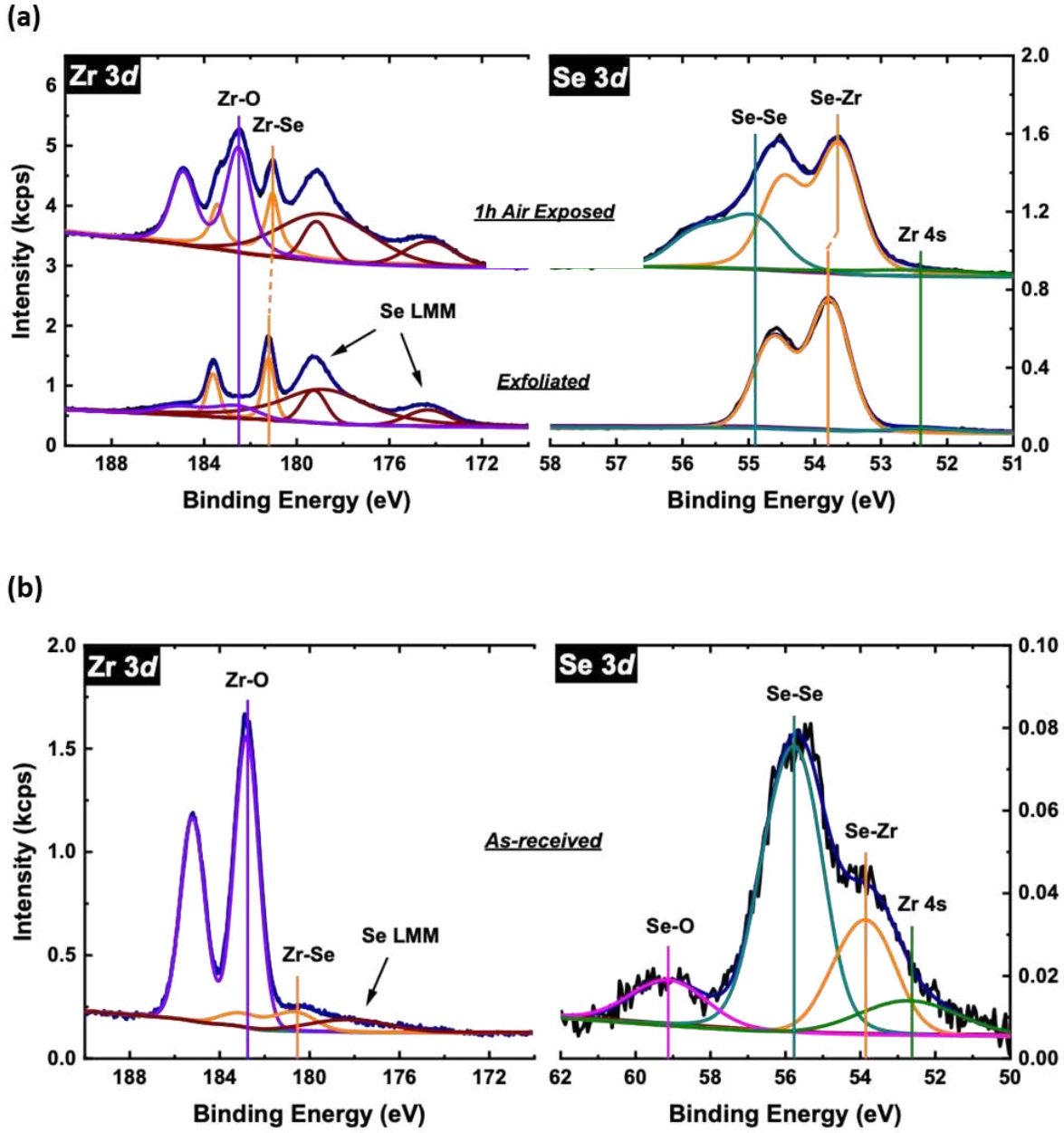

Figure 3.19: Surface chemical evolution of $ZrSe_2$ upon air exposure. (a) High-resolution XPS spectra of Zr 3*d* and Se 3*d* core levels in bulk $ZrSe_2$ comparing a freshly exfoliated flake and the same flake after 1 hour of air exposure. The Zr 3*d* core level overlaps with Se LMM Auger peaks. (b) Zr 3*d* and Se 3*d* XPS core-level spectra of the oxidized surface of $ZrSe_2$ crystal.

3.4.7 Theoretical insight into Se segregation via DFT simulations

To provide further insight into the experimental observation of Se-rich protrusions and nanowire formation, DFT calculations modelling the early and advanced stages of oxidation on $ZrSe_2$ were performed. The simulations consider increasing concentration of oxygen atoms adsorbed into a $ZrSe_2$, representing the progression of ambient exposure. The simulation results

are illustrated in Figure 3.20, which shows how oxygen incorporation leads to progressive Se detachment and clustering.

Oxygen atoms preferentially adsorb onto undercoordinated Zr atoms, especially at edge sites and surface defects. This is in line with STM/STS and DFT results showing that atomic-scale disorder in $ZrSe_2$ can locally alter the electronic landscape, potentially enhancing the reactivity of defective and edge regions[51]. This leads to a progressive weakening and eventual breaking of nearby Zr-Se bonds. These simulations indicate that as oxygen concentration increases, oxygen penetrates the top layers of $ZrSe_2$, forming Zr-O bonds and destabilizing the Zr-Se lattice. These effects emerge at relatively low oxygen coverage, consistent with the experimental observation that degradation begins within seconds-to-minutes of ambient air exposure (see STM results in Section 3.4.1 and XPS data in Section 3.4.6).Under extended oxidation, detached selenium atoms migrate across the surface and cluster atop or near the ZrO_2 regions, consistent with the poor wettability of Se on oxides and the phase-separated structures seen in cross-sectional TEM and EDX analysis. The simulations show the emergence of stable Se-Se bonds, supporting this clustering behaviour.

These findings correlate with and explain the experimental results, where hemispherical Se blisters and nanowires were observed via AFM, SEM, STM, and STEM. Experimentally, Se-rich protrusions were formed as early as 3 hours post-exfoliation (Figure 3.1d), with a significant increase in density and size after 1 day (Figure 3.2a). Over longer periods (1-4 months), these features evolve into larger aggregates and eventually Se nanowires (Figures 3.13 and 3.15). Thus, the Se clustering begins within hours and continues progressively over weeks to months.

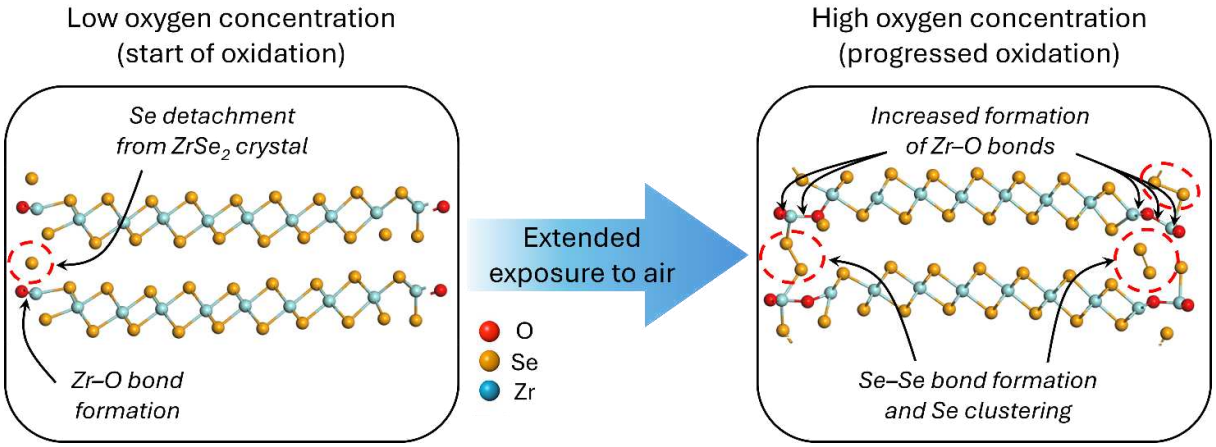

Figure 3.20. DFT simulation of oxidation progression in $ZrSe_2$. Density functional theory models showing how oxygen incorporation disrupts Zr-Se bonds, resulting in the progressive detachment and clustering of Se atoms. Left: initial stage with low oxygen concentration showing Zr-O bond formation and Se atoms beginning to displace. Right: advanced stage with higher oxygen concentration forming Se-rich clusters detached from the $ZrSe_2$ lattice.

3.4.8 Encapsulation strategy: Suppressing oxidation and preserving material's integrity

The previous sections highlight that preventing or limiting the degradation process is critical for $ZrSe_2$, both for fundamental studies and for device fabrication.

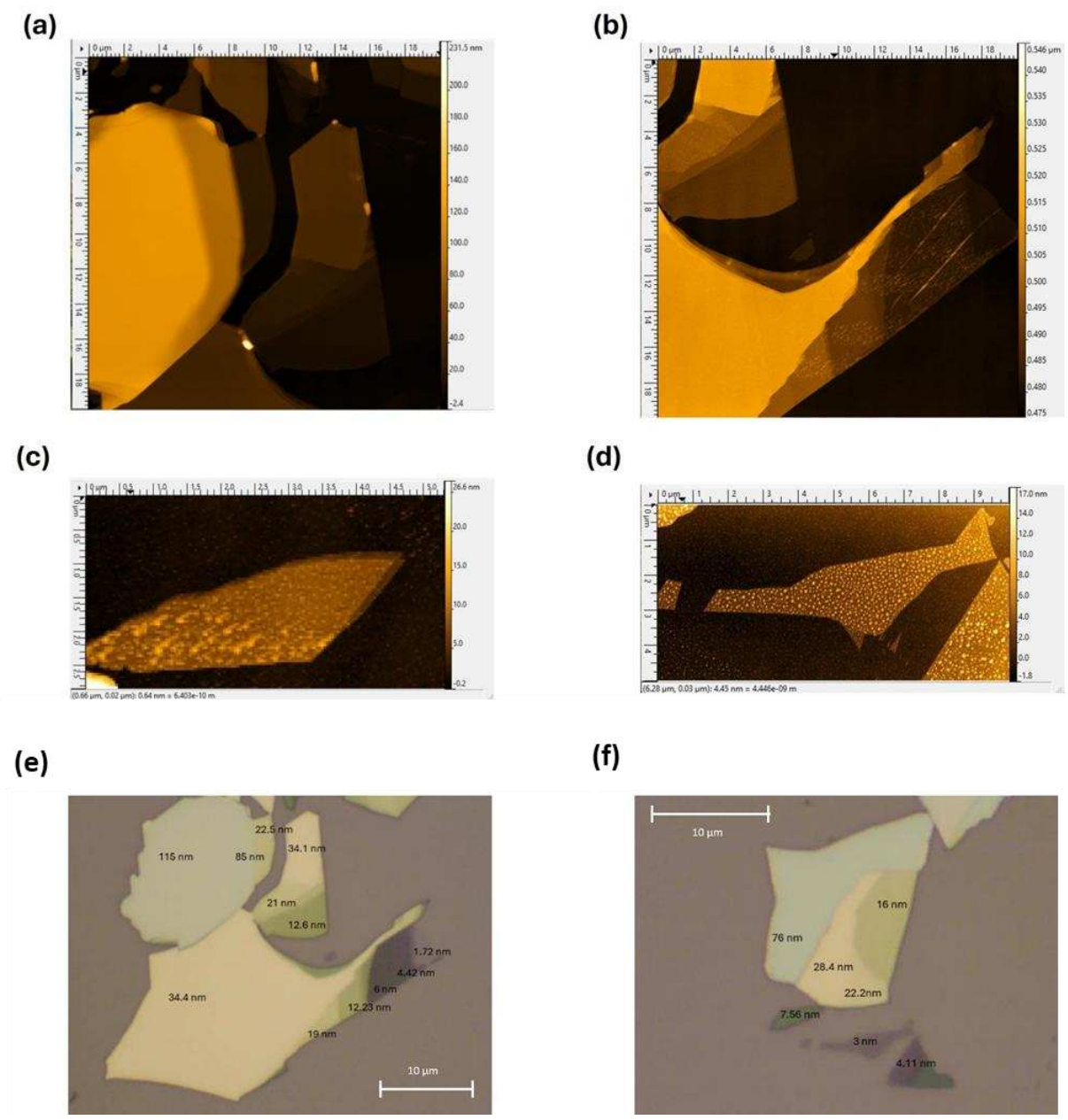

Figure 3.21: (a), (b), (c), (d) AFM images of $ZrSe_2$ flakes of different thicknesses exfoliated on Si/SiO_2 substrates and encapsulated with ZrO_2, acquired 2 months after the exfoliation. (e), (f) Optical images of encapsulated multi-stepped flakes, where the colour is linked with the thickness of $ZrSe_2$.

To address this, the following encapsulation strategy is proposed. As mentioned in the methods section, after exfoliating $ZrSe_2$ flakes on Si/SiO_2 (85 nm) substrates in a glovebox, a ZrO_2 film (2 nm nominal thickness) was e-beam evaporated to encapsulate the samples. Air exposure is

limited to 40 seconds solely to mount them in the evaporator. ZrO_2 was chosen because it minimizes compatibility issues between the semiconductor and the dielectric layer, as both materials share Zr as a constituent.

The reliability of the process is initially evaluated by AFM measurements performed two months after encapsulation on multi-stepped flake, see Figure 3.21. AFM images in Figure 3.21a and 3.21b do not show any appreciable signs of degradation in the regions thicker than ~ 12 nm. However, the higher density of protrusions observed in thinner flakes ($\lesssim 6$ nm) in Figure 3.21c and 3.21d, is likely due to their brief exposure to air prior to encapsulation, which is more critical for thin layers because of their higher surface-to-volume ratio and the greater presence of structural defects and edge sites. Moreover, possible incomplete coverage of the flake edges by the ZrO_2 layer, along with structural imperfections in the oxide, facilitates oxidation throughout the entire thickness, unlike in thicker flakes. AFM on encapsulated flakes helps in qualitatively linking the thickness of the $ZrSe_2$ flakes to their apparent colour on 85 nm of SiO_2 under optical microscopy, which is a useful way to rapidly identify thin flakes - see Figure 3.21e and 3.21f.

Raman spectroscopy, also performed a couple of months after fabrication, provides more quantitative and precise information than AFM. Raman spectra reveal signal from $ZrSe_2$ regions of different thickness. To have a visual understanding of the situation, some spectra are displayed in Figure 3.22, while the whole set of data is collected in Table 3.2. The thickness values reported in the respective column include the ZrO_2 layer thickness. For flakes with thickness $\gtrsim 4.42$ nm, both E_g and A_{1g} mode are detected. In contrast, A_{1g} peak alone is visible for the 4.11 nm thick flake and none of the two peaks can be identified for the 3 nm-thick flake[15]. The oxidation status of the different parts can be qualitatively identified by examining the A_{2u} peak, as previously asserted. Focusing on the position of the peak, a transition from the A_{2u} to the Se peak is observed, as the thickness of $ZrSe_2$ decreases and the respective degradation increases. Precisely, this additional peak is found at ~262–264 cm^{-1} in regions thicker than 6 nm. At the critical thickness of 6 nm, it shifts to ~260 cm^{-1}, and for thinner flakes, it further shifts to ~252–254 cm^{-1}.

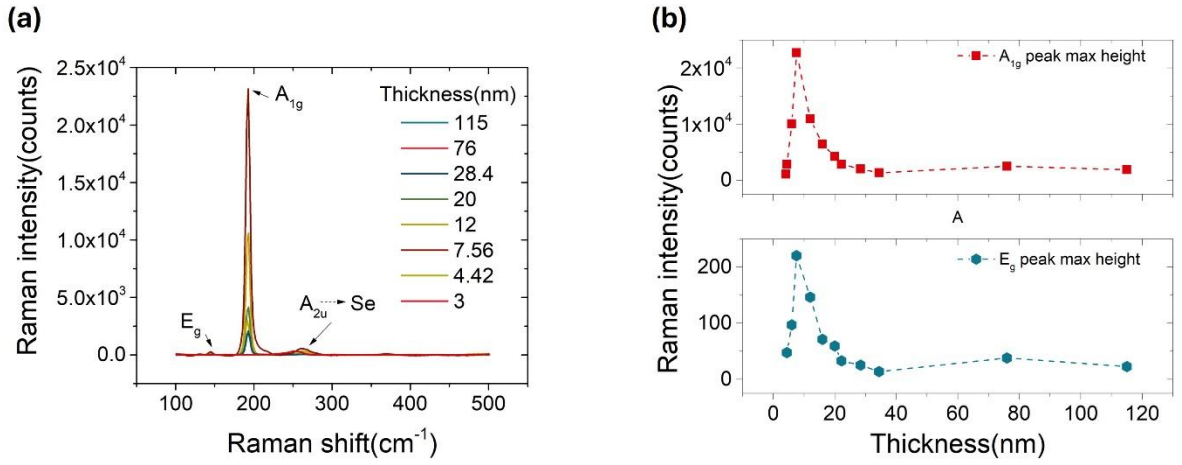

Figure 3.22: Thickness dependence of $ZrSe_2$ Raman modes. (a) Raman spectra of $ZrSe_2$ flakes with varying thicknesses (3-115 nm), showing the evolution of the E_g and A_{1g} peaks. (b) Maximum intensity

of A_{1g} (top) and E_g (bottom) Raman peaks as a function of flake thickness, extracted from the spectra in (a). Both modes exhibit strong thickness-dependent behaviour.

Figure 3.22b, on the other hand, displays the peaks' height of the two vibrational modes as a function of the thickness of the flake. The peaks' intensity does not have a monotonic behaviour but instead shows a peak-shape profile. Moving from 115 nm down to thinner flakes, it increases reaching a maximum for ~8 nm thick flakes, and then it decreases again until the peaks are not detectable anymore. Moreover, Raman signal of bulk $ZrSe_2$ is weaker than that of 4.42 nm thick flake. This nonmonotonic dependence of Raman intensities on the sample thickness has been previously observed in graphene[52] and in other TMDs, like MoS_2[53], $TaSe_2$[54], and others[55].

Table 3.2. Thickness dependence of $ZrSe_2$ Raman peaks

	E_g			A_{1g}			Additional peak ($A_{2u} \rightarrow$ Se)		
Thickness (nm)	**FWHM (cm^{-1})**	**Max height (counts)**	**Position (cm^{-1})**	**FWHM (cm^{-1})**	**Max height (counts)**	**Position (cm^{-1})**	**FWHM (cm^{-1})**	**Max height (counts)**	**Position (cm^{-1})**
115	6.2	22.6	144.39 ± 1.1	6.15±0.04	1893± 8	192.69 ±0.02	23 ± 3	55 ± 4	263.2 ±0.8
76	5.67	34.6	144.7 ±1.6	6.49 ± 0.05	2518 ± 17	192.57 ± 0.02	20 ± 4	55 ± 10	262.6 ± 1.7
34.4	4.21	13.76	145.2 ± 1.4	6.29 ± 0.04	1338 ± 7	192.69 ± 0.02	18 ±2	33 ± 4	262.3 ± 1.1
28.4	7.07	27.14	145.5 ± 1.5	6.43 ± 0.05	2031 ± 13	192.746 ± 0.19	17 ± 4	35 ± 8	263.8 ±1.9
22.2	5.047	32.89	145.1 ±1.6	6.36 ± 0.05	2851 ± 19	192.71 ± 0.03	16± 4	52 ± 11	262.8 ± 1.8
20	6.20	59.30	144 ± 1	6.10 ± 0.04	4241 ± 19	192.56 ± 0.02	19.6 ± 2.5	96 ± 10	263.4 ± 1.1
16	4.89	71.02	145.1 ± 1.5	6.45 ± 0.05	6435 ± 40	192.62 ±0.03	16 ± 4	114 ± 25	262.8 ± 1.8
12	7.67	172.79	144.8 ± 0.9	5.99 ± 0.03	10942 ± 49	192.414 ± 0.024	19 ± 4	216 ± 28	264.9 ± 1.2
7.56	6.30	267.05	144.5 ± 2.2	6.89 ±0.06	22742 ± 164	192.36	22.34869	488 ± 99	262.9 ± 1.9
6	7.80	97.12	143.5 ± 2.3	6.89 ± 0.05	10036 ± 60	192.14 ± 0.03	26.5 ± 2.1	397 ± 30	260.5 ± 1.1
4.42	7.78	47.55	141.7 ± 1.6	7.56 ± 0.07	2856 ± 21	191.59 ± 0.03	27.2 ± 1.4	258 ± 11	254.1 ± 0.6
4.11				9.42 ± 0.02	1091 ± 28	191.38 ± 0.13	11 ± 0.15	183 ± 19	252.1 ± 1.1
3							20 ± 3	320 ± 24	252.9 ± 1.6

It is attributed to optical interference effects arising from multiple reflections of both the excitation laser and the emitted Raman signal within the material, at the air interface, and at the SiO_2 substrate. The presence of the oxide layer on top of the silicon substrate leads to optical field enhancement, which strengthens the Raman signal of thinner flakes and results in a peak when constructive interference occurs.

3.4.9 $ZrSe_2$-based field-effect transistor

As described in the methods section, exploratory back gated field effect transistors (FETs) were fabricated by depositing Cr/Au (15/150 nm) contact leads by e-beam evaporation on the encapsulated $ZrSe_2$ flakes exfoliated on Si/SiO_2 (85nm) substrates. The encapsulation layer is expected to act as a thin tunnel barrier for charge injection between the metal contacts and the $ZrSe_2$ flakes. The schematic of the device along with the measurement setup is depicted in Figure 3.23a. Drain current vs. drain voltage (I_{ds}-V_{ds}) and drain current vs. gate voltage (I_{ds}-V_{gs}) measurements were performed at room temperature in the dark.

The inset of Figure 3.23b shows the optical image of one of the devices with a channel length of L ~ 2.5 µm and a width of W ~ 7.5 µm. The I_d-V_{ds} characteristic in Figure 3.23b, obtained by sweeping V_{ds} from -1 to 1 V, shows a non-linear and asymmetric behaviour, suggesting asymmetric Schottky-like barriers at the metal contacts[56,57]. However, a maximum current of about 1 µA is reached at V_{ds} = 1 V. Figure 3.23c displays the output curves, obtained by sweeping V_{ds} from –1 to 1 V and stepping V_{gs} from –40 to 40 V. Positive gate biases results in a higher current compared to the negative ones and a more symmetric shape, indicating n-type conduction in $ZrSe_2$, despite the weak gate dependence. The n-type current transport is further confirmed by the transfer curve in Figure 3.23d, obtained by double sweeping the gate bias from 40 to –40 V at a fixed V_{ds} = 0.5 V. The gate current is on the order of pA, which indicates that there is no gate leakage. A relatively high mobility of $\mu = (1.67 \pm 0.17)$ $cm^2V^{-1}s^{-1}$, comparable with other works on $ZrSe_2$[2], is calculated by the slope of the linear fit of the upper part of the transfer curve at positive biases, using equation 2.12 , where C_{ox} is the oxide capacitor per unit area ($C_{ox} = 4.06 \times 10^{-8}$ F/cm^2). Despite this result, the device exhibits a noisy signal, a limited I_{on}/I_{off} ratio and a pronounced hysteresis width of about 60 V. Hysteresis refers to the difference between the forward and reverse electrical sweeps, indicating that the device response depends on its biasing history. Operationally, it is commonly quantified as the maximum voltage separation between the two branches at a fixed current level, and it is commonly associated with charge trapping/detrapping at the dielectric interface and slow surface processes in 2D transistors. Further insight into these effects is provided in the following chapter.

These transport features can be attributed to intrinsic defects in the $ZrSe_2$ flake, and to the defective interfaces with both SiO_2 and Cr/Au metal contacts[58,59]. Recent atomic-scale STM/STS and DFT studies have provided valuable insight into how defects and edge configurations can impact the electronic landscape of $ZrSe_2$. In particular, simple Zr and Se vacancies were found not to introduce deep in-gap trap states, whereas grain boundaries can shift the Fermi level and modify band alignment without destroying the semiconducting gap.

In contrast, zigzag edge terminations may generate midgap electronic states, which could become relevant for leakage currents and contact behavior in nanoscale transistors[51].

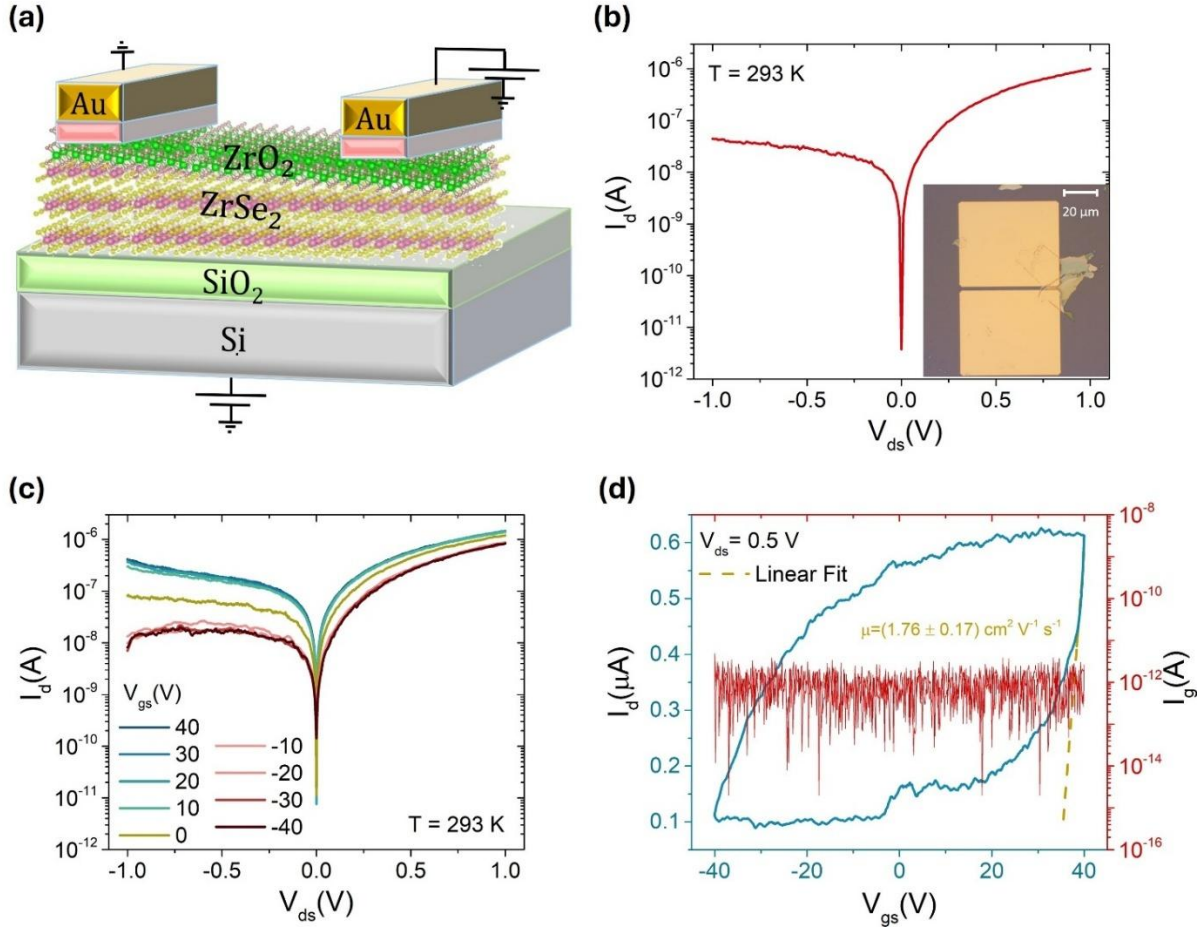

Figure 3.23: Back-gated $ZrSe_2$ FET device. (a) Schematic illustration of the $ZrSe_2$ FET with the electrical measurement set up. (b) I_{ds}-V_{ds} characteristic measured at 0 V gate bias in the dark at room temperature. The inset shows the optical image of the device, with a channel length of ~2.5 µm. (c) Output curves under different gate voltages. (d) Transfer characteristic obtained by double sweeping V_{gs} in the (-40, 40) V range at a fixed V_{ds} = 0.5 V (right axis). Left axis refers to the leakage current through the gate oxide, which is on the order of picoamperes.

Trapped charges and interfacial roughness at the semiconductor/SiO_2 interface can further degrade the device performance and compromise electrostatic control[60]. Moreover, the charge injection mechanism through the ZrO_2 encapsulating layer at the metal contacts may also limit overall device performance.

Although encapsulation mitigates the oxidation process, these initial results highlight the need to further address material and interface quality issues. Possible strategies include fully inert-atmosphere fabrication to prevent air exposure, the use of thinner flakes to enhance gate modulation, optimization of the ZrO_2 deposition process to minimize interface damage, and improved contact design to facilitate charge injection and device stability. A deeper discussion of trapping-related phenomena and interface-limited transport in 2D transistors is provided in the next chapter.

References

(1) Yang, J.; Liu, X.; Dong, Q.; Shen, Y.; Pan, Y.; Wang, Z.; Tang, K.; Dai, X.; Wu, R.; Jin, Y.; Zhou, W.; Liu, S.; Sun, J. Oxidations of Two-Dimensional Semiconductors: Fundamentals and Applications. *Chin. Chem. Lett.* **2022**, *33* (1), 177–185. https://doi.org/10.1016/j.cclet.2021.06.078.

(2) Mleczko, M. J.; Zhang, C.; Lee, H. R.; Kuo, H.-H.; Magyari-Köpe, B.; Moore, R. G.; Shen, Z.-X.; Fisher, I. R.; Nishi, Y.; Pop, E. HfSe 2 and ZrSe 2 : Two-Dimensional Semiconductors with Native High-k Oxides. *Sci. Adv.* **2017**, *3*, e1700481. https://doi.org/10.1126/sciadv.1700481.

(3) Illarionov, Y. Y.; Knobloch, T.; Jech, M.; Lanza, M.; Akinwande, D.; Vexler, M. I.; Mueller, T.; Lemme, M. C.; Fiori, G.; Schwierz, F.; Grasser, T. Insulators for 2D Nanoelectronics: The Gap to Bridge. *Nat. Commun.* **2020**, *11* (1), 3385. https://doi.org/10.1038/s41467-020-16640-8.

(4) Molle, A.; Grazianetti, C.; Tao, L.; Taneja, D.; Alam, Md. H.; Akinwande, D. Silicene, Silicene Derivatives, and Their Device Applications. *Chem. Soc. Rev.* **2018**, *47* (16), 6370–6387. https://doi.org/10.1039/C8CS00338F.

(5) Huang, Y.; Qiao, J.; He, K.; Bliznakov, S.; Sutter, E.; Chen, X.; Luo, D.; Meng, F.; Su, D.; Decker, J.; Ji, W.; Ruoff, R. S.; Sutter, P. Interaction of Black Phosphorus with Oxygen and Water. *Chem. Mater.* **2016**, *28* (22), 8330–8339. https://doi.org/10.1021/acs.chemmater.6b03592.

(6) Hou, F.; Zhang, D.; Sharma, P.; Singh, S.; Wu, T.; Seidel, J. Oxidation Kinetics of WTe2 Surfaces in Different Environments. *ACS Appl. Electron. Mater.* **2020**, *2* (7), 2196–2202. https://doi.org/10.1021/acsaelm.0c00380.

(7) Li, Q.; Zhou, Q.; Shi, L.; Chen, Q.; Wang, J. Recent Advances in Oxidation and Degradation Mechanisms of Ultrathin 2D Materials under Ambient Conditions and Their Passivation Strategies. *J. Mater. Chem. A* **2019**, *7* (9), 4291–4312. https://doi.org/10.1039/C8TA10306B.

(8) Mirabelli, G.; McGeough, C.; Schmidt, M.; McCarthy, E. K.; Monaghan, S.; Povey, I. M.; McCarthy, M.; Gity, F.; Nagle, R.; Hughes, G.; Cafolla, A.; Hurley, P. K.; Duffy, R. Air Sensitivity of MoS2, MoSe2, MoTe2, HfS2, and HfSe2. *J. Appl. Phys.* **2016**, *120* (12), 125102. https://doi.org/10.1063/1.4963290.

(9) Wang, G.; Pandey, R.; Karna, S. P. Physics and Chemistry of Oxidation of Two-Dimensional Nanomaterials by Molecular Oxygen. *WIREs Comput. Mol. Sci.* **2017**, *7* (1), e1280. https://doi.org/10.1002/wcms.1280.

(10) Li, P.; Zhang, D.; Liu, J.; Chang, H.; Sun, Y.; Yin, N. Air-Stable Black Phosphorus Devices for Ion Sensing. *ACS Appl. Mater. Interfaces* **2015**, *7* (44), 24396–24402. https://doi.org/10.1021/acsami.5b07712.

(11) Long, E.; O'Brien, S.; Lewis, E. A.; Prestat, E.; Downing, C.; Cucinotta, C. S.; Sanvito, S.; Haigh, S. J.; Nicolosi, V. An in Situ and Ex Situ TEM Study into the Oxidation of Titanium (IV) Sulphide. *Npj 2D Mater. Appl.* **2017**, *1* (1), 1–9. https://doi.org/10.1038/s41699-017-0024-4.

(12) Hwang, J.; Mun, J.; Lee, K.-T.; Lee, T.; Kim, J.; Min, J.; Park, K. Impact of Humidity on Long-Term Stability of HfS2 Grown on Sapphire Substrate by Chemical Vapor Deposition and Strategies to Prevent Native Oxidation. *Mater. Sci. Semicond. Process.* **2025**, *192*, 109471. https://doi.org/10.1016/j.mssp.2025.109471.

(13) Chae, S. H.; Jin, Y.; Kim, T. S.; Chung, D. S.; Na, H.; Nam, H.; Kim, H.; Perello, D. J.; Jeong, H. Y.; Ly, T. H.; Lee, Y. H. Oxidation Effect in Octahedral Hafnium Disulfide Thin Film. *ACS Nano* **2016**, *10* (1), 1309–1316. https://doi.org/10.1021/acsnano.5b06680.

(14) Zhang, M.; Zhu, Y.; Wang, X.; Feng, Q.; Qiao, S.; Wen, W.; Chen, Y.; Cui, M.; Zhang, J.; Cai, C.; Xie, L. Controlled Synthesis of ZrS2 Monolayer and Few Layers on Hexagonal Boron Nitride. *J. Am. Chem. Soc.* **2015**, *137* (22), 7051–7054. https://doi.org/10.1021/jacs.5b03807.

(15) Mañas-Valero, S.; García-López, V.; Cantarero, A.; Galbiati, M. Raman Spectra of ZrS2 and ZrSe2 from Bulk to Atomically Thin Layers. *Appl. Sci.* **2016**, *6* (9), 264. https://doi.org/10.3390/app6090264.

(16) Chang, L.; Frank, D. J.; Montoye, R. K.; Koester, S. J.; Ji, B. L.; Coteus, P. W.; Dennard, R. H.; Haensch, W. Practical Strategies for Power-Efficient Computing Technologies. *Proc. IEEE* **2010**. https://doi.org/10.1109/JPROC.2009.2035451.

(17) Kheirabadi, S. J.; Behzadi, F.; Gity, F.; Hurley, P. K.; Khorrami, S. K.; Behroozi, M.; Sanaee, M.; Ansari, L. Defective ZrSe2: A Promising Candidate for Spintronics Applications. *J. Phys. Condens. Matter* **2023**, *36* (13), 135501. https://doi.org/10.1088/1361-648X/ad13d3.

(18) Foucher, A. C.; Mortelmans, W.; Bing, W.; Sofer, Z.; Jaramillo, R.; Ross, F. M. Structural Changes in HfSe2 and ZrSe2 Thin Films with Various Oxidation Methods. *J. Mater. Chem. C* **2024**, *12* (26), 9677–9684. https://doi.org/10.1039/D3TC04698B.

(19) *XPS OASIS*. https://xpsoasis.org/ (accessed 2025-05-30).

(20) Smidstrup, S.; Markussen, T.; Vancraeyveld, P.; Wellendorff, J.; Schneider, J.; Gunst, T.; Verstichel, B.; Stradi, D.; Khomyakov, P. A.; Vej-Hansen, U. G.; Lee, M.-E.; Chill, S. T.; Rasmussen, F.; Penazzi, G.; Corsetti, F.; Ojanperä, A.; Jensen, K.; Palsgaard, M. L. N.; Martinez, U.; Blom, A.; Brandbyge, M.; Stokbro, K. QuantumATK: An Integrated Platform of Electronic and Atomic-Scale Modelling Tools. *J. Phys. Condens. Matter* **2019**, *32* (1), 015901. https://doi.org/10.1088/1361-648X/ab4007.

(21) van Setten, M. J.; Giantomassi, M.; Bousquet, E.; Verstraete, M. J.; Hamann, D. R.; Gonze, X.; Rignanese, G.-M. The PseudoDojo: Training and Grading a 85 Element Optimized Norm-Conserving Pseudopotential Table. *Comput. Phys. Commun.* **2018**, *226*, 39–54. https://doi.org/10.1016/j.cpc.2018.01.012.

(22) Zheng, X. H.; Zheng, J. X. On the Use of Monkhorst–Pack Scheme to Evaluate Superconductivity and the Issue of Umklapp Electron–Phonon Interactions. *Phys. Chem. Chem. Phys.* **2023**, *25* (18), 13049–13060. https://doi.org/10.1039/D3CP01053H.

(23) Grimme, S.; Antony, J.; Ehrlich, S.; Krieg, H. A Consistent and Accurate Ab Initio Parametrization of Density Functional Dispersion Correction (DFT-D) for the 94 Elements H-Pu. *J. Chem. Phys.* **2010**, *132* (15), 154104. https://doi.org/10.1063/1.3382344.

(24) Park, J. H.; Vishwanath, S.; Liu, X.; Zhou, H.; Eichfeld, S. M.; Fullerton-Shirey, S. K.; Robinson, J. A.; Feenstra, R. M.; Furdyna, J.; Jena, D.; Xing, H. G.; Kummel, A. C. Scanning Tunneling Microscopy and Spectroscopy of Air Exposure Effects on Molecular Beam Epitaxy Grown WSe2 Monolayers and Bilayers. *ACS Nano* **2016**, *10* (4), 4258–4267. https://doi.org/10.1021/acsnano.5b07698.

(25) Budania, P.; Baine, P.; Montgomery, J.; McGeough, C.; Cafolla, T.; Modreanu, M.; McNeill, D.; Mitchell, N.; Hughes, G.; Hurley, P. Long-Term Stability of Mechanically Exfoliated MoS2 Flakes. *MRS Commun.* **2017**, *7* (4), 813–818. https://doi.org/10.1557/mrc.2017.105.

(26) Liu, H.; Han, N.; Zhao, J. Atomistic Insight into the Oxidation of Monolayer Transition Metal Dichalcogenides: From Structures to Electronic Properties. *RSC Adv.* **2015**, *5* (23), 17572–17581. https://doi.org/10.1039/c4ra17320a.

(27) KC, S.; Longo, R. C.; Wallace, R. M.; Cho, K. Surface Oxidation Energetics and Kinetics on MoS2 Monolayer. *J. Appl. Phys.* **2015**, *117* (13), 135301. https://doi.org/10.1063/1.4916536.

(28) Ren, M.-Q.; Han, S.; Fan, J.-Q.; Wang, L.; Wang, P.; Ren, W.; Peng, K.; Li, S.; Wang, S.-Z.; Zheng, F.-W.; Zhang, P.; Li, F.; Ma, X.; Xue, Q.-K.; Song, C.-L. Semiconductor–Metal Phase Transition and Emergent Charge Density Waves in 1T-ZrX2 (X = Se, Te) at the Two-Dimensional Limit. *Nano Lett.* **2022**, *22* (1), 476–484. https://doi.org/10.1021/acs.nanolett.1c04372.

(29) Reshak, A. H.; Auluck, S. Theoretical Investigation of the Electronic and Optical Properties of ZrX2 (X=S, Se and Te). *Phys. B Condens. Matter* **2004**, *353* (3), 230–237. https://doi.org/10.1016/j.physb.2004.10.001.
(30) Jia, Z.; Zeng, W.; Zhang, Y.; Shi, C.; Quan, B.; Wu, J. The Color Changes and Tensile Properties of Oxidized Ti–6A1–2Mo–1.5Cr–2Zr–2Sn–2Nb Alloy. *J. Alloys Compd.* **2015**, *640*, 488–496. https://doi.org/10.1016/j.jallcom.2015.03.227.
(31) Cruz, A.; Mutlu, Z.; Ozkan, M.; Ozkan, C. S. Raman Investigation of the Air Stability of 2H Polytype HfSe2 Thin Films. *MRS Commun.* **2018**, *8* (3), 1191–1196. https://doi.org/10.1557/mrc.2018.185.
(32) Lu, W.; Li, Z.; Feng, M.; Yan, H.-J.; Yan, B.; Hu, L.; Zhang, X.; Liu, S.; Hu, J.-S.; Xue, D.-J. Melt- and Air-Processed Selenium Thin-Film Solar Cells. *Sci. China Chem.* **2022**, *65* (11), 2197–2204. https://doi.org/10.1007/s11426-022-1332-3.
(33) Berger, L. I. *Semiconductor Materials*; CRC Press: London, 2020. https://doi.org/10.1201/9780138739966.
(34) Xia, Y.; Yang, P.; Sun, Y.; Wu, Y.; Mayers, B.; Gates, B.; Yin, Y.; Kim, F.; Yan, H. One-Dimensional Nanostructures: Synthesis, Characterization, and Applications. *Adv. Mater.* **2003**, *15* (5), 353–389. https://doi.org/10.1002/adma.200390087.
(35) Gates, B.; Mayers, B.; Cattle, B.; Xia, Y. Synthesis and Characterization of Uniform Nanowires of Trigonal Selenium. *Adv. Funct. Mater.* **2002**, *12* (3), 219–227. https://doi.org/10.1002/1616-3028(200203)12:3%3C219::AID-ADFM219%3E3.0.CO;2-U.
(36) Liu, L.; Peng, Q.; Li, Y. Preparation of Monodisperse Se Colloid Spheres and Se Nanowires Using Na2SeSO3 as Precursor. *Nano Res.* **2008**, *1* (5), 403–411. https://doi.org/10.1007/s12274-008-8040-5.
(37) Chen, H.; Shin, D.-W.; Nam, J.-G.; Kwon, K.-W.; Yoo, J.-B. Selenium Nanowires and Nanotubes Synthesized via a Facile Template-Free Solution Method. *Mater. Res. Bull.* **2010**, *45* (6), 699–704. https://doi.org/10.1016/j.materresbull.2010.02.016.
(38) Rahman, A.; Guisbiers, G. Synthesis of Trigonal Selenium Rods, Wires and Fibers by Pulsed Laser Ablation in Ethanol. *Mater. Lett.* **2024**, *377*, 137476. https://doi.org/10.1016/j.matlet.2024.137476.
(39) Yang, Y.; Niu, G.; Lu, J.; Geng, X.; He, R.; Zhang, Y.; Li, S.; Zhang, Y.; Sun, L.; Gao, L.; Cai, J. From 2D AgTe Monolayer to 1D AgTe Nanowires: Tellurium Concentration Modulated Structural and Electronic Properties Transformation. *Small Methods* **2024**, e2402025. https://doi.org/10.1002/smtd.202402025.
(40) Niu, G.; Lu, J.; Gao, L.; Geng, J.; Xiong, W.; Zhang, Y.; Zhang, H.; Li, S.; Yang, Y.; Fu, B.; Zhang, Y.; Cai, J. Atomically Precise Fabrication of Ultranarrow Zigzag CuTe Nanoribbons via Dimensional Regulation. *ACS Nano* **2025**, *19* (3), 3656–3664. https://doi.org/10.1021/acsnano.4c14204.
(41) Ghosh, B.; Sahu, M.; Samanta, D.; Mukherjee, G. D. Strain-Induced Structural and Electronic Phase Transitions in ZrSe2: High Pressure X-Ray Diffraction and Raman Studies. *Bull. Mater. Sci.* **2022**, *45* (4), 221. https://doi.org/10.1007/s12034-022-02821-2.
(42) Oliver, S. M.; Fox, J. J.; Hashemi, A.; Singh, A.; Cavalero, R. L.; Yee, S.; Snyder, D. W.; Jaramillo, R.; Komsa, H.-P.; Vora, P. M. Phonons and Excitons in ZrSe2–ZrS2 Alloys. *J. Mater. Chem. C* **2020**, *8* (17), 5732–5743. https://doi.org/10.1039/D0TC00731E.
(43) Alsulami, A.; Alharbi, M.; Alsaffar, F.; Alolaiyan, O.; Aljalham, G.; Albawardi, S.; Alsaggaf, S.; Alamri, F.; Tabbakh, T. A.; Amer, M. R. Lattice Transformation from 2D to Quasi 1D and Phonon Properties of Exfoliated ZrS2 and ZrSe2. *Small Weinh. Bergstr. Ger.* **2023**, *19* (11), e2205763. https://doi.org/10.1002/smll.202205763.

(44) Goldan, A. H.; Li, C.; Pennycook, S. J.; Schneider, J.; Blom, A.; Zhao, W. Molecular Structure of Vapor-Deposited Amorphous Selenium. *J. Appl. Phys.* **2016**, *120* (13), 135101. https://doi.org/10.1063/1.4962315.

(45) Lu, W.; Li, Z.; Feng, M.; Zheng, L.; Liu, S.; Yan, B.; Hu, J.-S.; Xue, D.-J. Structure of Amorphous Selenium: Small Ring, Big Controversy. *J. Am. Chem. Soc.* **2024**, *146* (9), 6345–6351. https://doi.org/10.1021/jacs.4c00219.

(46) Sun, L.; Chen, C.; Zhang, Q.; Sohrt, C.; Zhao, T.; Xu, G.; Wang, J.; Wang, D.; Rossnagel, K.; Gu, L.; Tao, C.; Jiao, L. Suppression of the Charge Density Wave State in Two-Dimensional 1T-TiSe2 by Atmospheric Oxidation. *Angew. Chem. Int. Ed.* **2017**, *56* (31), 8981–8985. https://doi.org/10.1002/anie.201612605.

(47) Tsipas, P.; Tsoutsou, D.; Marquez-Velasco, J.; Aretouli, K. E.; Xenogiannopoulou, E.; Vassalou, E.; Kordas, G.; Dimoulas, A. Epitaxial ZrSe2/MoSe2 Semiconductor v.d. Waals Heterostructures on Wide Band Gap AlN Substrates. *Microelectron. Eng.* **2015**, *147*, 269–272. https://doi.org/10.1016/j.mee.2015.04.113.

(48) Barreca, D.; Battiston, G. A.; Gerbasi, R.; Tondello, E.; Zanella, P. Zirconium Dioxide Thin Films Characterized by XPS. *Surf. Sci. Spectra* **2000**, *7* (4), 303–309. https://doi.org/10.1116/1.1375573.

(49) Chavez, D.; Berube, A. D.; Davis, L. M. Zirconium Disulfide Single Crystal, ZrS2(0001), Characterized by X-Ray Photoelectron Spectroscopy. *Surf. Sci. Spectra* **2025**, *32* (1), 014004. https://doi.org/10.1116/6.0004276.

(50) Yue, R.; Barton, A. T.; Zhu, H.; Azcatl, A.; Pena, L. F.; Wang, J.; Peng, X.; Lu, N.; Cheng, L.; Addou, R.; McDonnell, S.; Colombo, L.; Hsu, J. W. P.; Kim, J.; Kim, M. J.; Wallace, R. M.; Hinkle, C. L. HfSe2 Thin Films: 2D Transition Metal Dichalcogenides Grown by Molecular Beam Epitaxy. *ACS Nano* **2015**, *9* (1), 474–480. https://doi.org/10.1021/nn5056496.

(51) Jamalzadeh Kheirabadi, S.; Persichetti, L.; Ansari, L.; Anselmi, G.; Hurley, P. K.; Camilli, L.; Gity, F. Atomic-Scale Defects and Edge Engineering of $ZrSe_2$ Nanosheets: Correlated Microscopy, Spectroscopy and DFT Study with Implications for Quantum Device Applications. *ACS Appl. Nano Mater.* **2025**, *8* (43), 20848–20857. https://doi.org/10.1021/acsanm.5c03451.

(52) Wang, Y. Y.; Ni, Z. H.; Shen, Z. X.; Wang, H. M.; Wu, Y. H. Interference Enhancement of Raman Signal of Graphene. *Appl. Phys. Lett.* **2008**, *92* (4), 043121. https://doi.org/10.1063/1.2838745.

(53) Lee, C.; Yan, H.; Brus, L. E.; Heinz, T. F.; Hone, J.; Ryu, S. Anomalous Lattice Vibrations of Single- and Few-Layer MoS2. *ACS Nano* **2010**, *4* (5), 2695–2700. https://doi.org/10.1021/nn1003937.

(54) Cui, L.; He, R.; Li, G.; Zhang, Y.; You, Y.; Huang, M. Raman Spectroscopy of Optical Phonon and Charge Density Wave Modes in 1T-TiSe2 Exfoliated Flakes. *Solid State Commun.* **2017**, *266*, 21–25. https://doi.org/10.1016/j.ssc.2017.08.014.

(55) Li, S.-L.; Miyazaki, H.; Song, H.; Kuramochi, H.; Nakaharai, S.; Tsukagoshi, K. Quantitative Raman Spectrum and Reliable Thickness Identification for Atomic Layers on Insulating Substrates. *ACS Nano* **2012**, *6* (8), 7381–7388. https://doi.org/10.1021/nn3025173.

(56) Di Bartolomeo, A.; Grillo, A.; Urban, F.; Iemmo, L.; Giubileo, F.; Luongo, G.; Amato, G.; Croin, L.; Sun, L.; Liang, S.-J.; Ang, L. K. Asymmetric Schottky Contacts in Bilayer MoS $_2$ Field Effect Transistors. *Adv. Funct. Mater.* **2018**, *28* (28), 1800657. https://doi.org/10.1002/adfm.201800657.

(57) Grillo, A.; Di Bartolomeo, A. A Current–Voltage Model for Double Schottky Barrier Devices. *Adv. Electron. Mater.* **2021**, *7* (2), 2000979. https://doi.org/10.1002/aelm.202000979.

(58) Intonti, K.; Faella, E.; Viscardi, L.; Kumar, A.; Durante, O.; Giubileo, F.; Passacantando, M.; Lam, H. T.; Anastasiou, K.; Craciun, M. F.; Russo, S.; Di Bartolomeo, A. Hysteresis and Photoconductivity of Few-Layer ReSe2 Field Effect Transistors Enhanced by Air Pressure. *Adv. Electron. Mater. n/a* (n/a), 2300066. https://doi.org/10.1002/aelm.202300066.

(59) Intonti, K.; Coleman, E.; Blake, A.; Lyons, C.; Hydes, A.; Di Bartolomeo, A.; Gity, F.; Hurley, P. Role of Interface and Bulk Traps on the Capacitance-Voltage Characteristics of Ws2/Al2o3/Si Capacitors. Rochester, NY April 25, 2023. https://doi.org/10.2139/ssrn.4429239.

(60) John, J. W.; Mishra, A.; Debbarma, R.; Verzhbitskiy, I.; Goh, K. E. J. Probing Charge Traps at the 2D Semiconductor/Dielectric Interface. *Nanoscale* **2023**, *15* (42), 16818–16835. https://doi.org/10.1039/D3NR03453D.

Chapter 4

Environmental effects on charge transport and photoresponse: ReS2 as a Case Study

Pressure and temperature dependent transport and photoconductivity in few-layer ReS2-based field effect transistors

4.1 Introduction

As reported in the previous chapter, surface reactivity and interface quality critically determine the stability of 2D semiconductors and affect charge transport in device configurations. While in air-sensitive materials like $ZrSe_2$, oxidation drives irreversible structural modifications, in more stable TMDs surface interactions remain largely reversible and can instead provide an additional degree of tunability to modulate the electrical and optoelectronic performance of devices. In this context, few-layer ReS_2 field-effect transistors offer a well-suited platform to investigate how adsorbates, defect states, and contact interfaces shape the operation of TMD-based FETs under controlled environmental conditions.

By combining pressure- and temperature-dependent measurements, it is demonstrated that molecular adsorption at surface defect sites plays a key role in governing hysteresis, carrier mobility, and photocurrent transients. Progressive desorption under vacuum enhances conductivity and leads to faster and more reproducible photoresponse, while temperature-dependent measurements further reveal the contribution of interface traps and Schottky barriers at the dielectric–semiconductor and metal–semiconductor junctions. Building on this understanding, time-resolved photocurrent measurements were conducted to investigate which photogeneration mechanisms dominate at different temperatures, revealing the interplay between bolometric effects and adsorbate-mediated processes.

4.2 Material overview

ReS_2 belongs to the more recently identified family of group VII TMDs[1]. Rhenium is a heavy transition metal characterized by strong spin–orbit coupling and seven valence electrons. As a

consequence, ReS_2 crystallizes in a distorted 1T′ structure, in which rhenium atoms form Re_4 clusters arranged into diamond-shaped zig-zag Re–Re chains along the crystallographic *b* direction of the basal plane. This structural peculiarity arises because each Re atom can form bonds not only with six surrounding sulfur atoms but also with neighboring Re atoms within the same monolayer[2–4].

The formation of these Re–Re chains leads to a strong in-plane structural anisotropy and a significant reduction of the overall layer polarizability, resulting in weak van der Waals interactions between layers[5]. Due to this weak interlayer coupling, bulk ReS_2 behaves electronically and vibrationally as a stack of nearly decoupled monolayers[6,7]. The ReS_2 unit cell is made up of 12 atoms which lead to 46 vibrational modes and thus 36 phonon modes at the Γ point of the first Brillouin zone: of these 18 are accessible through Raman spectroscopy[8]. The small difference between the Raman spectrum of the bulk material and the monolayer is indicative of the weak interlayer interaction.

Consequently, in contrast to group VI TMDs, which typically undergo an indirect-to-direct bandgap transition when thinned down to a monolayer, ReS_2 preserves a direct bandgap regardless of the number of layers[9]. This unusual and unique thickness-independent electronic structure makes both few-layer and bulk ReS_2 particularly attractive and robust for high-efficiency optoelectronic applications.

In terms of bandgap values, bulk ReS_2 exhibits a bandgap in the range of 1.35–1.47 eV, while the monolayer bandgap increases slightly to approximately 1.5 eV[10,11]. It has been shown that the bandgap, together with the effective mass and mobility of carriers can be modulated by the application of a strain along the three directions a,b, and c of the unit cell: such a strain reduces the bandgap and affects the mobility and effective mass of holes, while having a reduced impact on electrons[12].

Its optical response is strongly anisotropic within the plane, with the absorption coefficient depending on the polarization of the incident light and reaching a maximum when the electric field is aligned parallel to the Re–Re chain[13]. Moreover, the photoluminescence behavior of ReS_2 differs from that of group VI TMDs: whereas the photoluminescence intensity in MoS_2- or WSe_2-based systems typically increases when moving from bulk to monolayer, ReS_2 displays the opposite trend, with stronger emission in thicker samples[7].

In this light, few-layer and multi-layer ReS_2-based devices have been extensively studied. Zhang et al. fabricated top-gate field effect transistors exhibiting a strong dependence of the photocurrent on the laser power, attributed to the photogeneration mechanism, and a photoresponsivity of 16.14 A/W at 25 nW laser power[14]. Higher photoresponsivity of 10^3 A/W was obtained by Liu et al. who investigated the optical properties of 3 nm thin ReS_2 under a green semiconductor laser of 2.4 eV. They showed that the photocurrent follows a power law as a function of the laser power $I_{ph} \sim P^{\gamma}$, where γ is 0.3. This sublinear dependency was attributed to complex carrier generation, trapping, and recombination processes[15].

Shim et al., instead, fabricated a thin-film transistor and photodetector on a multi-layer (above 30 nm) ReS_2 film, by implementing a simple top-down approach to control the material thickness. They performed an oxygen (O_2) plasma treatment to achieve a high I_{on}/I_{off} current ratio, a high mobility and a photoresponsivity of 10^7 A/W. This high photoresponsivity was

ascribed to the direct bandgap of ReS_2 and the high absorbance of the thick film as well as to the prolonged lifetime of carriers trapped in O_2 plasma-induced defects[16].
An anomalous broadband spectrum, spanning from visible to the infrared range, was detected in multi-layer ReS_2 transistor, by Xiang et al. This behavior was attributed to photo bolometric effect, in which light absorption causes local heating of the channel and, consequently, a change in its electrical conductance. Thanks to this mechanism, the device is able to detect sub-bandgap photons. Moreover, the ReS_2 phototransistor shows a low noise-equivalent power and a fast response time, below 3 ms [17].

The electronic structure of bulk ReS_2 also enables a favorable compromise between a high surface-to-volume ratio that typically requires thin layers, and sufficient carrier density and optical absorption, which are enhanced in thicker flakes. This balance is particularly advantageous for gas-sensing applications. In this context, Zulkefli et al. systematically investigated the oxygen-sensing performance of few-layer ReS_2 field-effect transistors under combined light illumination and gate bias. Their results showed that oxygen adsorption and photoexcitation modulate the electron population in ReS_2 in a gate-dependent manner, leading to an enhanced and tunable sensing response[18]. Humidity sensors were also realized by exploiting the charge transfer from the absorbed H_2O molecules to the n doped ReS_2 nanosheets by Yang et al[19].

The above-mentioned investigations of the photoresponse of ReS_2 were carried out at room temperature. However, there has been increasing interest in temperature dependent properties of 2D materials[20,21]. In particular, the development of optoelectronic devices must also address their operation under extreme environmental conditions, especially at low temperature, where the physical mechanisms affecting the photoresponse are not yet fully understood. In reality, some research indicates that low temperature leads to poorer performance because of carriers freezing and lower absorption, while other works report that low temperatures improve the photoelectric characteristics[22].

Pradhan et al. examined the temperature dependence of the electrical properties of ReS_2, from 300 to 2 K. They obtained that the field effect mobility increases up to 350 $cm^2V^{-1}s^{-1}$ as the temperature is decreased to 100 K, because the carrier scattering rate from phonons decreases as the temperature is lowered. Below, impurity scattering, carrier localization or the suppression of thermionic emission of carriers across the Schottky barriers make the mobility saturate[23]. An increase in mobility when the temperature is lowered to 77 K was reported also by Corbet et al. for dual gated ReS_2 field effect transistors[24]. Similarly, Zhang et al. showed that the mobility decreases above 120 K because of the electron-phonon scattering, according to the relation $\mu \sim T^{-\gamma}$ with $\gamma=2.6$[14].

Herein, electrical transport and photoresponse in few-layer ReS_2 FETs have been investigated under different pressure and temperature conditions.

4.3 Materials and methods

Ultrathin ReS_2 flakes were obtained by mechanical exfoliation from bulk ReS_2 single crystals. The crystal structure is displayed in Figure 4.1a. By using an adhesive tape, the flakes were transferred onto a highly doped n-type (resistivity 0.005 Ω·cm) silicon substrate, covered by a

290 nm thick SiO_2 layer, which acts as a global back gate. The Raman spectrum of ReS_2 (Figure 4.1b) in the 100-250 cm^{-1} range, where the strongest modes occur, indicated a flake of 7-8 layers.

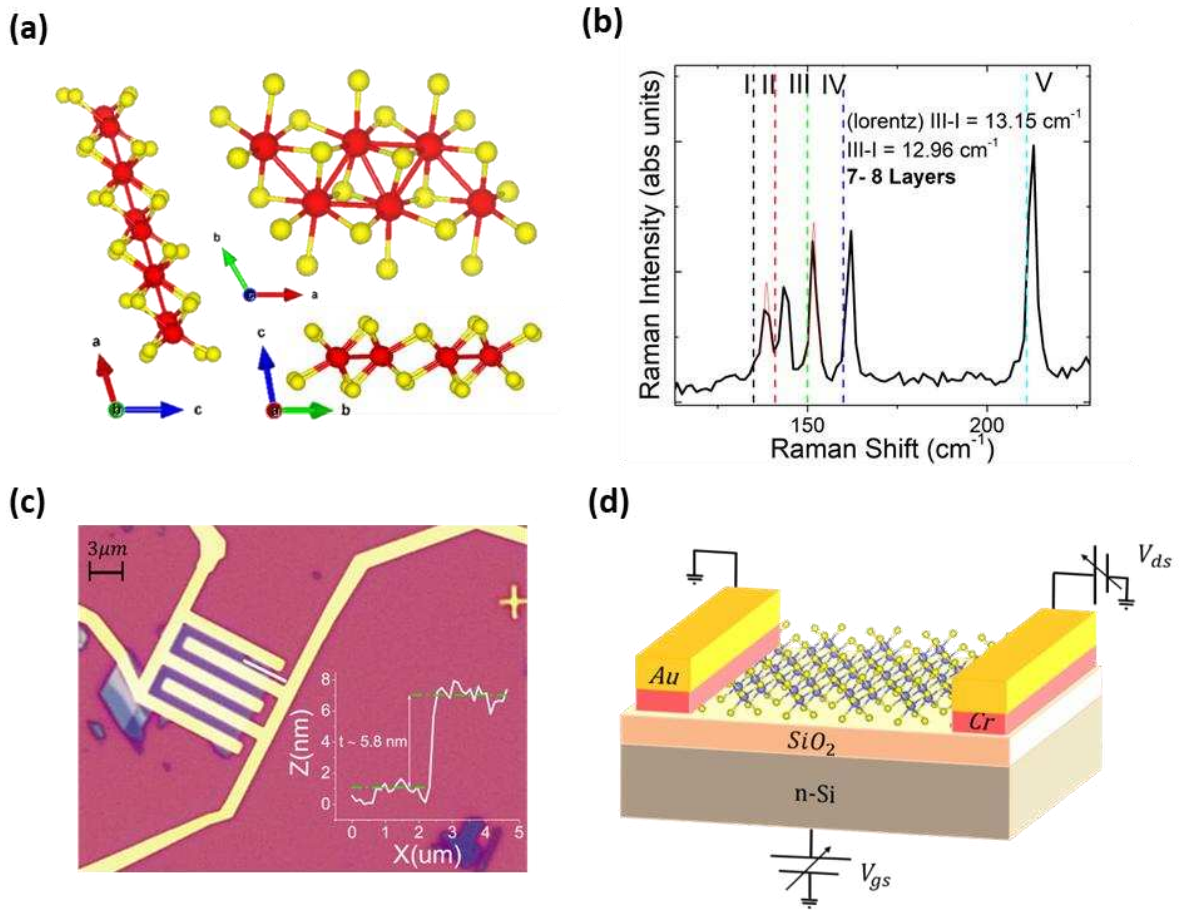

Figure 4.1: (a) ReS_2 crystal structure along the a, b, and c axes. The Re-Re bonds, due to the extra valence electron of Re, induces a Re-Re chain along the crystal. (b) Raman spectrum of ReS_2 restricted between 100 and 250 cm^{-1}. (c) Optical image of the device, which shows the interdigitated layout. In the inset, the AFM profile acquired along the white trace shown in the optical image. (d) Schematic of the device made of a ReS_2 flake transferred onto a SiO_2-Si substrate and contacted with Cr-Au leads. Gate and drain voltage are applied to perform electrical measurements.

The flake thickness can be extracted from the energy difference between some high-energy modes of ReS_2. In detail, the difference between the peak positions of the I and III mode decreases with the increasing number of layers, giving a reliable method to estimate this parameter[25,26]. Raman spectroscopy has been performed with a fixed polarization angle. It is noted that the peak intensity ratios are sensitive to the direction of the polarization and are modified even if the crystal is rotated with the same laser and collection polarizations, because of the anisotropy of the vibrational properties in ReS_2[23]. Back-gated FET devices were fabricated by depositing Cr-Au (5-100 nm) contact leads by thermal evaporation. The electrical transport is direction-dependent within the crystal plane, with the conductivity along the b-axis several times higher than that on the perpendicular axis. To perform anisotropy transport measurements, many electrode pairs are necessary, disposed at different angles. In this case,

the two metallic contacts are randomly deposited, so it is not possible to select a single crystalline direction and appreciate the anisotropic electrical properties of the material. An interdigitated layout was adopted for the metal leads, shown in the optical image in Figure 4.1c, which yields a total length L = 0.89 μm and width W = 42 μm. In the inset, the AFM profile confirms that the flake is 8 layers thick, since the single layer has a thickness of around 0.7 nm[27]. The schematic of the device is shown in Figure 4.1d, along with the circuit diagram used to apply the gate and the source-drain biases, V_{gs} and V_{ds}, respectively, to the 2D semiconducting channel. Electrical measurements were performed in a Janis probe station, and data were acquired through a semiconductor characterization system Keithley 4200.

4.4 Results and discussion

4.4.1 Pressure-dependent electrical properties

Electrical measurements reported in Figure 4.2 were performed in the dark at room temperature and ambient pressure.

The output curves (I_d vs V_{ds} at fixed V_{gs}) in Figure 4.2a were obtained by sweeping V_{ds} from -0.05 to 0.05 V while stepping V_{gs} in the (-60, 60) V range. Preliminary tests confirmed that gate voltages up to 60 V could be safely applied without inducing breakdown of the 290 nm-thick SiO_2 gate dielectric. Despite the application of relatively small drain biases, on the order of a few tens of millivolts, drain current values reaching the microampere range are observed. This indicates a high concentration of carriers and efficient charge transport within the channel. The absence of pronounced asymmetry between the positive and negative V_{ds} branches, together with the linear behavior of the output curves and the high on-current at V_{ds} = 0.05 V, suggests the presence of low Schottky barriers at the ReS_2/Cr–Au interfaces[28,29]. However, since linear current voltage characteristics may also arise from Schottky interfaces on highly doped semiconductors, this behaviour is not conclusive about the nature of the contacts[30]. The output curves further demonstrate that the drain current can be effectively modulated by both the drain and gate voltages. In particular, the increase in current under positive gate bias indicates that the device behaves as an n-type semiconductor[15]. As commonly observed in other TMDs, the n-doping of ReS_2 is often attributed to chalcogen vacancies, which are the most common defects in intrinsic ReS_2 and, more generally, in mechanically exfoliated TMD flakes[31,32]. These defects might induce localized trap states that can be detected through capacitance-voltage measurements, as demonstrated in an earlier study on WS_2[33].

The transfer characteristic was measured by sweeping V_{gs} from 60 to -60 V with a fixed V_{ds} of 0.04 V. It is reported on linear (purple) and semi-log (blue) scale in Figure 4.2b. From the linear fit (red) of the upper part of the purple line it is possible to extract the maximum field effect mobility $\mu \sim 2.9$ $cm^2V^{-1}s^{-1}$ by using equation 2.12 (C_{OX} = 1.15x10^{-8} F cm^{-2} is the dielectric capacitance gate per unit area). This value is consistent with other works on similar devices, and is typical of several TMDs[14,15]. Since high biases were applied, the current through the oxide was also monitored to be confident that no gate leakage was affecting the measurements.

By linear fitting the lower part of the transfer curve, a negative threshold voltage of Vth ~ -3 V can be determined. It acts as a reference voltage between the on and off state of the transistor. The switching properties of the device can be evaluated by looking at the subthreshold region of the transistor that is better visualized in semi-log scale (blue curve in Figure 4.2b). The device shows a high I_{on}/I_{off} ratio of about 10^4, but the subthreshold swing, calculated according to equation 2.9, yields SS ~ 19 V/decade, which reveals poor switching properties. One of the reasons of the high SS might be the usually defective interface that 2D materials form with the SiO_2 dielectric layer[34,35].

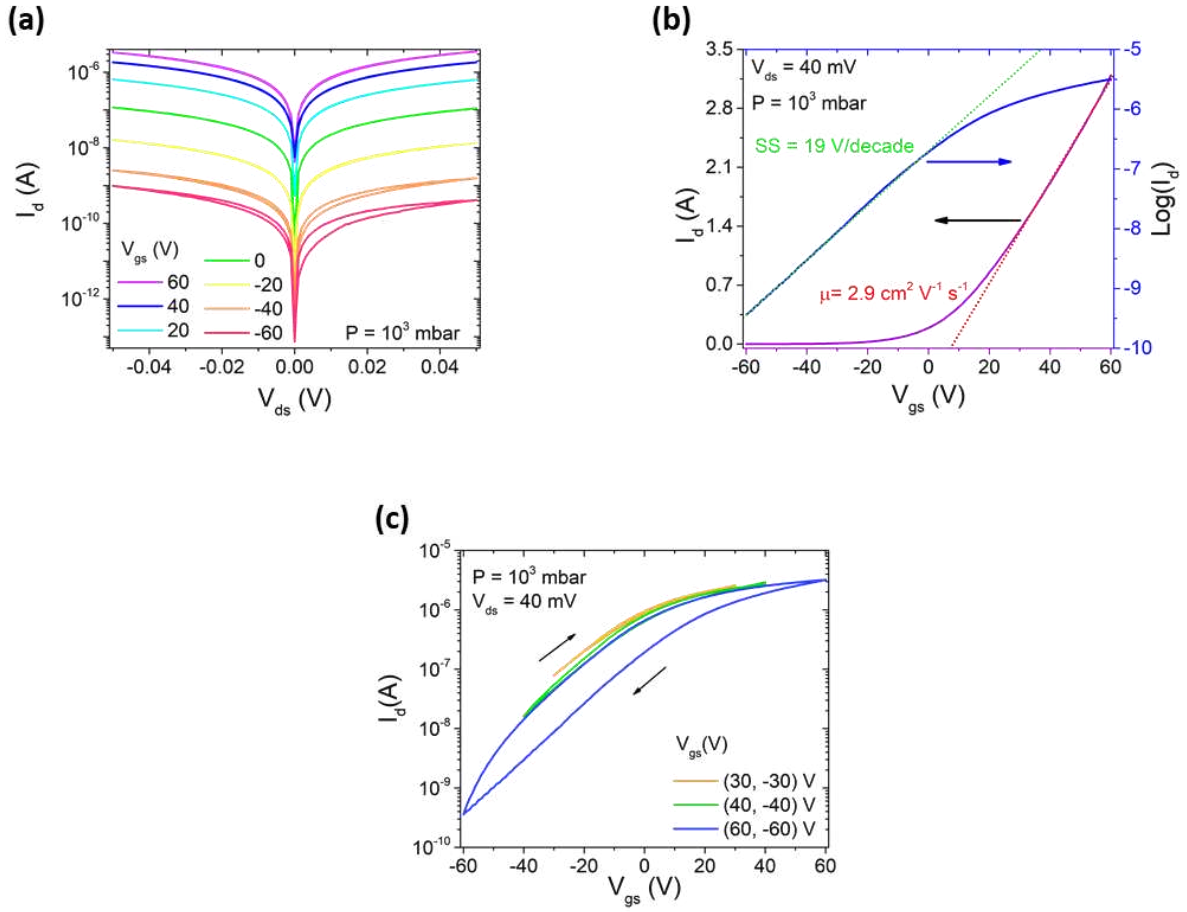

Figure 4.2: (a) Output characteristics on semi-log scale, performed at ambient pressure and room temperature, by stepping the gate voltage from -60 to 60 V (b) Transfer characteristic obtained by sweeping the gate voltage in the (-60, 60) V range on a linear (purple) and log (blue) scale. (c) Transfer curves obtained by double sweeping the gate voltage in the (30,-30), (40,-40) and (60,-60) V ranges.

By double sweeping the gate bias in forward and reverse mode, hysteresis occurs, as shown in Figure 4.2c. As already demonstrated, hysteresis in the transfer characteristics of 2D-material-based transistors is quite common and it is due to the different capture and emission times of charge traps when bands shift under the application of an external field, which is equivalent to move the Fermi level towards and apart the conduction band[36,37]. As shown by the arrows, the hysteresis follows a clockwise direction, determining a lower threshold voltage in the forward branch. This behavior is induced by acceptor-type traps, which expose negative charge when they are filled up with electrons during the forward sweep of the gate bias[38,39].

However, when the sweep is reversed, from positive to negative biases, the trapped electrons are not immediately released due to their finite emission time. The additional negative charge hinders channel formation, resulting in a higher threshold voltage (V_{th} ~-3 V) in the reverse sweep. At negative biases, the electrons are released and a lower threshold voltage occurs in the forward sweep (V_{th} ~-12 V). Figure 4.2c further reveals that the forward and reverse branches of the transfer characteristics nearly overlap within moderate gate-bias intervals, such as (−30, 30) V and (−40, 40) V. In contrast, a clear hysteresis loop develops when larger gate voltages are applied. This observation suggests that higher electrostatic fields are required to activate or fill the trap states responsible for the hysteretic behavior in this device. Similar results have been obtained for other few-layer ReS_2-based FETs and reported at the end of the chapter to further support these statements.

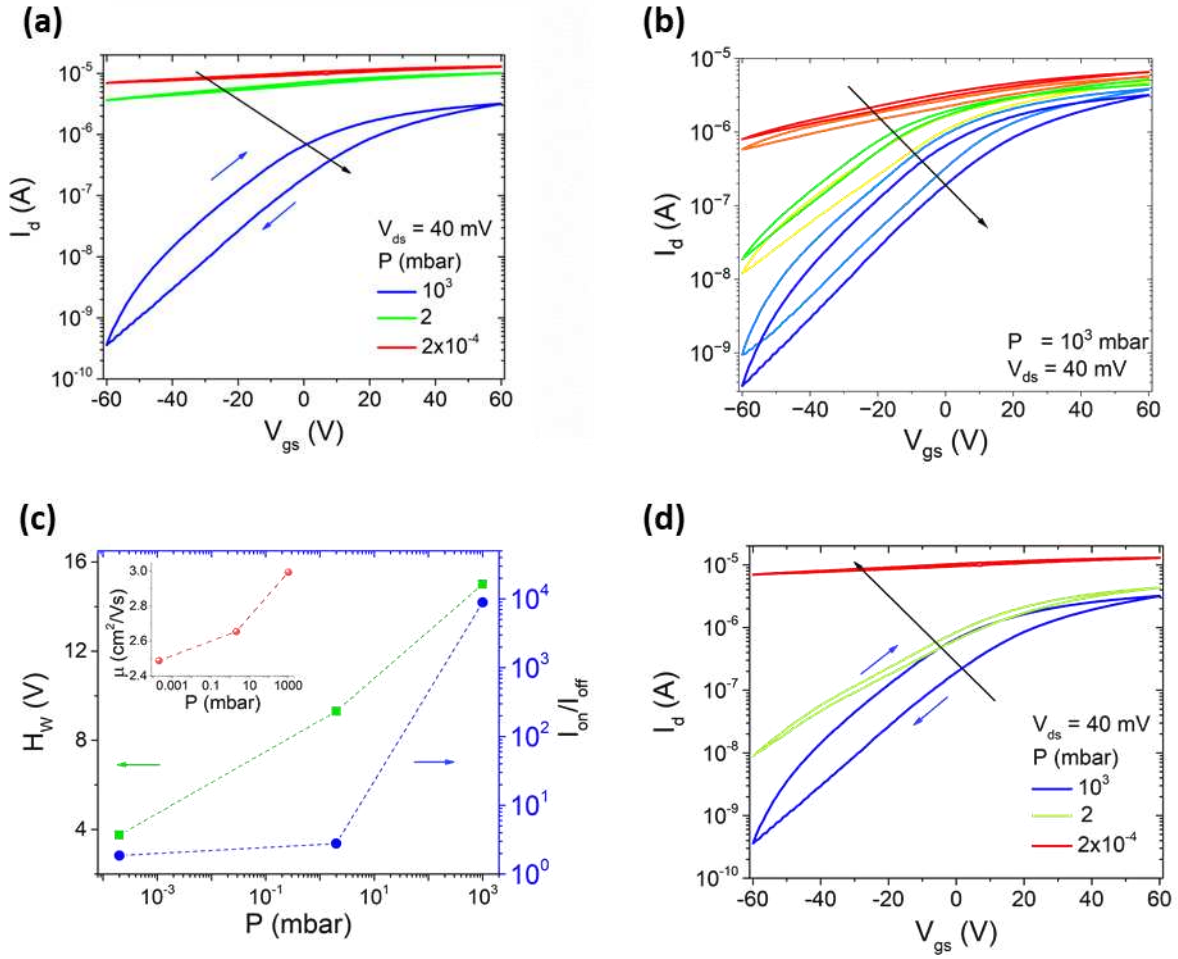

Figure 4.3: (a) Transfer curves obtained by increasing pressure from 10^{-4} mbar (red), to 2 mbar (green), to ambient pressure (blue). (b) Evolution of hysteretic behaviour in ambient pressure. (b) Hysteresis width (green), I_{on}/I_{off} ratio (blue) as a function of pressure. In the inset, mobility vs. pressure. (d) Transfer curves obtained by decreasing pressure from ambient pressure (blue) to 2 mbar (green), to 2 x 10^{-4} mbar (red).

Additional insight into the origin of these trap states, whether they arise from defects at the oxide/semiconductor interface, from adsorbed molecular species, or from intrinsic lattice imperfections, can be obtained through pressure-dependent measurements. For this purpose,

the device was first characterized under high-vacuum conditions to minimize the influence of surface adsorbates. The pressure was then gradually increased, ensuring that a stable equilibrium was reached at each pressure level before recording the electrical characteristics[40,41]. Figure 4.3a compares the transfer curves obtained at $2 \cdot 10^{-4}$ mbar, at 2 mbar, and at ambient pressure. The narrow hysteresis observed in vacuum conditions, together with the gradual evolution of the hysteretic behavior at ambient pressure until a stable condition is reached, shown in Figure 4.3b, indicate that the dominant trap states responsible for hysteresis originate from air molecules adsorbed on the ReS_2 surface.

DFT calculations reported in the literature indicate that both O_2 and H_2O molecules interact weakly with the ReS_2 surface, exhibiting relatively low binding energies in the range of approximately 70–140 meV, and an almost reversible interaction[42]. Adsorption preferentially occurs at defect sites rather than on the pristine basal plane. During the growth of two-dimensional ReS_2 sheets, various point defects can form, including atomic vacancies, adatoms, and substitutional defects. Experimental studies combined with theoretical calculations reveal that sulfur vacancies have the lowest formation energy in monolayer ReS_2, whereas defects involving rhenium atoms require significantly higher energies and are therefore less likely to occur[43]. Sulfur vacancies introduce dangling bonds in the lattice, which are readily passivated under ambient conditions through oxygen adsorption, making O_2 binding at sulfur vacancy sites particularly favorable[44].

The hysteresis width (H_w) reported in Figure 4.3c has been evaluated as the voltage difference between the two branches of the transfer curve at a fixed value of current determined as the middle value between $Log(I_{on})$ and $Log(I_{off})$.

The desorption of water and oxygen molecules induced by pressure reduction leads to the release of electrons previously trapped by these electronegative adsorbates, resulting in a leftward shift of the threshold voltage. As a consequence, the transistor exhibits a reduced gate modulation within the investigated voltage range[45]. In particular, the I_{on}/I_{off} ratio decreases to less than one order of magnitude as the pressure is lowered, as shown in Figure 4.3a.

At the same time, the reinjection of electrons into the channel increases the carrier concentration, and consequently the current levels. While a slight reduction in the extracted mobility can be observed (inset of Figure 4.3c), the overall channel conductance is enhanced in high-vacuum conditions, primarily due to the increased carrier density. Similar pressure-dependent trends have been observed in other ReS_2-based FET, as reported at the end of the chapter.

Measurements were also performed by reversing the pressure sequence, starting from ambient pressure and progressively lowering it down to high vacuum, again waiting for the device stabilization. Figure 4.3d reveals that at the intermediate pressure of 2 mbar the device is affected by the previous operating condition of the device and, in particular, on whether this condition is approached from ambient pressure or from high vacuum.

Since desorption in high vacuum is generally more effective than re-adsorption during pressure increase, the resulting carrier concentration and transport parameters can differ even at the same nominal pressure. Compared to the pressure ramp shown in Figure 4.3a and the parameters extracted in Figure 4.3c, mobility and hysteresis width do not exhibit significant variations when the pressure is reduced following this reversed sequence. In contrast, noticeable

changes are observed in the carrier concentration and in the I_{on}/I_{off} ratio, which assume values closer to those extracted at ambient pressure.

4.4.2 Impact of pressure on the photoresponse

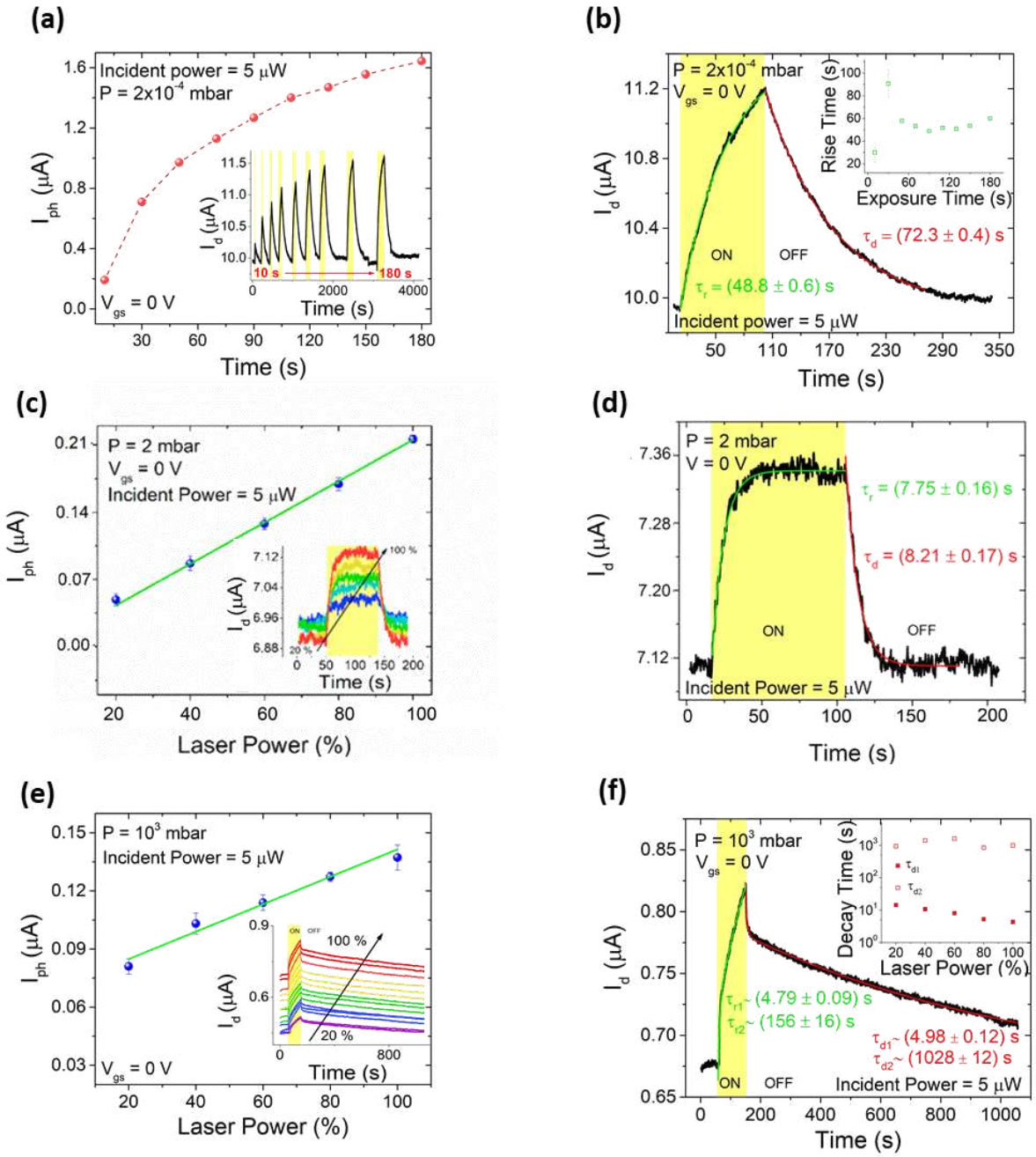

Figure 4.4: Photocurrent as a function of exposure time/ incident laser power, together with the temporal photocurrent profiles used to extract rise and decay time constants, measured at (a), (b) high vacuum, (c), (d) 2 mbar after high-vacuum exposure, and (e),(f) ambient pressure.

The photoresponse mechanisms of the ReS_2 field-effect transistor under supercontinuum white-light illumination were investigated through time-resolved measurements of the device switching behavior under the same pressure conditions discussed above: from high vacuum to

ambient pressure and in the reversed order. This approach allows disentangling intrinsic photoresponse effects from those related to adsorption–desorption dynamics.

The maximum incident optical power was approximately 5 μW. All the photoresponse measurements were carried out at zero gate bias (V_{gs} = 0 V) in order to exclude electrostatic gating effects and focus on light-induced processes.

Under high-vacuum conditions (P = $2 \cdot 10^{-4}$ mbar), the drain current was monitored under light pulses of increasing duration, ranging from 10 to 180 s – see Figure 4.4a. As shown in the inset of Figure 4.4a, the current does not reach saturation within this time-window but instead continues to increase as the illumination time is extended, indicating a slow photoinduced process. The transient response under a 90 s pulse at maximum optical power is displayed, as a representative case, in Figure 4.4b. Both the rise and decay dynamics can be described by single-exponential behavior,

$$y = Ae^{-t/\tau} \quad (4.1)$$

with characteristic times on the order of several tens of seconds ($\tau_r \approx$ 48–90 s), as reported in the inset[46]. The absence of saturation and the long response times suggest that, in high vacuum, the photoresponse is dominated by intrinsic trapping and detrapping processes, which might be associated with non-passivated sulfur vacancies that act as trap states[47].

When the pressure is increased to low vacuum conditions (P = 2 mbar), the photoresponse exhibits a marked change. Here, the drain current reaches clear saturation within the investigated time interval of illumination and a strong dependence on the laser power. When considering the saturation level, the photocurrent increases linearly with the incident optical power (Figure 4.4c), a desirable feature for photodetector applications. As shown for the representative case of 90 s long pulse (Figure 4.4d), the temporal response is significantly faster than in high vacuum. Single-exponential fits yield rise and decay times shorter than 10 s for the investigated incident powers, indicating that moderate adsorption of air molecules partially suppresses slow trapping dynamics while still preserving efficient photogeneration. These rise and decay times are shorter than previously reported values by other authors[48,49].

An almost linear dependence of the photocurrent on the optical power can be also identified at ambient pressure (Figure 4.4e). In this condition (P = 10^3 mbar), the transient profile further evolves, as illustrated in Figure 4.4f. Under illumination, the drain current exhibits an initial fast increase followed by a much slower growth. Similarly, after the light is switched off the current experiences a fast decrease and then decays very slowly and does not return to its original dark value within the investigated time scale. Both the rise and decay transients require a double-exponential fit[50,51]

$$y = y_0 + Ae^{-t/\tau_1} + Be^{-t/\tau_2}, \quad (4.2)$$

with a fast component on the order of a few seconds that can be attributed to photoconduction mechanisms and a slow component extending from several hundred seconds when the illumination is on to thousands of seconds when it is switched off [52]. This behavior resembles a persistent-photoconductivity–like response, which occurs for all the investigated optical powers, as reported in the inset of Figure 4.4e. Persistent photoconductivity is a light induced

change in the free carrier concentration which persists after the optical excitation has been removed and has been reported in other 2D materials–based devices[53–55]. It is commonly related to long-lived trapping of photogenerated carriers in the substrate[56,57] or in the adsorbate-induced states[58], or at defect sites[54], from which release is energetically unfavorable even when the light source is removed. In contrast to the fast band-to-band recombination of electron-hole pairs, the recombination through the trap centers takes a longer time. In this case, the slow photoresponse has been attributed to surface adsorbates induced traps.

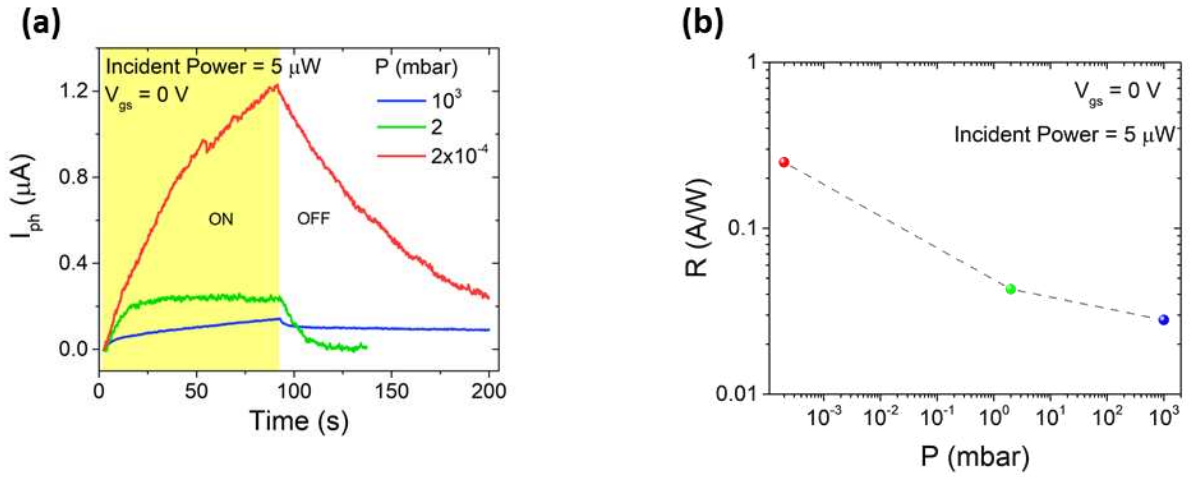

Figure 4.5: (a) Comparison of the photocurrent profiles under three pressure conditions. (b) Corresponding responsivity values as a function of pressure.

Figure 4.5a directly compares the photocurrent transients at the three investigating pressure conditions, further elucidating the different photocurrent profiles. Corresponding responsivity values, calculated for the 90 s long pulse at the maximum incident optical power, according to the formula 2.15, range from 0.25 A/W in high vacuum to tens of mA/W at higher pressures, as reported in Figure 4.5b.

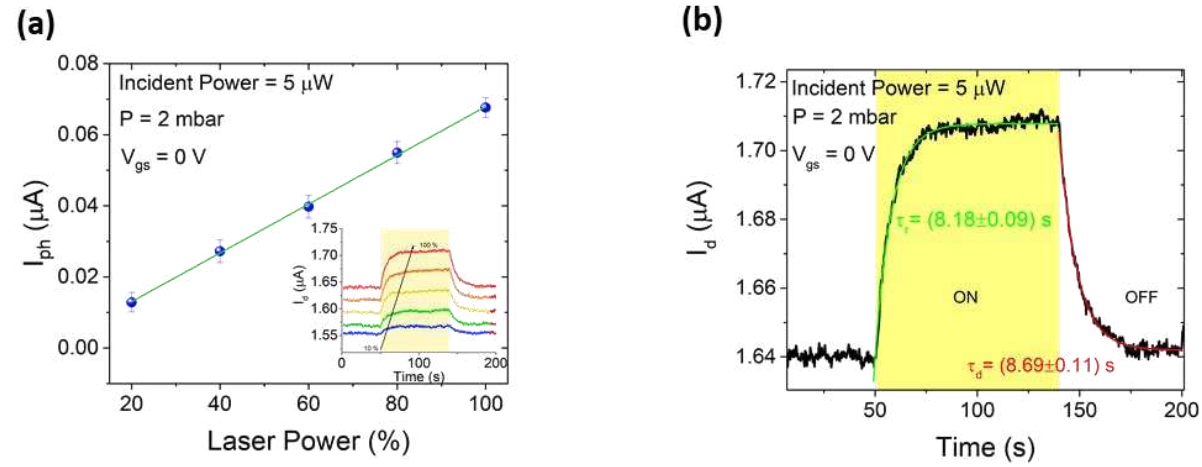

Figure 4.6: (a) Photocurrent as a function of the laser power. (b) Current profile under 90 s long pulse with extraction or rise and decay times.

Figures 4.6a and 4.6b show the photoresponse of the device at 2 mbar when the condition is approached from ambient pressure. Although the absolute photocurrent values differ, in accordance with the modification observed in the transfer curves, the linear dependence on the incident optical power is preserved. Moreover, the transient profile of the current under illumination, together with the short rise and decay time constants, remains unchanged. This indicates that these features of the photoresponse are robust against the adsorption/desorption history.

The impact of environmental atmospheric pressures on the electrical and optical properties of TMDs has been investigated in other materials. In particular, a similar study on $ReSe_2$, another group VII-TMD, has been previously carried out[45].

4.4.3 Temperature-dependent electrical measurements

To further explore the mechanisms governing the electrical and optical properties of ReS_2-based FET, temperature dependent measurements were performed. They were carried out in low vacuum to avoid condensation or freezing inside the measurement chamber during the cooling phase. At the same time, this pressure regime represents an intermediate condition in which surface-related effects are still present, while the device response remains sufficiently stable, robust and fast to enable a systematic temperature-dependent investigation of the photoresponse.

A first analysis considered the 180-350 K range, which is a suitable range for the application of the Arrhenius model that is not reliable at low temperatures since the thermionic component results in a smaller current than the usual leakage for any considerable Schottky barrier height[30].

Figure 4.7a reports the I_d-V_{ds} curves at zero-gate voltage, with V_{ds} ranging from -0.05 to 0.05 V. A linear relationship is exhibited at every temperature. The increase in conductance with the rising temperature confirms a semiconducting trend that can be fitted by the Arrhenius equation $G(T) = G_0 e^{\frac{-E_a}{k_B T}}$, as shown in the inset of Figure 4.7a. The thermal activation energy of the majority carriers is $E_a = (100 \pm 2)$ meV revealing the presence of energy levels close to the conduction band that would cause Fermi level pinning and low Schottky barriers[59].

More insights are provided by the transfer curves at different temperatures measured by forward and reverse sweeping the gate voltage in the (-60; 60) V range at a fixed $V_{ds} = 0.04$ V. In the I_d-V_{gs} curves of Figure 4.7b, the three different operation modes that Schottky-barrier MOSFETs usually pass through for increasing V_{gs} can be qualitatively identified. For gate voltage up to about -20 V, carriers are injected in the channel through thermionic emission (TE) from the source (I). The lower the gate bias, the more deeply the device operates in the off state, resulting in a larger temperature-dependent variation of the current. The conduction-band maximum in the channel lies energetically above the Schottky barrier and shifts to lower energies as the gate voltage increases. As long as the conduction-band maximum remains above the Schottky barrier, the latter does not significantly influence the transistor current, since electron transport is limited by the band profile within the channel.

When the conduction-band maximum aligns with the Schottky-barrier level, the flat-band condition is reached. By increasing the gate voltage beyond the flat band condition, the

conduction band maximum goes below the Schottky barrier and thermal-assisted tunneling (TT) is enabled. Then, the channel current is the result of both TE and TT (II). This transition is identified by a kink in the transfer curves at the gate voltage corresponding to the flat-band voltage. The higher the tunneling probability through the Schottky barrier, the less pronounced is the kink. At higher gate voltages, the conduction band in the channel bends further, making the potential barrier thinner and thinner, thus enhancing the transmission probability through it. When the channel conduction band is slightly above the source Fermi level (threshold condition), the transistor turns on. This manifests as a change in the current from exponential to quadratic/linear behavior (apparent saturation of the drain current at high gate voltages on the semilogarithmic I_d–V_{gs} plot in Figure 4.7b). Above the threshold region, the tunneling mechanism is dominant (III)[60].

In the TE regime, the current is given by:

$$I_d \sim A_{2D}^{*} T^{3/2} \exp\left[-\frac{q\Phi_{B,eff}(V_{gs})}{k_B T} \right] \quad (4.3)$$

where $q\Phi_{B,eff}(V_{gs})$ is the effective barrier height, which depends on the shape and the width of the potential barrier seen by the electrons at the source edge, determined by the conduction band profile at a certain gate voltage. A_{2D}^{*} is the modified Richardson constant and T is temperature. In the TE regime, the current exponentially depends on temperature and gate voltage. At the flat band voltage, the effective barrier height coincides with the Schottky barrier, $\Phi_{B,eff}(V_{FB}) = \Phi_{Bn}$. In details, the $\ln(I_d/T^{3/2})$ vs. $1000/T$ data at a given V_{gs} in the range -60 to 60 V are plotted in Figure 4.7c, and linearly fitted to calculate the effective barrier $\Phi_{B,eff}$ at each gate bias:

$$q\Phi_{B,eff}(V_{gs}) = k_B \left[\frac{d\ln(I_d/T^{3/2})}{dT^{-1}} \right] \quad (4.4)$$

$\Phi_{B,eff}$ becomes smaller as the channel conduction band bends downward towards the source Fermi level. The plot $\Phi_{B,eff}(V_{gs})$, shown in Figure 4.7d, is characterized by three different zones, which are consistent with the three marked areas in Figure 4.7b. In correspondence of the kink observed at $V_{gs} \approx -20\ V$ it is possible to extract the Schottky barrier.

The Schottky barrier height is $q\Phi_{Bn} = 0.091\ eV$, consistent with the estimated position of the trap centres that can cause Fermi level pinning. Considering the electron affinity of ReS_2 ($\sim 4.30\ eV$) [61] and the Cr work function ($\sim 4.5\ eV$), the ideal Cr-Au/ReS_2 Schottky barrier given by the difference between electron affinity and work function, should be 0.20 eV[62]. The extracted smaller value suggests that Cr Fermi level is actually pinned near the ReS_2 conduction band[63]. The Fermi level pinning can be attributed to defect-induced gap states, which are also a source of free carriers[64]. Atomic vacancies can, in fact, induce interface states that modify the contact properties[65,66].

From the fit of the linear part of $q\Phi_{B,eff}(V_{gs})$ curve below V_{fb}, it is possible to extract the body factor $\gamma = \left(1 + \frac{C_{it}}{C_{ox}}\right)^{-1} = (1.61 \pm 0.04) \cdot 10^{-3}$ and, consequently estimate the capacitance of the localized states at the interface between the material and the oxide $C_{it} \sim (7.1 \pm 0.2) \cdot 10^{-6}\ F/cm^2$. Such a capacitance is related to the trap density $D_{it} = C_{it}/e^2 \sim (4.5 \pm 0.2) \cdot 10^{13}\ eV^{-1}cm^{-2}$ [67].

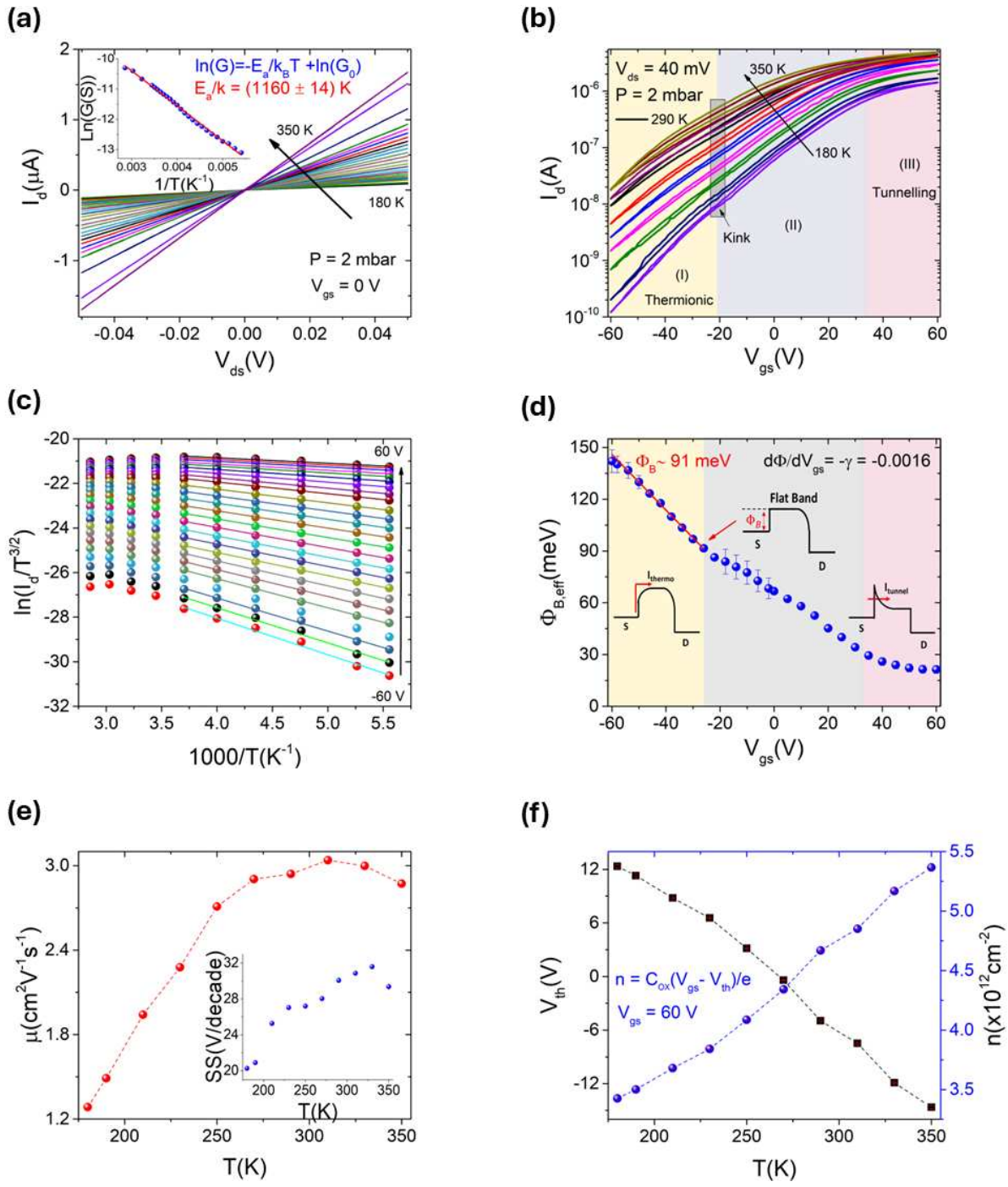

Figure 4.7: At 2 mbar: (a) Current-voltage (I_d-V_{ds}) curves obtained at different temperatures, from 180 to 350 K. The inset shows the conductance (G) vs. 1/T plot and is used to extract the activation energy at V_{gs} = 0 V. (b) Transfer curves at different temperature on semi-log scale. The three coloured regions qualitatively demark the thermionic (I), mixed (II) and tunnelling (III) dominated operation modes. (c) Arrhenius plot. (d) Effective Schottky barrier as a function of the gate voltage, with the three-operation modes, shown as coloured zones. (e) Mobility and subthreshold swing as a function of temperature. (f) Threshold voltage (black squares) and carrier concentration (blue spheres) as a function of temperature.

From the transfer characteristics, it is also possible to extract the temperature dependence of several key FET figures of merit. The field-effect mobility trend shown in Figure 4.7e is consistent with that reported for other TMD-based FETs, where the mobility as a function of temperature typically exhibits a peak-like behaviour. The temperature at which this peak occurs marks the transition between the regime dominated by charged-impurity scattering and that dominated by electron–phonon scattering[68]. This peak is generally around 100-120 K [14,23], while here the mobility increases up to room temperature before slightly reducing at higher temperatures. Such behaviour suggests that phonon scattering is not the primary limiting mechanism in the investigated temperature range; instead, transport may be largely governed by charge trapping processes and interface-related scattering, which can mask the expected phonon-limited decrease in mobility[15]. The maximum value is around $\mu \sim 3\ cm^2V^{-1}s^{-1}$.

The subthreshold swing almost follows the same trend of mobility, while the I_{on}/I_{off} ratio increases by two orders of magnitude while lowering temperature, reaching 10^4 at 180 K. At low temperature, the threshold voltage is slightly right-shifted with respect to higher temperature, as shown in Figure 4.7f, since it is more difficult to turn the transistor on because of the reduced thermionic component and reduced carrier concentration. The charge concentration values per unit area at V_{gs} = 60 V, computed according to the parallel-plate capacitor model: $n_{2d} = \frac{C_{ox}\Delta V}{e}$, where $C_{ox} = \frac{\epsilon_0 \epsilon_{ox}}{d_{ox}}$ and $\Delta V = V_{gs} - V_{th}$[69], range from $5.5 \cdot 10^{12}$ to $3.5 \cdot 10^{12}$ cm^{-2} as the temperature decreases. The threshold voltage is identified by the x-axis intercept of the straight-line fitting the transfer curve on linear scale.

4.4.4 Temperature dependent photoresponse

High temperature of 350 K and low temperature of 80 K were chosen to investigate the impact of temperature on the photoresponse of ReS_2. The transistor completely switches off at 80 K in the investigated voltage range, as demonstrated by the transfer curve in Figure 4.8a, where noise is detected below -50 V. The device exhibits a reduced conductivity with a mobility around μ = 0.11 $cm^{-2}V^{-1}s^{-1}$ due to the freezing of carriers but enhanced switching properties with a higher I_{on}/I_{off} ratio and lower SS = 5.8 V/decade[70]. This feature derives from the lower concentration of active traps at low temperature. Additionally, at this temperature, the separation between the thermionic-dominated region, the tunnelling-dominated region and the mixed transition region is even better marked.

At 80 K the device was subjected to 30 s long laser pulses with an incident optical power increasing from 0.5 to 5 µW at V_{gs} = 0 V (Figure 4.8b). Similarly to the room temperature profile, the drain current reaches saturation after a steep rise under illumination and rapidly decays when the laser is switched off, restoring the original dark level. Even if the photocurrent is one order of magnitude lower, it still shows a linear dependence on the laser power, as reported in Figure 4.8c. Further, the speed of the device was evaluated through the estimation of the rise and decay times, obtained by fitting the edge transients with single exponentials. The response times are independent of the laser power and reach approximately 5 s, which is shorter than previously reported at 290 K.

To further investigate the stability and reproducibility of the device, its time-resolved behaviour was analyzed under trains of repeated light pulses with different exposure times, using an incident optical power of 104.5 mW.

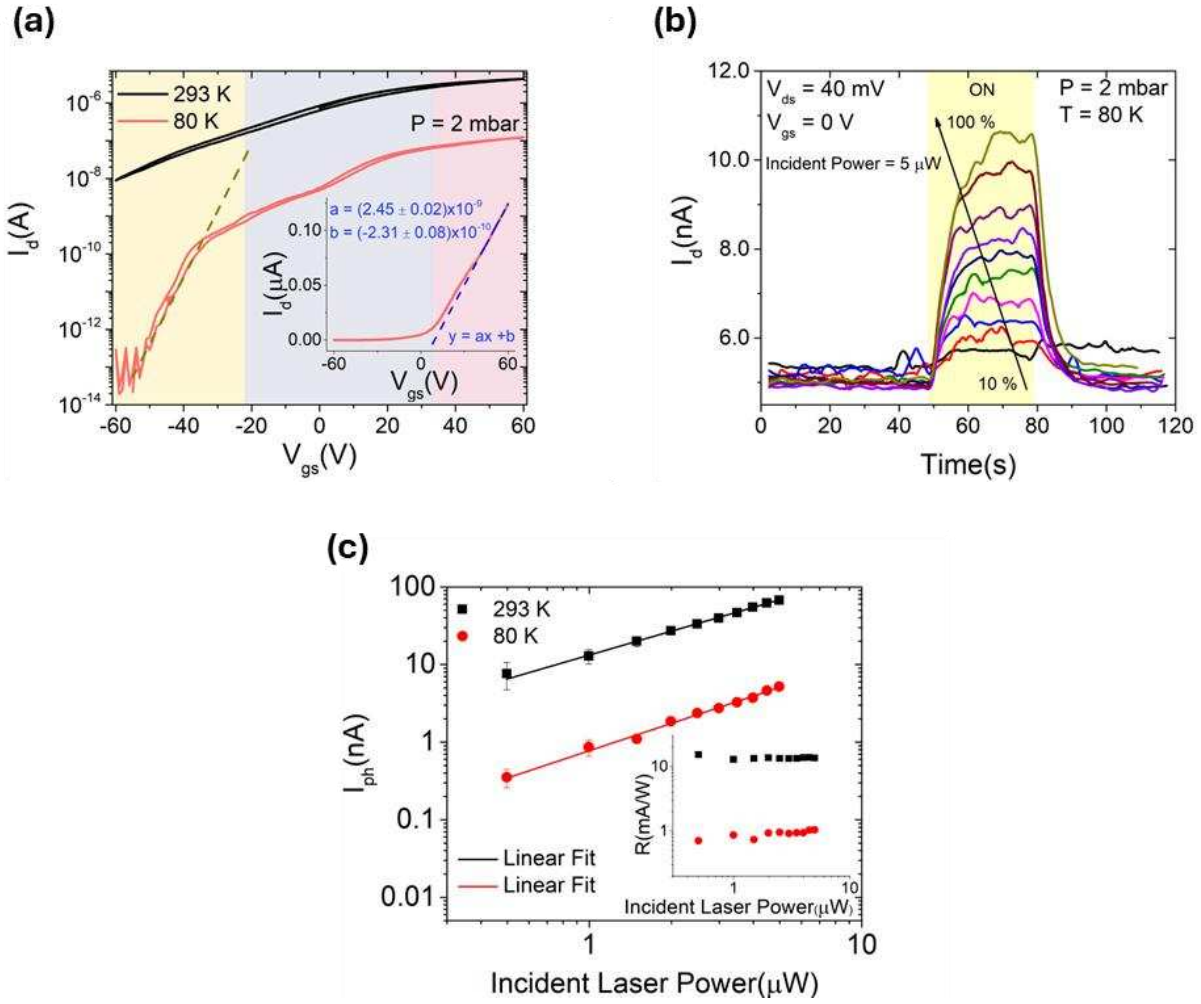

Figure 4.8 At 2 mbar: **(a)** Transfer characteristics on semi-log scale both at 80 K and 293 K. **(b)** Drain current vs. Time under 30s laser pulses of increasing intensities at T =80 K. **(c)** Photocurrent vs. Incident Laser Power data at T= 293 K (black) and T=80 K (red). A linear behavior occurs in both cases. Responsivity as a function of the incident laser power is reported in the inset.

As shown in Figure 4.9a, as expected, neither pulse repetition nor prolonged illumination significantly affect the photocurrent at 80 K, confirming that the photoresponse is dominated by fast and reversible mechanisms.

In contrast, at room temperature, a progressive rise in the baseline current is observed during repeated pulse illumination. Once the light is turned off, the dark current stabilizes at a slightly higher value than the original dark level, as shown in the inset of Figure 4.9b, indicating incomplete recovery between successive train pulses.

The steeper baseline slope observed at high temperature compared to room temperature indicates a temperature-dependent contribution to the drain current, which affects the profile

of the photocurrent transients. Considering the single-pulse response reported in the inset of Figure 4.9c, at 350 K the photocurrent does not exhibit a clear saturation within the investigated illumination time. Instead, two distinct contributions are observed: a rapid current increase immediately after the laser is switched on, followed by a slower and sustained rise during continued illumination. When the light is switched off, the drain current stabilizes at a new level which ranges around 40-70% of the photocurrent level, resulting in a persistent-like offset in the dark current.

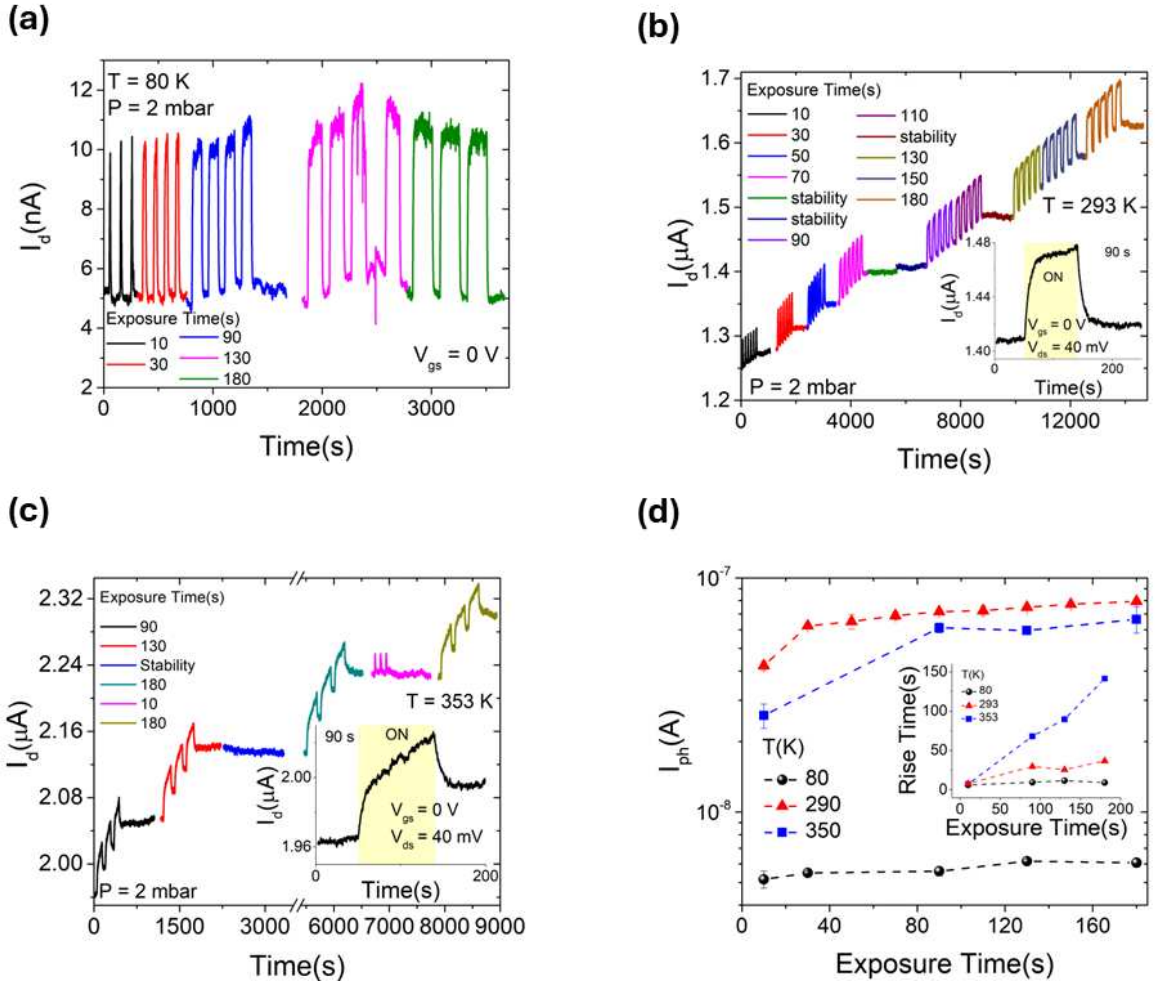

Figure 4.9: Drain current vs. time for several exposure times under the laser (a) at 80 k, (b) at 293 K (the inset shows a zoom of the shape of the drain current under 90s laser pulses) and (c) at 353 K (the inset shows a zoom of the shape of the drain current under 90s laser pulses). (d) Comparison of the photocurrent vs. the exposure time under the laser at 80, 293, 350 K temperatures. The rise times as a function of the exposure times are reported for the three temperatures in the inset. Dashed lines are eye guides. All measurements are at the 2 mbar pressure.

The transient profiles do not consistently display a well-defined transition between single- and double-exponential behavior for all the pulses. For this reason, rise and decay times are extracted using the 10–90% method. As a result, the overall rise time increases and becomes dependent on the exposure duration, as summarized in the inset of Figure 4.9d.

Figure 4.9d also reports the values of the photocurrent as a function of the exposure times at the three operating temperatures. The highest photocurrent observed at 293 K rather than at 353 K can be attributed to the higher carrier mobility at room temperature, as extracted from transport measurements (Figure 4.7e), given that the photocurrent magnitude is linked to the transport properties of the channel. At higher temperatures, the enhancement of non-radiative recombination processes further limits the photocurrent.

The observed transient photoresponse reflects the combined action of photobolometric effect and light induced desorption of adsorbates[58,71,72]. The photobolometric effect is related to the direct heating of the material by the incident radiation, leading to changes in its transport parameters, such as carrier mobility and carrier concentration, and consequently to a reduction of the channel resistance. This thermal contribution is boosted at higher temperature and determines a slower response. In parallel, the combined effect of light and elevated temperature promotes the desorption of residual surface adsorbates, further enhancing the n-type doping of ReS_2 and causing the device to stabilize at progressively higher current levels after each illumination cycle[73].

A similar temperature-dependent photoresponse, governed by the interplay between photobolometric effects and light-induced desorption of adsorbates, has been reported in other two-dimensional materials such as MoS_2[74].

4.4.5 Supporting measurements

The results presented in the previous sections are further supported by additional measurements.

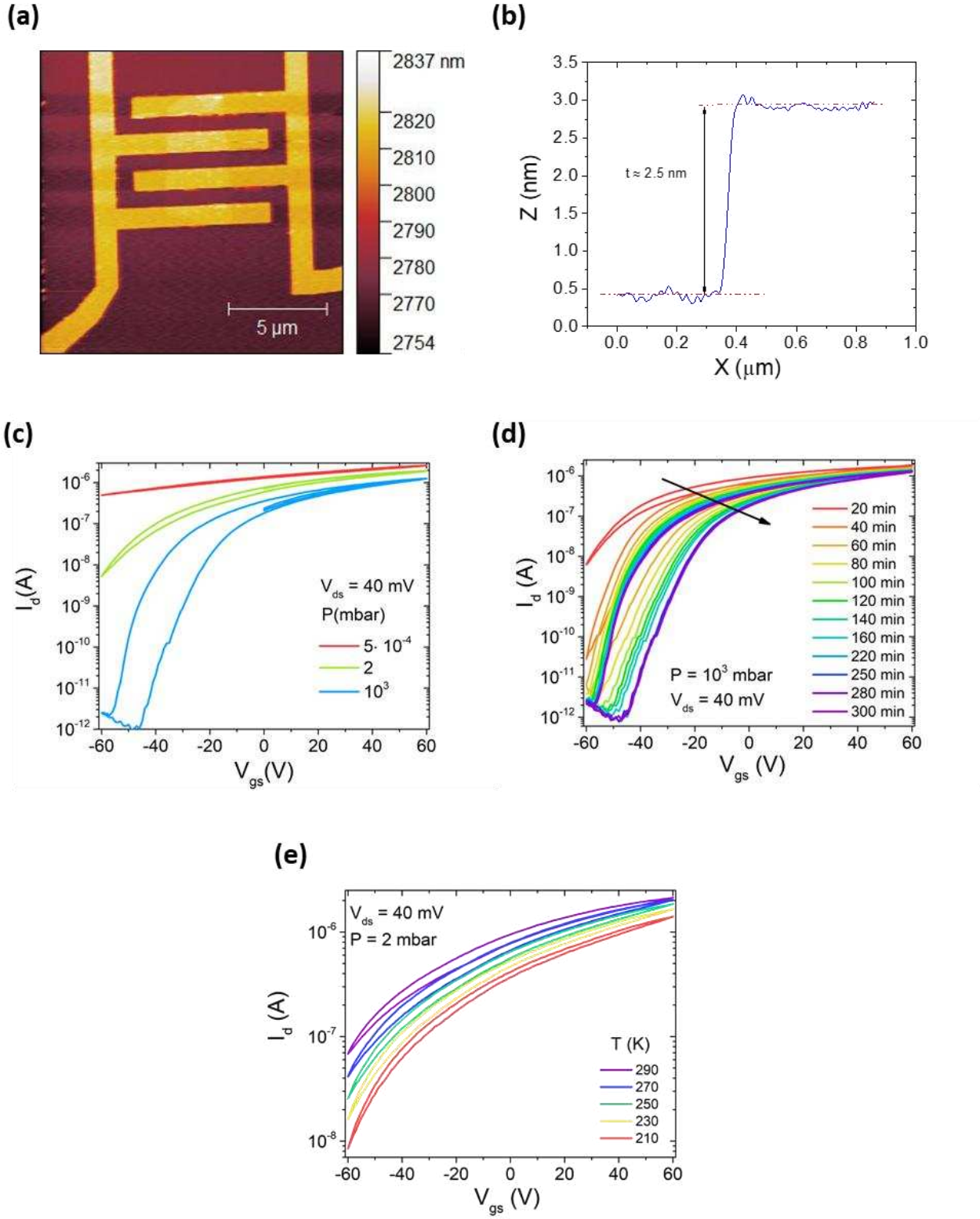

Figure 4.10: (a) AFM image of the device and (b) AFM profile. (c) Comparison between transfer curves

at different pressures. (d) Evolution of the transfer curve at ambient pressure. (f) Temperature dependent measurements performed in low vacuum conditions.

They were performed on other mechanically exfoliated few-layer ReS_2 -based FETs, fabricated with the same procedure. Some representative data are briefly reported here.

Figures 4.10a and 4.10b reveal that the device under investigation is based on a few-layer ReS_2 flake. Its pressure- and temperature-dependent electrical behavior is consistent with the trends discussed in the previous sections. In particular, Figure 4.10c shows that, at ambient pressure, the transfer curve exhibits a wider hysteresis, a higher I_{on}/I_{off} ratio, and a lower channel conductivity compared to measurements performed in low and high vacuum. Also in this case, the transfer curve evolution in air (Figure 4.10d) was monitored over time, revealing a progressive increase of the hysteresis and a gradual switching-off of the transistor within the explored gate-voltage range. This behavior further supports the interpretation that the hysteresis mainly originates from trap states induced by surface adsorbates.

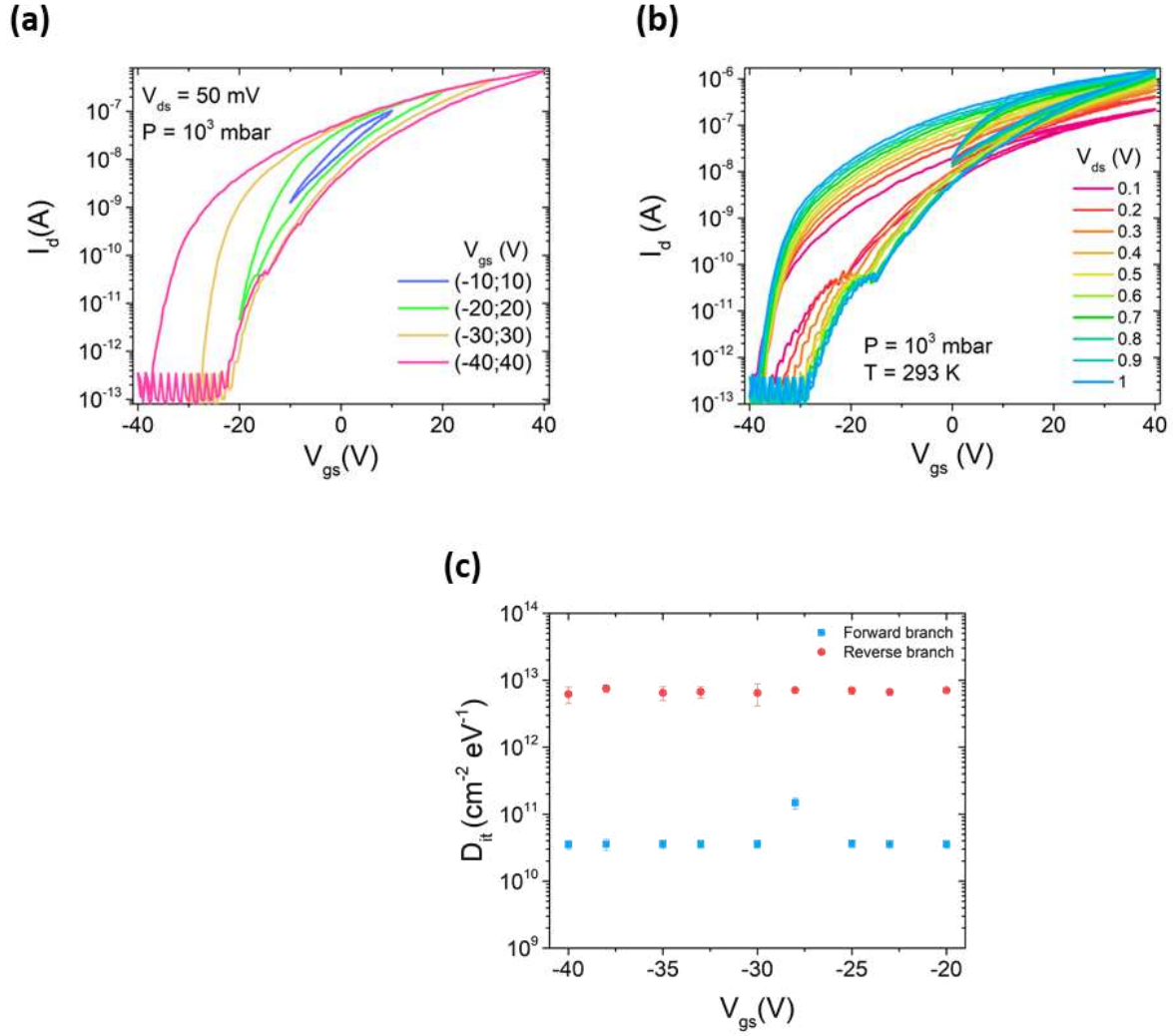

Figure 4.11: (a) Transfer curves as a function of the gate bias range. (b) Transfer curves at different V_{ds}. (c) D_{it} extraction.

Temperature-dependent measurements were also performed in low vacuum (Figure 4.10e). Although a smaller temperature range was investigated, the results are in good agreement with those previously discussed, confirming the reproducibility of the observed transport behavior in few-layer ReS_2 FETs.

The dependence of the hysteresis on the applied electrical bias was further investigated on a third few-layer ReS_2-based FET. Figure 4.11a shows the transfer curves measured by sweeping the gate voltage over progressively wider voltage ranges. In this case, V_{gs} was swept up to ± 40 V, since the device already turns off within this interval. As the gate-voltage sweep range is increased, the hysteresis width correspondingly enlarges, reaching values of the order of 20 V for the widest sweep. This behavior confirms that the hysteresis is strongly dependent on the applied gate bias. In contrast, only minor variations of the transfer curves are observed when changing V_{ds}, as shown in Figure 4.11b, indicating a weak dependence of the hysteresis on it. From the transfer curves in Figure 4.11b it is possible to estimate the interface trap density at ambient pressure[75]. In the subthreshold region of the transfer characteristics, the drain current can be described by the relation

$$I_{ds} = I_m \left[1 - \exp\left(-\frac{qmV_{ds}}{nkT}\right)\right] \qquad (4.5)$$

where $m = 1 + C_d/C_{ox}$ and $n = 1 + (C_d + C_{it})/C_{ox}$. Here, C_{ox} is the gate-oxide capacitance, C_d is the depletion capacitance, and C_{it} is the interface trap capacitance. By extracting n and m from the transfer curves, according to the model in Ref[76], D_{it} can be extracted as a function of V_{gs} according to the formula:

$$D_{it} = \frac{C_{ox}}{q}(n - m) \qquad (4.6)$$

The results are reported in Figure 4.11c and they further support the presence of a substantial density of electrically active interface traps that govern the hysteretic behavior of ReS_2-based FETs.

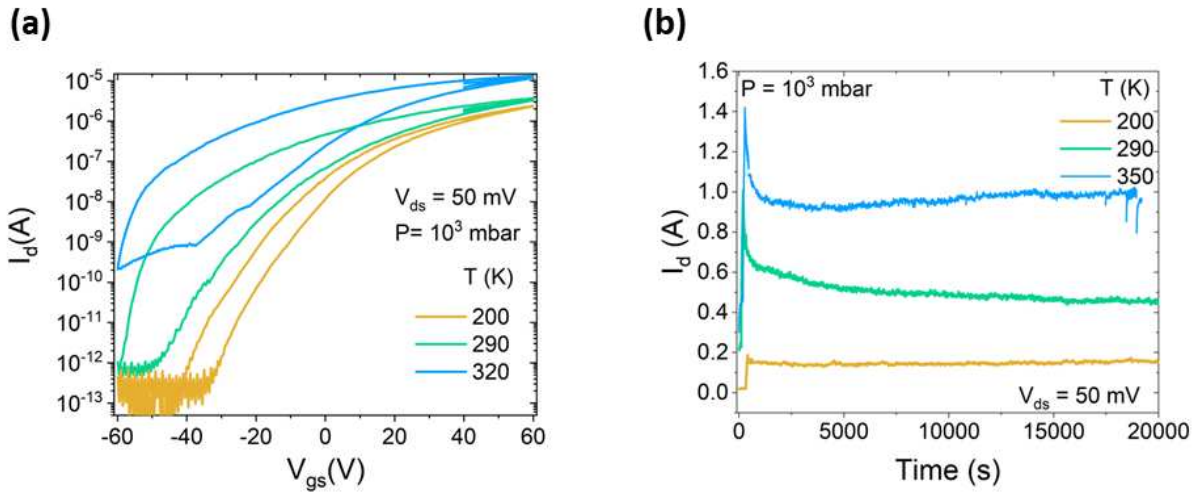

Figure 4.12: (a) Transfer curves at ambient pressure as a function of temperature (b) Investigation of the persistent photoconductivity at different temperatures.

Persistent photoconductivity under ambient-pressure conditions, discussed in the preceding section, was further investigated at different temperatures on another ReS_2-based FET. Figure 4.12 reports measurements performed at 200 K, 290 K, and 350 K. In all three cases, the drain current does not reach the previous dark state after illumination, indicating the presence of a persistent-like photoconductive response. At low temperature (200 K), when the illumination is switched off, the drain current remains nearly at the photocurrent level, showing only a very slight decrease and then stabilizing. This almost flat post-illumination behavior might indicate that photogenerated carriers remain effectively trapped and that recombination processes are strongly suppressed on the experimental time scale, since the detrapping process is slower at low temperatures.

At room temperature (290 K), the temporal evolution of the photocurrent can be accurately described by a double-exponential decay, as discussed in the previous section, revealing the coexistence of fast and slow recombination channels. At elevated temperature (350 K) when the illumination is switched off, the drain current initially starts to decrease, following a trend similar to that observed at room temperature. However, after this initial decay, the current evolution is progressively influenced by a thermally activated contribution to the channel conductance. As a result, a weak increase of the current is observed rather than a continued decay.

In conclusion, the reproducible behaviour across several devices demonstrates that the electrical and optical performance of ReS_2 FETs is strongly modulated by pressure- and temperature-dependent surface interactions and trapping processes.

References

(1) Rahman, M.; Davey, K.; Qiao, S.-Z. Advent of 2D Rhenium Disulfide (ReS2): Fundamentals to Applications. *Adv. Funct. Mater.* **2017**, *27* (10), 1606129. https://doi.org/10.1002/adfm.201606129.

(2) Lamfers, H.-J.; Meetsma, A.; Wiegers, G. A.; de Boer, J. L. The Crystal Structure of Some Rhenium and Technetium Dichalcogenides. *J. Alloys Compd.* **1996**, *241* (1), 34–39. https://doi.org/10.1016/0925-8388(96)02313-4.

(3) Friemelt, K.; Akari, S.; Lux-Steiner, M.-Ch.; Schill, T.; Bucher, E.; Dransfeld, K. Scanning Tunneling Microscopy with Atomic Resolution on ReS2 Single Crystals Grown by Vapor Phase Transport. *Ann. Phys.* **1992**, *504* (4), 248–253. https://doi.org/10.1002/andp.19925040403.

(4) Murray, H. H.; Kelty, S. P.; Chianelli, R. R.; Day, C. S. Structure of Rhenium Disulfide. *Inorg. Chem.* **1994**, *33* (19), 4418–4420. https://doi.org/10.1021/ic00097a037.

(5) Lin, Y.-C.; Komsa, H.-P.; Yeh, C.-H.; Björkman, T.; Liang, Z.-Y.; Ho, C.-H.; Huang, Y.-S.; Chiu, P.-W.; Krasheninnikov, A. V.; Suenaga, K. Single-Layer ReS2: Two-Dimensional Semiconductor with Tunable In-Plane Anisotropy. *ACS Nano* **2015**, *9* (11), 11249–11257. https://doi.org/10.1021/acsnano.5b04851.

(6) Zhang, Q.; Fu, L. Novel Insights and Perspectives into Weakly Coupled ReS2 toward Emerging Applications. *Chem* **2019**, *5* (3), 505–525. https://doi.org/10.1016/j.chempr.2018.11.004.

(7) Tongay, S.; Sahin, H.; Ko, C.; Luce, A.; Fan, W.; Liu, K.; Zhou, J.; Huang, Y.-S.; Ho, C.-H.; Yan, J.; Ogletree, D. F.; Aloni, S.; Ji, J.; Li, S.; Li, J.; Peeters, F. M.; Wu, J. Monolayer

Behaviour in Bulk ReS2 Due to Electronic and Vibrational Decoupling. *Nat. Commun.* **2014**, *5* (1), 3252. https://doi.org/10.1038/ncomms4252.

(8) Feng, Y.; Zhou, W.; Wang, Y.; Zhou, J.; Liu, E.; Fu, Y.; Ni, Z.; Wu, X.; Yuan, H.; Miao, F.; Wang, B.; Wan, X.; Xing, D. Raman Vibrational Spectra of Bulk to Monolayer $\mathrm{Re}{\mathrm{S}}_{2}$ with Lower Symmetry. *Phys. Rev. B* **2015**, *92* (5), 054110. https://doi.org/10.1103/PhysRevB.92.054110.

(9) Liu, E.; Fu, Y.; Wang, Y.; Feng, Y.; Liu, H.; Wan, X.; Zhou, W.; Wang, B.; Shao, L.; Ho, C.-H.; Huang, Y.-S.; Cao, Z.; Wang, L.; Li, A.; Zeng, J.; Song, F.; Wang, X.; Shi, Y.; Yuan, H.; Hwang, H. Y.; Cui, Y.; Miao, F.; Xing, D. Integrated Digital Inverters Based on Two-Dimensional Anisotropic ReS2 Field-Effect Transistors. *Nat. Commun.* **2015**, *6* (1), 6991. https://doi.org/10.1038/ncomms7991.

(10) Friemelt, K.; Kulikova, L.; Kulyuk, L.; Siminel, A.; Arushanov, E.; Kloc, Ch.; Bucher, E. Optical and Photoelectrical Properties of ReS2 Single Crystals. *J. Appl. Phys.* **1996**, *79* (12), 9268–9272. https://doi.org/10.1063/1.362602.

(11) Zhang, X.; Li, Q. Electronic and Magnetic Properties of Nonmetal Atoms Adsorbed ReS2 Monolayers. *J. Appl. Phys.* **2015**, *118* (6), 064306. https://doi.org/10.1063/1.4928460.

(12) Yu, S.; Zhu, H.; Eshun, K.; Shi, C.; Zeng, M.; Li, Q. Strain-Engineering the Anisotropic Electrical Conductance in ReS2 Monolayer. *Appl. Phys. Lett.* **2016**, *108* (19), 191901. https://doi.org/10.1063/1.4947195.

(13) Cui, Q.; He, J.; Bellus, M. Z.; Mirzokarimov, M.; Hofmann, T.; Chiu, H.-Y.; Antonik, M.; He, D.; Wang, Y.; Zhao, H. Transient Absorption Measurements on Anisotropic Monolayer ReS2. *Small* **2015**, *11* (41), 5565–5571. https://doi.org/10.1002/smll.201501668.

(14) Zhang, E.; Jin, Y.; Yuan, X.; Wang, W.; Zhang, C.; Tang, L.; Liu, S.; Zhou, P.; Hu, W.; Xiu, F. ReS2-Based Field-Effect Transistors and Photodetectors. *Adv. Funct. Mater.* **2015**, *25* (26), 4076–4082. https://doi.org/10.1002/adfm.201500969.

(15) Liu, E.; Long, M.; Zeng, J.; Luo, W.; Wang, Y.; Pan, Y.; Zhou, W.; Wang, B.; Hu, W.; Ni, Z.; You, Y.; Zhang, X.; Qin, S.; Shi, Y.; Watanabe, K.; Taniguchi, T.; Yuan, H.; Hwang, H. Y.; Cui, Y.; Miao, F.; Xing, D. High Responsivity Phototransistors Based on Few-Layer ReS2 for Weak Signal Detection. *Adv. Funct. Mater.* **2016**, *26* (12), 1938–1944. https://doi.org/10.1002/adfm.201504408.

(16) Shim, J.; Oh, A.; Kang, D.-H.; Oh, S.; Jang, S. K.; Jeon, J.; Jeon, M. H.; Kim, M.; Choi, C.; Lee, J.; Lee, S.; Yeom, G. Y.; Song, Y. J.; Park, J.-H. High-Performance 2D Rhenium Disulfide (ReS2) Transistors and Photodetectors by Oxygen Plasma Treatment. *Adv. Mater.* **2016**, *28* (32), 6985–6992. https://doi.org/10.1002/adma.201601002.

(17) Xiang, D.; Liu, T.; Wang, J.; Wang, P.; Wang, L.; Zheng, Y.; Wang, Y.; Gao, J.; Ang, K.-W.; Eda, G.; Hu, W.; Liu, L.; Chen, W. TMD-Based Phototransistors: Anomalous Broadband Spectrum Photodetection in 2D Rhenium Disulfide Transistor (Advanced Optical Materials 23/2019). *Adv. Opt. Mater.* **2019**, *7* (23), 1970088. https://doi.org/10.1002/adom.201970088.

(18) Zulkefli, A.; Mukherjee, B.; Hayakawa, R.; Iwasaki, T.; Nakaharai, S.; Wakayama, Y. Light-Assisted and Gate-Tunable Oxygen Gas Sensor Based on Rhenium Disulfide Field-Effect Transistors. *Phys. Status Solidi RRL – Rapid Res. Lett.* **2020**, *14* (11), 2000330. https://doi.org/10.1002/pssr.202000330.

(19) Yang, A.; Gao, J.; Li, B.; Tan, J.; Xiang, Y.; Gupta, T.; Li, L.; Suresh, S.; Idrobo, J. C.; Lu, T.-M.; Rong, M.; Koratkar, N. Humidity Sensing Using Vertically Oriented Arrays of ReS2 Nanosheets Deposited on an Interdigitated Gold Electrode. *2D Mater.* **2016**, *3* (4), 045012. https://doi.org/10.1088/2053-1583/3/4/045012.

(20) Kumar, A.; Viscardi, L.; Faella, E.; Giubileo, F.; Intonti, K.; Pelella, A.; Sleziona, S.; Kharsah, O.; Schleberger, M.; Di Bartolomeo, A. Temperature Dependent Black Phosphorus Transistor and Memory. *Nano Express* **2023**, *4* (1), 014001. https://doi.org/10.1088/2632-959X/acbe11.

(21) Liu, Y.; Liu, Z.; Lew, W. S.; Wang, Q. J. Temperature Dependence of the Electrical Transport Properties in Few-Layer Graphene Interconnects. *Nanoscale Res. Lett.* **2013**, *8* (1), 335. https://doi.org/10.1186/1556-276X-8-335.

(22) Wu, L.; Ji, Y.; Ouyang, B.; Li, Z.; Yang, Y. Low-Temperature Induced Enhancement of Photoelectric Performance in Semiconducting Nanomaterials. *Nanomaterials* **2021**, *11* (5), 1131. https://doi.org/10.3390/nano11051131.

(23) Pradhan, N. R.; McCreary, A.; Rhodes, D.; Lu, Z.; Feng, S.; Manousakis, E.; Smirnov, D.; Namburu, R.; Dubey, M.; Hight Walker, A. R.; Terrones, H.; Terrones, M.; Dobrosavljevic, V.; Balicas, L. Metal to Insulator Quantum-Phase Transition in Few-Layered ReS2. *Nano Lett.* **2015**, *15* (12), 8377–8384. https://doi.org/10.1021/acs.nanolett.5b04100.

(24) Corbet, C. M.; McClellan, C.; Rai, A.; Sonde, S. S.; Tutuc, E.; Banerjee, S. K. Field Effect Transistors with Current Saturation and Voltage Gain in Ultrathin ReS2. *ACS Nano* **2015**, *9* (1), 363–370. https://doi.org/10.1021/nn505354a.

(25) Chenet, D. A.; Aslan, B.; Huang, P. Y.; Fan, C.; van der Zande, A. M.; Heinz, T. F.; Hone, J. C. In-Plane Anisotropy in Mono- and Few-Layer ReS2 Probed by Raman Spectroscopy and Scanning Transmission Electron Microscopy. *Nano Lett.* **2015**, *15* (9), 5667–5672. https://doi.org/10.1021/acs.nanolett.5b00910.

(26) Nagler, P.; Plechinger, G.; Schüller, C.; Korn, T. Observation of Anisotropic Interlayer Raman Modes in Few-Layer ReS2. *Phys. Status Solidi RRL – Rapid Res. Lett.* **2016**, *10* (2), 185–189. https://doi.org/10.1002/pssr.201510412.

(27) Chenet, D. A.; Aslan, B.; Huang, P. Y.; Fan, C.; van der Zande, A. M.; Heinz, T. F.; Hone, J. C. In-Plane Anisotropy in Mono- and Few-Layer ReS2 Probed by Raman Spectroscopy and Scanning Transmission Electron Microscopy. *Nano Lett.* **2015**, *15* (9), 5667–5672. https://doi.org/10.1021/acs.nanolett.5b00910.

(28) Faella, E.; Intonti, K.; Viscardi, L.; Giubileo, F.; Kumar, A.; Lam, H. T.; Anastasiou, K.; Craciun, M. F.; Russo, S.; Di Bartolomeo, A. Electric Transport in Few-Layer ReSe2 Transistors Modulated by Air Pressure and Light. *Nanomaterials* **2022**, *12* (11), 1886. https://doi.org/10.3390/nano12111886.

(29) Di Bartolomeo, A.; Grillo, A.; Urban, F.; Iemmo, L.; Giubileo, F.; Luongo, G.; Amato, G.; Croin, L.; Sun, L.; Liang, S.-J.; Ang, L. K. Asymmetric Schottky Contacts in Bilayer MoS2 Field Effect Transistors. *Adv. Funct. Mater.* **2018**, *28* (28), 1800657. https://doi.org/10.1002/adfm.201800657.

(30) Mitta, S. B.; Choi, M. S.; Nipane, A.; Ali, F.; Kim, C.; Teherani, J. T.; Hone, J.; Yoo, W. J. Electrical Characterization of 2D Materials-Based Field-Effect Transistors. *2D Mater.* **2020**, *8* (1), 012002. https://doi.org/10.1088/2053-1583/abc187.

(31) Zhang, S.; Wang, C.-G.; Li, M.-Y.; Huang, D.; Li, L.-J.; Ji, W.; Wu, S. Defect Structure of Localized Excitons in a ${\mathrm{WSe}}_{2}$ Monolayer. *Phys. Rev. Lett.* **2017**, *119* (4), 046101. https://doi.org/10.1103/PhysRevLett.119.046101.

(32) Horzum, S.; Çakır, D.; Suh, J.; Tongay, S.; Huang, Y.-S.; Ho, C.-H.; Wu, J.; Sahin, H.; Peeters, F. M. Formation and Stability of Point Defects in Monolayer Rhenium Disulfide. *Phys. Rev. B* **2014**, *89* (15), 155433. https://doi.org/10.1103/PhysRevB.89.155433.

(33) Intonti, K.; Coleman, E.; Blake, A.; Lyons, C.; Hydes, A.; Di Bartolomeo, A.; Gity, F.; Hurley, P. K. Role of Interface and Bulk Traps on the Capacitance–Voltage Characteristics of

WS2/Al2O3/Si Capacitors. *Solid-State Electron.* **2023**, *207*, 108697. https://doi.org/10.1016/j.sse.2023.108697.

(34) Li, W.; Jia, Q.; Dong, H.; Wang, Z.; Wang, Y.; Wu, Y.; Zhao, X.; Chen, Z.; Wang, S. ReS2 Nanosheet-Based Channels for Two-Dimensional Field Effect Transistors and Phototransistors with High Photoresponsivity. *ACS Appl. Nano Mater.* **2023**, *6* (1), 512–522. https://doi.org/10.1021/acsanm.2c04600.

(35) Malik, M.; Iqbal, M. A.; Choi, J. R.; Pham, P. V. 2D Materials for Efficient Photodetection: Overview, Mechanisms, Performance and UV-IR Range Applications. *Front. Chem.* **2022**, *10*. https://doi.org/10.3389/fchem.2022.905404.

(36) Late, D. J.; Liu, B.; Matte, H. S. S. R.; Dravid, V. P.; Rao, C. N. R. Hysteresis in Single-Layer MoS2 Field Effect Transistors. *ACS Nano* **2012**, *6* (6), 5635–5641. https://doi.org/10.1021/nn301572c.

(37) Pelella, A.; Intonti, K.; Viscardi, L.; Durante, O.; Capista, D.; Passacantando, M.; Giubileo, F.; Romano, P.; Alshehri, M. A. S.; Alghamdi, M. S. G.; Craciun, M. F.; Russo, S.; Di Bartolomeo, A. Two-Dimensional ∝-In2Se3 Field Effect Transistor for Wide-Band Photodetection and Non-Volatile Memory. *J. Phys. Chem. Solids* **2023**, *183*, 111653. https://doi.org/10.1016/j.jpcs.2023.111653.

(38) Urban, F.; Giubileo, F.; Grillo, A.; Iemmo, L.; Luongo, G.; Passacantando, M.; Foller, T.; Madauß, L.; Pollmann, E.; Geller, M. P.; Oing, D.; Schleberger, M.; Di Bartolomeo, A. Gas Dependent Hysteresis in MoS2 Field Effect Transistors. *2D Mater.* **2019**, *6* (4), 045049. https://doi.org/10.1088/2053-1583/ab4020.

(39) Di Bartolomeo, A.; Genovese, L.; Giubileo, F.; Iemmo, L.; Luongo, G.; Foller, T.; Schleberger, M. Hysteresis in the Transfer Characteristics of MoS2 Transistors. *2D Mater.* **2017**, *5* (1), 015014. https://doi.org/10.1088/2053-1583/aa91a7.

(40) Qiu, H. (邱浩); Pan, L. (潘力佳); Yao, Z. (姚宗妮); Li, J. (李俊杰); Shi, Y. (施毅); Wang, X. (王欣然). Electrical Characterization of Back-Gated Bi-Layer MoS2 Field-Effect Transistors and the Effect of Ambient on Their Performances. *Appl. Phys. Lett.* **2012**, *100* (12), 123104. https://doi.org/10.1063/1.3696045.

(41) Urban, F.; Martucciello, N.; Peters, L.; McEvoy, N.; Di Bartolomeo, A. Environmental Effects on the Electrical Characteristics of Back-Gated WSe2 Field-Effect Transistors. *Nanomaterials* **2018**, *8* (11), 901. https://doi.org/10.3390/nano8110901.

(42) Huo, N.; Yang, S.; Wei, Z.; Li, S.-S.; Xia, J.-B.; Li, J. Photoresponsive and Gas Sensing Field-Effect Transistors Based on Multilayer WS_2 Nanoflakes. *Sci. Rep.* **2014**, *4*, 5209. https://doi.org/10.1038/srep05209.

(43) Horzum, S.; Çakır, D.; Suh, J.; Tongay, S.; Huang, Y.-S.; Ho, C.-H.; Wu, J.; Sahin, H.; Peeters, F. M. Formation and Stability of Point Defects in Monolayer Rhenium Disulfide. *Phys. Rev. B* **2014**, *89* (15), 155433. https://doi.org/10.1103/PhysRevB.89.155433.

(44) Plumadore, R.; Baskurt, M.; Boddison-Chouinard, J.; Lopinski, G.; Modarresi, M.; Potasz, P.; Hawrylak, P.; Sahin, H.; Peeters, F. M.; Luican-Mayer, A. Prevalence of Oxygen Defects in an In-Plane Anisotropic Transition Metal Dichalcogenide. *Phys. Rev. B* **2020**, *102* (20), 205408. https://doi.org/10.1103/PhysRevB.102.205408.

(45) Intonti, K.; Faella, E.; Viscardi, L.; Kumar, A.; Durante, O.; Giubileo, F.; Passacantando, M.; Lam, H. T.; Anastasiou, K.; Craciun, M. F.; Russo, S.; Di Bartolomeo, A. Hysteresis and Photoconductivity of Few-Layer ReSe2 Field Effect Transistors Enhanced by Air Pressure. *Adv. Electron. Mater.* **2023**, *9* (8), 2300066. https://doi.org/10.1002/aelm.202300066.

(46) Sarker, B. K.; Arif, M.; Khondaker, S. I. Near-Infrared Photoresponse in Single-Walled Carbon Nanotube/Polymer Composite Films. *Carbon* **2010**, *48* (5), 1539–1544. https://doi.org/10.1016/j.carbon.2009.11.065.

(47) Jiang, J.; Ling, C.; Xu, T.; Wang, W.; Niu, X.; Zafar, A.; Yan, Z.; Wang, X.; You, Y.; Sun, L.; Lu, J.; Wang, J.; Ni, Z. Defect Engineering for Modulating the Trap States in 2D Photoconductors. *Adv. Mater. Deerfield Beach Fla* **2018**, e1804332. https://doi.org/10.1002/adma.201804332.

(48) Liu, E.; Long, M.; Zeng, J.; Luo, W.; Wang, Y.; Pan, Y.; Zhou, W.; Wang, B.; Hu, W.; Ni, Z.; You, Y.; Zhang, X.; Qin, S.; Shi, Y.; Watanabe, K.; Taniguchi, T.; Yuan, H.; Hwang, H. Y.; Cui, Y.; Miao, F.; Xing, D. High Responsivity Phototransistors Based on Few-Layer ReS2 for Weak Signal Detection. *Adv. Funct. Mater.* **2016**, *26* (12), 1938–1944. https://doi.org/10.1002/adfm.201504408.

(49) Shim, J.; Oh, A.; Kang, D.-H.; Oh, S.; Jang, S. K.; Jeon, J.; Jeon, M. H.; Kim, M.; Choi, C.; Lee, J.; Lee, S.; Yeom, G. Y.; Song, Y. J.; Park, J.-H. High-Performance 2D Rhenium Disulfide (ReS2) Transistors and Photodetectors by Oxygen Plasma Treatment. *Adv. Mater.* **2016**, *28* (32), 6985–6992. https://doi.org/10.1002/adma.201601002.

(50) De Stefano, S.; Durante, O.; Sessa, A.; Politano, A.; D'Olimpio, G.; Dadiani, T.; Faella, E.; Dinescu, A.; Parvulescu, C.; Hetherington, C.; Kuo, C.-N.; Lue, C. S.; Aldrigo, M.; Passacantando, M.; Di Bartolomeo, A. Neuromorphic Photoresponse in Ultrathin SnS2-Based Field Effect Transistor. *ACS Appl. Mater. Interfaces* **2025**, *17* (36), 50901–50915. https://doi.org/10.1021/acsami.5c11651.

(51) Mazzotti, A.; Durante, O.; De Stefano, S.; Viscardi, L.; Pelella, A.; Kharsah, O.; Daniel, L.; Sleziona, S.; Schleberger, M.; Di Bartolomeo, A. BP/MoS_2 Van Der Waals Heterojunctions for Self-Powered Photoconduction. *Adv. Opt. Mater.* **2025**, *13* (22), 2500811. https://doi.org/10.1002/adom.202500811.

(52) Czerniak-Łosiewicz, K.; Gertych, A. P.; Świniarski, M.; Judek, J.; Zdrojek, M. Time Dependence of Photocurrent in Chemical Vapor Deposition MoS2 Monolayer—Intrinsic Properties and Environmental Effects. *J. Phys. Chem. C* **2020**, *124* (34), 18741–18746. https://doi.org/10.1021/acs.jpcc.0c04452.

(53) Thole, L.; Ben Kalefa, A.; Belke, C.; Locmelis, S.; Bockhorn, L.; Behrens, P.; Haug, R. J. Long-Persistent Photoconductivity in Transistor Structures Made from Thin ZrS3-Films. *ACS Appl. Electron. Mater.* **2023**, *5* (11), 6286–6291. https://doi.org/10.1021/acsaelm.3c01163.

(54) George, A.; Fistul, M. V.; Gruenewald, M.; Kaiser, D.; Lehnert, T.; Mupparapu, R.; Neumann, C.; Hübner, U.; Schaal, M.; Masurkar, N.; Arava, L. M. R.; Staude, I.; Kaiser, U.; Fritz, T.; Turchanin, A. Giant Persistent Photoconductivity in Monolayer MoS2 Field-Effect Transistors. *Npj 2D Mater. Appl.* **2021**, *5* (1), 15. https://doi.org/10.1038/s41699-020-00182-0.

(55) Gao, S.-L.; Qiu, L.-P.; Zhang, J.; Han, W.-P.; Ramakrishna, S.; Long, Y.-Z. Persistent Photoconductivity of Metal Oxide Semiconductors. *ACS Appl. Electron. Mater.* **2024**, *6* (3), 1542–1561. https://doi.org/10.1021/acsaelm.3c01549.

(56) Wu, Y.-C.; Liu, C.-H.; Chen, S.-Y.; Shih, F.-Y.; Ho, P.-H.; Chen, C.-W.; Liang, C.-T.; Wang, W.-H. Extrinsic Origin of Persistent Photoconductivity in Monolayer MoS2 Field Effect Transistors. *Sci. Rep.* **2015**, *5* (1), 11472. https://doi.org/10.1038/srep11472.

(57) Cho, K.; Kim, T.-Y.; Park, W.; Park, J.; Kim, D.; Jang, J.; Jeong, H.; Hong, S.; Lee, T. Gate-Bias Stress-Dependent Photoconductive Characteristics of Multi-Layer MoS2 Field-Effect Transistors. *Nanotechnology* **2014**, *25* (15), 155201. https://doi.org/10.1088/0957-4484/25/15/155201.

(58) Zhang, W.; Huang, J.-K.; Chen, C.-H.; Chang, Y.-H.; Cheng, Y.-J.; Li, L.-J. High-Gain Phototransistors Based on a CVD MoS2 Monolayer. *Adv. Mater.* **2013**, *25* (25), 3456–3461. https://doi.org/10.1002/adma.201301244.

(59) De, D.; Manongdo, J.; See, S.; Zhang, V.; Guloy, A.; Peng, H. High on/off Ratio Field Effect Transistors Based on Exfoliated Crystalline SnS2 Nano-Membranes. *Nanotechnology* **2012**, *24* (2), 025202. https://doi.org/10.1088/0957-4484/24/2/025202.

(60) Knoch, J. *Nanoelectronics: Device Physics, Fabrication, Simulation*; De Gruyter Oldenbourg, 2020. https://doi.org/10.1515/9783110575507.

(61) Park, J. Y.; Joe, H.-E.; Yoon, H. S.; Yoo, S.; Kim, T.; Kang, K.; Min, B.-K.; Jun, S. C. Contact Effect of ReS2/Metal Interface. *ACS Appl. Mater. Interfaces* **2017**, *9* (31), 26325–26332. https://doi.org/10.1021/acsami.7b06432.

(62) Pradhan, N. R.; Garcia, C.; Isenberg, B.; Rhodes, D.; Feng, S.; Memaran, S.; Xin, Y.; McCreary, A.; Walker, A. R. H.; Raeliarijaona, A.; Terrones, H.; Terrones, M.; McGill, S.; Balicas, L. Phase Modulators Based on High Mobility Ambipolar ReSe2 Field-Effect Transistors. *Sci. Rep.* **2018**, *8* (1), 12745. https://doi.org/10.1038/s41598-018-30969-7.

(63) Kim, C.; Moon, I.; Lee, D.; Choi, M. S.; Ahmed, F.; Nam, S.; Cho, Y.; Shin, H.-J.; Park, S.; Yoo, W. J. Fermi Level Pinning at Electrical Metal Contacts of Monolayer Molybdenum Dichalcogenides. *ACS Nano* **2017**, *11* (2), 1588–1596. https://doi.org/10.1021/acsnano.6b07159.

(64) Liu, Y.; Guo, J.; Zhu, E.; Liao, L.; Lee, S.-J.; Ding, M.; Shakir, I.; Gambin, V.; Huang, Y.; Duan, X. Approaching the Schottky–Mott Limit in van Der Waals Metal–Semiconductor Junctions. *Nature* **2018**, *557* (7707), 696–700. https://doi.org/10.1038/s41586-018-0129-8.

(65) Kim, C.; Moon, I.; Lee, D.; Choi, M. S.; Ahmed, F.; Nam, S.; Cho, Y.; Shin, H.-J.; Park, S.; Yoo, W. Fermi Level Pinning at Electrical Metal Contacts of Monolayer Molybdenum Dichalcogenides. *ACS Nano* **2017**, *11*. https://doi.org/10.1021/acsnano.6b07159.

(66) Bampoulis, P.; van Bremen, R.; Yao, Q.; Poelsema, B.; Zandvliet, H. J. W.; Sotthewes, K. Defect Dominated Charge Transport and Fermi Level Pinning in MoS2/Metal Contacts. *ACS Appl. Mater. Interfaces* **2017**, *9* (22), 19278–19286. https://doi.org/10.1021/acsami.7b02739.

(67) Cui, X.; Shih, E.-M.; Jauregui, L. A.; Chae, S. H.; Kim, Y. D.; Li, B.; Seo, D.; Pistunova, K.; Yin, J.; Park, J.-H.; Choi, H.-J.; Lee, Y. H.; Watanabe, K.; Taniguchi, T.; Kim, P.; Dean, C. R.; Hone, J. C. Low-Temperature Ohmic Contact to Monolayer MoS2 by van Der Waals Bonded Co/h-BN Electrodes. *Nano Lett.* **2017**, *17* (8), 4781–4786. https://doi.org/10.1021/acs.nanolett.7b01536.

(68) Radisavljevic, B.; Kis, A. Mobility Engineering and a Metal–Insulator Transition in Monolayer MoS2. *Nat. Mater.* **2013**, *12* (9), 815–820. https://doi.org/10.1038/nmat3687.

(69) Radisavljevic, B.; Kis, A. Mobility Engineering and a Metal-Insulator Transition in Monolayer MoS2. *Nat. Mater.* **2013**, *12* (9), 815–820. https://doi.org/10.1038/nmat3687.

(70) Tobehn-Steinhäuser, I.; Reiche, M.; Schmelz, M.; Stolz, R.; Fröhlich, T.; Ortlepp, T. Carrier Mobility in Semiconductors at Very Low Temperatures. *Eng. Proc.* **2021**, *6* (1), 86. https://doi.org/10.3390/I3S2021Dresden-10086.

(71) Yang, C.; Wang, G.; Liu, M.; Yao, F.; Li, H. Mechanism, Material, Design, and Implementation Principle of Two-Dimensional Material Photodetectors. *Nanomaterials* **2021**, *11* (10), 2688. https://doi.org/10.3390/nano11102688.

(72) Grillo, A.; Faella, E.; Pelella, A.; Giubileo, F.; Ansari, L.; Gity, F.; Hurley, P. K.; McEvoy, N.; Di Bartolomeo, A. Coexistence of Negative and Positive Photoconductivity in Few-Layer PtSe2 Field-Effect Transistors. *Adv. Funct. Mater.* **2021**, *31* (43), 2105722. https://doi.org/10.1002/adfm.202105722.

(73) Zulkefli, A.; Mukherjee, B.; Hayakawa, R.; Iwasaki, T.; Nakaharai, S.; Wakayama, Y. Light-Assisted and Gate-Tunable Oxygen Gas Sensor Based on Rhenium Disulfide Field-Effect Transistors. *Phys. Status Solidi RRL – Rapid Res. Lett.* **2020**, *14* (11), 2000330. https://doi.org/10.1002/pssr.202000330.

(74) Jain, S.; Low, M.; Vashishtha, P.; Nirantar, S.; Zhu, L.; Ton, C.; Ahmed, T.; Sriram, S.; Walia, S.; Gupta, G.; Bhaskaran, M. Influence of Temperature on Photodetection Properties of Honeycomb-like GaN Nanostructures. *Adv. Mater. Interfaces* **2021**, *8*. https://doi.org/10.1002/admi.202100593.

(75) Ahn, J.-H.; Parkin, W. M.; Naylor, C. H.; Johnson, A. T. C.; Drndić, M. Ambient Effects on Electrical Characteristics of CVD-Grown Monolayer MoS2 Field-Effect Transistors. *Sci. Rep.* **2017**, *7* (1), 4075. https://doi.org/10.1038/s41598-017-04350-z.

(76) Zeng, Y. (Anne); Softic, A.; White, M. H. Characterization of Interface Traps in the Subthreshold Region of Implanted 4H and 6H-SiC MOSFETs. *Solid-State Electron.* **2002**, *46* (10), 1579–1582. https://doi.org/10.1016/S0038-1101(02)00108-9.

Chapter 5

Interface Effects in TMD-based Devices: ReS_2/Si heterojunction as a case study

Investigation of the ReS_2/Si interface in 2D/3D vertical heterostructures

5.1 Introduction

The results of the previous chapter confirm that the performance of TMD-based optoelectronic devices can be influenced not only by the intrinsic properties of the material, but also by interfaces, contacts, and device geometry. While planar FET architectures provide a powerful platform to study tunable photoresponse, the ultrathin nature of the channel results in limited optical absorption and makes the device response highly sensitive to trap-assisted processes. These effects can slow down the transient dynamics and impact switching speed and operational stability, while at the same time contributing to higher responsivity.

This chapter extends the investigation toward vertical mixed-dimensional junctions, where built-in electric fields enable rapid separation of photogenerated carriers and more reproducible switching behaviour. Mixed-dimensional 2D ReS_2/3D Si van der Waals heterojunctions combine the strong light–matter interaction and direct bandgap of ReS_2 with the mature fabrication processes of silicon technology. Two different device architectures are fabricated, and their electrical behaviour, including rectification ratio and transport properties, is analyzed. Their photoresponse and transient characteristics under pulsed illumination are investigated through the main figures of merit of photodetectors, both at room temperature and under cryogenic conditions (77 K), motivated by the enhanced reversibility observed in low-temperature transistor measurements.

5.2 2D/3D heterostructures: overview

TMDs have many unique physical properties such as bandgap modulation[1], strong light-matter interaction[2], lack of dangling bonds[3], which make them appealing candidates for applications in optoelectronics, as already mentioned in the previous chapters. In the past decade,

impressive results have been reached in 2D material-based photodetectors, but there are still several issues to be solved. Lack of stable and reliable technology to produce high quality 2D materials films, difficulty in efficiently control the doping type, carrier concentration and stoichiometry of 2D materials, together with the insufficient light absorption resulting from the thin layers of 2D materials, constrain their practical applicability[4]. Moreover, in TMDs-based phototransistors, response speed might be limited by the relatively low carrier mobility, the long transit time of photogenerated carriers, the existence of defects, and the occurrence of persistent photoconductivity [5].

Conversely, traditional 3D semiconductors, such as Si and InGaAs, have experienced long-term development, and it has been progressively reached maturity in their material growth and device fabrication capabilities even if the process is often complex and costly[6]. Photodetector devices based on them have been widely investigated and implemented in photovoltaic devices and visible – near infrared photodetectors. However, the difficult heterogenous integration and the lattice mismatches due to conventional epitaxial techniques prevent further improvements. Consequently, large dark current, high noise, and low response speed are problematics to face within this type of detectors[7].

2D/3D van der Waals heterostructures combine the advantages of both 2D layered materials and traditional 3D bulk materials offering a platform to design multifunctional photodetectors that pure 2D or 3D materials-based devices cannot achieve[8,9]. The pioneering examples of these mixed-dimensional structures were graphene/Si Schottky photodiodes[10], fabricated by transferring graphene directly onto silicon surfaces. The photodiodes have exhibited photodetection properties comparable to commercial devices[11]. Furthermore, by utilizing thick graphene films in combination with silicon, these heterostructures extended their sensitivity into the mid-infrared spectrum, successfully detecting incident light at wavelengths as long as 4 μm[12].

Bulk Si, in fact, acts as an absorbing component, compensating the low light absorption in thin layered materials. Moreover, photodiodes based on vertical heterojunctions, such as Schottky diodes, p-n diodes, n-n or p-p diodes, as well as single barrier heterojunctions, can be realized by exploiting the diverse electrical properties of 2D materials. Thanks to the difference in Fermi levels between the 2D material and Si, an internal electrical field at the interface promotes the separation and transport of photogenerated electron-hole pairs, increasing the response speed. Additionally, 2D materials help in having low dark current, leading to improved specific detectivity, when the device is operated in reverse or zero bias. New functionalities and a broadband spectral response is then enabled by the heterojunction itself[7].

Yim et al. realized the first few-layer MoS_2/Si p-n photodiode, transferring on p-Si a MoS_2 film synthesized through sulfurization[13]. The photodiode showed strong photoconductivity which could be tuned by varying the thickness of MoS_2. Subsequently, TMDs/Si mixed dimensional based photodetectors have become a new research hotspot. Li et al. prepared mechanically exfoliated MoS_2 monolayers transferred on n-type and p-type Si substrates and in both cases a photodiode-like behaviour was observed. The higher photoresponsivity of the MoS_2/n-Si heterostructure was attributed to the larger built-in electric field at the interface, revealed by a Kelvin force microscope[14].

The photodetection performance of the heterojunctions critically depends on the quality of the TMD/Si interface, since contamination during the transfer of the material onto the surface of a Si substrate can degrade their efficiency. Therefore, other approaches have been explored, such as direct synthesis of 2D materials on Si.

For instance, Zhang et al. achieved wide-spectrum detection from 200 nm to 1550 nm by realizing a high-quality vdW Hs made of WSe_2 grown in situ on n-Si[15]. Lu et al employed pulsed laser deposition to deposit a $MoTe_2$ film directly on an n-Si substrate[16]. The carrier collection was further improved by transferring a transparent graphene layer on top or the material. The device showed a clear diode-like behaviour and specific detectivity of $6.8{\cdot}10^{13}$ Jones. Another study by Lei et al reported about a $MoTe_2$/Si heterojunction by growing a $MoTe_2$ film directly on Si using a shadow-mask assisted CVD method[17].

It has to be noted that in a 2D/Si heterojunction, the carrier extraction is less efficient when the 2D plane is parallel to the junction interface. To solve this issue, Wang et al realized a vertically standing MoS_2 layer on a p-Si substrate, reaching an outstanding responsivity up to 117 A/W[18]. Response times of the order of microseconds were measured in a $MoSe_2$/Si heterojunction[19] with the same structure. Further improvements can be obtained by using a nanostructured rather than planar Si substrate. Dhyani et al. prepared a $MoS2_2$/Si device with nanostructured porous Si, obtaining better performances compared to the MoS_2/planar Si, thanks to the higher interfacial barrier height, superior light trapping and larger junction area[20]. Wu et al also reported ultrabroad band photodiodes by using WS_2/pyramid Si heterojunctions[21].

This chapter investigates the electrical transport, photodetection performance, and self-driven operation of 2D/3D ReS_2–Si heterojunctions with different device architectures.

5.3 Materials and methods: Device 1

5.3.1 Device fabrication and characterization

In the first step of the work, large area ReS_2 flakes were mechanically exfoliated and subsequently transferred onto a low-doped n-type substrate. As evident from the optical image in Figure 5.1a, circular Ni/Au pads were patterned on top of the flake surface and a gold layer was deposited as a back contact. The area of the pad is around 2100 μm^2, while the triangular-shaped flake has an area around 7800 μm^2.

The elemental composition of the exfoliated flakes was analysed through Energy-dispersive X-Ray Spectroscopy (EDX). The spectrum of the large area flake used for the fabrication of the device is reported in Figure 5.1b. The concentrations of Re and S confirm a stoichiometric ratio of about 1:2, indicating that the quality of the original crystal was preserved during the exfoliation. The AFM profile, reported in Figure 5.1c, reveals a 219 nm thick flake. The large thickness helps against the low light absorption issue of vertical 2D material-based devices[22]. Indeed, light absorption might be less than 10% if the thickness is below 100 nm[23]. Figure 5.1d depicts a not-to-scale schematic representation of the device together with the measurement

set-up. Measurements were performed in a LakeShore probe station coupled with SCS Keithley 4200.

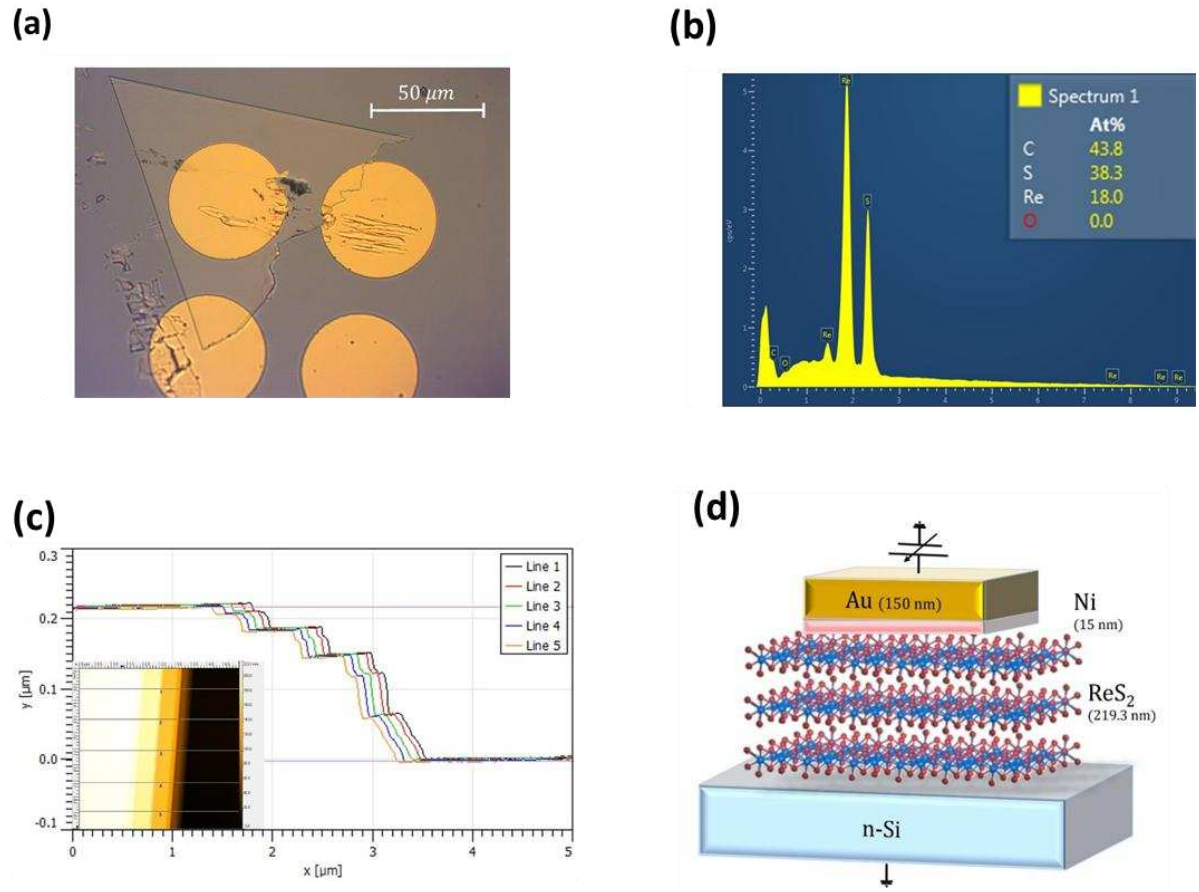

Figure 5.1. (a) Optical image of the device under test. (b) A representative EDX spectrum of the ReS_2 flake. (c) AFM profile across the edge of the flake. The inset shows the AFM image. (d) Schematic 3D structure of the device, with the measurement set up.

5.3.2 Density functional Theory calculations

Non-equilibrium quantum transport calculations were performed based on first-principles calculations. DFT together with the non-equilibrium Green's functions (NEGF) technique (DFT+NEGF) was utilized to represent realistic open systems as implemented in QuantumATK[24].

Use of the semi-infinite electrode boundary conditions is in contrast to using periodic boundary conditions normal to the junction interface, which leads to spurious interactions between periodic images of the interface. The use of electrode boundary conditions enables the isolation of a single junction with electrodes at equilibrium with electron reservoirs providing an accurate description of the charge transfer processes at the material interface forming the junction. Recursion iterative scheme has been used for calculating the self-energies[25]. Energy integral to obtain density matrix within the NEGF framework is performed through a complex contour integration, which includes integral over equilibrium states and non-equilibrium states. The integral over the equilibrium states has been done using semi-circular complex contour[26].

The integral over the non-equilibrium states along the real axis is performed using single contour method[26]. Linear combination of numerical atomic-orbital basis set and generalized gradient approximation (GGA) norm-conserving pseudopotentials from PseudoDojo with medium basis sets[27] are employed in the simulations.

Brillouin zone integrations are performed over a grid of k-points generated according to the Monkhorst-Pack scheme[28], with a density of approximately 10 k-points per angstrom. An energy cut-off of 110 Ha is considered for the discretized grid, and all structural relaxation is performed with a maximum force of less than 0.02 eV $Å^{-1}$. For discretized grid, ~700 k-point per angstrom have been used for the Green's function calculations, in the direction normal to the interface plane. Van-der-Waals interactions are included by adding a nonlocal vdW term to the local and the semi-local exchange correlation functionals utilizing Grimme's dispersion correction.[29] The strain arising from the lattice constant mismatch between the materials at the ReS_2/Si interface, leading to 0.5% biaxial strain, is applied to the ReS_2 lattice.

In the Ni/Si structure, the metal crystallographic orientation with common supercell with minimal strain for Ni[111] has been considered for commensurable interface leading to 1.9% strain which has been applied to the metal electrodes[30–32].The Ni/Si interface structure consists of 224 Ni atoms and 1416 Si atoms (total 1640). The ReS_2/Si interface includes total 1090 atoms (384 ReS2 atoms, 701 Si atoms and 5 hydrogen atoms). To reflect the impact of Si exposure to HF prior to ReS_2 exfoliation the Si surface dangling bonds are passivated with hydrogen.

5.4 Results and discussion: Device 1

The electrical transport through the ReS_2/Si heterostructure was investigated through I-V measurements, firstly performed in the dark and at room temperature. Figure 5.2 reports the typical I-V curve of the Ni/ReS_2/Si structure compared to the same curve obtained for a Ni/Si Schottky diode. A clear rectifying behavior is observed in the Ni/ReS_2/Si heterostructure, with a significantly suppressed current under reverse bias and an enhanced on/off ratio with respect to the Ni/Si junction. The reverse current, indeed, is about 4.1 nA and it is almost constant for negative biases. The rectification ratio is about $7 \cdot 10^2$ at ±1 V, exceeding values commonly reported for other 2D/3D heterojunctions. The turn-on voltage is relatively small, around 0.16 V, as extracted from the I-V curve in Figure 5.2a on a linear scale. Nearly ohmic contact of Ni to ReS_2 was previously confirmed, indicating that the ReS_2/Si junction is primarily responsible for the diode-like characteristic. To gain further insight into the dominant carrier transport mechanisms, temperature-dependent measurements were performed in the 293–393 K range. As reported in Figure 5.2b, increasing temperature leads to progressively more symmetric I–V curves and a reduction of the rectification ratio.

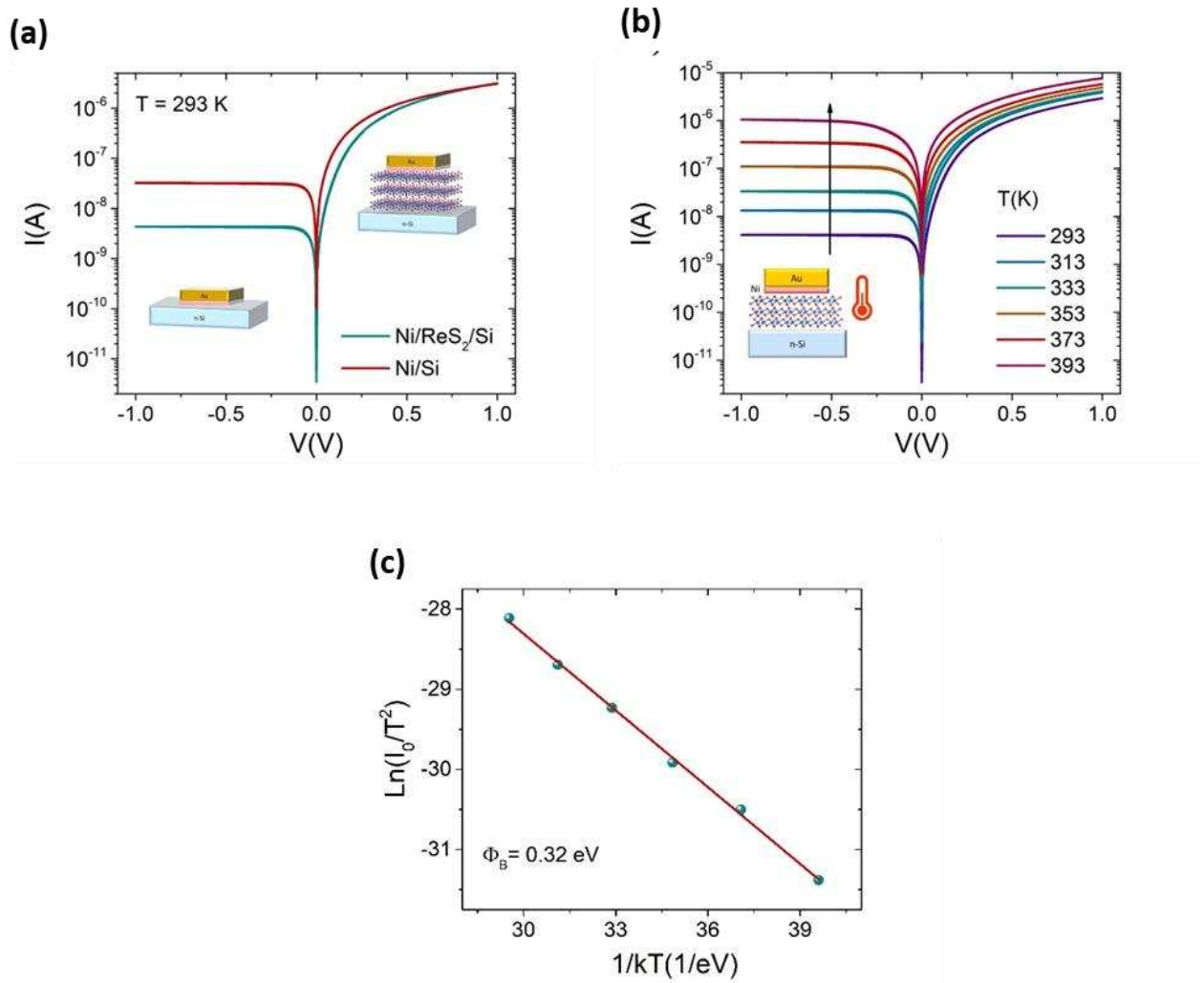

Figure 5.2. (a) Comparison between the I-V curves of the Ni/ReS_2/Si structure and the Ni/Si Schottky diode, in the dark and at room temperature. (b) I-V curves of the Ni/ReS_2/Si device measured at different temperatures, from 293 to 393 K. (c) Extraction of the energy barrier through the thermionic emission model.

The increase of the current with temperature both at positive and negative biases suggests that a temperature-activated electronic transport above an energy barrier occurs, such as a thermionic emission or thermionic field emission[35,36]. ReS_2 is a natural n-type semiconductor[37]. Therefore, the n-ReS_2/n-Si junction is a heterostructure where carrier transport is dominated by majority carriers, i.e. electrons. Thus, assuming a homogeneous barrier in the temperature range under investigation[38], the thermionic emission current equation can be applied[10,39] to extract the energy barrier at the interface.
In detail, the thermionic emission current is described by the equation:

$$I = I_0[\exp\left(\frac{qV}{nk_BT}\right) - 1] \quad (5.1)$$

where q is the electron charge, k_B is the Boltzmann constant, T is temperature, and n is the ideality factor. The saturation current I_o is defined as:

$$I_0 = AA^* T^2 \exp\left(-\frac{q\Phi_B}{k_B T}\right) \quad (5.2)$$

in which A is the junction area, A* is the Richardson constant, and Φ_B is the energy barrier. The I_o values at different temperatures were extracted from the intercepts of the linear fit of the I-V curves at small positive biases, near 0 V. From the Arrhenius plot of $\mathrm{Ln}\left(\frac{I_o}{T^2}\right)$ vs. $1/k_B T$ plot in Figure 5.2c:

$$\mathrm{Ln}\left(\frac{I_0}{T^2}\right) = \mathrm{Ln}(AA^*) - \frac{q\Phi_B}{k_B T} \quad (5.3)$$

it is possible to extract the value of AA* and the effective energy barrier that is around $\Phi_B = 0.32$ eV [36,40,41].

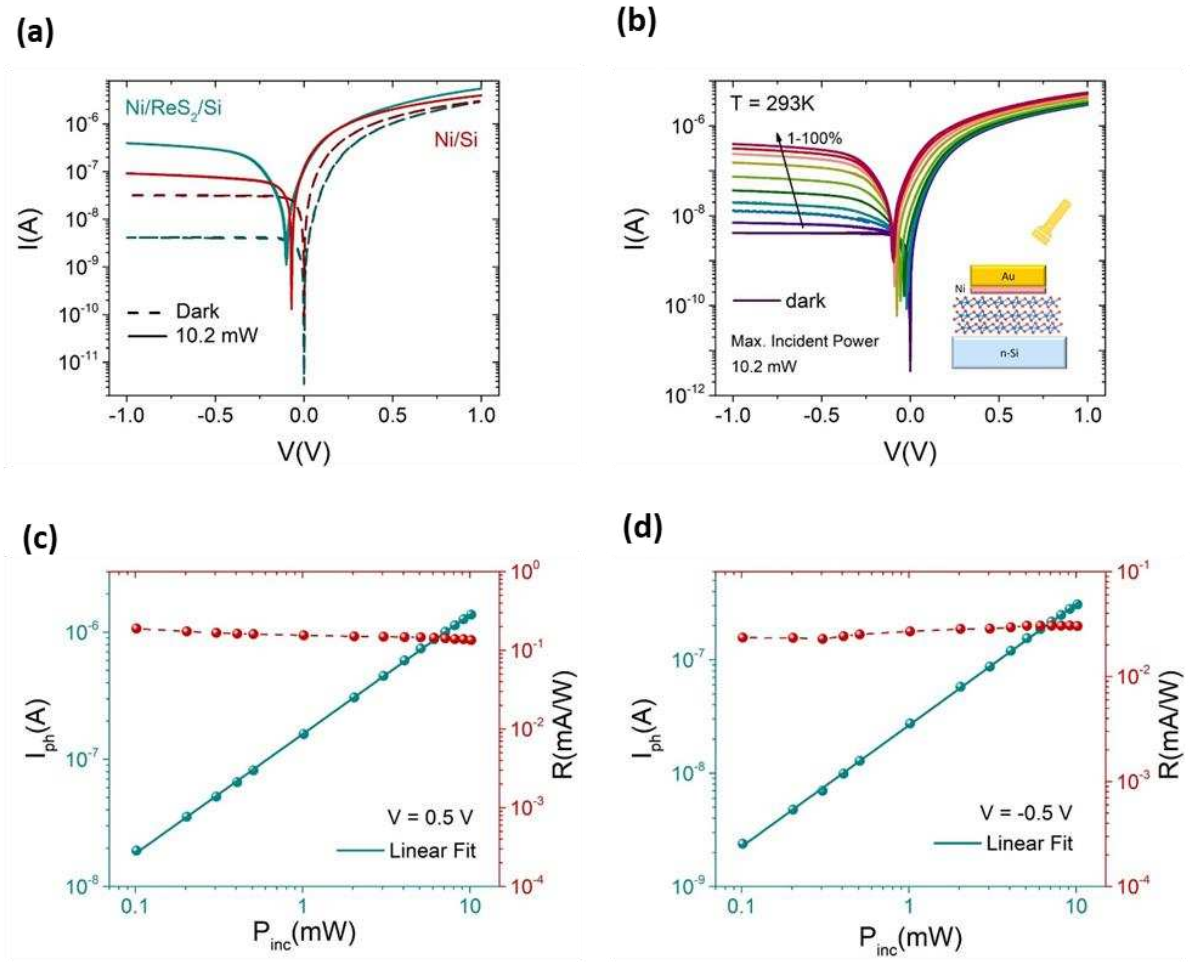

Figure 5.3 (a) Comparison between I-V curves in dark (dash line) and under illumination (solid line) of the Ni/ReS_2/Si heterostructure and the Ni/Si Schottky diode. (b) I-V curves on a semi-log scale under illumination by a supercontinuum white laser at increasing incident optical power, compared with the I-V measured in the dark. (c),(d) Log-log plot of the photocurrent, and the correspondent responsivity, as a function of the incident optical power at c) positive and d) negative bias.

The photoresponse of the ReS_2/Si diode was investigated using the SuperK Compact white supercontinuum laser. The illuminated I–V curves in Figure 5.3a show that the ReS_2/Si

junction produces a significantly higher photocurrent than the Ni/Si Schottky diode, reaching up to an order of magnitude more under reverse bias. The device response can also be tuned by varying the incident light intensity. Figure 5.3b reports the I–V characteristics measured as the optical power P_{inc} is increased from 0.10 to 10.2 mW. Although the current rises under both forward and reverse bias, the latter yields much larger photo-to-dark current ratios I_{ph}/I_{dark}, with values approaching 10^2, indicating more efficient charge separation under negative bias[42].

The majority of photodetector applications, including illumination meters and image sensors, need the extraction of the detected light's intensity from the photocurrent across a broad range of light intensities. Therefore, having a linear dependence of the photocurrent on the laser intensity, and, as a result, a constant responsivity, is highly desirable.

As highlighted by Figure 5.3c and Figure 5.3d, I_{ph} follows a linear trend across the whole light intensity range here investigated, from 0.1 to 10 mW, both at positive and negative biases; the fit of the data indicates that the functional law is $I_{ph} \sim P_{inc}^{\alpha}$, with $\alpha \simeq 1$. Therefore, considering the strongest and the weakest incident powers as P_{sat} and P_{low}, the LDR value, calculated according to equation 2.27, is roughly $r_{LDR} \sim 40$, but a wider range has to be considered to have a clearer representation of the linear trend.

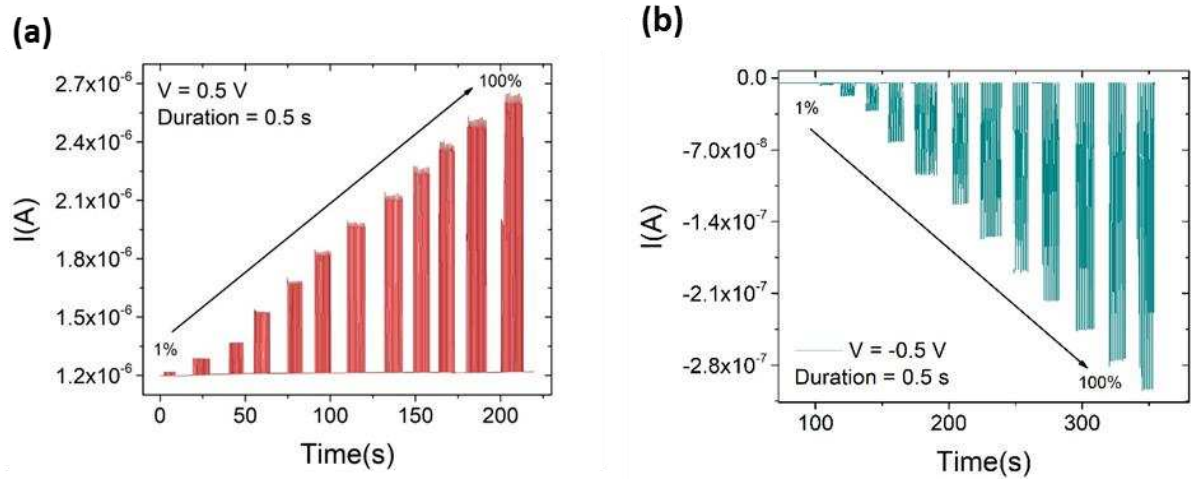

Figure 5.4. Switching response of the device with 1s-period, under increasing optical incident power at (a) positive and (b) negative biases.

Many studies report α values below 1 for 2D TMD/3D heterostructures, reflecting trap- or defect-assisted photogeneration and recombination processes[43,44]. The linear I_{ph}-P_{inc} dependence leads to an almost constant photoresponsivity in the visible range. As shown in Figures 5.3c and 5.3d, average responsivity values of (0.15±0.01) mA/W at V= 0.5 V and (0.028±0.003) mA/W at V=-0.5 V can be calculated according to the formula 2.15.

The switching properties of the heterojunction have been investigated through time-resolved measurements under pulsed illumination. Figure 5.4 shows the temporal response of the ReS_2/Si heterostructure to repeated sequences of light pulses, each obtained by turning on and off the laser with a period of one second and recorded at different powers. As soon as the device is illuminated, the current increases and it returns to its dark value upon turning off

the light, exhibiting a steep and rapid rise and decay. Notably, the absence of measurable data points along the transient edges indicates that the switching occurs within a single sampling interval (~0.05 s), confirming that the intrinsic response time is below the temporal resolution of the acquisition system. The device shows a stable and reproducible photoswitching response over multiple cycles, even under high-intensity light. No saturation or slowdown occurs at higher photocurrent levels, confirming its robustness.

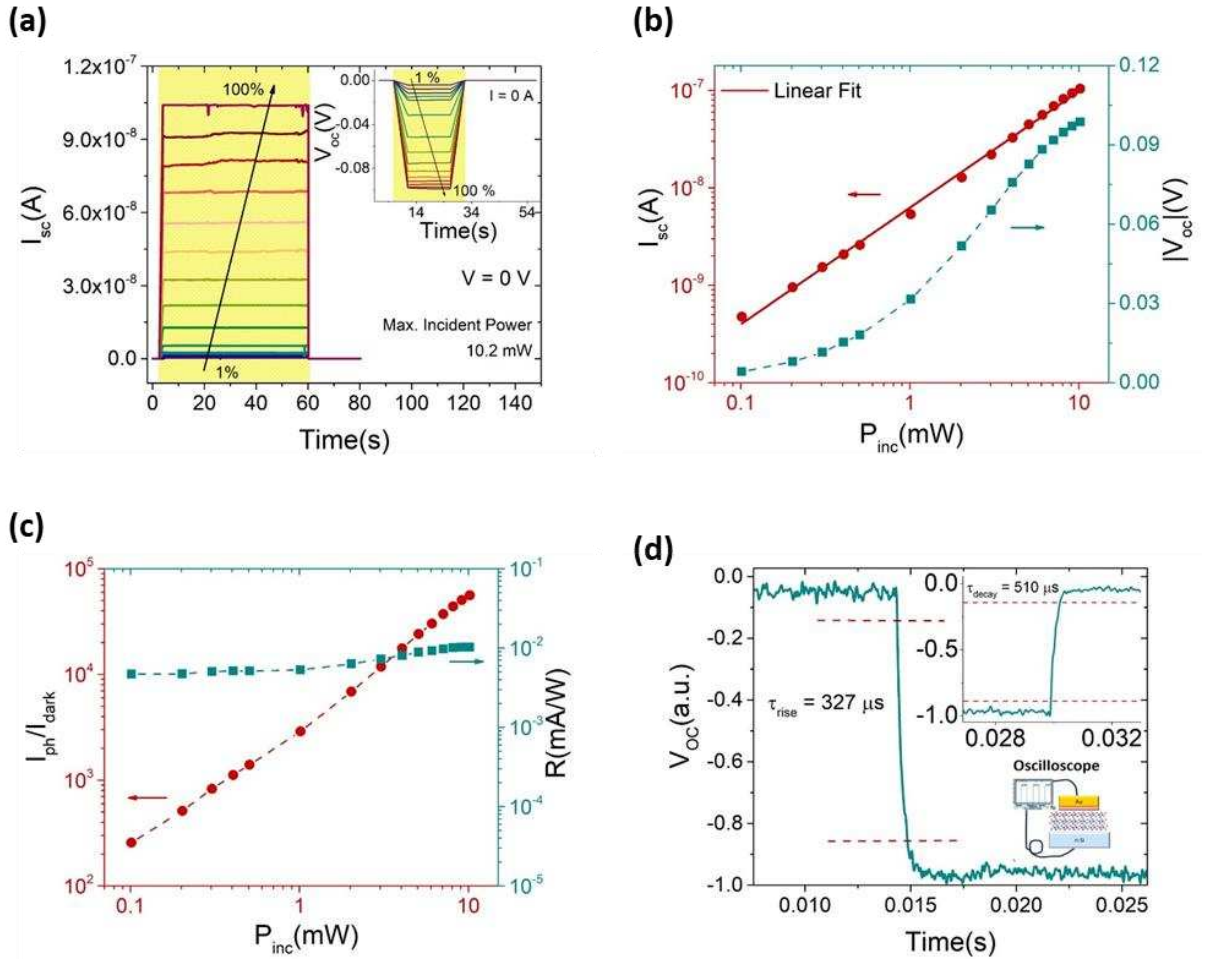

Figure 5.5. Photovoltaic behaviour of the ReS_2/Si device: a) Short circuit current I_{sc} and open circuit voltage V_{oc} (inset) under laser pulses of increasing incident power. b) I_{sc} and V_{oc} as a function of the incident optical power. Symbols are the data, the dashed line is an eye guide, while the solid lines represent the power law fitting to I_{sc}. c) Photocurrent over dark current ratio I_{ph}/I_{dark} (on the left) and responsivity R (on the right) vs. incident optical power P_{inc}. d) Rise and decay times extracted from the device's response to a light pulse.

From Figure 5.3b, it is also evident that the device can be operated in self-powered mode. Self-driven devices are an indispensable part of electronic and optoelectronic components; thanks to their high photoresponse, 2D materials based self-driven photodetectors have recently gathered significant attention[45,46].

To deeply investigate this operating condition, the device response to laser pulses of different intensities was recorded at zero external bias voltage, and zero external current, as shown in Figure 5.5a. The short-circuit current I_{sc} increases with the laser intensity by following

a linear trend as a function of the incident power, with an r_{LDR} about 40, as shown in Figure 5.5b. This remarkable result suggests an effective photo-charge separation and possibly a band offset modification in the heterojunction because of light absorption. At the maximum incident power of 10.2 mW, I_{sc} reaches the high value of 0.1 µA.

The open circuit voltage V_{oc} has a similar behaviour and increases with the increasing incident power, achieving the absolute value $|V_{oc}| = 0.1$ V under the maximum incident power. The I_{ph}/I_{dark} ratio, being the dark current about 1 pA, reaches a value of $5 \cdot 10^4$ as reported in Figure 5.5c, indicating a high self-driven capability of the photodetector, comparable to other homopolar 2D/3D heterostructures like n-MoS_2/n-GaAs[47], n-$MoTe_2$/n-Si[16].

Tuning the device structure and investigating a wider range of light intensities might be necessary to achieve performances competitive with those reported in other works[43,48]. Indeed, the effective responsivity ranges from 0.04 to 0.10 mA/W. A fast-photoswitching response is confirmed in Figure 5.5d, reporting rise and decay times of 300 and 500 µs, respectively.

To provide insight into the carrier transport mechanism through the Ni/ReS_2/Si heterostructure, density functional theory (DFT) and nonequilibrium Green's function (NEGF) calculations are implemented in QuantumATK[24].

The planar-averaged charge density difference (CDD), atomic structure and energy-resolved local DoS (LDoS) across the Ni/Si and ReS_2/Si junctions are plotted in Figure 5.6, respectively. LDoS is obtained with both sides of the junction held at equilibrium, and the Fermi level is shown by the dashed yellow line. As shown by the orange dashed lines in the LDoS profile at the ReS_2/Si interface, the Si conduction and valence bands bend 650 meV upwards near the junction. In the ReS_2 side of the junction, a rather small downward band bending of $\sim$ 110 meV is observed in the ReS_2 side of the junction. The resulting band offset at the conduction band at the ReS_2/Si interface is $\sim$ 0.72 eV, while the conduction band offset at the Ni/Si interface is $\sim$ 0.3 eV. The ideal interface under consideration, excluding certain smoothing effects that result in the effective barrier established through experimentation, can explain discrepancies with experimental results. In the fabricated device, there is a strong probability that some atoms of the Si surface are not passivated, leading to the presence of dangling bonds. These dangling bonds are anticipated to strongly impact the ReS_2/Si band offset, especially since both the Si and the ReS_2 are n-type. Further, the calculated band offset from LDoS is under equilibrium, while it is expected that the application of an external electric field reduces the band offset[49].

The CDD is obtained as the difference between the total valence charge density and a superposition of neutral atom valence charge density at each atomic site. To estimate the dipole at the junctions, the macroscopic planar-average of the CDD has been extracted as shown in Figure 5.6, where the same distance at either side of each sampling grid point is considered in the macroscopic averaging scheme. + and – indicate the direction of the electron transfer at the interfaces; i.e., from Si to ReS_2 at the ReS_2/Si and from Ni to Si at the Ni/Si junctions. As expected, a larger value of charge transfer has been obtained for the Ni/Si junction compared to the ReS_2/Si structure.

Experimental results and DFT calculations converge in the band diagrams reported in the following.

First, as depicted in Figure 5.7a, ReS_2 and Si form a type II N-n heterojunction at equilibrium, which has a different band alignment than conventional p-n heterojunction, where depletion regions are formed in both p and n-type semiconductors. Here, in accordance with DFT simulation, a depletion region occurs in the Si-side and an accumulation region is formed in the ReS_2 part. As mentioned before, the heterojunction possesses a majority carrier transport behaviour similar to a Schottky diode, different from what occurs in a p-n junction where minority carriers play an important role.

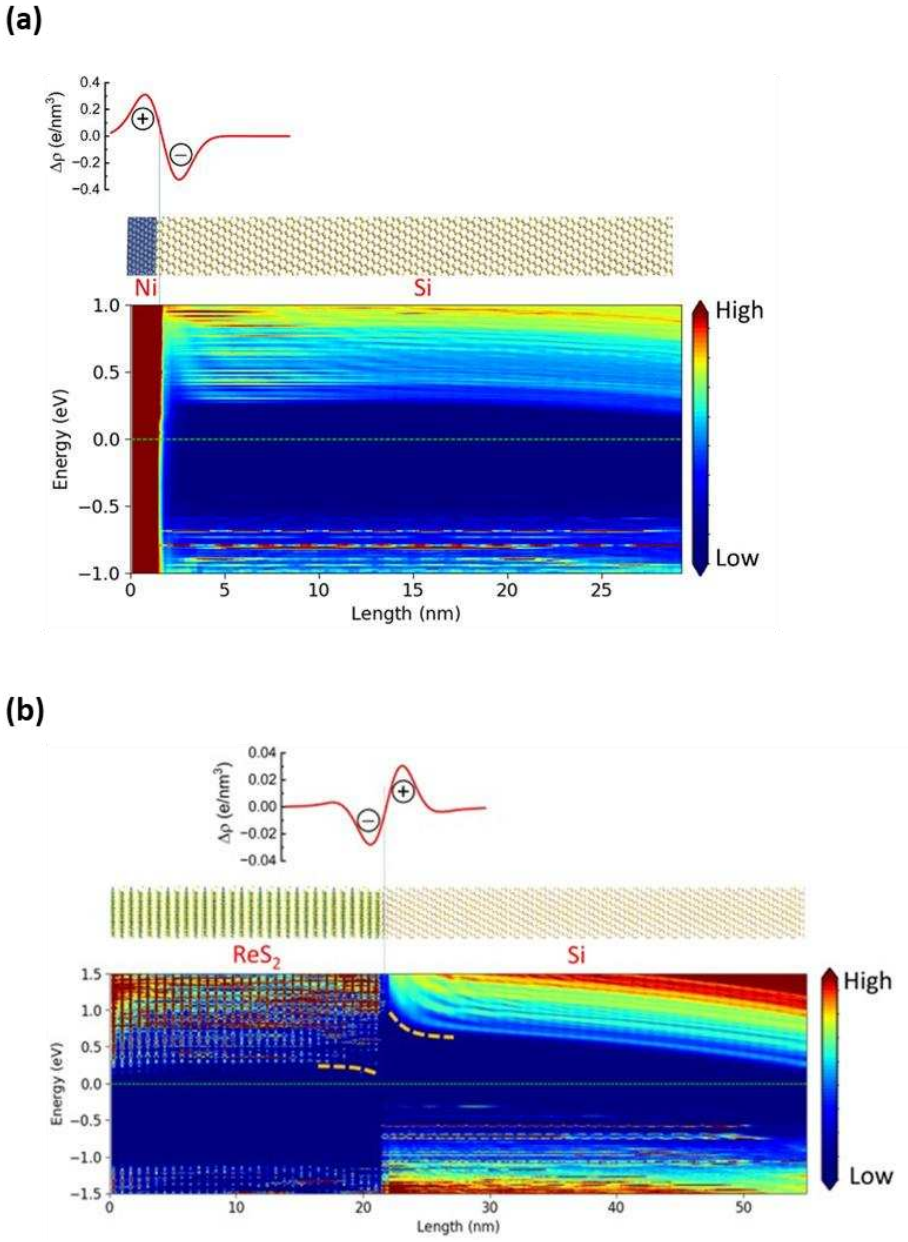

Figure 5.6. Planar-averaged CDD, atomic structure and energy-resolved LDoS of (a) Ni/Si and (b) ReS_2/Si.

When a negative bias is applied to the Ni contact, the electron transport is limited by the energy barrier at the ReS_2/Si interface. When the light is turned on, a negative photocurrent is recorded, which means that a current flows towards the Ni contact. As shown in Figure 5.7b

such a current is mainly due to photogeneration at the ReS_2/Si interface, where photogenerated carriers are rapidly separated by the strong electric field. Electrons move from ReS_2 to Si, while holes are transferred to the ReS_2 part and collected by the top electrode, contributing to the photocurrent.

If the junction is positively biased, electrons flow from the Si substrate towards ReS_2, as plotted in Figure 5.7c. The electrons experience a low barrier at the ReS_2/Si junction interface while moving towards the Ni contact, which originates the high current in forward bias. Under illumination, the current increases moderately because electron-hole pairs which effectively contribute to the photocurrent are mostly generated in the depletion layer, reduced by the applied bias.

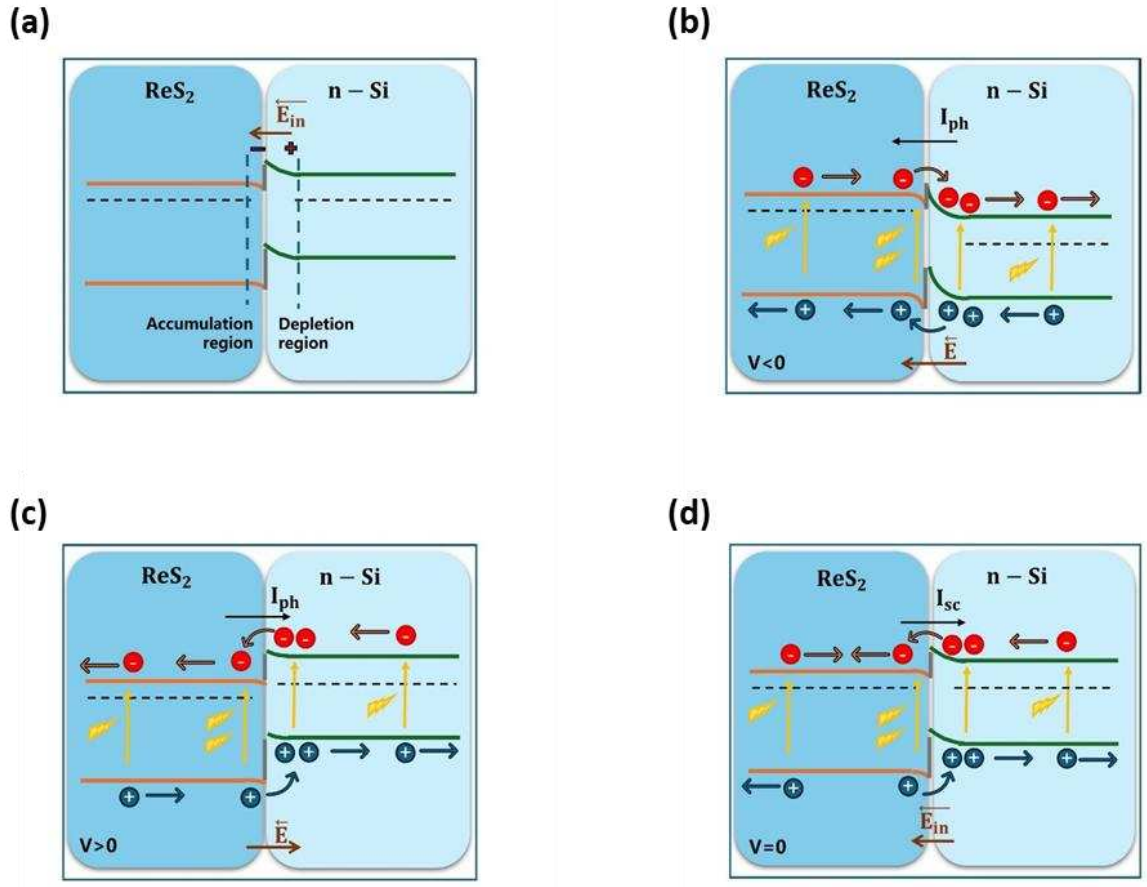

Figure 5.7. Band diagrams representing the dominant current mechanisms: (a) in an equilibrium condition, in the dark; (b) under negative external bias on the top contact, (c) under positive external bias on the top contacts, d) under zero external bias. (b), (c) and (d) represent the situation under illumination.

When no bias is applied, the measurements under illumination indicate the presence of a positive current in short-circuit condition and a negative voltage in open-circuit condition. This unusual behaviour could be due to several elements. First of all, to photogenerated electrons in the depletion region of Si that, being more energetic, move towards ReS_2, despite the built-in electric field, as represented in Figure 5.7d. Electrons at the ReS_2 side experience, instead,

the ReS_2/Si barrier. A reduction of band-bending at zero external bias at the Si interface under illumination could also account for this effect[50–52]. A positive photovoltage caused by holes produced by light adsorption in the depletion region and accumulated at the interface could provide a forward biasing of the heterojunction, giving a positive I_{sc}.

In conclusion, the ReS_2/Si heterojunction photodiode shows a fast and reproducible photoresponse. The device reliably follows laser pulses with reduced rise and decay times, maintaining stable operation even at higher photocurrent levels, showing potential for high-throughput optoelectronic applications, fast optical switching, and optical communication systems. Nonetheless, the responsivity of the present heterostructure remains relatively modest, indicating that further optimization, particularly in terms of interface quality, light absorption efficiency, and device geometry, is required.

5.5 Materials and methods: Device 2

One of the disadvantages of the structure presented in the previous section is that the metal electrode on top of the ReS_2 flake is not transparent and reflects most of the light. This makes it difficult to define the effective light-sensitive area, which is assumed to be the flake area exceeding the metal contact, which is completely exposed to the light from the optical fiber.

Therefore, a different fabrication approach was conceived and adopted. The 2D ReS_2 flakes were once again obtained by mechanical exfoliation using scotch tape and then transferred onto lightly doped n-type and p-type silicon substrates. Large-area flakes were selected via optical microscopy, and their thickness, measured with a profilometer, resulted in approximately 40 nm for the flake on n-type Si and about 60 nm for that on p-type Si.

A double resist layer was applied by spin coating, and standard photolithography was used to define a rectangular resist region on top of the selected flake, serving as a mask for the e-beam evaporation of an HfO_2 layer, with thicknesses of approximately 100 nm. Following lift-off, the resist mask was removed, leaving an open rectangular window on top of the ReS_2 flake. A second photolithography and lift-off step was then used to define the metal contacts, consisting of Ti/Au (15:200 nm for ReS_2/p-Si and 10:150 for ReS_2/n-Si) deposited via thermal evaporation[53]. Silver paste was used at the end to create back contacts after scratching the substrate. Although removing the deposited oxide layer during lift-off can be challenging, the procedure has the advantage of not requiring any acidic solutions to open an active area. The fabrication steps are summarized in Figure 5.8.

Figure 5.9a shows the optical image of the ReS_2/p-Si heterostructure, which has an exposed area of A = 651.9 μm^2, almost double with respect to the exposed area of 322.17 μm^2 of the ReS_2/n-type Si structure in Figure 5.9b. Raman measurements, reported in Figure 5.9c and 5.9d, were conducted after the final step to confirm the nature and quality of ReS_2 with a laser excitation wavelength of 532 nm. In accordance with literature works, the Raman modes are located in the 100-450 cm^{-1} range, where fifteen of the eighteenth active Raman modes are identified. These Raman peaks are mostly caused by the low crystal symmetry of the materials and are associated with fundamental Raman modes coupled to each other and to acoustic phonons. The two main peaks, at 160 and 211 cm^{-1} correspond to the in-plane (E_{2g}) and mostly out of plane (A_g like) vibration modes.

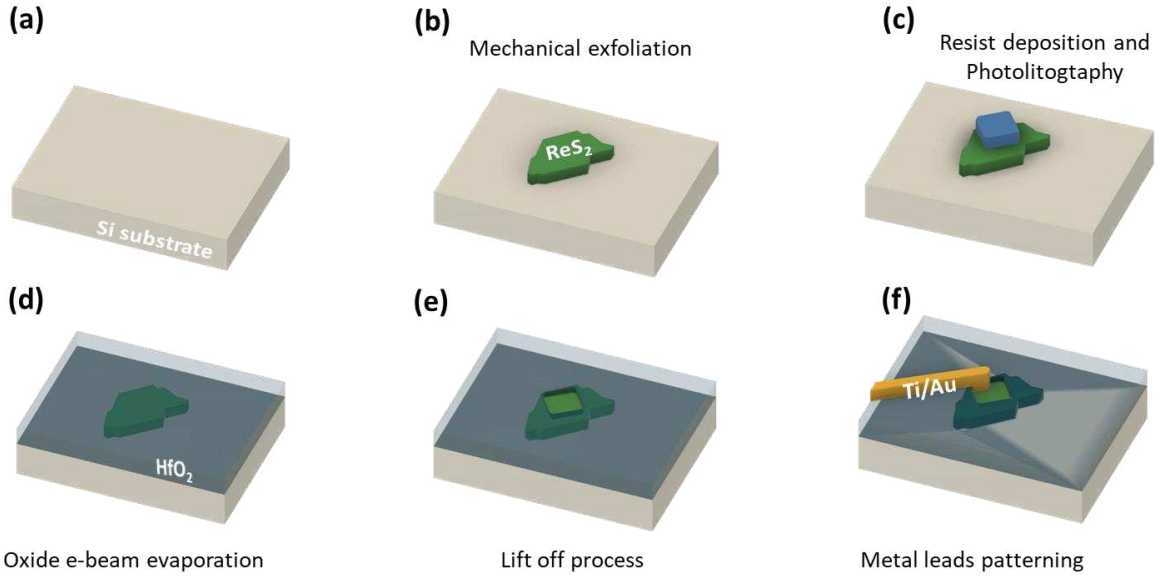

Figure 5.8. Fabrication procedure. (a), (b) Mechanical exfoliation of ReS_2 on Si substrates. (c) Photolithography process to obtain a resist-mask. (d) HfO_2 deposition. (e) Lift-off process to open the window on ReS_2. (f) Metal-leads patterning through photolithography/lift off processes.

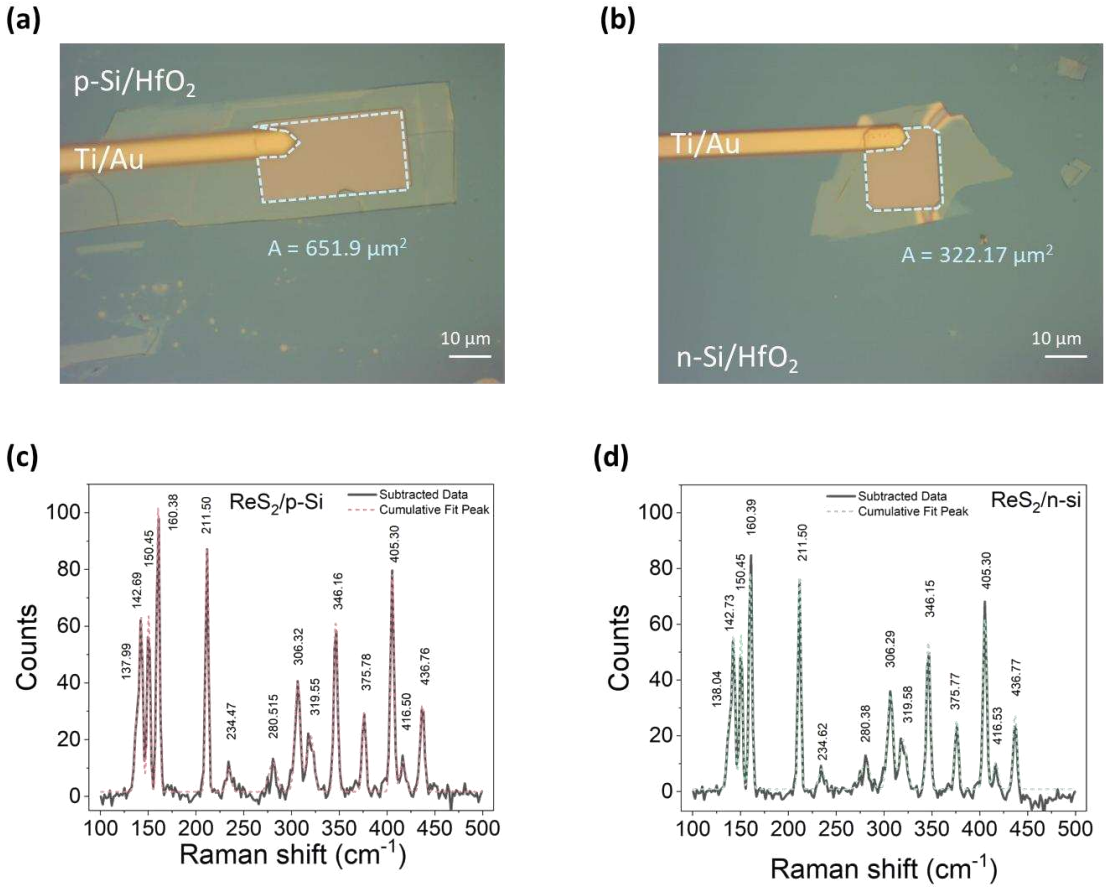

Figure 5.9 Optical image of (a) ReS_2/p-Si and (b) ReS_2/n-SI heterostructure. Raman spectrum of c) ReS_2/p-Si and d) ReS_2/n-Si heterostructure

5.6 Results and discussion: Device 2

Measurements were performed in high vacuum (P = $4.6 \cdot 10^{-3}$ mbar) to have a more stable environment, since no significant changes were observed with respect to the air pressure condition because of the thickness of ReS_2 flakes.

Figure 5.10 presents the dark I–V characteristics of the ReS_2/Si heterostructures measured at T = 293 K. For both devices, measurements were performed before and after a mild thermal annealing at 400 K. In the ReS_2/p-Si heterostructure, the forward regime is reached under positive bias, while negative voltages correspond to reverse-bias operation. Conversely, the ReS_2/n-Si device is forward biased at negative voltages and reverse biased at positive ones. Thermal annealing results in a noticeable reduction of the dark current in the ReS_2/p-Si junction, with nearly one order of magnitude suppression in the reverse branch. In contrast, a much weaker effect is observed in the n-type device, where the pre- and post-annealing I–V curves largely overlap, showing only minor deviations at biases below −1.5 V. After annealing, both heterojunctions exhibit clear rectifying behavior, with an I_{on}/I_{off} ratio of approximately two orders of magnitude at V=±3V.

For a more meaningful comparison between the two devices, the current density, rather than the absolute current, is reported. Even after normalization to the effective junction area, the current density of the ReS_2/p-Si heterostructure remains more than one order of magnitude higher than that of the ReS_2/n-Si device across the entire bias range, indicating a higher absorption and a more favorable band alignment in the ReS_2/p-Si junction.

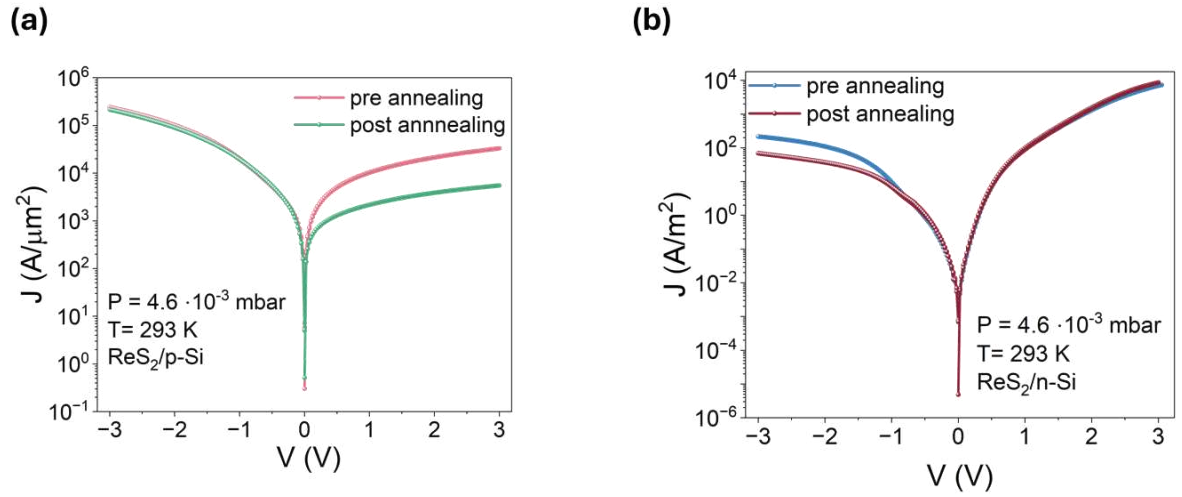

Figure 5.10. Comparison between pre and post annealing I-V curves of the (a) ReS2/p-Si and (b) ReS2/n-Si curves

The photoresponse of the devices was initially investigated at room temperature using a SuperK Compact supercontinuum white laser. Figures 5.11a and 5.11b show the J-V characteristics of the ReS_2/p-Si and ReS_2/n-Si heterostructures measured under different P_{inc}, from 0.78 to 70 mW. In the ReS_2/p-Si device, illumination enhances the current in both forward and reverse regimes, with a more pronounced increase under negative biases. By contrast, in

the ReS_2/n-Si heterostructure the forward branch remains nearly unchanged, and the current significantly rises only in reverse bias, beyond approximately −0.5 V.

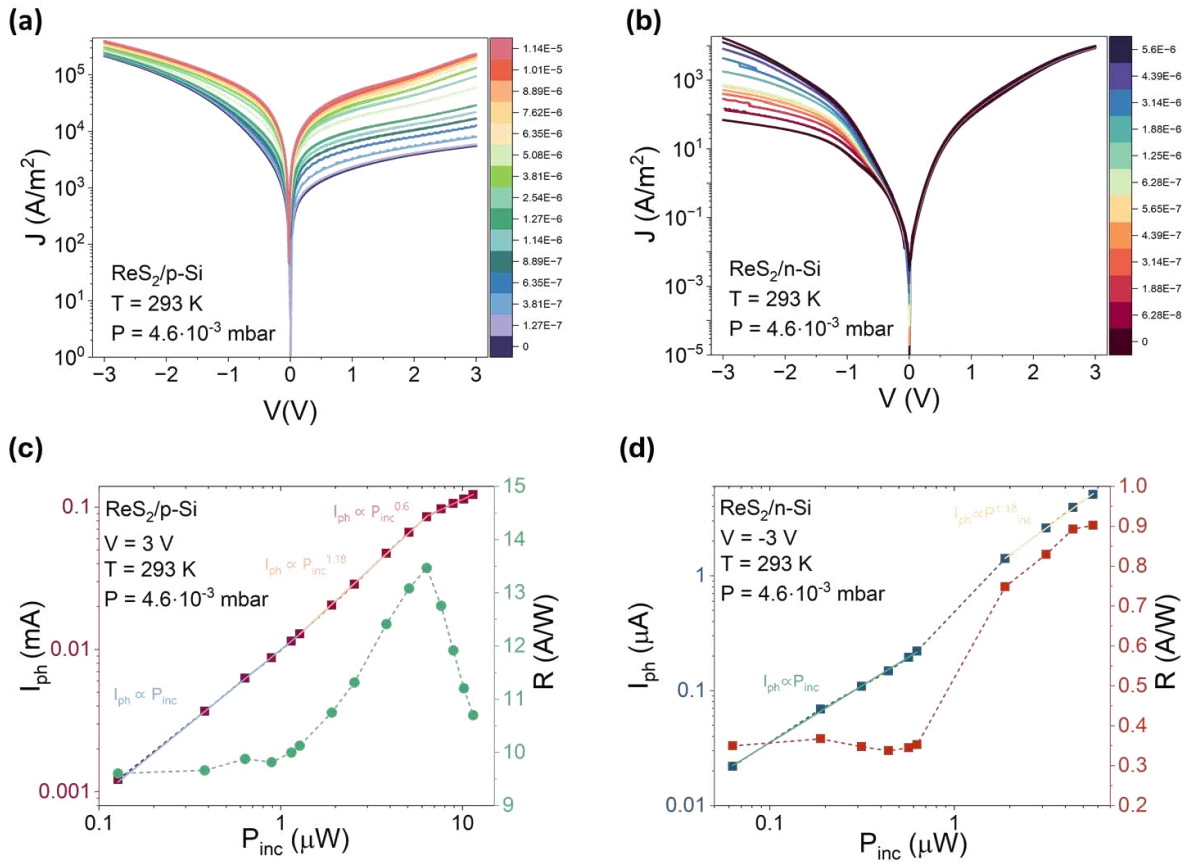

Figure 5.11. Comparison between I-V curves on semi-log scale under different optical power and the dark curve of the (a) ReS_2/p-Si and (b) ReS_2/n-Si device. Photocurrent (left) and Responsivity (right) vs incident optical power on a log-log scale of (c) ReS_2/p-Si and (d) ReS_2/n-Si device

Figures 5.11c and 5.11d report I_{ph}, recorded at 3 V for the ReS_2/p-Si device and -3 V for the ReS_2/n-Si device, as a function of P_{inc} on a double-logarithmic scale. At the maximum investigated power, the photocurrent reaches approximately 0.12 mA in the p-type device and about 5 μA in the n-type device.

Over the P_{inc} range between 0.1 and 6 μW, the photocurrent exhibits a dependence on the incident power that can be described within a linear-response framework. At low P_{inc} (below approximately 1 μW), the photocurrent increases with the optical power with an almost constant responsivity, indicating that the recombination and collection efficiency of photo-generated carriers scales with the absorbed photon flux.

In the 1–6 μW range, the photocurrent continues to increase with the incident power according to the $I_{ph} \sim P_{inc}^{\alpha}$ law, with $\alpha = 1.18$, and the correspondent responsivity progressively increases, reaching a maximum value of about 13 A/W for the ReS_2/p-Si device and approximately 0.9 A/W for the ReS_2/n-Si device. Similar superlinear behaviours of the photocurrent and power-dependent enhancements of the responsivity have been reported in

other 2D material-based photodetectors and heterostructures. They are attributed to a wider energy distribution of recombination centres and capture cross-sections that make some carriers have an increased lifetime or to higher injection efficiency with increasing excitation density[54–56].

At higher incident optical powers (above approximately 6 μW), explored in the p-type device, the photocurrent follows a sublinear power-law dependence with $\alpha = 1.18$, indicating the onset of saturation effects. Consistently, the responsivity decreases with increasing optical power. The solid lines represent power-law fits performed over selected intervals to highlight the different operational regimes.

To reduce dark current and noise, the photoresponse of the ReS_2/p-Si and ReS_2/n-Si heterostructures was also investigated at low temperature (77 K), with Figures 5.12a and 5.12b showing the J–V characteristics under different illumination intensities.

A pronounced reduction of the dark current is observed in both forward and reverse bias regimes for both heterostructures. In particular, the forward-bias current density is reduced by approximately three orders of magnitude with respect to the 293 K case, while a stronger suppression is observed in reverse bias, where the dark current reaches values in the picoampere and femtoampere range. This behavior is consistent with the reduced thermal activation of carriers and the suppression of thermally assisted transport mechanisms at low temperature[57].

Despite this, both devices retain a significant photoresponse under white-light illumination, with a clear modulation of the current as a function of P_{inc}. As at 293 K, the main figures of merit were evaluated in reverse bias, by monitoring the response under pulsed excitation. Figures 5.12c and 5.12d show that the photocurrent reaches several tens of microamperes at the highest powers and scales nearly linearly with P_{inc}, as confirmed by power-law exponents close to unity over the explored range.

The corresponding responsivity remains relatively stable across the investigated power range. For the ReS_2/p-Si heterostructure, two plateaus around 2 and 4 A/W are obtained, while the ReS_2/n-Si device shows a lower but still stable responsivity of about 0.3 A/W. These results indicate that, despite the reduced thermal energy of charge carriers at low temperature, photocarrier generation and collection remain efficient, and no pronounced saturation effects are observed within the investigated power window. Compared to room-temperature measurements, where a power dependence of the responsivity is observed, the low-temperature data reveals a more uniform and stable photoresponse over the investigated optical range.

Owing to the extremely low dark current at 77 K, the specific detectivity D*, calculated according to formula 2.26, is significantly enhanced, reaching values on the order of 10^{12} Jones. It is assumed that the dark current is dominated by the shot noise for estimating detectivity. The other source of noise (Johnson and flicker noise) are mainly thermal fluctuations, which can be neglected at 77 K[58]. In addition, the photo-to-dark current ratio, defined as I_{light}/I_{dark} reaches values up to six orders of magnitude, highlighting the high sensitivity of the devices under low-temperature operation.

The transient photoresponse of the ReS_2/Si heterostructures was evaluated by recording the current under repeated on/off illumination cycles, as exhibited in Figure 5.13. In both ReS_2/p-Si and ReS_2/n-Si devices, a clear, stable, and reproducible switching behavior is observed, with well-defined current plateaus during illumination and a repeatable relaxation

toward the dark current level when the light is switched off. The device is in the on-state for almost 3s and in the off-state for 7s.

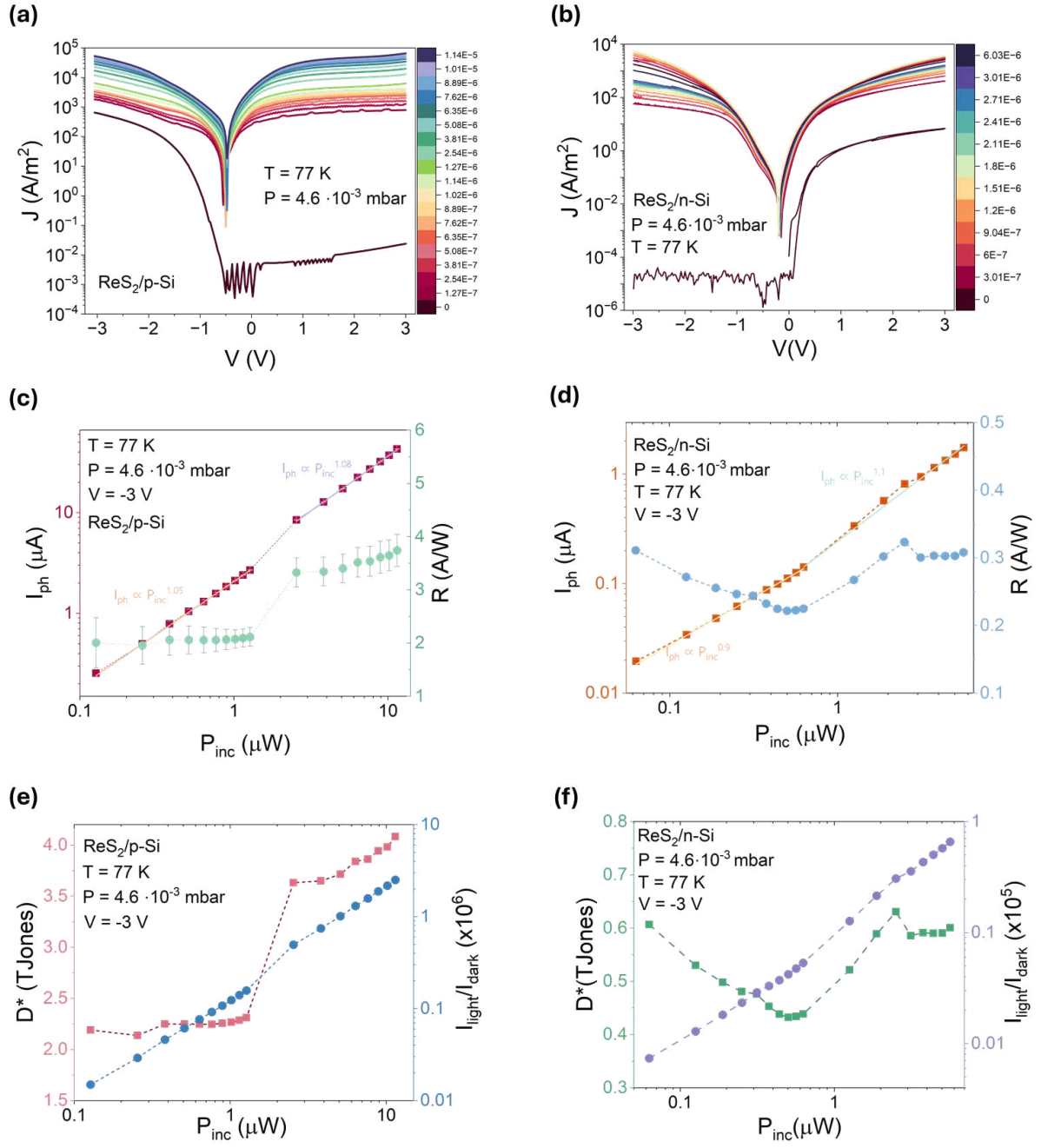

Figure 5.12 Photoresponse at 77 K. Comparison between I-V curves on semi-log scale under different optical power and the dark curve of the (a) ReS_2/p-Si and (b) ReS_2/n-Si device. Photocurrent (left) and Responsivity (right) vs incident optical power on a log-log scale of (c) ReS_2/p-Si and (d) ReS_2/n-Si device. Specific detectivity D* (right) and sensitivity (left) vs incident optical power on a log-log scale of (e) ReS_2/p-Si and (f) ReS_2/n-Si device.

For the ReS_2/p-Si device, the photocurrent plateau under illumination is centered around 38.5 µA, with fluctuations confined within a narrow range (38.4–38.6 µA), indicating good signal stability and low noise. Similarly, the ReS_2/n-Si device exhibits a photocurrent plateau around 1.86 µA, with values distributed within the range 1.85–1.87 µA. No noticeable degradation or drift of the photocurrent is observed during repeated switching cycles, confirming the robustness and reproducibility of the photoresponse at low temperature.

As shown in Figures 5.13c and 5.13d, the intrinsic response time of the devices cannot be fully resolved due to the sampling limitations of the acquisition system. Specifically, since the current spans several orders of magnitude, the observed 1 s interval between the dark and light states is primarily attributed to the instrument's latency during the auto-ranging process. This indicates that the actual carrier dynamics and the primary switching processes are significantly faster than the sampling rate allowed by the experimental setup under these conditions.

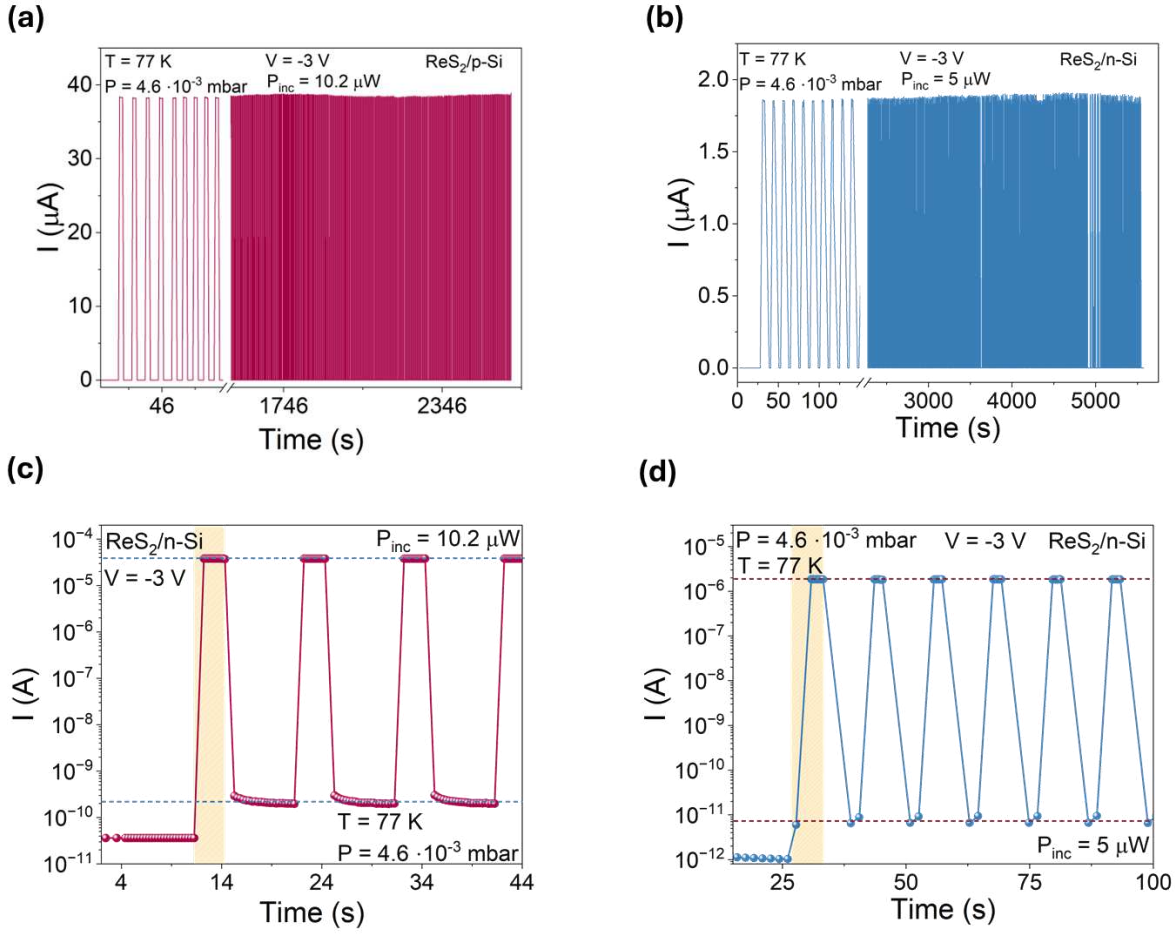

Figure 5.13 Switching operation over multiple cycles of (a) ReS_2/p-Si and (b) ReS_2/n-Si heterostructures. (c), (d) Zoom into their transient profile, respectively.

Nevertheless, the decay dynamics in the low-current region reveal additional relaxation processes superimposed on the primary fast response. In particular, the current requires longer times to fully recover the original dark level after illumination is switched off, manifesting as a

decreasing tail. In the ReS_2/p-Si device, for example, while the initial dark current is approximately $3{\cdot}10^{-11}$ A, during repeated illumination cycles the current stabilizes at a higher dark value of about $2{\cdot}10^{-10}$ A within the explored time window. This behavior suggests the presence of photogating-type effects driven by residual charge storage in trap states at the interface. These traps delay the complete relaxation toward equilibrium on the investigated time scales. Importantly, when this stabilized dark level is taken as the reference baseline, the photoresponse remains highly stable and reproducible over repeated cycles.

To assess the broadband photodetection performance, the spectral responsivity, specific detectivity and EQE of both heterostructures were calculated, as illustrated in Figure 5.14.

In the visible–near-infrared range (≈500–950 nm), both devices exhibit high responsivity, on the order of 10–100 A/W, with comparable values at room temperature. Specifically, in the ReS_2/p-Si case, the 460-800 nm range is dominated by the absorption properties of ReS_2, with two well resolved peaks at 740 and 800 nm, clearly visible in the ReS_2/p-Si device, related to excitonic transitions[59]. The near infrared region shows a broad enhancement around 940, which is characteristic of Si absorption. As the wavelength approaches 1000–1100 nm, the responsivity decreases sharply, in agreement with the absorption edge of silicon at low temperature.

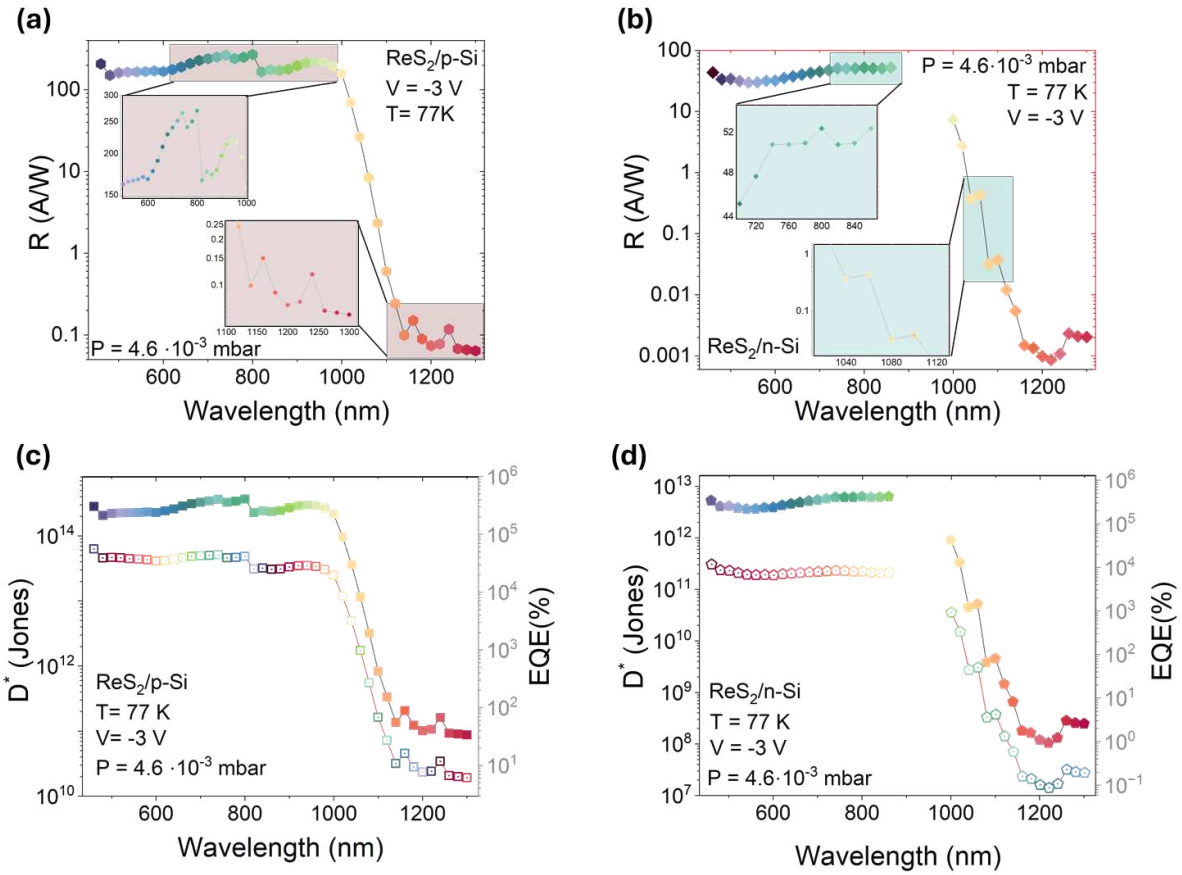

Figure 5.14: Responsivity as a function of the wavelength in (a) ReS_2/p-Si and (b) ReS_2-nSi devices. Specific detectivity (left) and EQE (right) as a function of wavelength in (c) ReS_2/p-Si and (d) ReS_2-nSi devices.

Beyond the silicon band edge, the responsivity is suppressed but remains finite, with values on the order of 0.1 A/W (p-Si) and 10^{-3} A/W (n-Si) up to ≈1300 nm. This residual photoresponse, and the peaks observed in this region, likely originates from sub-bandgap absorption processes, interface-related states, or enhanced carrier separation at the ReS_2/Si heterojunction rather than from efficient band-to-band absorption [60,61].

The high responsivity, together with EQE values largely exceeding 100%, see Figures 5.14c and 5.14d, demonstrates that the heterostructures operate with internal gain (see formula 2.21), surpassing the unity limit expected for conventional photodiodes. A quantitative estimation at 800 nm shows that the measured responsivity of 270 A/W, compared to the ideal unity-gain limit of 0.645 A/W ($R_{ideal} = \frac{\lambda}{1240}$), yields an experimental gain factor G ~ 418. This is consistent with photogating-type amplification mediated by long-lived carriers, likely trapped at the ReS_2/Si interface. This phenomenon might be responsible for the decay tail observed in Figure 5.13. This effect is commonly reported for other 2D-material-based photodetectors[60,62].

The sensitivity of the device is reflected in the specific detectivity (D*), which reaches peak values above 10^{14} Jones (Figure 5.14c). Such high sensitivity results from the combination of high internal gain and the significant suppression of dark current at 77.

Standard Si photodiodes usually show peak responsivities of about 0.4–0.7 A/W in this spectral region, with EQE values not exceeding unity in the absence of internal gain[63]. These silicon properties do not change significantly at cryogenic temperatures, apart from a slight blue-shift of the absorption edge due to the widening of the Si bandgap to 1.17 eV [64,65].

In summary, the spectral response reveals the complementary roles of the heterostructure components: silicon acts as the primary broadband absorber, while the ReS_2 layer provides an efficient photoactive interface enabling significant internal gain. The combination of high responsivity (up to 100 A/W) and fast transient dynamics suggests that interfacial amplification does not severely compromise device speed, thanks to the strong vertical built-in field promoting rapid carrier collection. Together with the excellent low-temperature stability, these features make the device a promising candidate for cryogenic applications, including space-borne sensors and cryogenic microscopy.

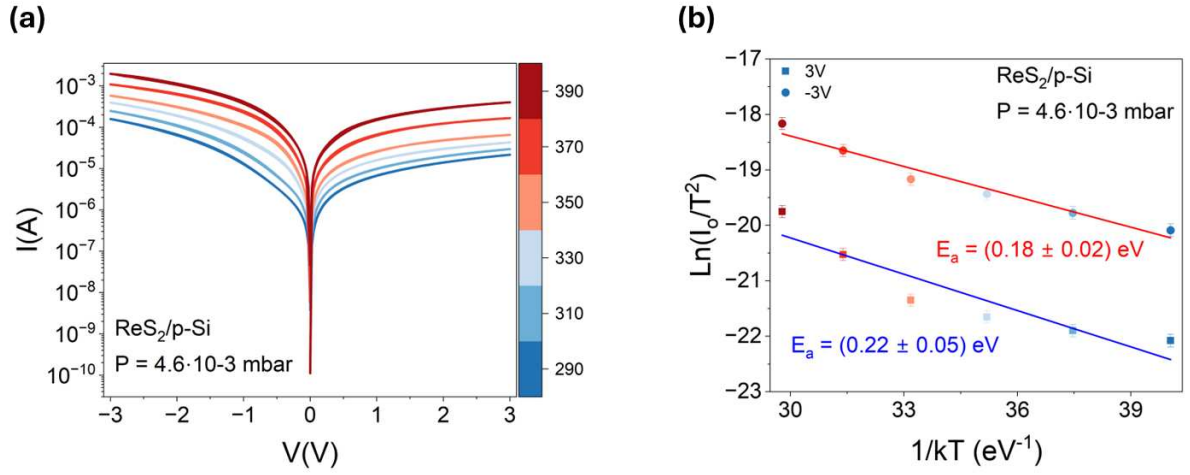

Figure 5.15 Temperature dependent measurements of the ReS2/p-Si junction. (a) I-V curves at different temperature. (b) Arrhenius plot referred to the extremes of the investigated bias range.

A preliminary temperature-dependent study was performed to have more insight into the relevant transport mechanisms of the devices.

Figure 5.15 reports the temperature-dependent electrical measurements of the ReS_2/p-Si heterostructure performed in the 290–390 K range. In this device, the current systematically increases with temperature in both forward and reverse bias, indicating the presence of thermally activated transport processes in both bias directions, consistent with a double-barrier -limited transport[66].

Richardson analyses carried out at low bias, close to zero voltage, yield effective barrier heights of approximately 0.23 and 0.24 eV for the forward and reverse branches, respectively. These values are consistent with a transport regime dominated by thermionic emission over effective barriers at low electric fields. The involvement of an additional barrier apart from ReS_2/Si, possibly related to the Si/back contact interface, cannot be excluded and may require further device optimization in the back-contact formation.

When considering the current at the extremes of the investigated bias range V = ± 3 V, the activation energies extracted from Arrhenius plots (Figure 5.15b), lower than those extracted at low biases, indicate a transition toward field-assisted thermionic emission at higher electric fields, with an improved charge injection as the applied bias increases.

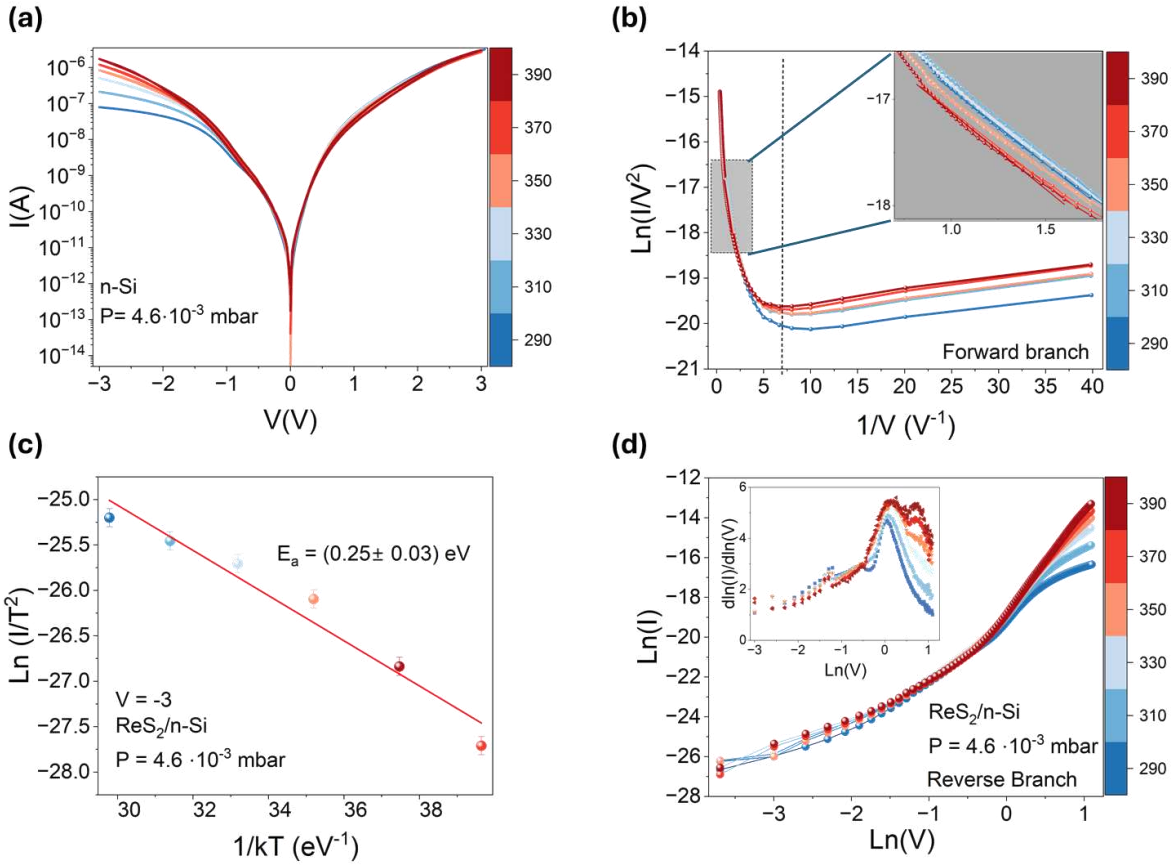

Figure 5.16: (a) Temperature dependent measurements of the ReS2/n-Si heterostructure (b) Ln(I/V2) vs 1/V of the forward branch. (c) Arrhenius analysis to extract the activation energy at V = -3 V.(d) Ln(I) vs Ln(V) of the reverse branches. The inset reports the dln(I)/dln(V) vs ln(V) plot.

Figure 5.16 shows the temperature-dependent I–V characteristics of the ReS_2/n-Si heterostructure in the 290–390 K range. In forward bias, see Figure 5.16b, the $\ln(I/V^2)$ versus $1/V$ plot displays an approximately linear region at high electric fields, which supports a tunneling-assisted transport mechanism, consistent with a Fowler–Nordheim–like behavior over a limited voltage range[67]. It could be associated with the presence of a thin native oxide between ReS_2 and Si, as often occurs in non-passivated silicon photodiodes.

In the low-bias regime, the extraction of a barrier height using a Richardson plot fails, indicating that pure thermionic emission does not dominate the transport. Conversely, in reverse bias, the separation of the I–V curves with temperature becomes evident at large fields, and an Arrhenius analysis performed at V=-3 V yields an activation energy $E_a \approx 0.25 \pm 0.03$ eV, as reported in Figure 5.16c.

Figure 5.16d reports the $\ln(I)$ versus $ln(V)$ characteristics in reverse bias, together with the local slope-derivative analysis $m = d\ln(I)/d\ln(V)$ in the inset, which evolves continuously with applied bias. At low reverse fields, m assumes values close to 2, which is commonly associated with space-charge-limited or trap-influenced conduction, which confirms the photogating-induced gain in the photoresponse. As the reverse bias increases, m progressively deviates from this value, indicating a gradual transition toward field-assisted transport mechanisms[68,69].

This analysis reveals the coexistence of multiple transport regimes, suggesting that different mechanisms dominate in different bias regions. Further investigations are required to fully clarify the microscopic origin of the observed behavior.

In conclusion, the investigation of mixed-dimensional ReS_2–Si heterojunctions highlight how built-in electric fields and interface quality govern charge transport and photodetection performance, establishing these junctions as an effective architecture for reproducible optoelectronic operation from room temperature down to cryogenic conditions.

References

(1) Ahmed, S.; Yi, J. Two-Dimensional Transition Metal Dichalcogenides and Their Charge Carrier Mobilities in Field-Effect Transistors. *Nano-Micro Lett.* **2017**, *9* (4), 50. https://doi.org/10.1007/s40820-017-0152-6.

(2) Zhao, L.; Shang, Q.; Li, M.; Liang, Y.; Li, C.; Zhang, Q. Strong Exciton-Photon Interaction and Lasing of Two-Dimensional Transition Metal Dichalcogenide Semiconductors. *Nano Res.* **2021**, *14* (6), 1937–1954. https://doi.org/10.1007/s12274-020-3073-5.

(3) Liu, Y.; Huang, Y.; Duan, X. Van Der Waals Integration before and beyond Two-Dimensional Materials. *Nature* **2019**, *567* (7748), 323–333. https://doi.org/10.1038/s41586-019-1013-x.

(4) Liu, W.; Yu, Y.; Peng, M.; Zheng, Z.; Jian, P.; Wang, Y.; Zou, Y.; Zhao, Y.; Wang, F.; Wu, F.; Chen, C.; Dai, J.; Wang, P.; Hu, W. Integrating 2D Layered Materials with 3D Bulk Materials as van Der Waals Heterostructures for Photodetections: Current Status and Perspectives. *InfoMat* **2023**, *5* (10), e12470. https://doi.org/10.1002/inf2.12470.

(5) Koppens, F. H. L.; Mueller, T.; Avouris, P.; Ferrari, A. C.; Vitiello, M. S.; Polini, M. Photodetectors Based on Graphene, Other Two-Dimensional Materials and Hybrid Systems. *Nat. Nanotechnol.* **2014**, *9* (10), 780–793. https://doi.org/10.1038/nnano.2014.215.

(6) Chang, C.; Xie, X.; Li, T.; Cui, J. Configuration of the Active Region for the Ge-on-Si Photodetector Based on Carrier Mobility. *Front. Phys.* **2023**, *11*. https://doi.org/10.3389/fphy.2023.1150684.

(7) Wei, Y.; Lan, C.; Zhou, S.; Li, C. Recent Advances in Photodetectors Based on Two-Dimensional Material/Si Heterojunctions. *Appl. Sci.* **2023**, *13* (19), 11037. https://doi.org/10.3390/app131911037.

(8) Dong, Y.; Zhao, C.; Wang, H.; Jiang, Y.; Fang, Y.; Wang, J.; Duan, S.; Fu, X.; Miao, J.; Hu, W. Van Der Waals Integration of Two-Dimensional Materials and Bulk Semiconductors for Infrared Photodetection Technology. *MRS Bull.* **2023**, *48* (9), 914–922. https://doi.org/10.1557/s43577-023-00599-0.

(9) Jariwala, D.; Marks, T. J.; Hersam, M. C. Mixed-Dimensional van Der Waals Heterostructures. *Nat. Mater.* **2017**, *16* (2), 170–181. https://doi.org/10.1038/nmat4703.

(10) Di Bartolomeo, A. Graphene Schottky Diodes: An Experimental Review of the Rectifying Graphene/Semiconductor Heterojunction. *Phys. Rep.* **2016**, *606*, 1–58. https://doi.org/10.1016/j.physrep.2015.10.003.

(11) An, X.; Liu, F.; Jung, Y. J.; Kar, S. Tunable Graphene–Silicon Heterojunctions for Ultrasensitive Photodetection. *Nano Lett.* **2013**, *13* (3), 909–916. https://doi.org/10.1021/nl303682j.

(12) Peng, L.; Liu, L.; Du, S.; Bodepudi, S. C.; Li, L.; Liu, W.; Lai, R.; Cao, X.; Fang, W.; Liu, Y.; Liu, X.; Lv, J.; Abid, M.; Liu, J.; Jin, S.; Wu, K.; Lin, M.-L.; Cong, X.; Tan, P.-H.; Zhu, H.; Xiong, Q.; Wang, X.; Hu, W.; Duan, X.; Yu, B.; Xu, Z.; Xu, Y.; Gao, C. Macroscopic Assembled Graphene Nanofilms Based Room Temperature Ultrafast Mid-Infrared Photodetectors. *InfoMat* **2022**, *4* (6), e12309. https://doi.org/10.1002/inf2.12309.

(13) Yim, C.; O'Brien, M.; McEvoy, N.; Riazimehr, S.; Schäfer-Eberwein, H.; Bablich, A.; Pawar, R.; Iannaccone, G.; Downing, C.; Fiori, G.; Lemme, M. C.; Duesberg, G. S. Heterojunction Hybrid Devices from Vapor Phase Grown MoS2. *Sci. Rep.* **2014**, *4* (1), 5458. https://doi.org/10.1038/srep05458.

(14) Li, Y.; Xu, C.-Y.; Wang, J.-Y.; Zhen, L. Photodiode-Like Behavior and Excellent Photoresponse of Vertical Si/Monolayer MoS2 Heterostructures. *Sci. Rep.* **2014**, *4* (1), 7186. https://doi.org/10.1038/srep07186.

(15) Zhang, X.; Shao, J.; Su, Y.; Wang, L.; Wang, Y.; Wang, X.; Wu, D. *In-Situ* Prepared WSe2/Si 2D-3D Vertical Heterojunction for High Performance Self-Driven Photodetector. *Ceram. Int.* **2022**, *48* (20), 29722–29729. https://doi.org/10.1016/j.ceramint.2022.06.231.

(16) Lu, Z.; Xu, Y.; Yu, Y.; Xu, K.; Mao, J.; Xu, G.; Ma, Y.; Wu, D.; Jie, J. Ultrahigh Speed and Broadband Few-Layer MoTe2/Si 2D–3D Heterojunction-Based Photodiodes Fabricated by Pulsed Laser Deposition. *Adv. Funct. Mater.* **2020**, *30* (9), 1907951. https://doi.org/10.1002/adfm.201907951.

(17) Lei, W.; Cao, G.; Wen, X.; Yang, L.; Zhang, P.; Zhuge, F.; Chang, H.; Zhang, W. High Performance MoTe2/Si Heterojunction Photodiodes. *Appl. Phys. Lett.* **2021**, *119* (13), 131902. https://doi.org/10.1063/5.0062788.

(18) Wang, L.; Jie, J.; Shao, Z.; Zhang, Q.; Zhang, X.; Wang, Y.; Sun, Z.; Lee, S.-T. MoS2/Si Heterojunction with Vertically Standing Layered Structure for Ultrafast, High-Detectivity, Self-Driven Visible–Near Infrared Photodetectors. *Adv. Funct. Mater.* **2015**, *25* (19), 2910–2919. https://doi.org/10.1002/adfm.201500216.

(19) Mao, J.; Yu, Y.; Wang, L.; Zhang, X.; Wang, Y.; Shao, Z.; Jie, J. Ultrafast, Broadband Photodetector Based on MoSe2/Silicon Heterojunction with Vertically Standing Layered Structure Using Graphene as Transparent Electrode. *Adv. Sci. Weinh. Baden-Wurtt. Ger.* **2016**, *3* (11), 1600018. https://doi.org/10.1002/advs.201600018.

(20) Dhyani, V.; Dwivedi, P.; Dhanekar, S.; Das, S. High Performance Broadband Photodetector Based on MoS2/Porous Silicon Heterojunction. *Appl. Phys. Lett.* **2017**, *111* (19), 191107. https://doi.org/10.1063/1.5004025.

(21) Wu, D.; Guo, C.; Wang, Z.; Ren, X.; Tian, Y.; Shi, Z.; Lin, P.; Tian, Y.; Chen, Y.; Li, X. A Defect-Induced Broadband Photodetector Based on WS2/Pyramid Si 2D/3D Mixed-Dimensional Heterojunction with a Light Confinement Effect. *Nanoscale* **2021**, *13* (31), 13550–13557. https://doi.org/10.1039/D1NR03243G.

(22) Varghese, A.; Saha, D.; Thakar, K.; Jindal, V.; Ghosh, S.; Medhekar, N. V.; Ghosh, S.; Lodha, S. Near-Direct Bandgap WSe_2 /ReS_2 Type-II Pn Heterojunction for Enhanced Ultrafast Photodetection and High-Performance Photovoltaics. *Nano Lett.* **2020**, *20* (3), 1707–1717. https://doi.org/10.1021/acs.nanolett.9b04879.

(23) Tang, Q.; Zhong, F.; Li, Q.; Weng, J.; Li, J.; Lu, H.; Wu, H.; Liu, S.; Wang, J.; Deng, K.; Xiao, Y.; Wang, Z.; He, T. Infrared Photodetection from 2D/3D van Der Waals Heterostructures. *Nanomaterials* **2023**, *13* (7), 1169. https://doi.org/10.3390/nano13071169.

(24) Smidstrup, S.; Markussen, T.; Vancraeyveld, P.; Wellendorff, J.; Schneider, J.; Gunst, T.; Verstichel, B.; Stradi, D.; Khomyakov, P. A.; Vej-Hansen, U. G.; Lee, M.-E.; Chill, S. T.; Rasmussen, F.; Penazzi, G.; Corsetti, F.; Ojanperä, A.; Jensen, K.; Palsgaard, M. L. N.; Martinez, U.; Blom, A.; Brandbyge, M.; Stokbro, K. QuantumATK: An Integrated Platform of Electronic and Atomic-Scale Modelling Tools. *J. Phys. Condens. Matter* **2019**, *32* (1), 015901. https://doi.org/10.1088/1361-648X/ab4007.

(25) Sancho, M. P. L.; Sancho, J. M. L.; Sancho, J. M. L.; Rubio, J. Highly Convergent Schemes for the Calculation of Bulk and Surface Green Functions. *J. Phys. F Met. Phys.* **1985**, *15* (4), 851. https://doi.org/10.1088/0305-4608/15/4/009.

(26) Brandbyge, M.; Mozos, J.-L.; Ordejón, P.; Taylor, J.; Stokbro, K. Density-Functional Method for Nonequilibrium Electron Transport. *Phys. Rev. B* **2002**, *65* (16), 165401. https://doi.org/10.1103/PhysRevB.65.165401.

(27) van Setten, M. J.; Giantomassi, M.; Bousquet, E.; Verstraete, M. J.; Hamann, D. R.; Gonze, X.; Rignanese, G.-M. The PseudoDojo: Training and Grading a 85 Element Optimized Norm-Conserving Pseudopotential Table. *Comput. Phys. Commun.* **2018**, *226*, 39–54. https://doi.org/10.1016/j.cpc.2018.01.012.

(28) Monkhorst, H. J.; Pack, J. D. Special Points for Brillouin-Zone Integrations. *Phys. Rev. B* **1976**, *13* (12), 5188–5192. https://doi.org/10.1103/PhysRevB.13.5188.

(29) Grimme, S.; Antony, J.; Ehrlich, S.; Krieg, H. A Consistent and Accurate Ab Initio Parametrization of Density Functional Dispersion Correction (DFT-D) for the 94 Elements H-Pu. *J. Chem. Phys.* **2010**, *132* (15), 154104. https://doi.org/10.1063/1.3382344.

(30) Bokdam, M.; Brocks, G.; Katsnelson, M. I.; Kelly, P. J. Schottky Barriers at Hexagonal Boron Nitride/Metal Interfaces: A First-Principles Study. *Phys. Rev. B* **2014**, *90* (8), 085415. https://doi.org/10.1103/PhysRevB.90.085415.

(31) Zhussupbekov, K.; Ansari, L.; Elibol, K.; Zhussupbekova, A.; Kotakoski, J.; Shvets, I. V.; Duesberg, G. S.; Hurley, P. K.; McEvoy, N.; Ó Coileáin, C.; Gity, F. Revealing the Influence of Edge States on the Electronic Properties of PtSe2. *Appl. Mater. Today* **2023**, *35*, 101926. https://doi.org/10.1016/j.apmt.2023.101926.

(32) Stradi, D.; Martinez, U.; Blom, A.; Brandbyge, M.; Stokbro, K. General Atomistic Approach for Modeling Metal-Semiconductor Interfaces Using Density Functional Theory and Nonequilibrium Green's Function. *Phys. Rev. B* **2016**, *93* (15), 155302. https://doi.org/10.1103/PhysRevB.93.155302.

(33) Wu, E.; Wu, D.; Jia, C.; Wang, Y.; Yuan, H.; Zeng, L.; Xu, T.; Shi, Z.; Tian, Y.; Li, X. In Situ Fabrication of 2D WS $_2$ /Si Type-II Heterojunction for Self-Powered Broadband Photodetector with Response up to Mid-Infrared. *ACS Photonics* **2019**, *6* (2), 565–572. https://doi.org/10.1021/acsphotonics.8b01675.

(34) Yim, C.; McEvoy, N.; Riazimehr, S.; Schneider, D. S.; Gity, F.; Monaghan, S.; Hurley, P. K.; Lemme, M. C.; Duesberg, G. S. Wide Spectral Photoresponse of Layered Platinum Diselenide-Based Photodiodes. *Nano Lett.* **2018**, *18* (3), 1794–1800. https://doi.org/10.1021/acs.nanolett.7b05000.

(35) Son, S. B.; Kim, Y.; Cho, B.; Choi, C.-J.; Hong, W.-K. Temperature-Dependent Electronic Charge Transport Characteristics at MoS2/p-Type Ge Heterojunctions. *J. Alloys Compd.* **2018**, *757*, 221–227. https://doi.org/10.1016/j.jallcom.2018.05.034.

(36) Janardhanam, V.; Jyothi, I.; Yuk, S.-H.; Munkhsaikan, Z.; Choi, C.-J. Temperature-Dependent Interface Barrier Behavior in MoS2/n-GaN 2D/3D Heterojunction. *Mater. Lett.* **2021**, *296*, 129893. https://doi.org/10.1016/j.matlet.2021.129893.

(37) Rahman, M.; Davey, K.; Qiao, S.-Z. Advent of 2D Rhenium Disulfide (ReS2): Fundamentals to Applications. *Adv. Funct. Mater.* **2017**, *27* (10), 1606129. https://doi.org/10.1002/adfm.201606129.

(38) Tung, R. T. Electron Transport at Metal-Semiconductor Interfaces: General Theory. *Phys. Rev. B* **1992**, *45* (23), 13509–13523. https://doi.org/10.1103/PhysRevB.45.13509.

(39) Moun, M.; Kumar, M.; Garg, M.; Pathak, R.; Singh, R. Understanding of MoS2/GaN Heterojunction Diode and Its Photodetection Properties. *Sci. Rep.* **2018**, *8* (1), 11799. https://doi.org/10.1038/s41598-018-30237-8.

(40) Janardhanam, V.; Jyothi, I.; Kim, Y.; Lee, S.-N.; Yun, H.-J.; Hong, W.-K.; Choi, C.-J. Carrier Conduction Mechanisms of WSe2/p-Type Ge Epilayer Heterojunction Depending on the Measurement Temperature and Applied Bias. *J. Alloys Compd.* **2020**, *842*, 155843. https://doi.org/10.1016/j.jallcom.2020.155843.

(41) Roul, B.; Bhat, T. N.; Kumar, M.; Rajpalke, M. K.; Sinha, N.; Kalghatgi, A. T.; Krupanidhi, S. B. Barrier Height Inhomogeneities in InN/GaN Heterostructure Based Schottky Junctions. *Solid State Commun.* **2011**, *151* (20), 1420–1423. https://doi.org/10.1016/j.ssc.2011.07.008.

(42) Mondal, S.; Halder, S.; Basak, D. Ultrafast and Ultrabroadband UV–Vis-NIR Photosensitivity under Reverse and Self-Bias Conditions by n $^+$ -ZnO/n-Si Isotype Heterojunction with >1 kHz Bandwidth. *ACS Appl. Electron. Mater.* **2023**, *5* (2), 1212–1223. https://doi.org/10.1021/acsaelm.2c01668.

(43) Wu, D.; Guo, C.; Wang, Z.; Ren, X.; Tian, Y.; Shi, Z.; Lin, P.; Tian, Y.; Chen, Y.; Li, X. A Defect-Induced Broadband Photodetector Based on WS2/Pyramid Si 2D/3D Mixed-Dimensional Heterojunction with a Light Confinement Effect. *Nanoscale* **2021**, *13* (31), 13550–13557. https://doi.org/10.1039/D1NR03243G.

(44) Jo, B.; Seo, K.; Park, K.; Jeong, C.; Poornaprakash, B.; Lee, M.; Ramu, S.; Hahm, M. G.; Kim, Y. L. Trap-Assisted Monolayer ReSe2/Si Heterojunction with High Photoconductive Gain and Self-Driven Broadband Photodetector. *Front. Mater.* **2024**, *11*. https://doi.org/10.3389/fmats.2024.1354522.

(45) Zhou, C.; Zhang, S.; Lv, Z.; Ma, Z.; Yu, C.; Feng, Z.; Chan, M. Self-Driven WSe2 Photodetectors Enabled with Asymmetrical van Der Waals Contact Interfaces. *Npj 2D Mater. Appl.* **2020**, *4* (1), 1–9. https://doi.org/10.1038/s41699-020-00179-9.

(46) Wang, Q.; Zhou, C.; Chai, Y. Breaking Symmetry in Device Design for Self-Driven 2D Material Based Photodetectors. *Nanoscale* **2020**, *12* (15), 8109–8118. https://doi.org/10.1039/D0NR01326A.

(47) Jia, C.; Wu, D.; Wu, E.; Guo, J.; Zhao, Z.; Shi, Z.; Xu, T.; Huang, X.; Tian, Y.; Li, X. A Self-Powered High-Performance Photodetector Based on a MoS2/GaAs Heterojunction with High Polarization Sensitivity. *J. Mater. Chem. C* **2019**, *7* (13), 3817–3821. https://doi.org/10.1039/C8TC06398B.

(48) Shin, G. H.; Park, J.; Lee, K. J.; Lee, G.-B.; Jeon, H. B.; Choi, Y.-K.; Yu, K.; Choi, S.-Y. Si–MoS2 Vertical Heterojunction for a Photodetector with High Responsivity and Low Noise Equivalent Power. *ACS Appl. Mater. Interfaces* **2019**, *11* (7), 7626–7634. https://doi.org/10.1021/acsami.8b21629.

(49) Jelver, L.; Stradi, D.; Stokbro, K.; Wedel Jacobsen, K. Schottky Barrier Lowering Due to Interface States in 2D Heterophase Devices. *Nanoscale Adv.* **2021**, *3* (2), 567–574. https://doi.org/10.1039/D0NA00795A.

(50) Reshchikov, M. A.; Foussekis, M.; Baski, A. A. Surface Photovoltage in Undoped N-Type GaN. *J. Appl. Phys.* **2010**, *107* (11), 113535. https://doi.org/10.1063/1.3430979.

(51) Kilin, D. S.; Micha, D. A. Surface Photovoltage at Nanostructures on Si Surfaces: Ab Initio Results. *J. Phys. Chem. C* **2009**, *113* (9), 3530–3542. https://doi.org/10.1021/jp808908x.

(52) Munakata, C.; Matsubara, S. The Photovoltaic Observation of Semiconductor Surfaces. *J. Phys. Appl. Phys.* **1983**, *16* (6), 1093–1098. https://doi.org/10.1088/0022-3727/16/6/017.

(53) Mukherjee, S.; Samanta, G.; Hasan, M. N.; Moulick, S.; Kulkarni, R.; Watanabe, K.; Taniguchi, T.; Thamizhavel, A.; Karmakar, D.; Pal, A. N. Achieving Nearly Barrier Free Transport in High Mobility ReS2 Phototransistors with van Der Waals Contacts. *Npj 2D Mater. Appl.* **2024**, *8* (1), 71. https://doi.org/10.1038/s41699-024-00507-3.

(54) Meng, X.; Du, Y.; Wu, W.; Joseph, N. B.; Deng, X.; Wang, J.; Ma, J.; Shi, Z.; Liu, B.; Ma, Y.; Yue, F.; Zhong, N.; Xiang, P.-H.; Zhang, C.; Duan, C.-G.; Narayan, A.; Sun, Z.; Chu, J.; Yuan, X. Giant Superlinear Power Dependence of Photocurrent Based on Layered Ta2NiS5 Photodetector. *Adv. Sci.* **2023**, *10* (20), 2300413. https://doi.org/10.1002/advs.202300413.

(55) Wang, L.; Yue, Q.; Pei, C.; Fan, H.; Dai, J.; Huang, X.; Li, H.; Huang, W. Scrolling Bilayer WS2/MoS2 Heterostructures for High-Performance Photo-Detection. *Nano Res.* **2020**, *13* (4), 959–966. https://doi.org/10.1007/s12274-020-2725-9.

(56) Massicotte, M.; Schmidt, P.; Vialla, F.; Watanabe, K.; Taniguchi, T.; Tielrooij, K. J.; Koppens, F. H. L. Photo-Thermionic Effect in Vertical Graphene Heterostructures. *Nat. Commun.* **2016**, *7* (1), 12174. https://doi.org/10.1038/ncomms12174.

(57) Tobehn-Steinhäuser, I.; Reiche, M.; Schmelz, M.; Stolz, R.; Fröhlich, T.; Ortlepp, T. Carrier Mobility in Semiconductors at Very Low Temperatures. *Eng. Proc.* **2021**, *6* (1), 86. https://doi.org/10.3390/I3S2021Dresden-10086.

(58) Dhyani, V.; Das, S. High-Speed Scalable Silicon-MoS2 P-N Heterojunction Photodetectors. *Sci. Rep.* **2017**, *7* (1), 44243. https://doi.org/10.1038/srep44243.

(59) Dhakal, K. P.; Lee, E.; Anh, T. V.; Ghimire, G.; Choi, W.; Kim, Y.-M.; Duong, D. L.; Kim, J. Investigation of Exciton States of ReS2 by Temperature- and Polarization-Dependent Photoluminescence and Oxygen Plasma Treatment. *Appl. Surf. Sci.* **2023**, *638*, 158093. https://doi.org/10.1016/j.apsusc.2023.158093.

(60) Lopez-Sanchez, O.; Lembke, D.; Kayci, M.; Radenovic, A.; Kis, A. Ultrasensitive Photodetectors Based on Monolayer MoS2. *Nat. Nanotechnol.* **2013**, *8* (7), 497–501. https://doi.org/10.1038/nnano.2013.100.

(61) Wu, E.; Wu, D.; Jia, C.; Wang, Y.; Yuan, H.; Zeng, L.; Xu, T.; Shi, Z.; Tian, Y.; Li, X. In Situ Fabrication of 2D WS2/Si Type-II Heterojunction for Self-Powered Broadband Photodetector with Response up to Mid-Infrared. *ACS Photonics* **2019**, *6* (2), 565–572. https://doi.org/10.1021/acsphotonics.8b01675.

(62) Furchi, M. M.; Pospischil, A.; Libisch, F.; Burgdörfer, J.; Mueller, T. Photovoltaic Effect in an Electrically Tunable van Der Waals Heterojunction. *Nano Lett.* **2014**, *14* (8), 4785–4791. https://doi.org/10.1021/nl501962c.

(63) Boivin, L.-P. Spectral Responsivity of Various Types of Silicon Photodiode at Oblique Incidence: Comparison of Measured and Calculated Values. *Appl. Opt.* **2001**, *40* (4), 485–491. https://doi.org/10.1364/AO.40.000485.

(64) Kjornrattanawanich, B.; Korde, R.; Boyer, C. N.; Holland, G. E.; Seely, J. F. Temperature Dependence of the EUV Responsivity of Silicon Photodiode Detectors. *IEEE Trans. Electron Devices* **2006**, *53* (2), 218–223. https://doi.org/10.1109/TED.2005.862500.

(65) Stathatos, E.; Chen, Y.; Dionysiou, D. D. Quasi-Solid-State Dye-Sensitized Solar Cells Employing Nanocrystalline TiO2 Films Made at Low Temperature. *Sol. Energy Mater. Sol. Cells* **2008**, *92* (11), 1358–1365. https://doi.org/10.1016/j.solmat.2008.05.009.

(66) Pelella, A.; Intonti, K.; Durante, O.; Kumar, A.; Viscardi, L.; De Stefano, S.; Romano, P.; Giubileo, F.; Neill, H.; Patil, V.; Ansari, L.; Roycroft, B.; Hurley, P. K.; Gity, F.; Di Bartolomeo, A. Multilayer WS2 for Low-Power Visible and near-Infrared Phototransistors. *Discov. Nano* **2024**, *19* (1), 57. https://doi.org/10.1186/s11671-024-04000-0.

(67) Amrani, M. E.; Buckley, J.; Kaltsounis, T.; Arguello, D. P.; Rammouz, H. E.; Alquier, D.; Charles, M. Study of Leakage Current Transport Mechanisms in Pseudo-Vertical GaN-on-Silicon Schottky Diode Grown by Localized Epitaxy. *Crystals* **2024**, *14* (6). https://doi.org/10.3390/cryst14060553.

(68) Lampert, M.; Mark, P. Current Injection in Solids; 1970.

(69) Tunnel Devices. In *Physics of Semiconductor Devices*; John Wiley & Sons, Ltd, 2006; pp 415–465. https://doi.org/10.1002/9780470068328.ch8.

Chapter 6

Light-induced Functionalities in Ambipolar 2D Field-effect Transistors

Bidirectional photoconductivity in $MoTe_2$ FETs and light-induced anti-ambipolar transport in WSe_2- based FETs.

6.1 Introduction

The previous chapters demonstrated that the interplay between surface interactions, interface traps, and electrostatic control can significantly influence charge transport and photoresponse in two-dimensional materials. While this inherent sensitivity can limit stability and device performance, it also provides opportunities to access emerging optoelectronic functionalities that are not available in conventional semiconductors.

Ambipolar transport, in particular, introduces additional degrees of freedom in the modulation of the channel current, since both electron and hole conduction can be selectively accessed within the same device. Under the combined action of illumination and gate bias, this behaviour can give rise to non-trivial photoinduced phenomena, where optical excitation and electrostatic control act as external parameters to dynamically tune the device response.

In this chapter, a primary investigation on $MoTe_2$-based FETs demonstrates gate-tunable bidirectional photoconductivity, where the sign of the photocurrent can be switched between positive and negative depending on the electrostatic configuration and on the dynamics of interface trap states. A more extensive study is then conducted on WSe_2-based transistors, which reveal a light-driven transition from ambipolar to anti-ambipolar transport, governed by gate-modulated Schottky barriers and photo-generated carriers. This behaviour results in a distinctive Λ-shaped transfer characteristic and the emergence of multiple gate-dependent current states, suggesting potential pathways toward multilevel optoelectronic functionalities that extend beyond conventional binary operation.

6.2 Bidirectional photodetectors

Bidirectional photoresponse in 2D optoelectronic devices has recently attracted increasing attention, as it enables the coexistence of positive and negative photoconductivity (PPC and

NPC) within the same device platform. Unlike conventional unipolar photodetectors, such bipolar behaviour provides polarity-tunable output states and represents a key ingredient for expanding information dimensionality and enabling adaptive sensing and signal modulation[1,2]. In addition, PPC and NPC can emulate excitation and inhibition processes, drawing inspiration from biological visual systems.

From a device-physics perspective, PPC corresponds to an increase in current under illumination, whereas NPC manifests as a current suppression with respect to the dark state[3]. In ambipolar field-effect transistors, the sign and magnitude of the photocurrent depend critically on the electrostatic configuration, making the definition of an appropriate dark reference crucial for identifying PPC or NPC. These effects are reflected in the current–voltage and transfer characteristics, where illumination produces either upward or downward deviations or effective horizontal shifts.

Bidirectional photoresponses in optoelectronic systems can be driven by several distinct mechanisms, including gate-controlled, wavelength-dependent, polarization-dependent, and input-power-dependent effects. Gate-driven bidirectional behavior is most commonly observed in field-effect transistors, where electrostatic modulation of the channel doping enables two main mechanisms[4,5]. In the first mechanism, bipolar doping conditions determine the final photocurrent direction[6], while, in the second mechanism gate-induced shifts in the channel doping level modify band bending and carrier injection conditions, thereby determining the direction of the photoresponse[7].

Many materials and approaches have been explored to obtain gate-tunable bidirectional photoresponse, such as exploiting a floating gate in ReS_2/h-BN/MoS_2 devices[4], or a gate-tunable built-in electric field in 2D/2D heterostructures like WSe_2/$SnSe_2$ heterojunctions[5]. Anisotropic materials like $ReSe_2$[8], BP[9], $PtSe_2$[3] can also be used to enable additional degrees of freedom by modulating the photocurrent through different polarizations or by the change in atmospheric pressure.

Ambipolar materials such as $MoTe_2$ are very promising for gate-tunable bidirectional responses. $MoTe_2$ exhibits three main crystal structures at room temperature: the hexagonal semiconducting 2H phase, the monoclinic semimetallic 1T′ phase, and the orthogonal phase 1T[10]. In its monolayer form, $MoTe_2$ is a direct-bandgap semiconductor with an optical bandgap ranging from 1.10 to 1.14 eV[11]. While bilayers remain direct-gap semiconductors, tetralayer $MoTe_2$ becomes indirect-gap, and trilayers exhibit nearly degenerate direct and indirect gaps. Thanks to the narrow bandgap, moreover, $MoTe_2$ is particularly attractive for near-infrared and broadband photodetection[12]. Several strategies, including heterojunctions, optical cavities, gradient bandgap engineering, phase engineering between 2H and 1T′, and coupling with dielectric metalenses, have significantly improved responsivity, detectivity, and response speed[13,14].

From a transistor perspective, $MoTe_2$ is predicted to exhibit higher phonon-limited acoustic mobility than MoS_2 and $MoSe_2$[15]. A key advantage lies in its ability to form seamless in-plane heterophase junctions between semiconducting 2H and semimetallic 1T′ phases, enabling low-resistance ohmic contacts and reduced Schottky barriers[16,17]. h-BN encapsulation combined with thermal annealing[18] enables polarity switching and mobility enhancement by modifying contact barriers and interface states[19].

These approaches collectively demonstrate that $MoTe_2$-based FETs offer a highly tunable platform suitable not only for logic devices but also for memory, neuromorphic, and multifunctional transistor applications [20].

Herein, an initial investigation of bidirectional photoresponse in $MoTe_2$ is reported.

6.3 Materials and methods

The $MoTe_2$ flakes, whose atomic structure is displayed in Figure 6.1a, were exfoliated using a standard mechanical exfoliation method, and they were transferred onto highly doped p-type silicon substrates (resistivity 0.001 $\Omega \cdot$ cm) covered by an 85 nm thick SiO_2 layer, which globally acts as a back gate.

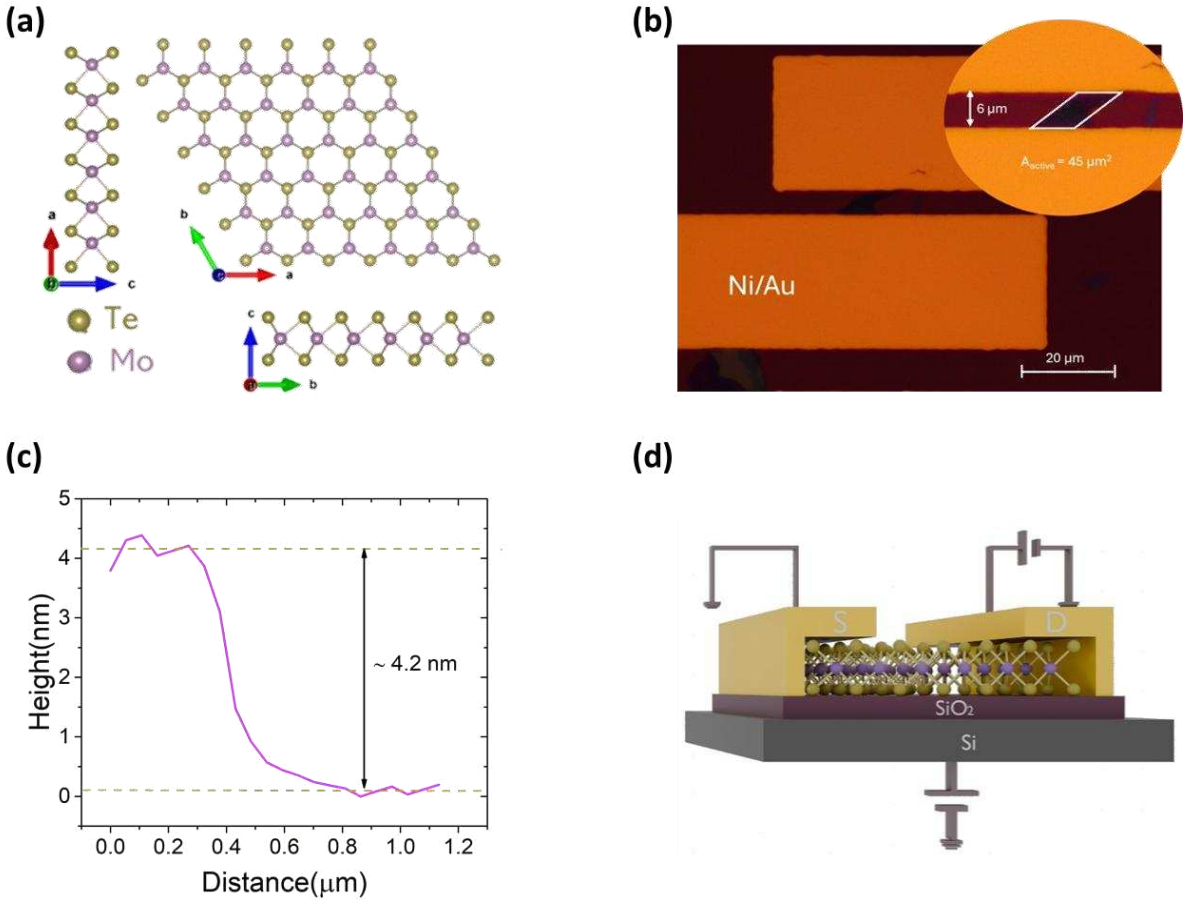

Figure 6.1: (a) Atomic structure of $MoTe_2$ along three axes. (b) Optical image of the device. In the right-top corner, a zoom of the target flake is shown. (c) AFM height profile of the target flake. (d) Schematic of the device together with the measurement set up.

The optical image of the device under investigation in Figure 6.1b illustrates how evaporated Ni/Au metal contacts were then patterned on the targeted flake using photolithography and a standard lift-off process. The magnification at the top right corner of Figure 6.1b zooms into the $MoTe_2$ flake, which has an optical active area of $A_{active} = 45$ µm^2. Figure 6.1c shows the height profile extracted through AFM. The profile indicates a thickness of about 4.2 nm, which corresponds to six layers. The schematic of the device is reported in Figure 6.1d together with

the measurement set up. Electrical measurements were performed in a two-probe configuration in a Lakeshore probe station and the data were acquired through the semiconductor characterization system Keithley 4200 SCS.

6.4 Results and discussion

6.4.1 Electrical characteristics in the dark

Electrical measurements were carried out in high vacuum (P = $1 \cdot 10^{-4}$ mbar), since $MoTe_2$ is highly sensitive to the adsorption of atmospheric species such as O_2 or H_2O. Tellurides of VI-group TMDs, much more than sulphides and selenides, can undergo surface oxidation when exposed to air[21].

After loading the sample into the probe station, the chamber was pumped down and the temporal evolution of the electrical characteristics was monitored until a stable configuration was reached by repeating the transfer curves over a couple of days. Figure 6.2a shows the ambipolar transport behaviour of the transistor within the (-40;40) V gate-voltage range. This observation is consistent with first-principle simulations indicating nearly symmetric injection barriers at the Ni/$MoTe_2$ interface, which facilitate ambipolar conduction[22].

The device initially exhibited a predominant p-type behaviour[23], which can be attributed to the adsorption of oxygen molecules during device fabrication and storage in ambient conditions. From XPS and UPS studies reported in the literature, pristine $MoTe_2$ flakes generally exhibit a n-type behaviour, likely due to intrinsic Te vacancies with low formation energy that generate energy states close to the conduction band edge. Upon vacuum pumping, the progressive removal of atmospheric adsorbates led to electron reinjection into the channel and a gradual shift toward dominant n-type conduction, indicating that the initial p-type behaviour was primarily governed by reversible adsorption processes, rather than by irreversible oxidation mechanisms.

The evolution is clearly visible in Figure 6.2a and 6.2b , which show the progressive change in the polarity of the transfer curve over time[24]. The corresponding transistor figures of merit evolve accordingly. The on current at the p-side reduces from micro amperes to nano amperes, making the I_{on}/I_{off} ratio decrease from 10^6 to $2 \cdot 10^3$. The hole mobility, calculated according to the formula 2.12 with $C_{ox} = 4.06 \cdot 10^{-8}$ F/cm^2, decreases from 3 to 0.04 cm^{2}V^{-1}s^{-1}, while the subthreshold swing slightly modifies, ranging from 1.6 to 2.7 V/decade. At the same time, on the n-side, an increase in the I_{on}/I_{off} ratio and in the mobility is detected, with a maximum value of 0.12 cm^{2}V^{-1}s^{-1}. The subthreshold swing also slightly increases from 2 to 2.8 V/decade.

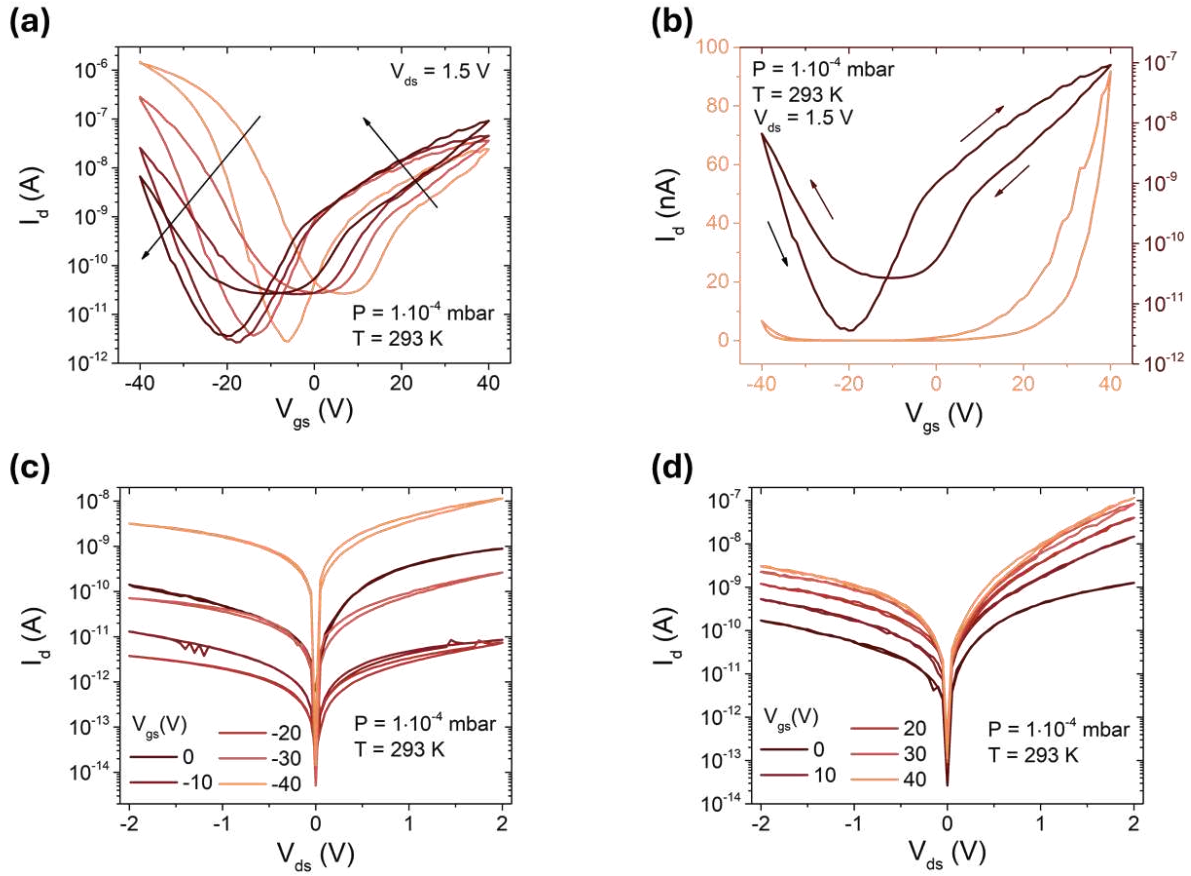

Figure 6.2: (a) Time evolution of the transfer curves of the device measured over several days under high vacuum condition, showing the gradual transition from p-dominant to n-dominant conduction. (b) Stabilized transfer characteristic reported on a linear (right axis) and logarithmic (left axis) scale. Output curves acquired at negative (c) and positive (d) gate voltages. A more pronounced asymmetry in the output curves is observed under positive V_{gs}.

The stabilized transfer characteristic is reported in Figure 6.2b both on linear (left axis) and logarithmic (right axis) scale for better clarity. Figure 6.2c and 6.2d report the output curves at negative and positive V_{gs}, respectively. V_{ds} was limited to 2V and V_{gs} to $\pm$ 40V to prevent damage to the device and to the SiO_2 dielectric layer. The deviation from linearity in the output curves suggest that Schottky barriers occur at the metal-semiconductor interfaces. Moreover, for both negative and positive gate voltages the curves are not symmetric, but the current is generally higher at positive V_{ds}. The asymmetry reveals different Schottky barriers at the drain and source sides for both electrons and holes. Qualitative band diagrams in Figure 6.3 display the different injection capability across the barriers.

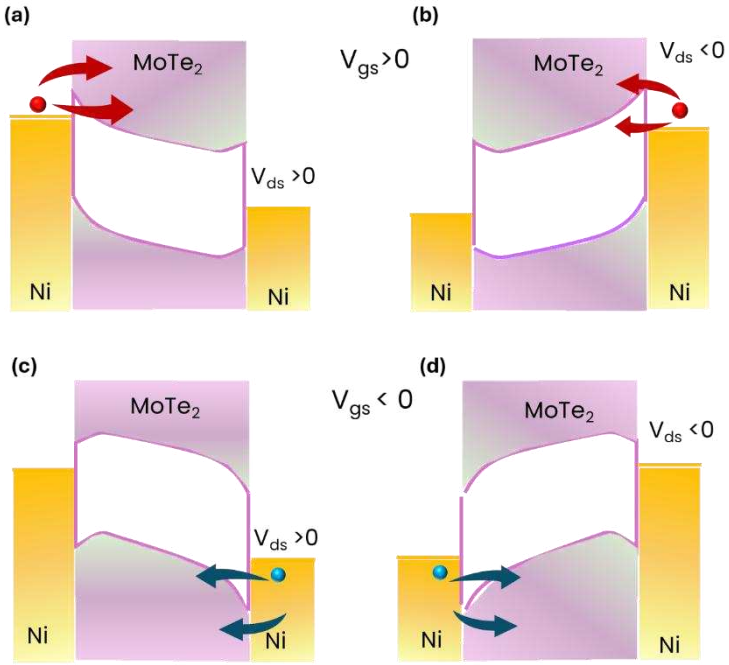

Figure 6.3: Band diagrams illustrating the impact of Schottky barrier asymmetry on charge injection. (a) Positive drain bias favors electron injection more effectively than (b) negative drain bias. Similarly, (c) positive drain bias is more favorable for hole injection compared to (d) negative drain bias.

6.4.2 Photoresponse investigation

The photoresponse of the device was investigated under local illumination delivered by a nano-positioned optical fiber, coupled with a SuperK Compact white laser. Figure 6.4a and 6.4b report the I-V curves and transfer curves at different P_{inc}, ranging from 4.49 to 89.4 µW.

At zero gate bias, the device exhibits clear sensitivity to the incident optical power as shown in Figure 6.4a. Under illumination, the I–V characteristics become more symmetric, which can be attributed to the enhanced collection of photogenerated electrons and holes at the drain and source contacts, respectively. Notably, at low P_{inc}, the drain current at positive V_{ds} is lower than the dark value, as highlighted in the inset, indicating the emergence of negative photoconductivity. At higher powers, instead, the current increases at both polarities, revealing an intensity-dependent bidirectional response likely associated with competing trapping and detrapping processes.

More insight is provided by the transfer curves in Figure 6.4b, acquired under double sweep gate voltage cycles. The photoresponse is clearly bipolar and depends on both the applied electrostatic configuration and the sweep history. Distinct gate-voltage regions characterized by either PPC or NPC can be identified, as more clearly visualized in the photocurrent maps of Figures 6.4c and 6.4d. Along the reverse branch, from 40 to −40 V, the photocurrent is positive within an intermediate window of approximately −25 to +25 V, while it becomes negative outside this range. Along the forward branch, the PPC region extends over a broader interval, approximately from −30 to +30 V.

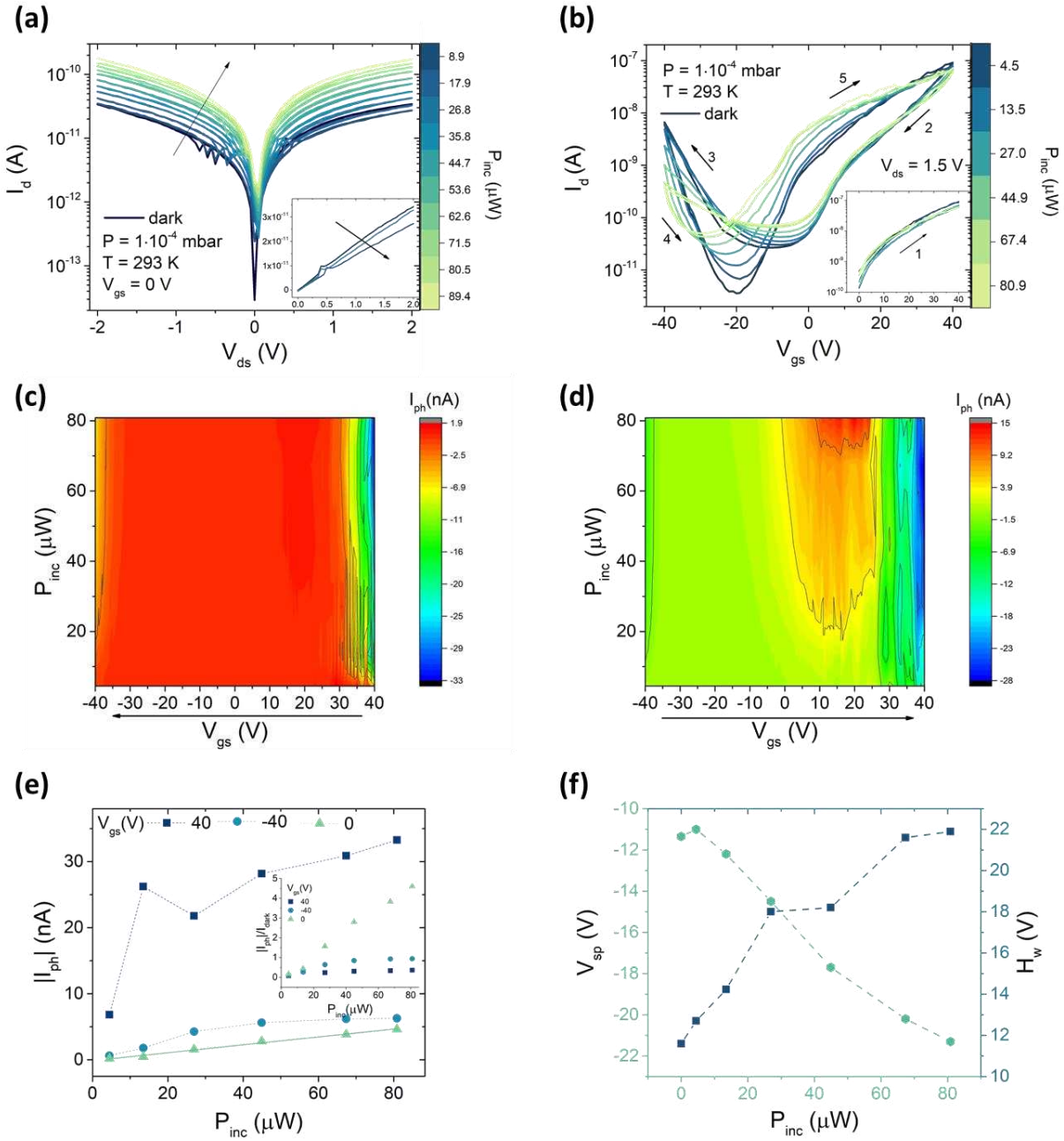

Figure 6.4: (a) I_d-V_{ds} curves at increasing incident optical powers. The inset shows that at low incident optical powers (~ 8.9 and 17.9 μW) the I_d-V_{ds} curves are below the dark one at positive drain voltages (b) Transfer characteristics at increasing incident optical powers. The inset shows the initial branch of the transfer, obtained by sweeping the gate voltage from 0 to 40 V, in the dark, and under different intensities. (c) Photocurrent map as a function of the incident optical power, obtained by sweeping the gate voltage from 40 to -40 V. (d) Photocurrent map as a function of the incident optical power, obtained by sweeping the gate voltage from -40 to 40 V. (e) Photocurrent as a function of the incident optical power at several gate voltages. The inset reports the photocurrent over the dark level as a function of the intensity of the light. (f) Position of the ambipolar switching point (right) and width of the hysteresis (left) as a function of the incident optical power.

Moreover, along the reverse branch, the photocurrent is almost constant as a function of the bias and P_{inc} in the (25, -25) V range, while there is a larger variability in the NPC regime. Conversely, in the forward branch the photocurrent shows a stronger dependence on the incident light intensity. At V_{gs} = 0 V, for instance, a linear trend of the photocurrent as a function of P_{inc} is observed, while a sublinear behaviour is identified at $V_{gs} = \pm$ 40 V – see Figure 6.4e. Figure 6.4f summarizes the evolution of the hysteresis width H_w as a function of P_{inc}, calculated as the voltage difference between the forward and reverse branch at the fixed drain current of $I_d = 3 \cdot 10^{-9}$ A, together with the progressive leftward shift of the polarity switching point V_{sp}.

The coexistence of PPC and NPC, together with the systematic shift of the ambipolar switching point under illumination, indicate that multiple photo-induced mechanisms are involved, with trapping phenomena likely playing a central role.

In photogating-dominated optoelectronic devices, trapped photogenerated carriers act as localized floating gates, modulating the channel conductivity and inducing an effective shift of the transfer characteristics. This mechanism naturally leads to gate-tunable photoconductivity and can enable the observation of NPC[25].

More generally, NPC in 2D materials is commonly associated with trapping of the majority carriers, accompanied by recombination of the opposite carrier species, resulting in a net reduction of the free carrier density in the channel. Trap states may originate from intrinsic defects of the material, defects at the semiconductor–oxide interface, or residual surface adsorbates[26]. The latter are here largely suppressed by the vacuum condition.

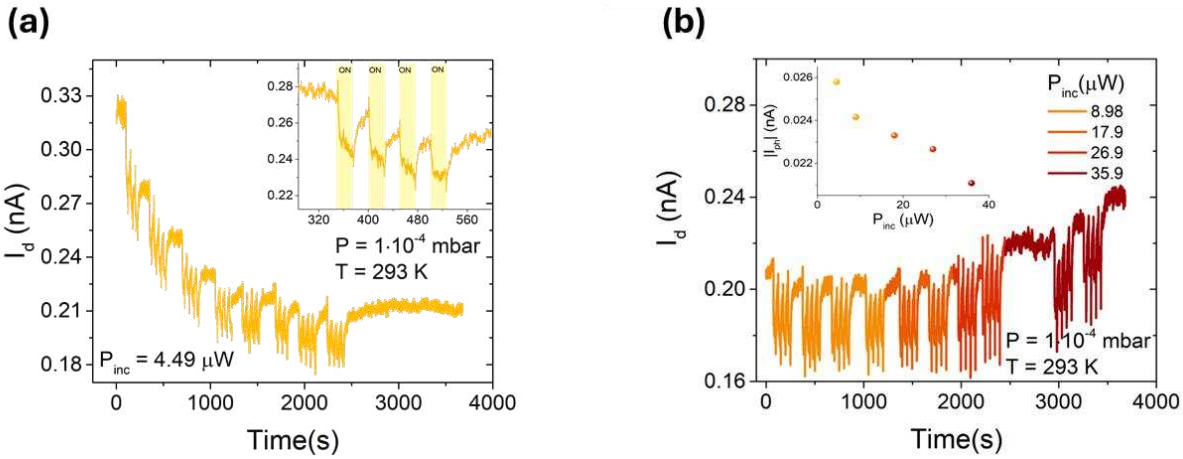

Figure 6.5: Drain current vs. time. (a) The sample was irradiated with 30 s long light pulses of P_{inc} = 4.49 µW, obtained by switching on and off the laser. The inset is a zoom of the plot that shows the negative photoresponse. (b) The device is illuminated under 30 s long light pulses as a function of increasing optical powers. The inset reports the photocurrent value at the respective intensities.

However, a simple global shift of the transfer characteristics is insufficient to fully explain the observed behavior. The emergence of negative photoconductivity at large positive and negative gate biases, together with the stretching of the transfer curve, indicates the presence of additional gate-dependent trapping processes. At large positive V_{gs}, electrons are the majority carriers. Photogenerated electrons are preferentially trapped by states located near the conduction band, leading to a suppression of electron transport and to NPC. Similarly, at

large negative gate biases, hole transport dominates. Hole traps close to the valence band become active, reducing the hole current and again resulting in negative photoconductivity[26].

The occurrence of NPC at zero gate bias requires additional consideration, since the device operates close to the transition point between electron and hole conduction, where transport is influenced by the Schottky barriers. Preliminary measurements of the device biased on the branch n°1 of the transfer curve under 30 s long laser pulses are reported in Figure 6.5a. The drain current was monitored while switching on and off the laser at a low P_{inc} = 4.49 µW. When the device is illuminated, the current decreases with a steep rise, showing a remarkable negative photoconductivity. When the laser is switched off, the current does not come back to the original dark level over the investigated time scale, indicating persistent trapping dynamics[27]. This feature results in an overall decreasing trend of I_{dark}. By increasing P_{inc} from 4.49 to 35.9 µW, a negative photocurrent is still detected as shown in Figure 6.5b, but its absolute value decreases as a function of the incident power, as reported in the inset. Moreover, I_{dark} rises for successive laser pulses. This behaviour confirms the decreasing trend of $|I_{ph}|$ as a function of P_{inc} at V_{gs} = 0 V, anticipated by the inset in Figure 6.4b. However, a clear response to the laser pulses is not detected anymore at higher intensities, revealing a transition to a different regime[28]. Overall, these observations support the role of slow trap-mediated processes at V_{gs} = 0V, which deserve further investigation.

At a proof-of-concept level, the photoresponse of the $MoTe_2$ transistor can be mapped onto key signal-processing roles of retinal bipolar cells. In the biological retina, bipolar cells separate visual information into ON and OFF pathways that encode luminance contrast, responding with opposite polarities to increases or decreases in photoreceptor input and enabling dynamic gain control. Analogously, the $MoTe_2$ device exhibits gate-tunable positive and negative photoconductivity, where PPC and NPC emerge depending on the electrostatic configuration and operating branch. In this mapping, PPC and NPC correspond to ON-like and OFF-like responses, respectively, while the gate voltage plays a role analogous to synaptic or circuit-level modulation in the retina, selecting the polarity and strength of the response.

Similar retina-inspired mappings have been previously proposed in BP-based transistors[9].

6.5 Anti-ambipolarity

Anti-ambipolar behaviour has recently emerged as a novel feature in 2D materials-based devices. It refers to the drain current reaching a local maximum at a specific gate voltage, which results in an "Λ-shaped" current vs. gate voltage curve rather than the typical "V-shape" of ambipolar devices. Devices based on this feature can implement numerous logic functions, such as having more than two logic states for information storage and information transmission, which are crucial to simplify the circuit design and increase their energy efficiency.

This phenomenon was first observed in carbon nanotubes/MoS_2 p-n heterojunctions[29] by Jariwala et al. and it was attributed to the tunability with gate bias of the resistance of the p and n semiconductors in series, which affects the net series resistance of the channel.

More recently, anti-ambipolarity was investigated in 2D/2D p-n heterojunctions. The performance of these junctions depends largely on the threshold voltages of their respective p-type and n-type materials. The threshold voltage of the p material needs to be higher than the

threshold voltage of the n material to have this feature, as highlighted by Li et al[30]. They fabricated p-n heterojunctions by using p-WSe_2, n-MoS_2 and n-SnS_2. Apart from choosing the right material combination, several improvement strategies, such as intentional doping and increasing carrier concentration by using thicker TMDs were discussed.

Accordingly, Sun et al.[31] combined a few-layer p-$MoTe_2$ with multi-layer n-InSe to obtain a type II band alignment, which results in an "Λ" shape of the transfer curve with a peak-to-valley ratio of 10^3. The quantum confinement effect and the strong interlayer coupling allow for modulating the bandgap and carrier concentration of 2D materials by changing their thickness. Therefore, the threshold voltage of the two components can be controlled separately by tuning the number of layers.

Lv et al.[32] have found the anti-ambipolar behaviour at room temperature in both dark and illuminated conditions in a p-WSe_2/n-SnS_2 type II heterojunction. They analysed the phenomenon with an equivalent circuit model and simulations based on Poisson and drift-diffusion equations. Having a type-II heterojunction with doped n and p materials is not necessarily enough to observe anti-ambipolarism. It is needed to have a large vdW barrier at the interface, together with recombination of electrons and holes at the space charge region to have a strong peak-to-valley ratio.

Also, other combinations, such as p-$MoTe_2$/n-MoS_2[33], and BP/MoS_2[34] have been discovered to show this feature in different conditions. However, it is still a challenge to fabricate 2D/2D anti-ambipolar devices with reliable and consistent performance, primarily because it requires a highly accurate control on the on-set voltage and the carrier density of both n-type and p-type components. Moreover, 2D/2D heterostructures strongly depend on precise interface quality and multi-layer fabrication processes that lead to high production costs and complexity, limiting practical deployment.

In the search for architectures based on a single material, WSe_2-based FETs have attracted significant attention. WSe_2 is a group VI TMD that crystallizes in the typical 2H phase[35]. Monolayer WSe_2 exhibits a high density of intrinsic defects, including Se vacancy, W vacancy and large vacancy complexes[36]. As other TMDs of group VI, it experiences a transition from an indirect bandgap in its bulk form to a direct bandgap of 1.64 eV as a monolayer and the bandgap value can be modulated with the number of layers[37]. Strain and stress are also effective in changing the bandgap of WSe_2[38], making it suitable for applications such as photoelectric devices, catalysis, energy storage and sensors[39]. Owing to its tuneable transport, from p-type to ambipolar, to n-type transport, WSe_2 has also been used in CMOS architectures[40,41], logic inverters[42,43], and rectifiers[44,45] .

Thakar and Lodha[46] demonstrated that ambipolar and anti-ambipolar transport in a WSe_2-based field-effect transistor can be reconfigured and tuned by using a dual electrostatic control scheme. Their device employs three back gates: one controls the channel region, while the other two, connected together, modulate the regions beneath the metal contacts, affecting the Schottky barriers. By adjusting the voltages applied to these two sets of gates, the polarity of each region can be independently controlled, enabling different transport regimes depending on the chosen bias configuration. This enables the realization of multi-bit encoding schemes. The physical mechanism is similar to that in p-n junction devices.

Simpler architectures were used by Wang et al.[47], who fabricated a WSe_2-based field effect transistor with large Schottky barriers at the metal contact interfaces. Because of large barriers, in dark conditions the transistor is in the off-state, but anti-ambipolar transport occurs under light illumination. Three logic states can be identified in the transfer curve under illumination by sweeping the gate bias.

In this section a back-gate WSe_2-based field effect transistor with Ni/Au metal contacts is presented.

6.6 Materials and methods

WSe_2 flakes, whose atomic structure along three axes are displayed in Figure 6.6a, were mechanically exfoliated by using scotch tape and successively transferred on a Si/SiO_2 (85 nm) substrate. Ni/Au (20 nm : 200 nm) metal contacts were deposited by metal evaporation and patterned through standard photolithography and lift-off processes, giving the device shown in the optical image in Figure 6.6b.

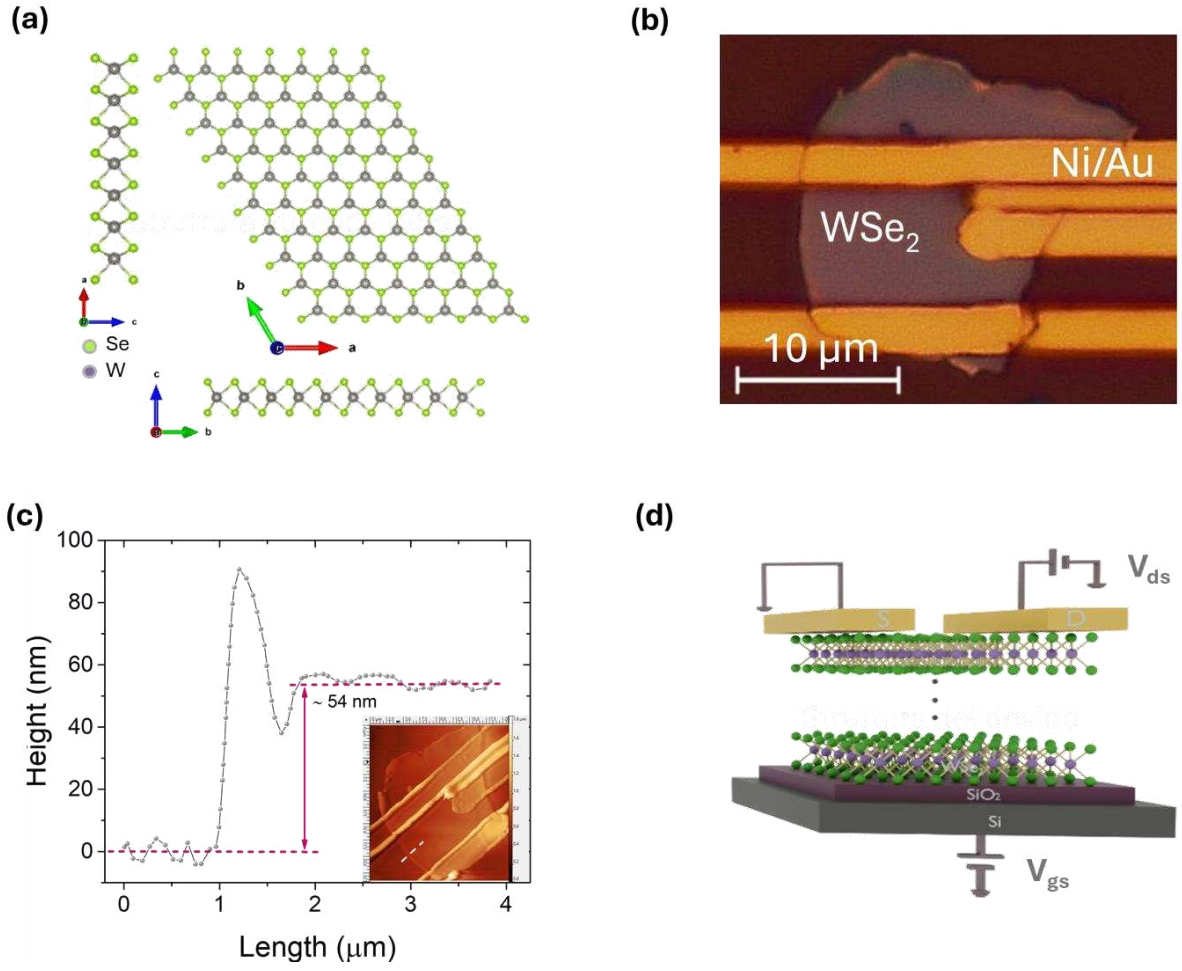

Figure 6.6: (a) Atomic structure of WSe2 along three axes. (b) Optical image of the WSe2-based field effect transistor with Ni/Au metal contacts. (c) AFM profile extracted from the white line represented in the AFM image in the inset. (d) Schematic of the device showing the measurement set up.

The asymmetry in the contacts, arising from the different geometry, is considered potentially beneficial, as similar configurations have shown useful effects in WSe_2 devices[48]. The height profiles, acquired through AFM in contact mode, reveal that the multi-layer flake is around 50 nm thick. A representative profile is shown in Figure 6.6c. As mentioned above, thicker flakes enable higher carrier concentration than in thin flakes. The schematic of the device together with the measurement set up is displayed in Figure 6.6d. Electrical measurements were performed in a two-probe configuration in a Janis probe station. The measurements were acquired through a Keithley 4200 SCS Parameter Analyzer at room temperature and pressure. The photoresponse of the device was investigated by using a white led ring with a maximum power of 1.4 W and a Thorlabs (639 nm) red laser with a nominal power of 4.37 mW.

6.7 Results and discussion

6.7.1 Electrical characterization in dark conditions

Electrical measurements were fist carried out in the dark. Figure 6.7a shows the output curves (I_{ds} vs V_{ds} as a function of V_{gs}) on a semi-log scale obtained by sweeping V_{ds} between -1 and 1 V and stepping V_{gs} from -20 to 20 V. At $V_{gs} = 0$ V, the deviation from linearity in the I_d -V_{ds} curve indicates the presence of Schottky barriers at the metal/WSe_2 interfaces[49]. The drain current is in the range of tens of pA, confirming that the contacts are highly resistive and that significant carrier injection requires applying a gate bias. This bias was limited to ±20 V to avoid stressing the gate oxide and because the current had already reached saturation within this range. Beyond the non-linear behaviour, the output curves are also asymmetric, revealing that the two metal/semiconductor interfaces contribute differently to charge injection. In particular positive drain biases favor charge injection more effectively, consistent with asymmetric Schottky barriers at the source and drain[50,51]. This asymmetry is more pronounced at positive gate voltages.

The drain current increases while stepping the gate bias both positively and negatively, revealing that the device shows a slight ambipolar behaviour. The ambipolar conduction is confirmed by the transfer curves (I_d vs V_{gs} at fixed V_{ds}) in Figure 6.7b and 6.7c, acquired at positive and negative V_{ds} respectively, by sweeping V_{gs} from 20 to -20 V. Ambipolarity is related to band shift under application of an external field, which is equivalent to displace the Fermi level between the valence and the conduction band, which is possible because of the weak Fermi level pinning at the metal/WSe_2 interface. The effective polarity depends on the thickness of WSe_2 and the work function of the metal contacts[52,53]. Ni contacts enable a transition from p-type transport for thin devices to ambipolar and then n-type behaviour as WSe_2 thickness increases[54]. The observed dominant n-type behaviour indicates that Ni Fermi level is closer to the conduction band of the 50 nm thick WSe_2, and injects electrons more easily than hole[55]. The p-type behaviour, also induced by electronegative adsorbates on the surface of the material[56,57], becomes more pronounced at higher V_{ds} since the barrier at the valence band becomes thinner.

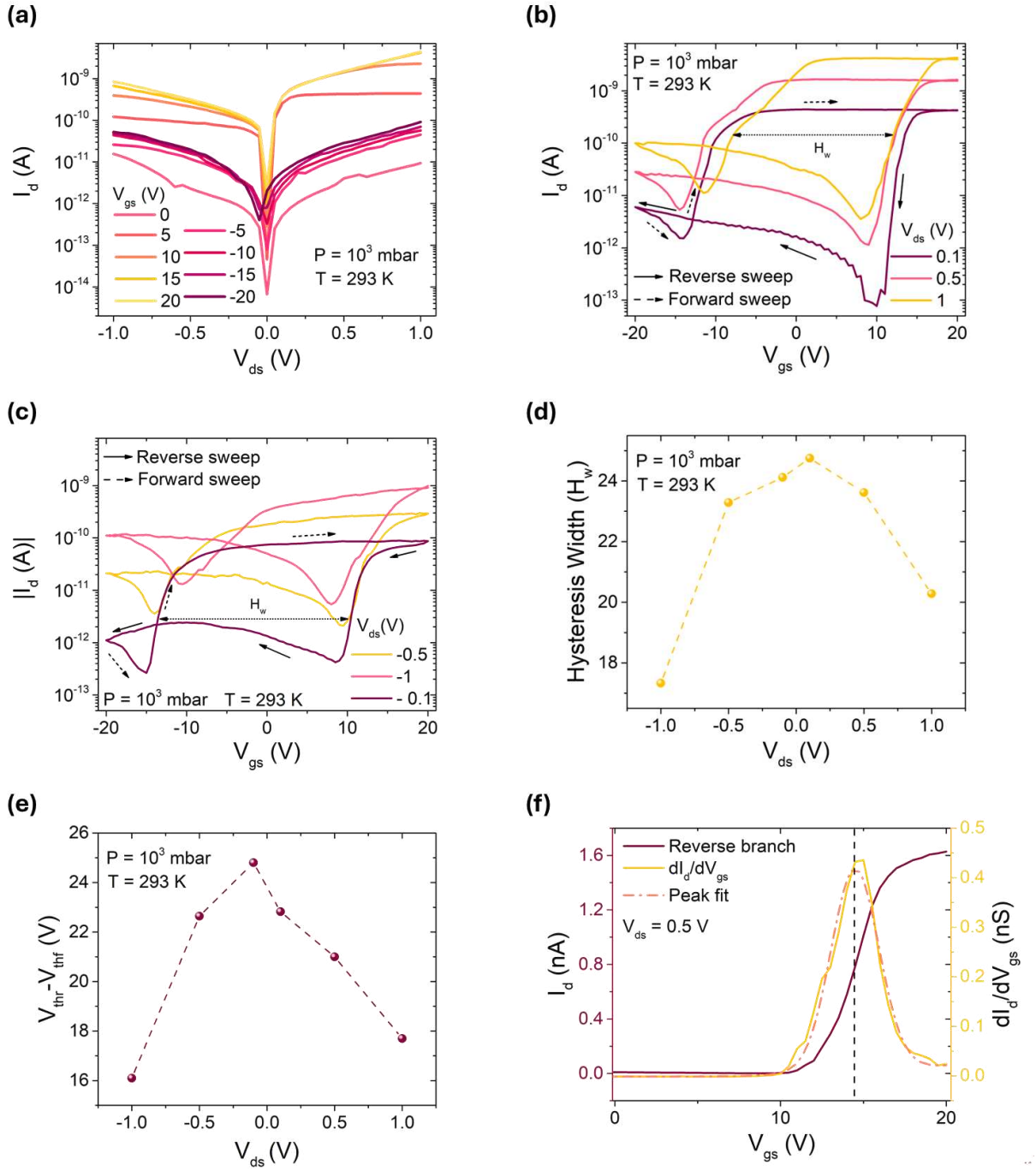

Figure 6.7: (a) Output curves obtained by sweeping V_{ds} between -1 and 1 V at different gate voltages. (b) Transfer curves obtained by double sweeping V_{gs} between 20 and -20 V at several positive V_{ds} and (c) negative V_{ds}. (d) Extraction of the hysteresis width from the transfer curves reported in (b) and (c). (e) Extraction of the shift in the threshold voltage between the forward and the reverse branches of the transfer curves. (f) Identification of the maximum transconductance along the reverse branch of the transfer curve at $V_{ds} = 0.5$ V.

The on-current I_{on} grows with V_{ds} both at the n and p-type side, but this does not determine an increase in the I_{on}/I_{off} ratio of the device. For the n-side it is about three orders of magnitude (10^3) at positive V_{ds} and two orders of magnitude at negative V_{ds}.

By double sweeping the gate bias, a wide hysteresis occurs, especially at the n-side. Because of the slight ambipolarity the device shows, it determines a butterfly shape in the transfer curve. The transition biases between n and p conduction, corresponding to the minimum I_d values in the transfer curves, exhibit a left shift along the reverse branch and a right shift along the forward branch, as V_{ds} increases in absolute value.

Hysteresis is predominantly due to the defective interface with the SiO_2 layer, but also to trapping mechanisms inside the material and surface-adsorbate-induced traps[58]. Measurements performed in high vacuum, indeed, reveal a narrower hysteresis[59]. The hysteresis width, extracted as the maximum voltage distance between the reverse and forward branches, and reported in Figure 6.7d, increases from ~17 to 24 as V_{ds} goes from -1 to -0.1 V and lowers from ~25 to 20 V as V_{ds} increases from 0.1 to 1 V. The separation between the threshold voltage on the reverse branch V_{thr} and on the forward branch $V_{thf,}$, consistently decreases as $|V_{ds}|$ increases, ranging from 22 to 16 V at positive V_{ds} and from 24 to 16 V at negative ones- see Figure 6.7e.

The maximum mobility has been calculated according to the formula 2.12 with $C_{ox} = 4.06 \cdot 10^{-8}$ F/cm^2 as the oxide capacitance per unit area. The electron mobility is higher than the hole one and reaches its maximum at positive V_{ds} in correspondence with the inflection point of the reverse branch, as pointed out by Figure 6.7f for the $V_{ds} = 0.5$ V case. However, the mobility is quite low, the maximum being around $(9 \pm 2) \cdot 10^{-3}$ cm^2/Vs. It is likely limited by scattering events with the defects of the material[60], surface states and mainly at the interface with the oxide[61]. The slight variations in FET electrical parameters for positive and negative V_{ds}, including on-current, on/off ratio, mobility, and hysteresis width, support the presence of asymmetric Schottky barriers, likely due to unequal metal contact areas that cause different contact resistances at the metal interfaces[51].

6.7.2 Electrical characterization under LED light

The photoresponse of the device was first recorded under the illumination of a white LED ring (400-700 nm), providing broadband illumination across the visible light range, where WSe_2 exhibits high optical absorption[62]. This allows a comprehensive evaluation of the device's behaviour under visible-light excitation, without biasing the measurement toward a specific wavelength. The I-V curve at $V_{gs} = 0$ V in Figure 6.8a shows a significant enhancement of the drain current when the light is on at both positive and negative V_{ds}. To investigate the impact of the gate bias on the drain current, transfer curves under light were recorded by double sweeping V_{gs} from 20 to -20 V. To emphasize the differences between the transfer characteristics in dark and illuminated conditions, a direct comparison is presented. For the sake of clarity, the analysis is restricted to $V_{ds} = 0.5$ V and -0.5 V - see Figure 6.8b and 6.8c, respectively, but analogous behaviour is observed at different V_{ds}.

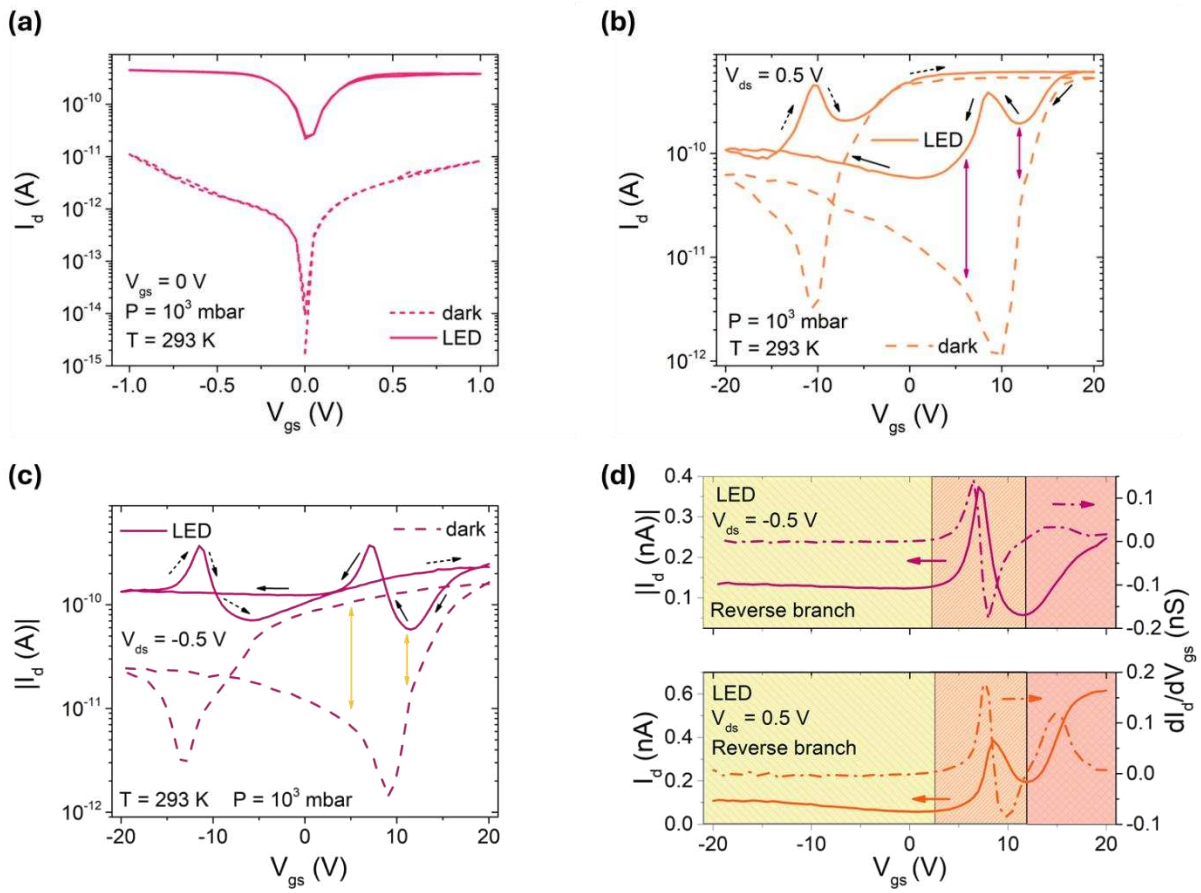

Figure 6.8: Comparison between (a) I_d–V_{ds} curves, (b) transfer curves at $V_{ds} = 0.5\,V$, and (c) transfer curves at $V_{ds} = -0.5\,V$, measured in the dark and under LED illumination. Colored arrows highlight the alignment between the inflection points of the dark transfer curves and the onset of the peak photoresponse. (d) The three coloured regions identify distinct operating regimes along the reverse sweep (solid lines) of the transfer curves at V_{ds} = -0.5 V (top) and $V_{ds} = 0.5\,V$ (bottom). Dashed lines represent the transconductance as a function of gate voltage in each case.

Under illumination, the device exhibits positive photoconductivity across all gate voltages, resulting in an overall upward shift of the transfer curve compared to the dark condition. However, ambipolar transport develops into a more complex scenario, as the gate voltage modulates the channel current to produce distinct peaks at specific gate biases, indicating the onset of anti-ambipolar behavior at both positive and negative V_{ds}.

The transfer curves under illumination also exhibit hysteresis. Two separate current peaks appear during the gate voltage double sweep at fixed V_{ds}: one along the reverse sweep at positive gate voltage, and the other along the forward sweep at negative gate voltage.

In Figure 6.8d, the reverse branches (solid lines) of the transfer curves at V_{ds} = -0.5 V and 0.5 V are separately shown and three distinct operating regions can be identified as a function of the gate bias. The same was observed in the forward sweep. Moving from left to right, the current initially remains nearly constant for $V_{gs} < 2$ V (yellow region), with a gentle decreasing slope as V_{gs} increases, resembling the p-type branch of the transfer curve in the dark. The peaked regions, instead, extend between ~2 and 12.5 V (orange region). At positive V_{ds}, the current of the peak follows the shape of the transfer curve: the current level on the right side

of the peak is higher than on the left, and the peak maximum does not correspond to the highest current value in the transfer curve. Conversely, the peak observed at negative V_{ds} shows the opposite trend, with the current on its right side lower than on the left, and it is more pronounced than in the positive counterpart. For $V_{gs} > 12$ V (pink region), the current enters a monotonically increasing region, resembling the n-branches of the dark transfer curves, and approaches saturation at positive V_{ds}.

Anti-ambipolar transport naturally gives rise to negative differential resistance (NDR), a nonlinear carrier transport phenomenon in which increasing the bias voltage leads to a reduction in current. Various architectures have been exploited to obtain it in TMD-based structures. For instance, Wang et al.[63] identified semiconducting TMDs hosting S-type NDR in a vertical electrode/TMD/electrode structure, and they attributed it to the thermal feedback conduction mechanism induced by Joule self-heating effect. Huo et al.[64], instead, proposed a VdW heterostructure made of semi-metallic Td-WTe_2 and $MoS_2/MoTe_2$, exploiting the formation of a type-III band alignment. In both cases, NDR appears as a peak in the I-V characteristics.

In this case, instead, anti-ambipolar transport manifests as negative transconductance (NTC) with respect to the gate voltage, see the dashed lines in Figure 6.8d. Such a feature is valuable for various emerging analog and digital applications. In the analog domain, it has been shown that single material-based transistors exhibiting the coexistence of positive and negative transconductance regions can generate in-phase, out-of-phase, and frequency-doubled signals when an AC input on the gate terminal is combined with a proper DC bias[37]. Additionally, in some anti-ambipolar architectures, the interplay between gate biasing and optical modulation has been employed to produce phase-, amplitude-, and frequency-selective output waveforms, suitable for analog modulation/encoding schemes in data communications. Multi-bit analog transmission has also been demonstrated in transistor designs that allow switching between ambipolar and anti-ambipolar transport by electrostatically control drain/source barriers and channel polarity [46]. Furthermore, NTC has been exploited to realize ternary inverters and ternary static random access memory[32,65,66].

Figures 6.9a and 6.9b show the reverse and forward branches of the transfer curve at V_{ds} = -0.5, respectively, under progressively stronger illumination, from 0.18 to 1.1 W. The peaks already appear at low power and get sharper with increasing intensity. At low light intensity, a dip in the current close to the maximum peak is observed along both branches; however, as the intensity increases, only one peak remains visible. Something similar was observed in $MoTe_2$-MoS_2 heterojunctions, where the dip in the transconductance was related to photodoping[75]. The peak on the reverse branch is indicated as *p1* and the one on the forward branch as *p2*.

The height of the peaks evaluated with respect to the baseline is almost the same on the two branches at fixed LED intensity. It ranges from $(3.2 \pm 0.2) \cdot 10^{-2}$ to $(2.46 \pm 0.08) \cdot 10^{-1}$ nA for p1, and from $(4.4 \pm 0.3) \cdot 10^{-2}$ to $(2.42 \pm 0.06) \cdot 10^{-1}$ nA for p2, as the LED intensity increases. This value is different from the maximum current, which is slightly higher and reaches 0.31 nA, as evident from Figures 6.9a and 6.9b. When plotting the peak height as a function of the LED power, a linear relationship is observed for both p1 and p2, as indicated by the full symbols in Figure 6.9c. The bias voltages at which p1 and p2 appear are indicated as V_{p1} and

V_{p2}. As the illumination increases, the position of p1 shifts slightly to the left, because of photo-trapping processes, while V_{p2} remains nearly unchanged.

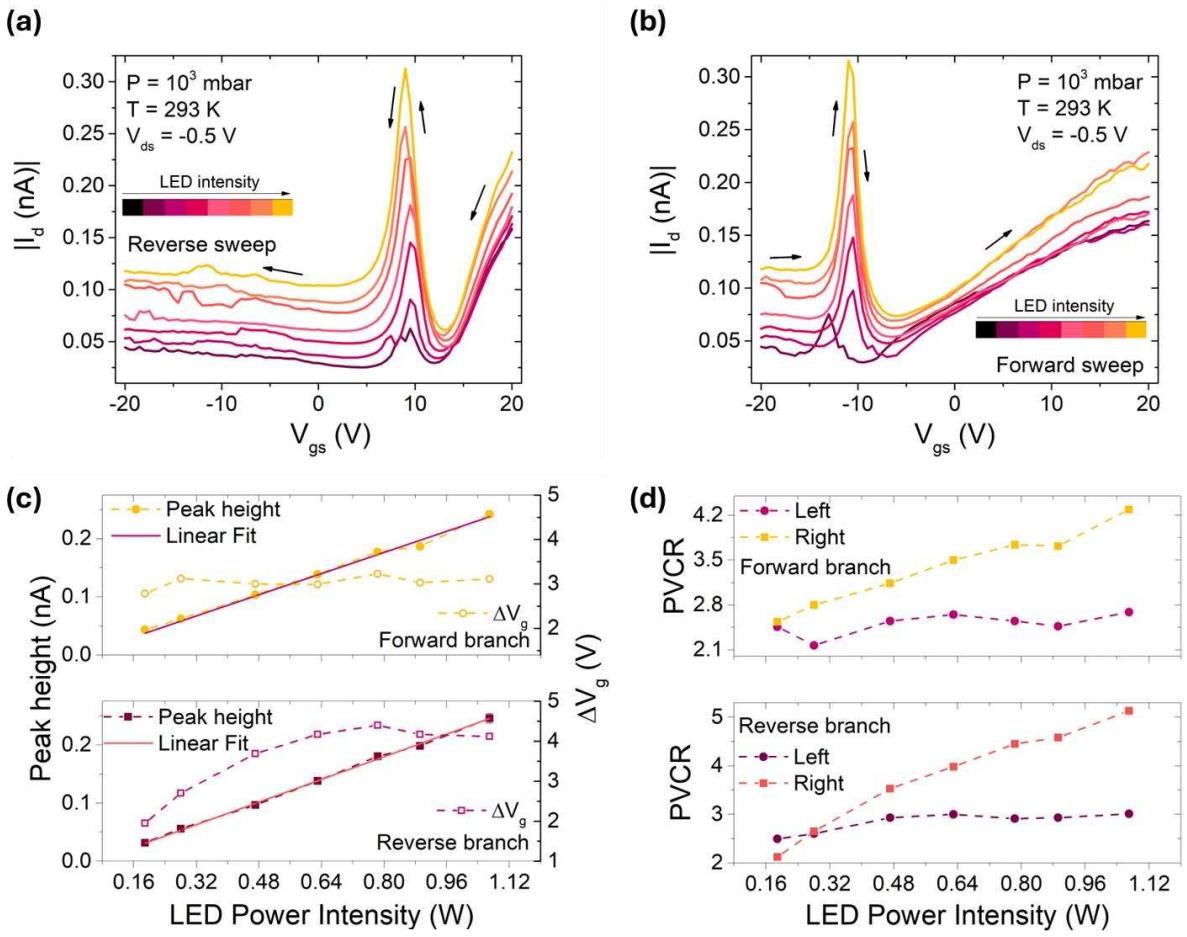

Figure 6.9: (a) Transfer curve under LED light obtained by reverse sweeping and (b) forward sweeping the gate bias at V_{ds} = - 0.5 V. (c) Amplitude of the peaks (left scale) and driving voltage range (right scale) extracted from the forward branch (top) and reverse branch (bottom) as a function of the LED power intensity. (d) Peak-to-valley current ratio calculated on the forward branch (top) and the reverse branch (bottom), considering the left side (square) and the right side (circle) of the peak

The driving voltage range (ΔV_g), defined as the voltage difference between the on-set and off-set of the peak, is narrower in this device compared to other reported devices and heterostructures[31,76], where ΔV_g typically spans several tens of volts. Herein ΔV_g corresponds to the bias region where both p- and n-type conduction branches are partially active; outside this region, one mode dominates.

Table 6.1. Comparison between figures of merit of anti-ambipolar devices.

Work	Device structure	Material	Operating condition	Vp	PVCR	ΔV_g
Yao et al[67]	p-n junction	MoTe2/MoS2	Dark	-20	<10	
Sun et al[68]	p-n junction	InSe/MoTe2	Dark	-20	10^3	60
Lv et al[69]	P-n junction	SnS/WSe2		5	10^2	30
	p-n junction	BP/ReS2	Dark	0.4	4.2-6.9	
Nourbakhsh et al [1]	p-n junction	WSe2/MoS2	Dark	20	10^3	20
Ii et al[70]	p-n junction	SnS2/WSe2	Dark	-10	200	20
Han et al[71]	**In plane homojunction**	**WSe2**	**Light**	**-2.5**	**29.3**	
Wang et al[72]	**Single-material FET**	**WSe2**	**Light (no signal in the dark)**	**-6**	**40**	**20**
Thakar et al[73]	**Multi-gate structure**	**WSe2**	**dark**	**0**	**10^2**	**4**
Liu et al[74]	Single material FET	MoS2	Dark, low temperature	-20	47	40
This work	**Single material FET**	**Wse2**	**Light (red laser)**	**-12**	**<10**	**5-7**

Inflection points in the dark curves align with the onset of the photoresponse peaks, as indicated by the coloured arrows in Figure 6.8b and 6.8c, reflecting the overlap of the initial, resistive portions of both branches. This reduced ΔV_g is favourable since it enables faster and more energy-efficient switching in logic circuits[66,77]. As reported in Figure 6.9c, ΔV_g is almost constant around 3 V in the forward sweep, while it can be tuned from approximately 2 to 4 V in the reverse sweep – see empty symbols in Figure 6.9c. The full width at half maximum (FWHM) of the forward peaks, indeed, are lower than the peaks on the reverse branch.

The peak-to-valley current ratio (PVCR) is not the same as the peak is approached from the left or from the right, because of the transfer curve shape, as highlighted in Figure 6.9d for both the reverse and the forward branches. At the maximum LED intensity, it reaches approximately ~4 on the forward branch and ~5 on the reverse, which is lower than in heterostructures, but comparable with other WSe_2-based devices[47]. However, it needs to be improved for efficient application.

Table 6.1 compares the main figures of merit of the device under study with those reported in the literature.

6.7.3 Electrical characterization under red laser

To gain deeper insight into the phenomenon, the device's photoresponse was also investigated under illumination with a monochromatic red laser ($\lambda \approx 639$ nm), corresponding to a photon

energy of approximately 1.94 eV. This energy lies above the WSe_2 bandgap (~1.2-1.7 eV)[78], enabling efficient photocarrier generation while avoiding high-energy induced effects. Red excitation is also standard in WSe_2 photodetector studies. The drain current significantly increases – see Figure 6.10a - by three orders of magnitude from the dark one. Figure 6.10b compares the transfer characteristics in dark and under light, at V_{ds} = - 0.5 V.

The overall behaviour is the same as under white light, but with a higher photocurrent. However, unlike the case under LED illumination, the forward and reverse branches of the curve can be sharply divided into three distinct current regions, as highlighted in Figure 6.10c at V_{ds} = -0.5 V. The same applies at positive V_{ds}. In both cases, in the yellow and pink regions, the gate bias barely modulates the drain current, which stays at two flat levels.

This behaviour is due to the laser's higher local power density and spatial confinement, which generate a large concentration of carriers in a small region, locally lowering the Schottky barriers and enhancing injection. As a result, the current becomes less sensitive to gate modulation, leading to flatter response levels. Nevertheless, a prominent peak appears in the central region despite the overall saturated regime, and the peak current is the highest obtained by sweeping the gate bias both at V_{ds} = -0.5 and 0.5 V. V_p and the driving voltage range ΔV_{gs} are consistent with that obtained under LED illumination.

In both branches in Figure 6.10c, the current in region I is approximately 1.33 nA, reaches a peak of 2.8 nA, and then drops to about 0.4 nA in region III. These three current levels are stable and well-defined, suggesting that the device can operate as a multi-level element under controlled illumination conditions. Multi-state devices are particularly attractive for circuit miniaturization because they can encode more information per device than binary CMOS. Whereas CMOS logic requires at least two transistors to encode a single bit, a ternary logic unit provides three distinct output states, increasing information density from 2^n to 3^n levels with the same number of units.

Considering that the peaks in the transfer curve under illumination almost coincide with the valley in the ambipolar transfer curves in dark, the dark-light switching behaviour of the device was investigated at $V_{gs} = V_{p2}$, as this gate voltage provides the largest separation between the current values measured in dark and under illumination. The current increases quickly, reaching a steady on-state current and then decreases rapidly when the light is switched off, indicating a rapid photodetection mechanism at this bias point. From the pulses in Figure 6.10d, the photocurrent is extracted as $I_{ph} = (3.73 \pm 0.07)$ nA. The corresponding responsivity (formula 2.15) is $R \approx 0.13 \frac{A}{W}$, while the specific detectivity was estimated to be $D^* = 1.3 \times 10^{12}$ Jones according to formula 2.26.

During operation with 10-second light pulses, the instantaneous power consumption in the ON state is ~1.85 nW, while in the dark state it drops to ~1 pW. The average power dissipation over a full light–dark cycle is below 1 nW:

$$P_{avg} = \frac{V_{ds} I_{light} t_{on} + V_{ds} I_{dark} t_{off}}{t_{on} + t_{off}} \sim 0.93 \text{ nW} \quad (6.1)$$

Additionally, the narrow driving voltage range minimizes dynamic power consumption. All these parameters highlight the anti-ambipolar transistor's promise for low-power optoelectronics.

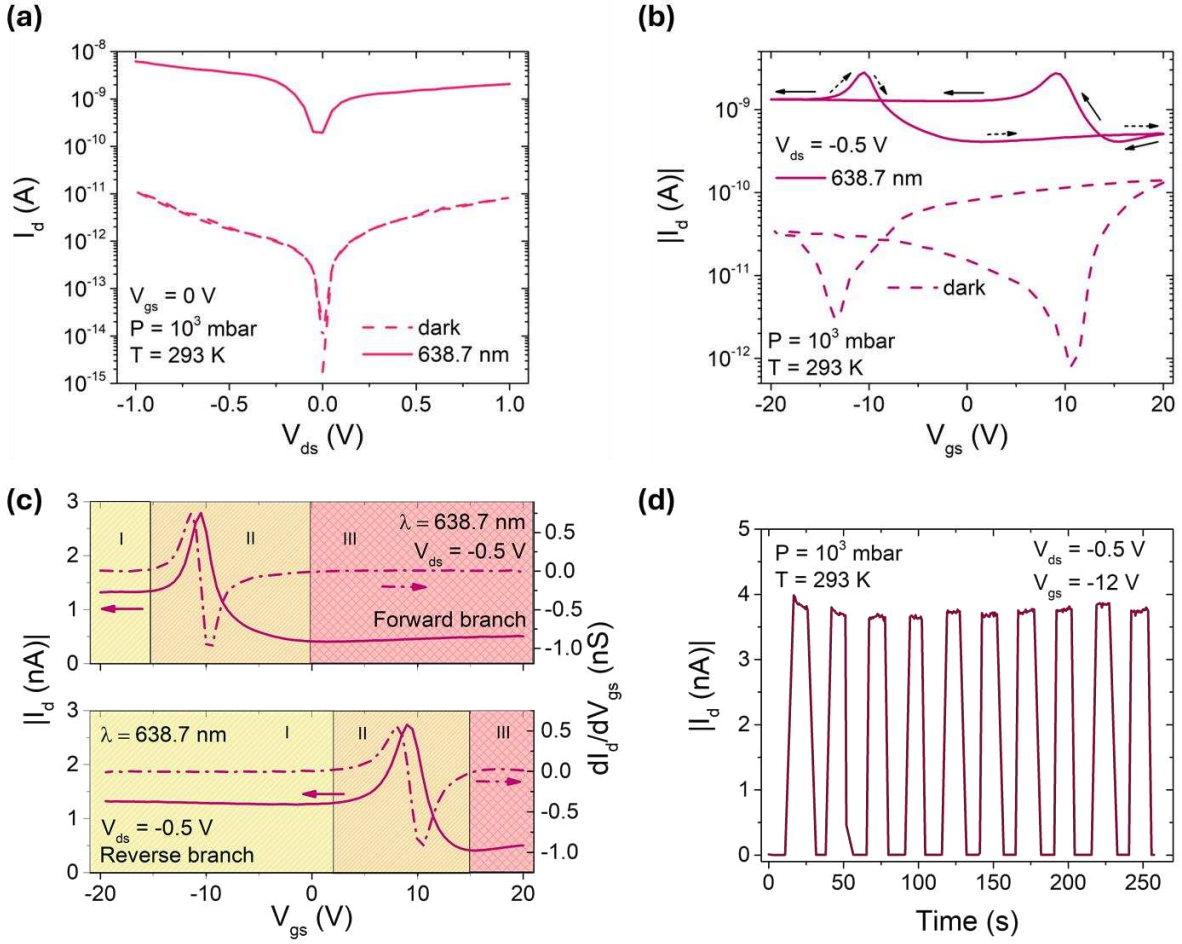

Figure 6.10: Comparison between (a) the I-V curves and (b) the transfer curves at Vds = -0.5 V in the dark and under red laser illumination. (c) Identification of three separate current levels (solid lines) in the forward (top) and reverse (bottom) branches of the transfer curves. Dashed lines represent the transconductance. (d) Switching behaviour of the device in response to repeated laser pulses, in correspondence of the peak on the forward branch.

6.7.4 Mechanism

Based on the direct comparison between the transfer curves in the dark and under illumination presented in the previous section, it emerges that the on-set gate bias of ambipolarity in the dark is linked with the current peak under light. Specifically, the vertex of the V-shaped ambipolar transfer curve in the dark is related to the peak of the Λ-shaped anti-ambipolar transfer characteristic under illumination.

The correspondence between the two points is not precise because the acquisition time for the transfer curves in the dark and under illumination differ. Even with identical measurement settings, the time required to record each data point depends on the current level: lower currents, as typically observed in the dark, result in longer measurement times.

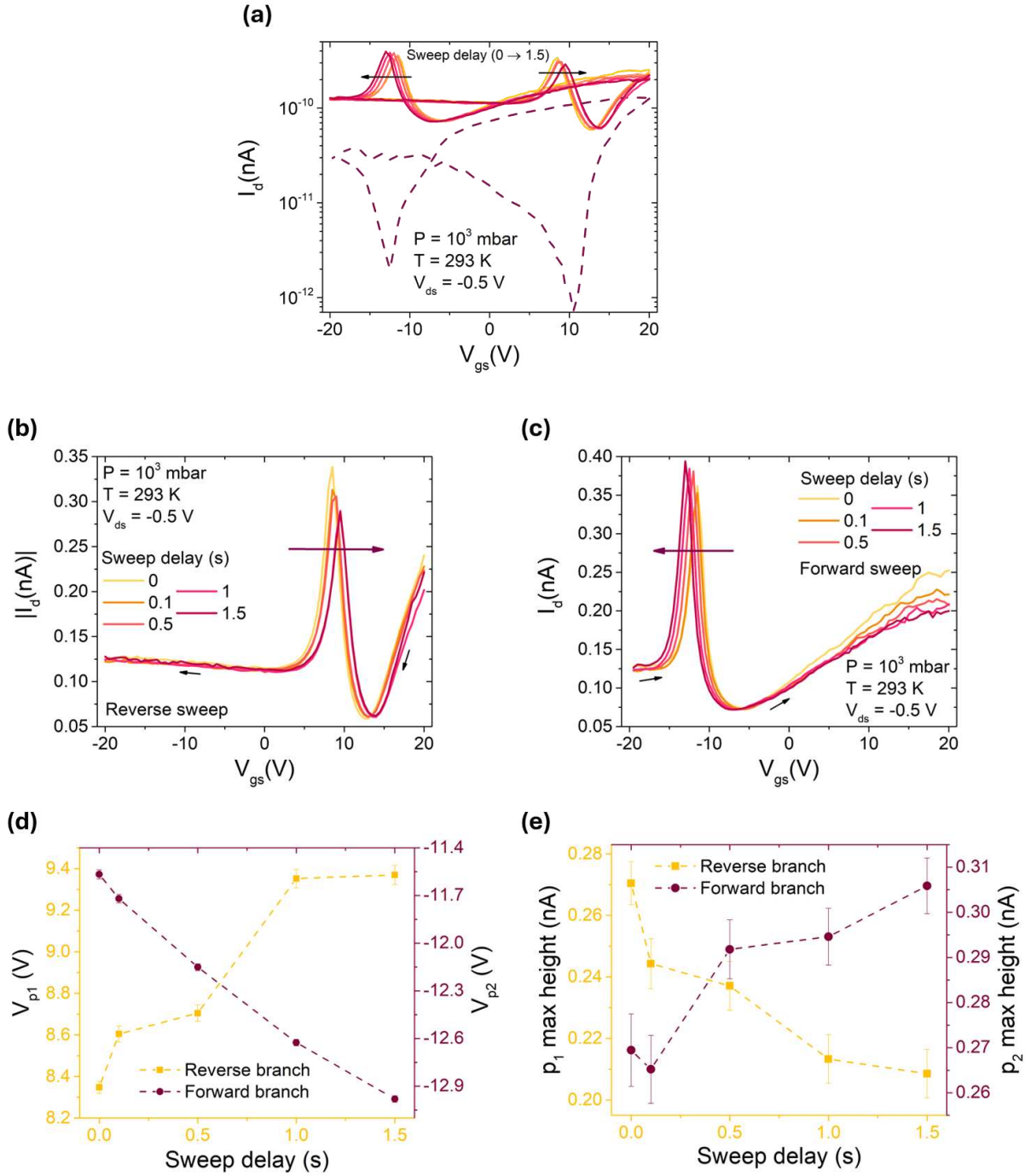

Figure 6.11: (a) Comparison between the dark transfer curve at Vds=-0.5 V and the transfer curves under LED illumination obtained with different sweep delays in the measurement acquisition. Focus on (b) the reverse sweep and (c) the forward sweep of the transfer curve under LED illumination at different sweep delays. (d) Maximum points and (e) amplitudes of the peaks as a function of the sweep delay on the reverse branch (left) and the forward branch (right).

Therefore, the measurement acquisition under light was slowed down by adding a sweep delay (see Figure 6.11) at each data point acquisition time. Under these conditions, p1 on the reverse sweep shifts to higher gate voltages, while p2 on the forward sweep shifts to lower gate

voltages. This indicates that during both reverse and forward V_{gs} sweeps, reducing the sweep speed causes the peaks to appear earlier along the gate voltage axis and they better align with the minimum points of the transfer curves in the dark. This result supports the hypothesis that anti-ambipolar peaks correspond to the ambipolar transition points.

In the dark, the drain current can be described as the sum of electron and hole contributions, each enabled by thermionic emission and tunneling through a gate dependent Schottky barrier. The dominant n-type behaviour observed in Figure 6.7 indicates that the energy barrier for electrons injection is lower than the hole barrier. As illustrated in Figure 6.12a, for $V_{gs} > V_p$, the electron barrier at the source becomes thinner, enhancing n-type conduction, while for $V_{gs} < V_p$, upward band bending at the drain side reduces the hole barrier, enabling the p-type transport (Figure 6.12b)[55]. At $V_{gs} = V_p$, both barriers are sufficiently large to suppress the injection of either carrier type, resulting in the minimum in the transfer curve (Figure 6.12c). As already mentioned, this minimum defines the transition point between n-type and p-type conduction.

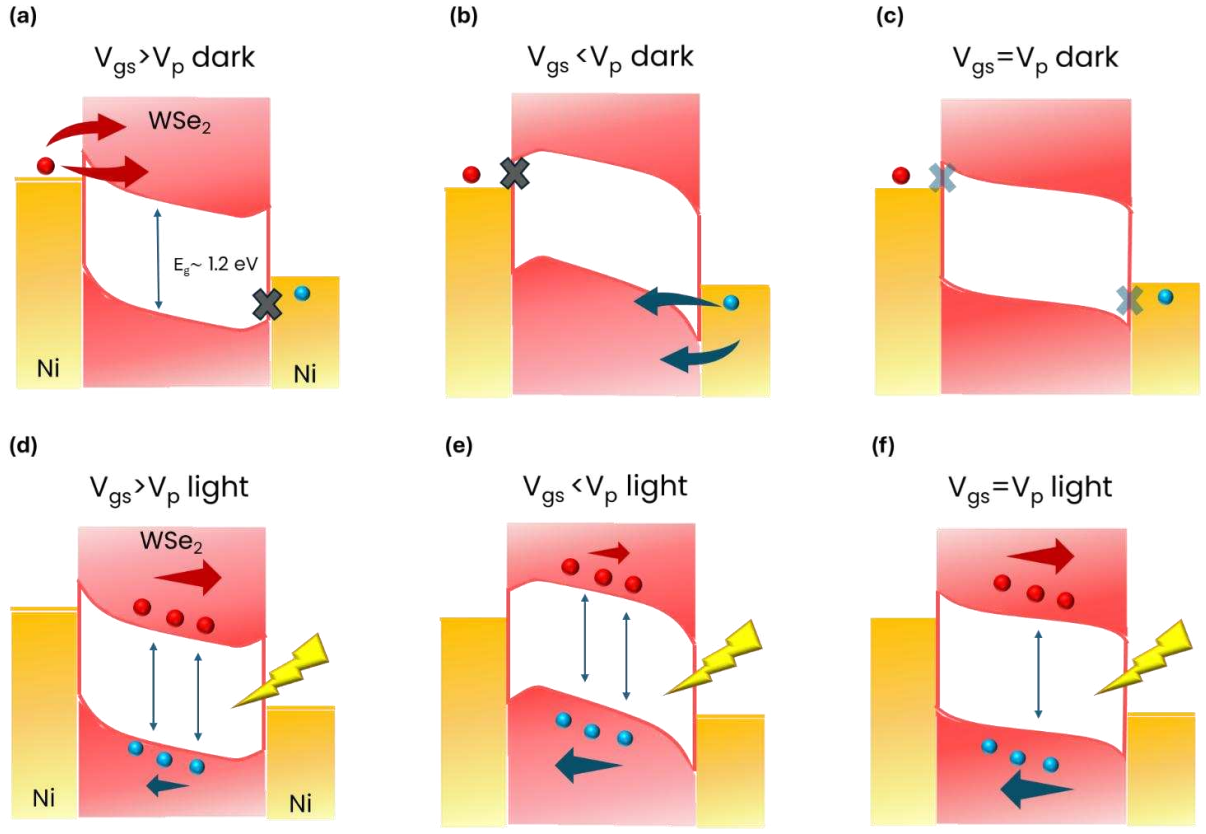

Figure 6.12: Band diagrams showing the band bending at the source-drain interfaces and along the channel together with the current transport in the dark at (a) $V_{gs} > V_p$, (b) $V_{gs} < V_p$; (c) $V_{gs} = V_p$. (d),(e),(f): The same under illumination.

A small deviation from this gate voltage enables either n-type or p-type transport, depending on the direction of the sweep. This behavior is typical of Schottky-contact transistors, where carrier injection is strongly modulated by gate-controlled band bending.

Under illumination, photogenerated electron-hole pairs modify the device operation- see Figure 6.12d, 6.12e, and 6.12f. At gate voltages far from V_p, the device remains largely unipolar: either photo-electrons ($V_g > V_p$) or photo-holes ($V_g < V_p$) dominate the photocurrent, as the opposite carriers face higher injection barriers and recombination processes. On the contrary, around $V_{gs} = V_p$, the band structure lets both photogenerated carriers to be transferred and collected efficiently as illustrated in Figure 6.12f: photoelectrons can flow to the drain and holes to the source, and their simultaneous collection produces a pronounced local maximum, giving rise to the characteristic Λ shaped anti-ambipolar response. When the gate bias is at the n-p crossover, both Schottky barriers are moderately high, too high for thermal injections, but not so high to impede photogenerated carriers' transport.

Thus, the observed light-induced anti-ambipolar peak results from the combined effects of dual Schottky barrier modulation at source and drain sides and efficient photogeneration and separation of both carrier types across the channel at V_p because of a proper band alignment. This scenario is supported by previous reports of anti-ambipolarity in both heterojunctions and multilayer homostructures and confirms the capacity of bulk WSe_2 to host multi-state transport under optical stimulation.

Overall, this chapter highlights that trap-mediated processes and high contact barriers in ambipolar TMD transistors can enable novel optoelectronic phenomena. This demonstrates that TMD-based transistors are not only useful as high-performance photodetectors but also as versatile platforms for tunable, reconfigurable, and multifunctional optoelectronic responses.

References

(1) Roy, K.; Jaiswal, A.; Panda, P. Towards Spike-Based Machine Intelligence with Neuromorphic Computing. *Nature* **2019**, *575* (7784), 607–617. https://doi.org/10.1038/s41586-019-1677-2.

(2) Han, J.; Deng, W.; Hu, F.; Han, S.; Wang, Z.; Fu, Z.; Zhou, H.; Yu, H.; Gou, J.; Wang, J. 2D Materials-Based Photodetectors with Bi-Directional Responses in Enabling Intelligent Optical Sensing. *Adv. Funct. Mater.* **2025**, *35* (24), 2423360. https://doi.org/10.1002/adfm.202423360.

(3) Grillo, A.; Faella, E.; Pelella, A.; Giubileo, F.; Ansari, L.; Gity, F.; Hurley, P. K.; McEvoy, N.; Di Bartolomeo, A. Coexistence of Negative and Positive Photoconductivity in Few-Layer PtSe2 Field-Effect Transistors. *Adv. Funct. Mater.* **2021**, *31* (43), 2105722.

(4) Wang, Y.; Liu, E.; Gao, A.; Cao, T.; Long, M.; Pan, C.; Zhang, L.; Zeng, J.; Wang, C.; Hu, W.; Liang, S.-J.; Miao, F. Negative Photoconductance in van Der Waals Heterostructure-Based Floating Gate Phototransistor. *ACS Nano* **2018**, *12* (9), 9513–9520. https://doi.org/10.1021/acsnano.8b04885.

(5) Ghosh, S.; Varghese, A.; Jawa, H.; Yin, Y.; Medhekar, N. V.; Lodha, S. Polarity-Tunable Photocurrent through Band Alignment Engineering in a High-Speed WSe2/SnSe2 Diode with Large Negative Responsivity. *ACS Nano* **2022**, *16* (3), 4578–4587. https://doi.org/10.1021/acsnano.1c11110.

(6) Glavin, N. R.; Rao, R.; Varshney, V.; Bianco, E.; Apte, A.; Roy, A.; Ringe, E.; Ajayan, P. M. Emerging Applications of Elemental 2D Materials. *Adv. Mater.* **2020**, *32* (7), 1904302. https://doi.org/10.1002/adma.201904302.

(7) Pi, L.; Wang, P.; Liang, S.-J.; Luo, P.; Wang, H.; Li, D.; Li, Z.; Chen, P.; Zhou, X.; Miao, F.; Zhai, T. Broadband Convolutional Processing Using Band-Alignment-Tunable Heterostructures. *Nat. Electron.* **2022**, *5* (4), 248–254. https://doi.org/10.1038/s41928-022-00747-5.

(8) Intonti, K.; Faella, E.; Viscardi, L.; Kumar, A.; Durante, O.; Giubileo, F.; Passacantando, M.; Lam, H. T.; Anastasiou, K.; Craciun, M. F.; Russo, S.; Di Bartolomeo, A. Hysteresis and Photoconductivity of Few-Layer ReSe2 Field Effect Transistors Enhanced by Air Pressure. *Adv. Electron. Mater. n/a* (n/a), 2300066. https://doi.org/10.1002/aelm.202300066.

(9) Kumar, A.; Intonti, K.; Viscardi, L.; Durante, O.; Pelella, A.; Kharsah, O.; Sleziona, S.; Giubileo, F.; Martucciello, N.; Ciambelli, P.; Schleberger, M.; Bartolomeo, A. D. Memory Effect and Coexistence of Negative and Positive Photoconductivity in Black Phosphorus Field Effect Transistor for Neuromorphic Vision Sensors. *Mater. Horiz.* **2024**, *11* (10), 2397–2405. https://doi.org/10.1039/D4MH00027G.

(10) Guo, J.; Liu, K. Recent Progress in Two-Dimensional MoTe2 Hetero-Phase Homojunctions. *Nanomaterials* **2022**, *12* (1), 110. https://doi.org/10.3390/nano12010110.

(11) Ruppert, C.; Aslan, B.; Heinz, T. F. Optical Properties and Band Gap of Single- and Few-Layer MoTe2 Crystals. *Nano Lett.* **2014**, *14* (11), 6231–6236. https://doi.org/10.1021/nl502557g.

(12) Chen, W.; Liang, R.; Zhang, S.; Liu, Y.; Cheng, W.; Sun, C.; Xu, J. Ultrahigh Sensitive Near-Infrared Photodetectors Based on MoTe2/Germanium Heterostructure. *Nano Res.* **2020**, *13* (1), 127–132. https://doi.org/10.1007/s12274-019-2583-5.

(13) Qiao, J.; Feng, F.; Cao, G.; Wei, S.; Song, S.; Wang, T.; Yuan, X.; Somekh, M. G. Ultrasensitive Near-Infrared MoTe2 Photodetectors with Monolithically Integrated Fresnel Zone Plate Metalens. *Adv. Opt. Mater.* **2022**, *10* (15), 2200375. https://doi.org/10.1002/adom.202200375.

(14) Li, C.; Tian, R.; Yi, R.; Hu, S.; Chen, Y.; Yuan, Q.; Zhang, X.; Liu, Y.; Hao, Y.; Gan, X.; Zhao, J. MoTe2 PN Homojunction Constructed on a Silicon Photonic Crystal Cavity for High-Performance Photodetector. *ACS Photonics* **2021**, *8* (8), 2431–2439. https://doi.org/10.1021/acsphotonics.1c00628.

(15) Zhang, W.; Huang, Z.; Zhang, W.; Li, Y. Two-Dimensional Semiconductors with Possible High Room Temperature Mobility. *Nano Res.* **2014**, *7* (12), 1731–1737. https://doi.org/10.1007/s12274-014-0532-x.

(16) Zhang, S.; Wu, Y.; Gao, F.; Shang, H.; Zhang, J.; Li, Z.; Fu, Y.; Hu, P. Field Effect Transistor Sensors Based on In-Plane 1T′/2H/1T′ MoTe2 Heterophases with Superior Sensitivity and Output Signals. *Adv. Funct. Mater.* **2022**, *32* (41), 2205299. https://doi.org/10.1002/adfm.202205299.

(17) Ma, R.; Zhang, H.; Yoo, Y.; Degregorio, Z. P.; Jin, L.; Golani, P.; Ghasemi Azadani, J.; Low, T.; Johns, J. E.; Bendersky, L. A.; Davydov, A. V.; Koester, S. J. MoTe2 Lateral Homojunction Field-Effect Transistors Fabricated Using Flux-Controlled Phase Engineering. *ACS Nano* **2019**, *13* (7), 8035–8046. https://doi.org/10.1021/acsnano.9b02785.

(18) Yu, T.; Zhao, Z. A Research on MoTe2-Based Memristor and Switching Stability Improvement. *J. Phys. Conf. Ser.* **2023**, *2613* (1), 012005. https://doi.org/10.1088/1742-6596/2613/1/012005.

(19) Liu, X.; Islam, A.; Guo, J.; Feng, P. X.-L. Controlling Polarity of MoTe2 Transistors for Monolithic Complementary Logic via Schottky Contact Engineering. *ACS Nano* **2020**, *14* (2), 1457–1467. https://doi.org/10.1021/acsnano.9b05502.

(20) Gao, J.; Lian, X.; Chen, Z.; Shi, S.; Li, E.; Wang, Y.; Jin, T.; Chen, H.; Liu, L.; Chen, J.; Zhu, Y.; Chen, W. Multifunctional MoTe2 Fe-FET Enabled by Ferroelectric Polarization-Assisted Charge Trapping. *Adv. Funct. Mater.* **2022**, *32* (17), 2110415. https://doi.org/10.1002/adfm.202110415.

(21) Pham, T. T.; Castelino, R.; Felten, A.; Sporken, R. Study of Surface Oxidation and Recovery of Clean MoTe2<math><msub Is="true"><mtext Is="true">MoTe</Mtext><mn Is="true">2</Mn></Msub></Math> Films. *Surf. Interfaces* **2022**, *28*, 101681. https://doi.org/10.1016/j.surfin.2021.101681.

(22) Patil, V.; Neill, H.; Sheehan, B.; Hurley, P. K.; Ansari, L.; Gity, F. Dopingless Ambipolar Field-Effect Transistors Based on MoTe2 2D Material for CMOS Nanoelectronics. *Adv. Electron. Mater.* **2025**, *11* (16), e00305. https://doi.org/10.1002/aelm.202500305.

(23) Mleczko, M. J.; Yu, A. C.; Smyth, C. M.; Chen, V.; Shin, Y. C.; Chatterjee, S.; Tsai, Y.-C.; Nishi, Y.; Wallace, R. M.; Pop, E. Contact Engineering High-Performance n-Type MoTe2 Transistors. *Nano Lett.* **2019**, *19* (9), 6352–6362. https://doi.org/10.1021/acs.nanolett.9b02497.

(24) Seo, S. G.; Jeong, J.; Jin, S. H. Influence of Air Atmosphere on Electrical Characteristics of P-Type MoTe2 FETs under DC and Pulsed Mode Operation. *Microelectron. Reliab.* **2020**, *111*, 113680. https://doi.org/10.1016/j.microrel.2020.113680.

(25) Karimi, M.; Zeng, X.; Witzigmann, B.; Samuelson, L.; Borgström, M. T.; Pettersson, H. High Responsivity of InP/InAsP Nanowire Array Broadband Photodetectors Enhanced by Optical Gating. *Nano Lett.* **2019**, *19* (12), 8424–8430. https://doi.org/10.1021/acs.nanolett.9b02494.

(26) Boyao Cui(崔博垚), Y. X. Negative photoconductivity in low-dimensional materials. *Chin. Phys. B* **2021**, *30* (2), 28507–0. https://doi.org/10.1088/1674-1056/abcf41.

(27) Di Bartolomeo, A.; Genovese, L.; Foller, T.; Giubileo, F.; Luongo, G.; Croin, L.; Liang, S.-J.; Ang, L. K.; Schleberger, M. Electrical Transport and Persistent Photoconductivity in Monolayer MoS $_2$ Phototransistors. *Nanotechnology* **2017**, *28* (21), 214002. https://doi.org/10.1088/1361-6528/aa6d98.

(28) Kim, H. J.; Lee, K. J.; Park, J.; Shin, G. H.; Park, H.; Yu, K.; Choi, S.-Y. Photoconductivity Switching in MoTe2/Graphene Heterostructure by Trap-Assisted Photogating. *ACS Appl. Mater. Interfaces* **2020**, *12* (34), 38563–38569. https://doi.org/10.1021/acsami.0c09960.

(29) Jariwala, D.; Sangwan, V. K.; Wu, C.-C.; Prabhumirashi, P. L.; Geier, M. L.; Marks, T. J.; Lauhon, L. J.; Hersam, M. C. Gate-Tunable Carbon Nanotube–MoS2 Heterojunction p-n Diode. *Proc. Natl. Acad. Sci.* **2013**, *110* (45), 18076–18080. https://doi.org/10.1073/pnas.1317226110.

(30) Li, Y.; Wang, Y.; Huang, L.; Wang, X.; Li, X.; Deng, H.-X.; Wei, Z.; Li, J. Anti-Ambipolar Field-Effect Transistors Based On Few-Layer 2D Transition Metal Dichalcogenides. *ACS Appl. Mater. Interfaces* **2016**, *8* (24), 15574–15581. https://doi.org/10.1021/acsami.6b02513.

(31) Sun, Y.; Gao, W.; Li, X.; Xia, C.; Chen, H.; Zhang, L.; Luo, D.; Fan, W.; Huo, N.; Li, J. Anti-Ambipolar Behavior and Photovoltaic Effect in p-MoTe2/n-InSe Heterojunctions. *J. Mater. Chem. C* **2021**, *9* (32), 10372–10380. https://doi.org/10.1039/D1TC02497C.

(32) Lv, Y.; Wu, C.-Y.; Zhao, Y.; Wu, G.; Abid, M.; Cho, J.; Choi, M.; Ó Coileáin, C.; Hung, K.-M.; Chang, C.-R.; Wu, Y.-R.; Wu, H.-C. Robust Anti-Ambipolar Behavior and Gate-Tunable Rectifying Effect in van Der Waals p–n Junctions. *ACS Appl. Electron. Mater.* **2022**, *4* (11), 5487–5497. https://doi.org/10.1021/acsaelm.2c01120.

(33) Paul, A. K.; Kuiri, M.; Saha, D.; Chakraborty, B.; Mahapatra, S.; Sood, A. K.; Das, A. Photo-Tunable Transfer Characteristics in MoTe2–MoS2 Vertical Heterostructure. *Npj 2D Mater. Appl.* **2017**, *1* (1), 17. https://doi.org/10.1038/s41699-017-0017-3.

(34) Huang, M.; Li, S.; Zhang, Z.; Xiong, X.; Li, X.; Wu, Y. Multifunctional High-Performance van Der Waals Heterostructures. *Nat. Nanotechnol.* **2017**, *12* (12), 1148–1154. https://doi.org/10.1038/nnano.2017.208.

(35) Cheng, Q.; Pang, J.; Sun, D.; Wang, J.; Zhang, S.; Liu, F.; Chen, Y.; Yang, R.; Liang, N.; Lu, X.; Ji, Y.; Wang, J.; Zhang, C.; Sang, Y.; Liu, H.; Zhou, W. WSe2 2D P-Type Semiconductor-Based Electronic Devices for Information Technology: Design, Preparation, and Applications. *InfoMat* **2020**, *2* (4), 656–697. https://doi.org/10.1002/inf2.12093.

(36) Yang, D.; Fan, X.; Zhang, F.; Hu, Y.; Luo, Z. Electronic and Magnetic Properties of Defected Monolayer WSe2 with Vacancies. *Nanoscale Res. Lett.* **2019**, *14* (1), 192. https://doi.org/10.1186/s11671-019-3002-2.

(37) Sahin, H.; Tongay, S.; Horzum, S.; Fan, W.; Zhou, J.; Li, J.; Wu, J.; Peeters, F. M. Anomalous Raman Spectra and Thickness-Dependent Electronic Properties of WSe${}_{2}$. *Phys. Rev. B* **2013**, *87* (16), 165409. https://doi.org/10.1103/PhysRevB.87.165409.

(38) Rehman, J.; Ali, R.; Ahmad, N.; Lv, X.; Guo, C. Theoretical Investigation of Strain-Engineered WSe2 Monolayers as Anode Material for Li-Ion Batteries. *J. Alloys Compd.* **2019**, *804*, 370–375. https://doi.org/10.1016/j.jallcom.2019.07.040.

(39) Zhou, L.; Fu, L. Strain Regulation of Two-Dimensional Transition Metal DICHALCOGENIDES. *Chin. Sci. Bull.* **2019**, *64* (17), 1817–1831. https://doi.org/10.1360/N972019-00236.

(40) Liu, S.; Yuan, K.; Xu, X.; Yin, R.; Lin, D.-Y.; Li, Y.; Watanabe, K.; Taniguchi, T.; Meng, Y.; Dai, L.; Ye, Y. Hysteresis-Free Hexagonal Boron Nitride Encapsulated 2D Semiconductor Transistors, NMOS and CMOS Inverters. *Adv. Electron. Mater.* **2019**, *5* (2), 1800419. https://doi.org/10.1002/aelm.201800419.

(41) Lin, S.; Kim, Y.-B.; Lombardi, F. Design and Analysis of a 32 Nm PVT Tolerant CMOS SRAM Cell for Low Leakage and High Stability. *Integration* **2010**, *43* (2), 176–187. https://doi.org/10.1016/j.vlsi.2010.01.003.

(42) Xu, J.; Shim, J.; Park, J.-H.; Lee, S. MXene Electrode for the Integration of WSe2 and MoS2 Field Effect Transistors. *Adv. Funct. Mater.* **2016**, *26* (29), 5328–5334. https://doi.org/10.1002/adfm.201600771.

(43) Yu, L.; Zubair, A.; Santos, E. J. G.; Zhang, X.; Lin, Y.; Zhang, Y.; Palacios, T. High-Performance WSe2 Complementary Metal Oxide Semiconductor Technology and Integrated Circuits. *Nano Lett.* **2015**, *15* (8), 4928–4934. https://doi.org/10.1021/acs.nanolett.5b00668.

(44) Smyth, C. M.; Addou, R.; McDonnell, S.; Hinkle, C. L.; Wallace, R. M. WSe2-Contact Metal Interface Chemistry and Band Alignment under High Vacuum and Ultra High Vacuum Deposition Conditions. *2D Mater.* **2017**, *4* (2), 025084. https://doi.org/10.1088/2053-1583/aa6bea.

(45) Prakash, A.; Appenzeller, J. Bandgap Extraction and Device Analysis of Ionic Liquid Gated WSe2 Schottky Barrier Transistors. *ACS Nano* **2017**, *11* (2), 1626–1632. https://doi.org/10.1021/acsnano.6b07360.

(46) Thakar, K.; Lodha, S. Multi-Bit Analog Transmission Enabled by Electrostatically Reconfigurable Ambipolar and Anti-Ambipolar Transport. *ACS Nano* **2021**, *15* (12), 19692–19701. https://doi.org/10.1021/acsnano.1c07032.

(47) Wang, H.; Gao, W.; Wen, P.; Yu, H.; Huang, Y.; Yue, Q.; Wang, X.; Huo, N. Light-Regulated Anti-Ambipolar Transport with Multi-Logic States in Metal-WSe2-Metal Transistor. *Adv. Electron. Mater.* **2022**, *8* (12), 2200649. https://doi.org/10.1002/aelm.202200649.

(48) Zhou, C.; Zhang, S.; Lv, Z.; Ma, Z.; Yu, C.; Feng, Z.; Chan, M. Self-Driven WSe2 Photodetectors Enabled with Asymmetrical van Der Waals Contact Interfaces. *Npj 2D Mater. Appl.* **2020**, *4* (1), 1–9. https://doi.org/10.1038/s41699-020-00179-9.

(49) Grillo, A.; Di Bartolomeo, A. A Current–Voltage Model for Double Schottky Barrier Devices. *Adv. Electron. Mater.* **2021**, *7* (2), 2000979. https://doi.org/10.1002/aelm.202000979.

(50) De Stefano, S.; Spuri, A.; Barbella, R.; Durante, O.; Mazzotti, A.; Sessa, A.; Di Bernardo, A.; Di Bartolomeo, A. Multilayer MoS2 Schottky Barrier Field Effect Transistor. *IEEE Open J. Nanotechnol.* **2025**, *6*, 51–57. https://doi.org/10.1109/OJNANO.2025.3553692.

(51) Di Bartolomeo, A.; Grillo, A.; Urban, F.; Iemmo, L.; Giubileo, F.; Luongo, G.; Amato, G.; Croin, L.; Sun, L.; Liang, S.-J.; Ang, L. K. Asymmetric Schottky Contacts in Bilayer MoS2 Field Effect Transistors. *Adv. Funct. Mater.* **2018**, *28* (28), 1800657. https://doi.org/10.1002/adfm.201800657.

(52) Wang, Z.; Li, Q.; Chen, Y.; Cui, B.; Li, Y.; Besenbacher, F.; Dong, M. The Ambipolar Transport Behavior of WSe2 Transistors and Its Analogue Circuits. *NPG Asia Mater.* **2018**, *10* (8), 703–712. https://doi.org/10.1038/s41427-018-0062-1.

(53) Pudasaini, P. R.; Oyedele, A.; Zhang, C.; Stanford, M. G.; Cross, N.; Wong, A. T.; Hoffman, A. N.; Xiao, K.; Duscher, G.; Mandrus, D. G.; Ward, T. Z.; Rack, P. D. High-Performance Multilayer WSe2 Field-Effect Transistors with Carrier Type Control. *Nano Res.* **2018**, *11* (2), 722–730. https://doi.org/10.1007/s12274-017-1681-5.

(54) Zhou, C.; Zhao, Y.; Raju, S.; Wang, Y.; Lin, Z.; Chan, M.; Chai, Y. Carrier Type Control of WSe2 Field-Effect Transistors by Thickness Modulation and MoO3 Layer Doping. *Adv. Funct. Mater.* **2016**, *26* (23), 4223–4230. https://doi.org/10.1002/adfm.201600292.

(55) Das, S.; Appenzeller, J. WSe2 Field Effect Transistors with Enhanced Ambipolar Characteristics. *Appl. Phys. Lett.* **2013**, *103* (10), 103501. https://doi.org/10.1063/1.4820408.

(56) Faella, E.; Intonti, K.; Viscardi, L.; Giubileo, F.; Kumar, A.; Lam, H. T.; Anastasiou, K.; Craciun, M. F.; Russo, S.; Di Bartolomeo, A. Electric Transport in Few-Layer ReSe2 Transistors Modulated by Air Pressure and Light. *Nanomaterials* **2022**, *12* (11), 1886. https://doi.org/10.3390/nano12111886.

(57) Urban, F.; Martucciello, N.; Peters, L.; McEvoy, N.; Di Bartolomeo, A. Environmental Effects on the Electrical Characteristics of Back-Gated WSe2 Field-Effect Transistors. *Nanomaterials* **2018**, *8* (11), 901. https://doi.org/10.3390/nano8110901.

(58) Ahmed, W.; Yang, L.; Zahoor, U.; Wang, F. Oxidation and Defects in WS2 and WSe2: The First-Principle Analysis of Their Monolayer and Bulk Structures. *J. Phys. Chem. Solids* **2025**, *204*, 112775. https://doi.org/10.1016/j.jpcs.2025.112775.

(59) Di Bartolomeo, A.; Urban, F.; Pelella, A.; Grillo, A.; Passacantando, M.; Liu, X.; Giubileo, F. Electron Irradiation of Multilayer PdSe2 Field Effect Transistors. *Nanotechnology* **2020**, *31* (37), 375204. https://doi.org/10.1088/1361-6528/ab9472.

(60) Wu, Z.; Luo, Z.; Shen, Y.; Zhao, W.; Wang, W.; Nan, H.; Guo, X.; Sun, L.; Wang, X.; You, Y.; Ni, Z. Defects as a Factor Limiting Carrier Mobility in WSe2: A Spectroscopic Investigation. arXiv August 6, 2016. https://doi.org/10.48550/arXiv.1608.02043.

(61) Lee, S.-Y.; Kim, S.-H.; Watanabe, K.; Taniguchi, T.; Yee, K.-J. Role of Hexagonal Boron Nitride Configuration in Gate-Induced Hysteresis of WSe2 Field-Effect Transistors. *Curr. Appl. Phys.* **2024**, *65*, 41–46. https://doi.org/10.1016/j.cap.2024.06.003.

(62) Shi, Y.; Sang, D.; Li, C.; Ge, S.; Yu, C.; Wang, Q.; Xiao, D. Recent Progress of Optoelectronic Applications Based on 2D WSe2 Nanomaterials and Heterostructures: A Review. *J. Mater. Chem. C* **2025**, *13* (36), 18555–18574. https://doi.org/10.1039/D5TC01545F.

(63) Wang, M.; Wang, C.-Y.; Wu, C.; Li, Q.; Pan, C.; Wang, C.; Liang, S.-J.; Miao, F. S-Type Negative Differential Resistance in Semiconducting Transition-Metal Dichalcogenides. *Adv. Electron. Mater.* **2019**, *5* (9), 1800853. https://doi.org/10.1002/aelm.201800853.

(64) Huo, S.; Qu, H.; Meng, F.; Zhang, Z.; Yang, Z.; Zhang, S.; Hu, X.; Wu, E. Negative Differential Resistance with Ultralow Peak-to-Valley Voltage Difference in Td-WTe_2 /2H-MoS_2 Heterostructure. *Nano Lett.* **2024**, *24* (38), 11937–11943. https://doi.org/10.1021/acs.nanolett.4c03263.

(65) Lee, T.; Jung, K.-S.; Seo, S.; Lee, J.; Park, J.; Kang, S.; Park, J.; Kang, J.; Ahn, H.; Kim, S.; Lee, H. W.; Lee, D.; Kim, K. S.; Kim, H.; Heo, K.; Kim, S.; Bae, S.-H.; Kang, S.; Kang, K.; Kim, J.; Park, J.-H. Junctionless Negative-Differential-Resistance Device Using 2D Van-Der-Waals Layered Materials for Ternary Parallel Computing. *Adv. Mater.* **2024**, *36* (24), 2310015. https://doi.org/10.1002/adma.202310015.

(66) Kim, J. H.; Moon, B. H.; Han, G. H. Anti-Ambipolar Transport and Logic Operation in Two-Dimensional Field-Effect Transistors Using in-Series Integration of GeAs and SnS2. *Appl. Phys. Lett.* **2024**, *124* (12), 123104. https://doi.org/10.1063/5.0197983.

(67) Yao, H.; Wu, E.; Liu, J. Frequency Doubler Based on a Single MoTe2/MoS2 Anti-Ambipolar Heterostructure. *Appl. Phys. Lett.* **2020**, *117* (12), 123103. https://doi.org/10.1063/5.0018882.

(68) *Anti-ambipolar behavior and photovoltaic effect in p-MoTe2/n-InSe heterojunctions - Journal of Materials Chemistry C (RSC Publishing)*. https://pubs.rsc.org/en/content/articlelanding/2021/tc/d1tc02497c (accessed 2025-09-20).

(69) *Robust Anti-Ambipolar Behavior and Gate-Tunable Rectifying Effect in van der Waals p–n Junctions | ACS Applied Electronic Materials*. https://pubs.acs.org/doi/abs/10.1021/acsaelm.2c01120 (accessed 2025-11-21).

(70) *Anti-Ambipolar Field-Effect Transistors Based On Few-Layer 2D Transition Metal Dichalcogenides | ACS Applied Materials & Interfaces*. https://pubs.acs.org/doi/10.1021/acsami.6b02513 (accessed 2025-11-21).

(71) Han, H.; Zhang, B.; Zhang, Z.; Wang, Y.; Liu, C.; Singh, A. K.; Song, A.; Li, Y.; Jin, J.; Zhang, J. Light-Triggered Anti-Ambipolar Transistor Based on an In-Plane Lateral Homojunction. *Nano Lett.* **2024**, *24* (28), 8602–8608. https://doi.org/10.1021/acs.nanolett.4c01679.

(72) Wang, H.; Gao, W.; Wen, P.; Yu, H.; Huang, Y.; Yue, Q.; Wang, X.; Huo, N. Light-Regulated Anti-Ambipolar Transport with Multi-Logic States in Metal-WSe2-Metal Transistor. *Adv. Electron. Mater.* **2022**, *8* (12), 2200649. https://doi.org/10.1002/aelm.202200649.

(73) *Multi-Bit Analog Transmission Enabled by Electrostatically Reconfigurable Ambipolar and Anti-Ambipolar Transport | ACS Nano*. https://pubs.acs.org/doi/full/10.1021/acsnano.1c07032 (accessed 2025-11-21).

(74) *Vertical Charge Transport and Negative Transconductance in Multilayer Molybdenum Disulfides | Nano Letters*. https://pubs.acs.org/doi/10.1021/acs.nanolett.7b02161 (accessed 2025-11-21).

(75) Paul, A. K.; Kuiri, M.; Saha, D.; Chakraborty, B.; Mahapatra, S.; Sood, A. K.; Das, A. Photo-Tunable Transfer Characteristics in MoTe2–MoS2 Vertical Heterostructure. *Npj 2D Mater. Appl.* **2017**, *1* (1), 17. https://doi.org/10.1038/s41699-017-0017-3.

(76) Chen, S.; Jin, J.; Wang, W.; Wang, S.; Du, X.; Wang, F.; Ma, L.; Wang, J.; Wang, C.; Zhang, X.; Liu, Q. Thermally Tunable Anti-Ambipolar Heterojunction Devices. *Phys. Chem. Chem. Phys.* **2024**, *26* (35), 23438–23446. https://doi.org/10.1039/D4CP02937B.

(77) Kobashi, K.; Hayakawa, R.; Chikyow, T.; Wakayama, Y. Interface Engineering for Controlling Device Properties of Organic Antiambipolar Transistors. *ACS Appl. Mater. Interfaces* **2018**, *10* (3), 2762–2767. https://doi.org/10.1021/acsami.7b14652.

(78) Gusakova, J.; Wang, X.; Shiau, L. L.; Krivosheeva, A.; Shaposhnikov, V.; Borisenko, V.; Gusakov, V.; Tay, B. K. Electronic Properties of Bulk and Monolayer TMDs: Theoretical Study Within DFT Framework (GVJ-2e Method). *Phys. Status Solidi A* **2017**, *214* (12), 1700218. https://doi.org/10.1002/pssa.201700218.

Conclusions

This thesis explored the relation between material properties, electronic transport and optoelectronic response in representative TMD-based devices, focusing on how surface chemistry, interface states, and device architecture jointly determine performance, stability, and functionality in 2D semiconductor platforms.

Across all the systems investigated, it emerges that the electrical and optoelectronic response of 2D semiconductors in device operation, while intrinsically versatile, is strongly influenced by extrinsic factors, such as adsorption-driven doping, interface quality, and contact barriers.

In Chapter 3, the oxidation-driven evolution of $ZrSe_2$ highlighted the challenges associated with long-term material stability in air-sensitive group-IV TMDs. Oxidation was shown to initiate preferentially at reactive sites such as edges and defects, leading to progressive structural and chemical transformation. While native oxide formation may be of conceptual interest, these findings emphasize the importance of encapsulation strategies and interface control as prerequisites for reliable device integration.

Chapter 4 demonstrated that reversible surface interactions and defect-mediated trapping can modulate electrical transport and photoresponse in few-layer ReS_2-based FETs. Pressure- and temperature-dependent measurements revealed a wide range of behaviours under controlled external conditions and provided insight into the competition between surface-related effects and contact-limited transport, confirming that interface traps represent a key factor in determining device speed and reproducibility.

In Chapter 5, moving beyond planar architectures, mixed-dimensional ReS_2/Si heterojunctions provided a more robust platform than phototransistor geometries, as the built-in electric field of the vertical junction enabled faster and more reproducible photodetection. Importantly, interfacial trapping dynamics were also found to support trap-assisted amplification mechanisms, contributing to the high responsivity values observed.

Finally, Chapter 6 illustrated that the intrinsic sensitivity of ambipolar TMD transistors to electrostatic gating, contact barriers, and interface traps enables access to optoelectronic functionalities beyond conventional photodetection. $MoTe_2$ devices exhibited gate-tunable bidirectional photoconductivity driven by trap-assisted processes, while WSe_2 transistors showed a light-induced transition toward anti-ambipolar transport through the interplay between contact Schottky barrier and efficient photogenerated carrier separation. These behaviours highlight the potential of TMD transistors for reconfigurable and neuromorphic-inspired optoelectronic functionalities.

Overall, this thesis provides a coherent experimental framework connecting material stability, interface control, and device-level optimization in TMD-based optoelectronics. By systematically examining how defects, environmental interactions, and architecture shape charge transport and photoresponse, the work contributes to a deeper understanding of both the opportunities and the challenges that must be addressed for the development of reliable, efficient, and reconfigurable 2D optoelectronic technologies.

Final Notes

The experimental work presented in this thesis was carried out with the direct involvement of the author, who performed the electrical and optoelectronic characterization of the devices, as well as the multi-technique data analysis, interpretation, scientific writing, and dissemination of the results. Regarding device fabrication, the author fabricated the $ZrSe_2$ devices discussed in Chapter 3 and developed the optimized ReS_2/Si heterostructure architecture presented in Chapter 5. The main outcomes of this research have been published in peer-reviewed journals and presented at international conferences. A complete list of publications and conference contributions is provided in Appendices 1 and 2.

The author would like to thank the collaborating universities and research institutions for providing facilities, materials, and technical support, including University of Salerno, CNR-SPIN Salerno, the Tyndall National Institute, University College Cork, the University of Exeter, the University of Leeds, the University of Rome "Tor Vergata", and the University of Texas at Dallas.

Appendix 1: List of publications

1. **Oxidation-driven structural, chemical and electrical transformation in ZrSe2**
   K. Intonti*, H. Neill, S. J. Kheirabadi, Z. Aslam, T. Moorsom, J. S. Prasanna, R. Addou, L. Persichetti, A. Sgarlata, L. Camilli, S. O'Sullivan, V. Patil, D. Singh, B. Sheehan, P. K. Hurley, L. Ansari, A. Di Bartolomeo, F. Gity
   Materials Today Advances, https://doi.org/10.1016/j.mtadv.2025.100654

2. **Pressure-dependent photoconductivity in two dimensional ReS2**
   K. Intonti, E. Faella, A. Kumar, L. Viscardi, F. Giubileo, H. T. Lam, K. Anastasiou, M.
   Craciun, S.Russo, and A. Di Bartolomeo
   IEEE Xplore, 10.1109/NMDC57951.2023.10343870

3. **Temperature dependent conduction and photoresponse in few-layer ReS2**
   K. Intonti, E. Faella, A. Kumar, L. Viscardi, F. Giubileo, N. Martucciello, H. T. Lam, K. Anastasiou, M. Craciun, S. Russo, A. Di Bartolomeo
   ACS Applied Materials & Interfaces, ***https://doi.org/10.1021/acsami.3c12973***

4. **ReS2/Si 2D/3D vertical heterojunction as a self-powered photodiode**
   K. Intonti, A. Pelella, H. Neill, V. Patil, P. K. Hurley, L. Ansari, F. Gity, A. Di Bartolomeo
   Applied Physics Letters, https://doi.org/10.1063/5.0231243

5. **Gate-Driven Bi-Directional Photoresponse in MoTe2 Based Field Effect Transistors**
   K. Intonti, A. Sessa, H. Neill, V. Patil, A. Pelella, N. Martucciello, L. Ansari, P. K Hurley, F. Gity, A. Di Bartolomeo
   IEEE Xplore, ***10.1109/NANO63165.2025.11113515***

6. **Ambipolar to anti-ambipolar light-induced transition in WSe2-based FETs**
   K. Intonti, A. Mazzotti, A. Pelella, F. Giubileo, N. Martucciello, S. O'Sullivan, V. Patil, P. K Hurley, L. Ansari, F. Gity, A. Di Bartolomeo.
   Materials Horizons, 10.1039/D5MH01871D

7. **Hysteresis and photoconductivity of few-layer ReSe2 field effect transistors enhanced by air pressure**
   K. Intonti, E. Faella, L. Viscardi, A.Kumar, O. Durante, F. Giubileo, M. Passacantando, H. T. Lam, A. Konstantinos, M. Craciun, S. Russo and A. Di Bartolomeo
   Advanced Electronic Materials, https://doi.org/10.1002/aelm.202300066

8. **Role of interface and bulk traps on the capacitance-voltage characteristics of WS2/Al2O3/Si capacitors**
   K. Intonti*, E. Coleman, A. Blake, C. Lyons, A. Hydes, A. Di Bartolomeo, F. Gity, P. K. Hurley
   Solid-State Electronics, https://doi.org/10.1016/j.sse.2023.108697

9. **Subthreshold current suppression in two-dimensional ReS2 field-effect transistors at high temperatures**
   O. Durante, **K. Intonti**, L. Viscardi, S. De Stefano, E. Faella, A. Kumar, A. Pelella, F. Romeo, F. Giubileo, M. S. Alghamdi, M. A. Alshehri, M. Craciun, S. Russo, A. Di Bartolomeo
   ACS Applied Nano Materials, https://doi.org/10.1021/acsanm.3c03685

10. **Electric Transport in Few-Layer $ReSe_2$ Transistors Modulated by Air Pressure and Light**
    E. Faella, **K. Intonti**, L. Viscardi, F. Giubileo, A. Kumar, H. T. Lam, K. Anastasiou, M. F. Cracium, S. Russo, A. Di Bartolomeo
    Nanomaterials, https://www.mdpi.com/2079-4991/12/11/1886

11. **Multilayer WS2 for low-power visible and near-infrared phototransistors**
    A. Pelella, **K. Intonti**, O. Durante, A. Kumar, L. Viscardi, S. De Stefano, P. Romano, F.
    Giubileo, H. Neill, V. Patil, L. Ansari, B. Roycroft, P. K. Hurley, F. Gity, A. Di Bartolomeo
    Discover Nano, https://doi.org/10.1186/s11671-024-04000-0

12. **Two-dimensional α-In2Se3 field effect transistor for wide-band photodetection and non-volatile memory**
    A. Pelella, **K. Intonti**, L. Viscardi, O. Durante, D. Capista, M. Passacantando, F. Giubileo, M. A. S Alshehri, M. S. G Alghamdi, M. Craciun, S. Russo, and A. Di Bartolomeo
    Journal of Physics and Chemistry of Solids,
    https://doi.org/10.1016/j.jpcs.2023.111653

13. **Memory effect and coexistence of negative and positive photoconductivity in black phosphorus field effect transistor for neuromorphic vision sensors-**
A. Kumar, **K. Intonti**, L. Viscardi, O. Durante, A. Pelella, O. Kharsah, S. Sleziona, F. Giubileo, N. Martucciello, P. Ciambelli, M. Schleberger, A. Di Bartolomeo
Materials Horizons, https://doi.org/10.1039/D4MH00027G

14. **Interface-Engineered MoSe2/CrOCl Complementary FETs Integrating Logic, Memory, and Neuromorphic Functions**
L. Viscardi, **K.Intonti**, A. Mazzotti, A. Pelella, F. Giubileo, Y. Guo, M. Sun, Z.V.Han, H. Wang, A. Di Bartolomeo
Small Structures, https://doi.org/10.1002/sstr.202500840

15. **Black phosphorus nanosheets in field effect transistors with Ni and NiCr contacts**
L. Viscardi, **K. Intonti**, A. Kumar, E. Faella, A. Pelella, F. Giubileo, S. Sleziona, O. Kharsah, M. Schleberger, A. Di Bartolomeo
Physica Status Solidi b, https://doi.org/10.1002/pssb.202200537

16. **Metal-semiconductor Schottky diode with Landauer's formalism**
A.Di Bartolomeo, **K. Intonti**, L. Peluso, R. Di Marco, G. Vocca, F. Romeo, F. Giubileo, A. Grillo, E. Orhan.
Nano Express, 10.1088/2632-959X/ade460

17. **Two-Dimensional MoS2 Logic Inverter**
Mazzotti, **K. Intonti**, L. Viscardi, O. Durante, A. Spuri, A. Di Bernardo, A. Di Bartolomeo
IEEE Xplore, 10.1109/NANO63165.2025.11113683

18. **Temperature behavior and logic circuit applications of InAs nanowire-based field-effect transistors**
L. Viscardi, E. Faella, **K. Intonti**, F. Giubileo, V. Demontis, D. Prete, V. Zannier, L. Sorba, F. Rossella, and A. Di Bartolomeo
Materials Science in Semiconductor Processing, 10.1016/j.mssp.2024.108167

19. **n-Type GaSe Thin Flake for Field Effect Transistor, Photodetector, and Optoelectronic Memory**
A. Kumar, A. Pelella, **K. Intonti**, L. Viscardi, O. Durante, F. Giubileo, P. Romano, H. Neill, V. Patil, L. Ansari, P. K. Hurley, F. Gity, A. Di Bartolomeo
Advanced Electronic Materials, https://doi.org/10.1002/aelm.202400010

20. **WS2 Nanotube Transistor for Photodetection and Optoelectronic Memory Applications**
A. Pelella, A. Kumar, **K. Intonti**, O. Durante, S. De Stefano, X. Han, Z. Li, Yao Guo, F. Giubileo, L. Camilli, M. Passacantando, A. Zak, A. Di Bartolomeo
Small, https://doi.org/10.1002/smll.202403965

21. **Dominant n-type conduction and fast photoresponse in BP/MoS2 heterostructures**
L. Viscardi, O. Durante, S. De Stefano, **K. Intonti**, A. Kumar, A. Pelella, F. Giubileo, O.Kharsah, L. Daniel, S. Sleziona, M. Schleberger, A. Di Bartolomeo
Surfaces and Interfaces, 10.1016/j.surfin.2024.104445

22. **Black Phosphorus Unipolar Transistor, Memory, and Photodetector**
A. Kumar, L. Viscardi, E. Faella, F. Giubileo, **K. Intonti**, A. Pelella, S. Sleziona, O. Kharsah, M. Schleberger, A. Di Bartolomeo
Journal of Materials Science, https://doi.org/10.1007/s10853-023-08169-0

23. **Temperature Dependent Black Phosphorus Transistor and Memory**
A. Kumar, L. Viscardi, E. Faella, F. Giubileo, **K. Intonti**, A. Pelella, S. Sleziona, O. Kharsah, M. Schleberger, A. Di Bartolomeo
Nano Express, https://doi.org/10.1088/2632-959X/acbe11

24. **Hierarchical WSe2 Nanoflowers for Efficient Field Emission**
F. Giubileo, E. Faella, S. De Stefano, L. Viscardi, **K. Intonti**, A. Mazzotti, A. Sessa, O. Durante, A. Pelella, G. Cheng, C. Mattevi, M. Passacantando, A. Di Bartolomeo
Advanced Electronic Materials, 10.1002/aelm.202500490

25. **Single WS_2 Nanotube-Based Field Effect Transistor: Ambipolar Conduction and Self-Powered Photodetection**
L. Viscardi, A. Pelella, F. Giubileo, L. Camilli, **K. Intonti**, M. Passacantando, Y. Guo, A. Zak, A. Di Bartolomeo
IEEE Xplore, 10.1109/NANO63165.2025.11113756

26. **Zinc oxide tetrapods as novel field emitters with low turn-on voltage**
F. Giubileo, E. Faella, A. Kumar, S. De Stefano, L. Viscardi, **K. Intonti**, O. Durante, A. Pelella, A. Mazzotti, N. Martucciello, E. Beliayev, Y. Kumar Mishra, M. Passacantando, A. Di Bartolomeo
Nano Express, 10.1088/2632-959X/ad9c9f

27. **Optoelectronic Memory in 2D MoS_2 Field Effect Transistor**
A. Kumar, E. Faella, O. Durante, F. Giubileo, A. Pelella, L. Viscardi, **K. Intonti**, S. Sleziona; M. Schleberger, A. Di Bartolomeo
Journal of Physics and Chemistry of Solids, https://doi.org/10.1016/j.jpcs.2023.111406

28. **Temperature-dependent photoconductivity in two-dimensional MoS_2 transistors**
A. Di Bartolomeo, A. Kumar, O. Durante, A. Sessa, E. Faella, L. Viscardi, **K. Intonti**, F. Giubileo, N. Martucciello, P. Romano, S. Sleziona, and M. Schleberger
Materials Today Nano,_https://doi.org/10.1016/j.mtnano.2023.100382

29. **Ambipolar conduction in gated tungsten disulphide nanotube**
A. Pelella , L. Camilli , F. Giubileo , A. Zak, M. Passacantando , Y. Guo , **K. Intonti** , A. Kumar, A. Di Bartolomeo
Nanoscale, 10.1039/D4NR04877F

30. **Flexible cold cathodes based on graphite nanoplatelet coatings on silicone rubber**
F. Giubileo, G. Carotenuto, A. Longo, M. Palomba, E. Faella, M. Lettieri, L. Viscardi, **K. Intonti**, A. Kumar, A. Pelella, M. Passacantando, A. Di Bartolomeo
Journal of Materials Chemistry C, 10.1039/D5TC02257F

Appendix 2: List of conference contributions

- **Role of Interface and Bulk Traps on the Capacitance-Voltage Characteristic of WS2/Al2O3/Si Capacitors**
  K. Intonti*, E. Coleman, A. Blake, C. Lyons, A. Hydes, A. Di Bartolomeo, F. Gity, P. K. Hurley
  23rd Conference on insulating films on semiconductors (INFOS 23)- Pizzo (VV), Italy
  Poster presentation

- **Investigation of the photo-response of few layer ReS2 field effect transistors at different pressures**
  K. Intonti, E. Faella, L. Viscardi, A.Kumar, O. Durante, F. Giubileo, M. Passacantando, H. T. Lam, A. Konstantinos, M. Craciun, S. Russo and A. Di Bartolomeo
  20^{th} international Conference on Nanoscience and Nanotechnologies (NN23)- Thessaloniki, Greece
  Poster presentation

- **Pressure-dependent photoconductivity in two dimensional ReS2**
  K. Intonti, E. Faella, A. Kumar, L. Viscardi, F. Giubileo, H.T. Lam, K. Anastasiou, M.Craciun, S.Russo , A. Di Bartolomeo
  IEEE Nanotechnology Materals and Devices 23 (IEEE NMDC 23) – Paestum, Italy
  Oral presentation

- **Investigation of the photoresponse of few-layer ReSe2 field effect transistors at different pressures**
  K. Intonti, E. Faella, L. Viscardi, A.Kumar, O. Durante, F. Giubileo, M. Passacantando, H. T. Lam, A. Konstantinos, M. Craciun, S. Russo and A. Di Bartolomeo
  III International Conference "Condensed Matter & Low Temperature Physics 2023" (CM & LTP 23) – Kharkiv,Ukraine
  Oral presentation

- **Impact of pressure on the photoresponse of ReS2-Based field effect transistors**
  K. Intonti, E. Faella, A. Kumar, L. Viscardi, F. Giubileo, H.T. Lam, K. Anastasiou, M.Craciun, S.Russo , A. Di Bartolomeo
  109° Congress of Italian Physics Society - Fisciano, Italy
  Oral presentation

- **Multi-mode photodetection of van der Waals ReS2/Si 2D/3D heterostructure**
  K. Intonti, A. Pelella, H. Neill, V. Patil, P.K. Hurley, L. Ansari, F. Gity, A. Di Bartolomeo
  Graphene 24 - Madrid, Spain
  Poster presentation

- **Gate-driven bi-directional photoresponse in MoTe2-based field effect transistors**
  K. Intonti, A. Sessa, H. Neill, V. Patil, A. Pelella, N. Martucciello, L. Ansari, P. K Hurley, F. Gity, A. Di Bartolomeo
  25th IEEE International Conference on Nanotechnology (IEEE NANO 2025)- Washington DC, USA
  Oral presentation

- **Study of oxidation and degradation mechanisms of ZrSe2 in ambient conditions**
  K. Intonti, H.Neill, V.Patil, L.Ansari, S.J. Kheirabadi , P.K.Hurley, A. Di bartolomeo, F. Gity
  NINETEENTH Conference- Salerno, Italy
  Oral presentation

- **Anti-ambipolarismin WSe2-based field effect transistor induced by light**
  K.Intonti
  Surface and Electronic Properties of Low Dimensional Materials (SELDoM 2025)- Naples, Italy
  Poster Presentation